Magnetic order, spin-induced ferroelectricity and structural studies in multiferroic $Mn_{1-x}Co_xWO_4$

by

IRENE URCELAY OLABARRIA

THESIS SUBMITTED TO THE
DEPARTAMENT DE FÍSICA OF THE FACULTAT DE CIÈNCES OF THE
UNIVERSITAT AUTÒNOMA DE BARCELONA
FOR THE DEGREE OF
DOCTOR OF PHILOSOPHY

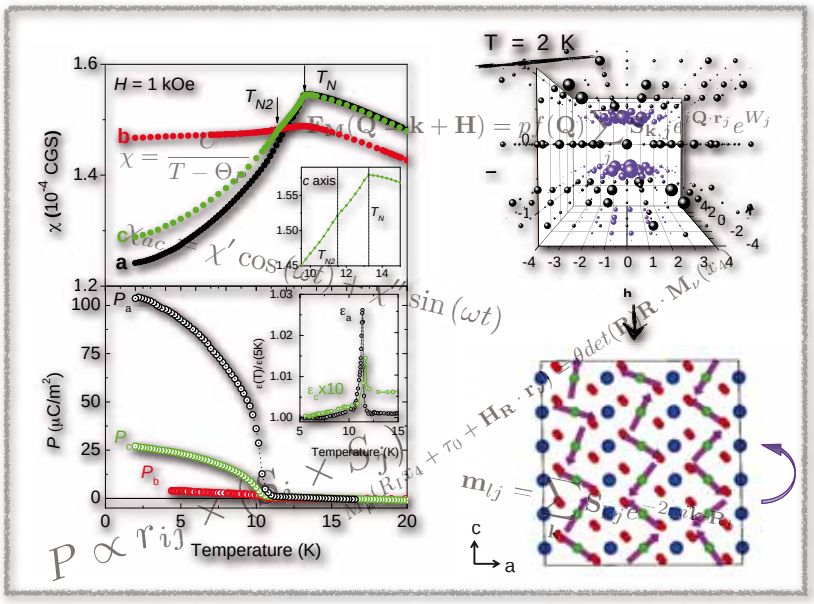

SUPERVISORS:
DR. VASSIL SKUMRYEV
DR. ERIC RESSOUCHE
DR. JOSE LUIS GARCÍA MUÑOZ

December, 2012

Universitat Autònoma de Barcelona

Magnetic order, spin-induced ferroelectricity and structural studies in multiferroic $Mn_{1-x}Co_xWO_4$

by

IRENE URCELAY OLABARRIA

THESIS SUBMITTED TO THE
DEPARTAMENT DE FÍSICA OF THE FACULTAT DE CIÈNCES OF THE
UNIVERSITAT AUTÒNOMA DE BARCELONA
FOR THE DEGREE OF
DOCTOR OF PHILOSOPHY

SUPERVISORS:
DR. VASSIL SKUMRYEV
DR. ERIC RESSOUCHE
DR. JOSE LUIS GARCÍA MUÑOZ

December, 2012

Dr. Vassil Skumryev, Dr. Eric Ressouche and
Dr. José Luis García Muñoz

CERTIFY

that the work reported in the present by Irene Urcelay Olabarria, entitled "Magnetic order, spin-induced ferroelectricity and structural studies in multiferroic $Mn_{1-x}Co_xWO_4$", has been done at the Institut Laue Langevin in Grenoble under their supervision. This work constitutes the Doctoral Thesis Memory submitted by the interested person to the Facultat de Ciències de la Universidad Autònoma de Barcelona to apply for the degree Doctor of Philosophy.

Bellaterra, 19^{th} of December, 2012.

Signature:	Signature:	Signature:
Dr. José Luis García Muñoz Research Professor of the Instituto de Ciencia de Materiales de Barcelona, Consejo Superior de Investigaciones Científicas.	Dr. Eric Ressouche Research Director, CEA/Grenoble, INAC/SPSMS.	Dr. Vassil Skumryev Professor of the Institut Català de Recerca i Estudis Avançats (ICREA) in the Dep. de Física of the Universitat Autònoma de Barcelona.

Ama ta aitandako

Acknowledgements

Time flies. Actually very fast. It is already more than three years since this story began. I have found many people in the path who, in some way or another, helped and supported me. I would like to thank them all, because without them reaching this point of the adventure would have been tougher than what it has been, or even impossible.

First of all, I would like to thank the Institut Laue-Langevin for giving me a three-year fellowship to do the thesis. I would like to thank Prof. J. Rodriguez-Carvajal for kindly accepting me in the Diffraction Group, as well as to all the members of this group.

This work would not be possible without the hundreds of hours of beam time used in distinct installations. Therefore, I am grateful to the Institut Laue-Langevin, to the CEA-Grenoble (CRG-D23), to the Spanish CRG-D15, Laboratoire Léon Brillouin and European Synchrotron Radiation Facility for the provision of beam time.

I acknowledge the financial support from MICINN (Spanish government) under Project No. MAT2009-09308.

I would like to thank my supervisors, for their help and guide.

I am very grateful to Prof. Alexander Mukhin and his team for providing us with the samples and the electric measurements as well as for the useful discus-

sions we have had.

I would like to thank Prof. Arsen Goukasov and Dr. Caroline Curfs for their help in the experiments performed in the Laboratoire Léon Brillouin and European Synchrotron Radiation Facility, respectively.

Thanks to Dr. N. Martin and Dr. L. P. Regnault we could perform a Larmor-diffraction experiment; Merci beaucoup!

Dr. N. Qureshi for kindly cutting the samples, which made easier certain diffraction experiments.

También quisiera agradecer al Prof. J. M. Perez-Mato por todo lo que me ha enseñado y por lo que me ha ayudado. El estudio de la supersimetría de las estructuras magnéticas incommensurables no habría sido posible sin su dedicación.

Por supuesto, no quiero olvidarme de compañeros y amigos, por las (habitualmente largas) discusiones de distinta índole (científicas, políticas, lingüísticas, muchas de ellas totalmente absurdas pero divertidísimas), cafés, cervezas, paseos en las montañas Grenobloises, excursiones . . . en definitiva por haber hecho que estos tres años estén llenos de buenos recuerdos: Óscar, Laura C., Laura O., Alberto, Edurne, Carlos, Luiso, Inés, Pedro y otros muchos.

Gracias Jessica por haberme ayudado en mis cortas estancias en Barcelona.

Eskerrik asko Txoli! Nahiz eta urrin egon eta gutxitan ikusi gan, hor zarelako beti!

Maitetxu! Eskerrik asko hor egotearren. . . eta zelako azken hilabetiak! Ospatu biharra dago! Bixok be nahikua aguantau dou alkarri. Eskerrik asko!!

Mersis Josu. Zure lanaren ondorio be badalako. Lehen aukera zuk eman zoztazulako. Zu barik ezinezkua izango zalako.

Eskerrik bereziena familiari, lan hau zeuon esfortzuaren fruitu be badalako.

Eta orain, uztak batzeko garaia da...

Preface

The manuscript summarizes the work done during the last three years in the Institut Laue Langevin (Grenoble) in collaboration with the Instituto de Ciencia de Materiales de Barcelona, the Universitat Autònoma de Barcelona and the Commissariat à l'énergie atomique et aux énergies alternatives (Grenoble).

Since ferroelectricity was found to be coupled to the magnetic order in $TbMnO_3$, there has been a renewed interest in multiferroics, both for fundamental reasons and for possible technological applications.

About five year ago, it was discovered that the electric polarization that emerges in $MnWO_4$ is coupled to a cycloidal magnetic structure. This material has three magnetic states: AF3 (13.5 K $\lesssim$ T $\lesssim$ 12.5 K), moments order collinearly along a direction $\hat{u}$ within the *ac* plane with a sinusoidally modulated amplitude and an incommensurate propagation vector $\mathbf{k}$ = (-0.214, $\frac{1}{2}$, 0.457); AF2 (12.5 K $\lesssim$ T $\lesssim$ 6.8 K), it presents an additional magnetic component along *b*, the propagation vector being the same. Thus, the magnetic ordering is an elliptical cycloidal spin structure within the *ub* plane. In this phase the electric polarization arises along the *b* axis and therefore, this is the multiferroic phase. AF1 (T $\lesssim$ 6.8 K), the magnetic structure is collinear (along $\hat{u}$) with $\mathbf{k}$ = ($\pm\frac{1}{4}$, $\frac{1}{2}$, $\frac{1}{2}$).

The succession of magnetic structures is induced by a strong magnetic competition which turns into magnetic frustration. The application of external fields or chemical substitution could unbalance the subtle equilibrium between the magnetic interactions. The work on the thesis was initiated by a publication in the

literature (on polycrystalline samples) which showed that a subtle substitution of manganese by cobalt induces changes and stabilizes the multiferroic structure at low temperatures. Moreover, new magnetic structures have been determined from neutron-powder experiments.

The thesis presents a study of the crystal and magnetic structures, and electric polarization of $Mn_{1-x}Co_xWO_4$ (x =0, 0.05, 0.10, 0.15 and 0.20) at zero and non-zero magnetic field. We have studied the interplay between the magnetic structure and the electric polarization. To achieve our purposes bulk magnetometry, pyroelectric measurements, neutron- and synchrotron-diffraction experiments have been carried out on single crystals.

The manuscript is organized in the following way:

(i) Part I, *Introduction*: multiferroics, magnetic structures, the studied materials and the experimental techniques used are introduced. At the end the interest and objectives of the thesis are enumerated.

(ii) Part II, *Magnetic, ferroelectric and structural properties of $Mn_{1-x}Co_xWO_4$ under zero magnetic field*.

(iii) Part III, *Magnetic-field-induced transitions*.

(iv) Part IV, *Summary and Conclusions*.

(v) Part V, *Appendices*.

Throughout the thesis I have participated in all neutron diffraction, synchrotron, and many of the bulk magnetic measurements, from the design of the experiments to the data analysis. The crystals and the electric polarization measurements were kindly provided by Prof. A. A. Mukhin, from the Prokhorov General Physics Institute (Moscow), with whom we closely collaborated.

Contents

Part I

Introduction

Chapter 1

Multiferroic and Magnetoelectric Materials

The concept of *multiferroicity* has attracted the attention of a large community of scientists due to its importance for the solid-state physics as well as because of possible technological applications that could be developed based on it. Along the lines of the first chapter, this concept will be introduced, focusing on those multiferroics that exhibit long range magnetic order and ferroelectricity simultaneously.

1.1 Brief historical survey of Multiferroic Magnetoelectric Materials (MMMs)

Magnetism and Electricity are both old fields in Physics. First steps in these disciplines were done by ancient civilizations who realized that lodestone and amber have amazing properties: both can attract different materials, however amber must be rubbed with cat's fur first. They did not understand the origin of these phenomena, but were able to use those materials for applications such as the compass. Nowadays the number of devices based on Magnetism and Electricity is countless, from very common and simple apparatus to very complex ones. This is a direct consequence of years of study: the more we know and understand the underlying mechanisms the more and more complex devices we can build. However, there is still a long way to find out all the mysteries that Magnetism and Electric-

ity hide, even more since it was observed that in some materials the magnetic and electric properties are coupled, i. e. since magnetoelectrics (and later multiferroics) were discovered.

It is more than a hundred years since the story of magnetoelectric materials started. In 1888 Röntgen [1] observed that a dielectric material moving in an electric field becomes magnetized, and in 1894 Pierre Curie [2], using symmetry considerations, foresaw theoretically the possibility of inducing electric polarization in a sample by applying a magnetic field, and vice versa, without having to move the sample. These are the first two references to magnetoelectric materials. This phenomenon consists of inducing either electric polarization by a magnetic field or magnetization by an electric field. Even if it was known long time ago, there were not experimental proofs until Astrov [3], in 1960, showed that Cr_2O_3, which is an antiferromagnetic material, is as well magnetoelectric. Astrov's work was actually inspired by the paper (published one year earlier) of Dzyaloshinskii [4] predicting, on the ground of symmetry considerations, that magnetoelectric effect could occur in Cr_2O_3.

In the 50's a new and revolutionary concept was born: *multiferroicity* [5, 6] (even though the name was given much later, in 1994, by H. Schmid [7]). By definition, multiferroic materials are those materials that exhibit more than one primary ferroic property simultaneously in the same phase. Ferromagnetism, ferroelectricity and ferroelasticity are primary ferroic properties[1], and denote materials where magnetization, electric polarization or deformation appear spontaneously, are stable and can be reversed following a hysteresis loop if a magnetic, electric or stress field is applied, respectively.

If a magnetoelectric material is ferromagnetic and ferroelectric in the same phase, it is a Magnetoelectric Multiferroic Material (MMM). One should be aware of the fact that not all the multiferroics are magnetoelectrics and vice versa. Figure 1.1 illustrates the classification of the materials taking into account their magnetic and electric properties.

1.2 Characteristics of MMMs

Intrinsic characteristics of ferroelectricity and ferromagnetism, which are often mutually exclusive, make MMM materials rare, in the sense that are not abundant

[1] Whether ferrotoroidicity is a primary ferroic property or not is still under debate in the community.

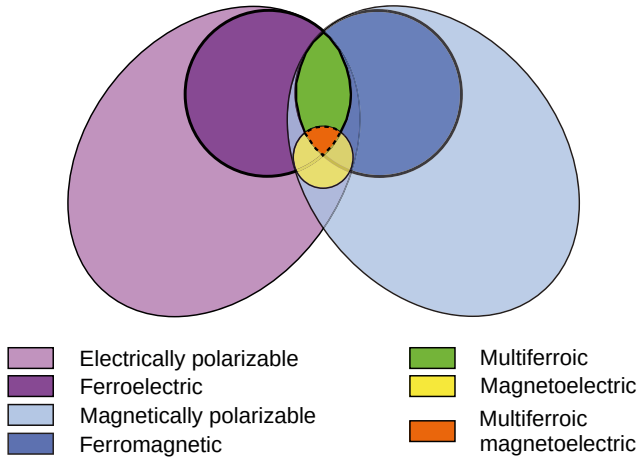

FIGURE 1.1: Classification of materials according to the electric and magnetic polarizability (adapted from Eerenstein *et. al.* [8]).

in nature [9].

- ◇ On one hand, each ferroic property has a different symmetry: the electric polarization is inverted under spatial inversion, magnetization is inverted under a time-reversal, and ferroelasticity is not inverted under either spatial or time-reversal operations. So, if the crystal structure of a compound contains a symmetry operation which reverses, for example, z into $-z$, electric polarization will never show up along the z axis (it would be compensated). In other words, Neumann's Principle has to be fulfilled: *the symmetry elements of the physical properties of the crystal have to include the symmetry operations of the point group of the crystal*. Thus, in order to have a multiferroic material it's symmetry must allow more than one primary ferroic property.

- ◇ On the other hand, each property requires different physical conditions that could exclude one or the other property. In the case of ferroelectrics, materials are insulators while most of the ferromagnetic materials are metals. Besides that, magnetism usually comes from incomplete d orbitals, whereas ferroelectricity often requires d^0 orbitals.

Nowadays the definition of multiferroics is more flexible and, frequently, antiferromagnetic (which often are insulators) and ferrimagnetic materials are also

considered as potential multiferroics. Therefore, in principle, the primary ferroic properties are not needed, but long range order. This broadening of the definition increases the amount of compounds that are considered as multiferroics and thus, as MMMs.

It is important to stress that unlike classic magnetoelectrics, MMM materials do not need any external field to become magnetically and electrically ordered in the same phase. However, since they are magnetoelectric both order parameters can be controlled by external fields, either magnetic or electric. This is why they become very interesting for technological applications. As an example, one could think about electronic devices where the magnetization is controlled by an electric field. Since electric current is no longer needed, energy losses produced by the heat coming from the Joule effect are avoided, and overheating of the system as well. For instance, nowadays, reading and writing systems of computers are based on Magnetic Random Access Memory (MRAM) devices but MagnetoElectric Random Access Memory (MERAM) are being developed with the hope that one day they could replace them [10].

1.3 Types of Magnetoelectric multiferroics

Magnetoelectric multiferroic materials are generally classified in two broad groups according to the interplay between ferroelectricity and the magnetic order: type I and type II [11].

1.3.1 Type I

This type of multiferroics were found first, and up to now they are the most numerous [6, 8, 12–22]. Their ferroelectricity and magnetism have different sources and appear rather independently. Usually ferroelectricity arises at higher temperatures than magnetic order does. This makes them bad candidates for technological applications. However, they are multiferroics at relatively high temperatures (the antiferromagnetic $BiFeO_3$ is a room temperature multiferroic [8]) and their electric polarization is rather big (10 - 100 $\mu C/cm^2$), qualities that work in their favor.

Whereas the origin of the magnetic order is always the same (see Chapter 2), there is a large variety of mechanisms that give rise to the ferroelectricity in these materials and hence, they can be classified according to that:

- ◇ Perovskite-like structures (ABO_3) are very interesting materials where different mechanisms can be used to induce ferroelectricity. One way is mixing d^0 and d^n ions in B position and consequently, the resulting ferroelectricity and magnetic order come from different origins.

- ◇ Materials with lone-pair atoms (which have outer free electrons), such as Bi^{3+} and Pb^{2+} are also good candidates for ferroelectrics. Hence, combining these ions with magnetic ones may lead to multiferroics. One of the most famous multiferroics $BiFeO_3$, belongs to this class [12–14].

- ◇ Ferroelectricity is often driven by charge ordering (see Ref. [15]), as in perovskite manganites [16, 17], magnetite [18–20] and frustrated $LuFe_2O_4$ [21] for example. This mechanism is based on the existence of inequivalent sites and bonds, the origin of which can have diverse nature.

- ◇ The geometry of the system itself may cause ferroelectricity, as it is the case of $YMnO_3$ where the rotation of the rigid polyhedra formed by Mn-O produces polarization, see Ref. [22].

1.3.2 Type II

This group is composed by materials in which ferroelectricity is induced by magnetism. Almost all such materials are multiferroics at relatively low temperature and show a strong coupling between the magnetism and the ferroelectricity, but the electric polarization is often weaker than in type I multiferroics.

They were discovered in the last decade and they are at the origin of the renewed interest in this field [23, 29–31]. The strong coupling between the magnetic ordering and the electric polarization was first reported by Kimura *et. al.* [23] when they showed that the electric polarization of $TbMnO_3$ rotates when a magnetic field is applied along a specific direction.

One can distinguish at least three subclasses depending on the origin of the electric polarization: non-collinear multiferroics, exchange-striction multiferroics and other spin electronic mechanisms.

- ◇ Non-collinear multiferroics: These are the most numerous type II materials. The ferroelectricity appears related to a specific spiral-like magnetic structure, which usually has a cycloidal component (see Chapter 2). The ferro-

electicity is in this case ruled by the following expression [24–28]:

$$\mathbf{P} \sim \mathbf{r}_{ij} \times (\mathbf{S}_i \times \mathbf{S}_j) \tag{1.1}$$

where $\mathbf{r}_{ij}$ is the vector between two neighboring spins, $\mathbf{S}_i$ and $\mathbf{S}_j$. According to this expression, the electric polarization is always perpendicular to the spin-chirality vector $(\mathbf{S}_i \times \mathbf{S}_j)$. In simple cases it can be translated to $\mathbf{P} \sim \mathbf{k} \times (\mathbf{S}_i \times \mathbf{S}_j)$, where $\mathbf{k}$ is the propagation vector of the magnetic structure. Then, in such cases, only magnetic structures with a cycloidal component would give rise to electric polarization. However, T. Arima [32] has shown that electric polarization can also show up in proper-screw structures ($\mathbf{k} \parallel \mathbf{S}_i \times \mathbf{S}_j$) in crystals with low symmetry, i. e. triclinic, monoclinic or trigonal crystals.

Several modulated magnetic structures are depicted in Figs. 1.2(a), 1.2(b) and 1.2(c), which are sinusoidal, cycloidal and screw-type structures respectively. In principle, if we restrict to the case where the polarization is linked to the cycloidal component of the magnetic structure, only Fig. 1.2(b) is multiferroic.

The mechanisms that drive the spin-induced electric polarization are still not firmly established. There are two main theories that could explain it: the Inverse-Dzyaloshinskii-Moriya interaction model (see Section 2.4 in Chapter 2) or the spin-current model[2]. Nevertheless, the role of the magnetic frustration is undeniable, since this is what enforces the complex magnetic structures. All these concepts will be explained in following sections.

◇ Exchange-striction multiferroics: Some examples of collinear magnetic orders coupled to ferroelectricity have been found rather recently [33, 38]. In these systems the exchange striction is usually the cause of the electric polarization. Choi *et. al.* reported in Ref. [33] that in Ca_3CoMnO_6 the polar phase emerges coupled to the magnetic transition into a magnetic structure of the type ↑↑↓↓. The different exchange striction between parallel and antiparallel moments give rise to a ferroelectric distortion. There is still some controversy whether $RNiO_3$ nickelates belong to this group or not because there are several proposed models for the magnetic structure, one of them being analogous to the one of Ca_3CoMnO_6, see [34, 35].

E-type multiferroics consist of zigzag-ferromagnetic chains. Some $RMnO_3$ manganites have this structure. Along the $a + c$ direction the structure is

[2]The spin-current, j_s, is induced between $\mathbf{S}_i$ and $\mathbf{S}_j$ being both non-parallel which in turn induces electric polarization. Unlike in the Dzyaloshinskii-Moriya interaction, atomic displacements are not involved in this mechanism [27, 28].

↑↑↓↓, and the exchange striction causes polar distortions, see Fig. 1.2(e). However, in this scenario the polarization shows up due to transverse displacements of oxygen atoms in contrast to previous cases. Moreover, depending on the strength of the super-exchange or double-exchange interaction the direction of the polarization is switched [36, 37].

◇ Other spin electronic mechanisms: Another mechanism that can generate ferroelectricity is the *electronic* ferroelectricity observed in frustrated magnets. If $\mathbf{S}_1$, $\mathbf{S}_2$ and $\mathbf{S}_3$ are spins located at the vertices of a regular triangle, then if $\mathbf{S}_1(\mathbf{S}_2 + \mathbf{S}_3) - 2\mathbf{S}_2\mathbf{S}_3$ is nonzero the polarization is nonzero. This situation was observed by Bulaevskii *et. al.* in some insulators, see Ref [38].

1.4 Ferroelectricity

Chapter 2 is devoted to magnetic order. Nevertheless, since ferroelectricity is also a pillar of this work, we will briefly introduce it this section.

Ferroelectrics consists of an ordered array of electric dipoles being all oriented in parallel directions. They are characterized by a spontaneous electric polarization, P, which is switchable by an applied electric field, E. Ferroelectric $P-E$ hysteresis loops are similar to $M-H$ hysteresis loops in ferromagnets. Indeed, the first $P-E$ hysteresis loop was observed in Rochelle Salt in 1921 [39] and it was described as equivalent to the magnetic one seen for iron. Thus, the term *ferroelectricity* was used to highlight the analogy. In either cases the macroscopic polarization (magnetic/electric) decreases with increasing the temperature and above the Curie temperature, T_C, the polarization vanishes and the material becomes unpolarized (paramagnetic/paraelectric). When the sample has multiple domains it may happen that no macroscopic polarization is observed even below T_C.

A material to have a must have a polar point-group[3] to exhibit spontaneous electric polarization. Besides that, the electric polarization must be switchable, a transition between two stable states of opposite polarization must be accessible. A fundamental requirement for a material to be ferroelectric is to be an insulator: otherwise an applied electric field would induce a current rather than reorient its polarization.

[3]Very often instead of the term *polar* it is used *non-centrosymmetric* point group which is a necessary condition but not sufficient. Note that for example 222 point group is neither centrosymmetric nor polar.

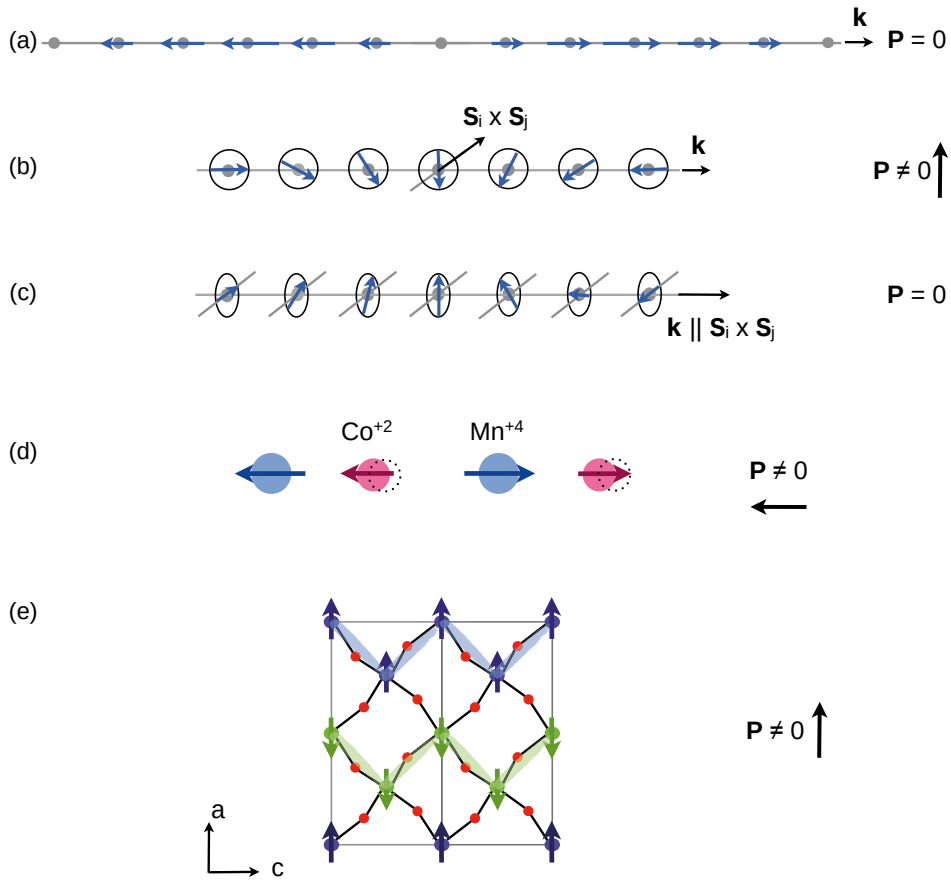

FIGURE 1.2: Sketch of magnetic structures. (a) Non-polar sinusoidally modulated collinear structure. (b) Cycloidal structure with electric polarization in the plane where the moments rotate. (c) Screw-type structure, which in principle is non-polar. (d) Situation where the exchange striction gives rise to electric polarization in a collinear structure. Dotted circles represent the original position of Co^{2+} before the transition to the ferroelectric states that occurs in Ca_3CoMnO_6. (e) Projection along the *b* axis of a $RMnO_3$ manganite where the E-type magnetic structure is visible.

Antiferroelectrics consists of an ordered array of electric dipoles, but with adjacent dipoles oriented in opposite directions [41, 42]. In an antiferroelectric, the macroscopic polarization is zero, since the adjacent dipoles cancel each other out. They are analogous to antiferromagnets.

Chapter 2

Magnetic order

Along the lines of this chapter the reader will find a brief introduction to the magnetic order: origin of the magnetic order, types of structures and the different methods to describe them.

2.1 General introduction

Magnetism is a direct consequence of the quantum nature of materials: spins and Pauli's exclusion principle are on its base. The magnetic ordered state is the eigenvector of the following Hamiltonian:

$$\mathcal{H} = \mathcal{H}_{Coulomb} + \mathcal{H}_{S-O} + \mathcal{H}_{CristalField} \tag{2.1}$$

where $\mathcal{H}_{Coulomb}$ takes into account the Coulomb interaction between non-coupled electrons, $\mathcal{H}_{S-O} = (\Lambda/\bar{h}/2)\hat{L}\cdot\hat{S}$ refers to the spin-orbit interaction and $\mathcal{H}_{CristalField}$ is the so-called crystal-field interaction which introduces the effect of the crystalline structure in the magnetic order, i. e. the Coulomb interaction of the electronic charge distribution $\rho_0(\mathbf{r})$ of an ion embedded in a solid with the surrounding charges in the crystal.

The total Hamiltonian, $\mathcal{H}$, can be simplified, within the Heisenberg model, as a function of the spins as:

$$\mathcal{H} = -\sum_{ij} J_{ij}\mathbf{S}_i \cdot \mathbf{S}_j \tag{2.2}$$

where J_{ij} refers to the exchange constant between $\mathbf{S}_i$ and $\mathbf{S}_j$ (explicitly located at the atom positions) and is a measure of the strength of the exchange interactions: $J_{ij} > 0$ indicates a ferromagnetic interaction, which tends to align the two spins parallel; $J_{ij} > 0$ indicates an antiferromagnetic interaction, which tends to align the two spins antiparallel. Below certain temperature, those magnetic interactions could eventually "freeze" the spins so that the materials become magnetically ordered.

As mentioned in Chapter 1, one necessary condition for magnetic order is to have unpaired electrons (e.g. $3d$, $4f$ elements). However at high enough temperature the order is destroyed by the thermal fluctuations. In this paramagnetic state the response of the randomly fluctuating magnetic moments to an external field, i. e. the magnetic susceptibility χ, usually follows the Curie-Weiss law:

$$\chi = \frac{C}{T - \Theta_P} \tag{2.3}$$

where C stands for the Curie constant ($\propto \mu_B^2 m_{eff}^2$) and Θ_P for the paramagnetic temperature. The latter is directly related to the exchange interactions.

Below, a brief oversimplified picture of the main types of magnetic structures and their principle characteristics is given. Figure 2.1 illustrates those structures and how their magnetization/susceptibility change with temperature.

Ferromagnets: The exchange interaction between neighbor spins is positive, $J_{ij} > 0$, and consequently, the magnetic moments have parallel alignment below the Curie temperature, T_C. Therefore, in the ordered state there is spontaneous magnetization, even in absence of any external magnetic field. The magnetic susceptibility tends to infinity (following the Curie-Weiss law) at the paramagnetic temperature, Θ_p, that ideally is equal to T_C, the point at which spontaneous magnetization emerges [equation (2.3)].

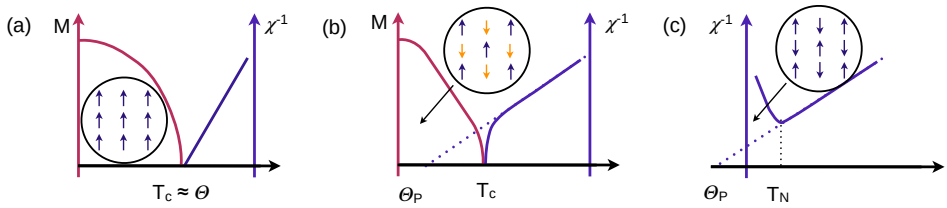

FIGURE 2.1: Temperature dependence of magnetization, M, and the inverse of magnetic susceptibility, χ, for (a) ferromagnets, (b) ferrimagnets and (c) antiferromagnets.

Ferrimagnets: The exchange interaction is negative, $J_{ij} < 0$, rending antiparallel alignment of the moments, but the neighboring atoms do not have equal spin, and hence do not compensate, in other words, these materials exhibit antiparallel alignment of non-equivalent neighbor moments below T_C. One can consider that there are two different ferromagnetic sublattices that interpenetrate each other in an antiparallel way and thus, the magnetic moments do not cancel resulting in net magnetization. In this circumstances, the susceptibility tends to infinity at the Curie temperature as well, but the paramagnetic temperature Θ_P, which is extrapolated from its behavior at high temperatures according to equation (2.3), does not coincide with the Curie temperature. Approaching T_C, the inverse susceptibility decreases in a concave fashion.

Antiferromagnets: If the sublattices in a ferrimagnet have equal moments, the material is an antiferromagnet. Thereby, the total magnetization is canceled out and no spontaneous magnetization arises in the material when it becomes ordered below the Néel temperature, T_N. The paramagnetic temperature, Θ_p, is usually negative and fulfill $T_N = |\Theta_P|$ which is a straight forward consequence of considering just first neighbors antiferromagnetic interaction. This is discussed in more details in Section 2.3. The magnetic susceptibility has a maximum at T_N ($\neq \Theta_P$).

Apart from the three situations introduced above, which can be considered as simple structures, there are many others such as canted ones, amplitude modulated structures, circular helixes, elliptical helixes, cycloidal structures, conical, transverse conical structures ... (some examples are depicted in Fig. 2.2). Note that the difference between a helix and a cycloid lies in the relation between the rotation plane of the spins and the direction of the propagation vector **k**: in a cycloidal structure **k** is within the rotation plane, whereas in helical structures they are perpendicular to each other. Although most of these exotic structures are very often considered as antiferromagnets (because they do not show any spontaneous magnetization and the magnetic susceptibility has a similar temperature dependence) it is clear that the previous classification is not precise enough for all the scenarios that arise in reality. Many of them are met with rare-earth elements.

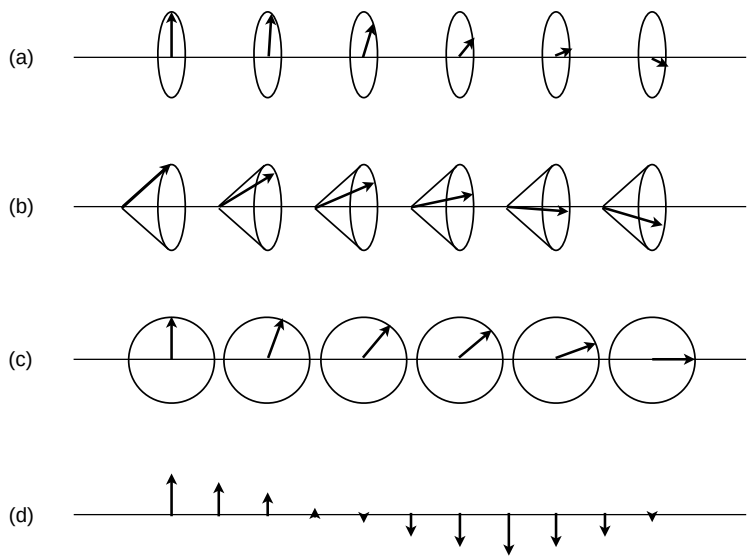

FIGURE 2.2: (a) Helical, (b) conical, (c) cycloidal and (d) sinusoidally modulated magnetic structures.

2.2 Magnetic anisotropy

Even if the exchange interactions are isotropic, spins tend to position along certain directions, i. e. along the *easy axes* or *easy directions*, which may or may not correspond to crystallographic directions. Therefore, the isotropic nature of the exchange interaction is shadowed by the effect of intrinsic and extrinsic properties of the crystals or samples that break such isotropy and fix certain directions energetically more favorable.

There are several kinds of anisotropies: magnetocrystalline anisotropy, shape anisotropy (note that there is no shape anisotropy in an antiferromagnet, because there is no demagnetizing field when $\mathbf{M} = 0$), stress anisotropy, induced anisotropy (by magnetic annealing, plastic deformation or irradiation) and exchange anisotropy. Among them, *magnetocrystalline anisotropy* is the unique one which is intrinsic to the material, and reflects the symmetry of the crystal. It is mainly driven by the spin-orbit coupling in systems where the atomic orbitals and crystal lattice are strongly coupled. The orientation of atomic orbits are fixed to the lattice and the energy barrier to change their orientations entails the application of large fields. Therefore, by means of spin-orbit coupling the moments become linked to the lattice. Depending on the strength of the latter coupling, the crystal anisotropy is more or less important. In other words, the $\mathcal{H}_{CristalField}$ term of equation (2.1) is

responsible for the magnetocrystalline anisotropy, and it is expressed as follows

$$\mathcal{H}_{CristalField} = \int \rho_0(\mathbf{r})\phi_{cf}(\mathbf{r})d^3r \tag{2.4}$$

where ϕ_{cf} is the potential produced by the distribution of charge $\rho_0(\mathbf{r}')$ in the rest of the crystal at the atomic position $\mathbf{r}$. This crystal field interaction tends to stabilize particular orbitals and the spin orbit coupling $\Lambda\mathbf{L}\cdot\mathbf{S}$ aligns the spins depending on the orientation of the orbitals.

Lets consider the case of cobalt, which has hexagonal symmetry. The easy direction of magnetization is the c crystallographic direction of the hexagonal close-packed structure, being all directions in the basal plane equally hard. Therefore, the magnetic anisotropy is uniaxial and the anisotropy energy, E_{an}, when trying to take out the moments from this direction can be expressed as a function of a single angle, θ, the angle that moments make with respect to c. The anisotropy-energy function must be even, because the energy should not depend on the direction of the moment within a certain axis and it has to be symmetric with respect to the angle. Hence, the energy can be expressed as follows:

$$E_{an} = K_0 + K_1 \sin^2\theta + K_2 \sin^4\theta + \ldots \tag{2.5}$$

where K_0, K_1 and K_2 are constant values particular for each material and are temperature dependent. Equation (2.5) is general for any system with uniaxial anisotropy and the relation between K_1 and K_2 fixes the orientation of the easy axis. Higher order terms may be needed for certain materials, where the dependence with the spherical angle ϕ appears.

In the simplest of the lowest order case the anisotropy energy can be considered uniaxial and can be expressed as follows:

$$E_{an} = K_u \sin^2\theta. \tag{2.6}$$

The field needed to saturate the magnetization along the hard direction, the so-called anisotropy field (H_{an}), depends on the strength of the anisotropy and in the simplest cases it can be expressed as

$$H_{an} = \frac{2K_u}{\mu_0 M}. \tag{2.7}$$

As a result of the magnetic anisotropy the magnetic properties will generally depend on the direction in which they are measured. Broadly speaking when magnetic field is applied along the easy axis the magnetization is saturated at low

fields (high enough to erase possible magnetic domains which appear as a result of minimizing the magnetoestatic energy in sample with finite dimensions), whereas along the hard axis higher fields are requested to align the moments along the field. Magnetic anisotropy is also responsible for the type of magnetic transitions that undergo the materials when an external field is applied along different magnetic axis. All this will be further discussed in Section 2.3.

The effect of the magnetic anisotropy is not only property of the magnetically ordered phase, but also of the paramagnetic state [43, 44]. In the case of free ions, as for example in a paramagnetic gas, with an angular momentum j all the $2j+1$ states will have the same energy in the absence of any field. This degeneracy, may be removed by a magnetic field, which splits the single energy level into $2j+1$ nearly equidistant levels by the so-called Zeeman effect. The resulting ion distribution gives a subsequent magnetic moment along the field (see Section 2.3.1). On the contrary, if the ions are not initially free, as for example in a crystal, and are subject of an electric field (the crystal field), the degeneracy in respect of the orbital moment, l, may be split by Stark effect[1] and therefore, the l moment tends to have a defined orientation in the field which interferes its response to an external magnetic field. The nature of the splitting will depend on the initial states involved, the nature, distances and symmetry of the surrounding atoms. The symmetry of the crystalline field surrounding a paramagnetic ion is not necessarily similar to the one of the crystal as a whole. Unless the crystalline field possesses cubic symmetry, one may expect not only magnetic anisotropy but also different values of the paramagnetic temperature θ [45].

2.3 Antiferromagnetism

As introduced in Section 2.1, negative exchange interaction $J_{ij} < 0$ gives rise either to antiferromagnets or ferrimagnets. From now on the matter will be focused on antiferromagnets. In 1936 Louis Néel suggested the scenario of two equal sublattices aligned in an antiparallel manner to explain a magnetic transition signed by a small peak in the magnetic susceptibility and an anomaly in the specific heat measurements, without showing any net magnetization below the Néel temperature, T_N [46]. In the 50s this was proved by neutron-diffraction experiments which directly measured the magnetization of each sub-lattice in MnO [47].

[1] It is analogous to the Zeeman effect but the splitting of a spectral line into several components occurs in the presence of an electric field.

The molecular field theory which explained the behavior of ferromagnets was extended to antiferromagnets. Within this theory, if each magnetic sub-lattice, A and B, have $\mathbf{M}_A = -\mathbf{M}_B$ magnetization, n_{AB} and n_{AA} represent the intersublattice and intrasublattice molecular field couplings, respectively, and H_0 is an external magnetic field, then the magnetic field felt by each sub-lattice is

$$\begin{aligned} \mathbf{H}_A &= n_{AA}\mathbf{M}_A + n_{AB}\mathbf{M}_B + \mathbf{H}_0, \\ \mathbf{H}_B &= n_{BA}\mathbf{M}_A + n_{BB}\mathbf{M}_B + \mathbf{H}_0. \end{aligned} \tag{2.8}$$

where $n_{AA} = n_{BB}$ and $n_{AB} = n_{BA}$. In the magnetically ordered state, $T < T_N$, at zero external field ($H_0 = 0$) the net magnetization is zero, however the spontaneous magnetization of each sub-lattice is governed by the Brillouin function as follows:

$$\mathbf{M}_{A,B} = \pm\mathbf{M}_{A0}\frac{n}{2}g\mu_B J\mathcal{B}(x_{A,B}) \tag{2.9}$$

where $x_{A,B} = \frac{\mu_0 g\mu_B J|H_{A,B}|}{k_B T}$ and n is the number of magnetic ions per volume unit.

In the paramagnetic state, $T > T_N$, the magnetization is zero unless an external field is applied. In such situation, the induced magnetization behaves according to

$$\mathbf{M}_{A,B} = \chi\mathbf{H}_{A,B}, \tag{2.10}$$

where $\chi = \frac{C'}{T} = \frac{n\mu_0 m_{eff}^2}{6k_B T}$. At $H_0 = 0$ and when the system reaches T_N, the spontaneous magnetization emerges, consequently, the relation between n_{ij} coefficients must be such that

$$(\frac{C'}{T_N}n_{AA} - 1)^2 - (\frac{C'}{T_N}n_{AB})^2 = 0 \tag{2.11}$$

which derives in

$$T_N = C'(n_{AA} - n_{AB}). \tag{2.12}$$

Thereby, the Néel temperature is expressed as a function of the intrasublattice and intersublattice interactions. In the presence of external magnetic field, the total magnetization of an antiferromagnetic material in the paramagnetic state must agree with the sum of the magnetization of both sub-lattices:

$$\mathbf{M} = \frac{C}{T - \Theta_P}\mathbf{H_0}, \tag{2.13}$$

being $C = 2C'$ and $\Theta_P = C'(n_{AA} + n_{AB})$ the paramagnetic Curie temperature, within the simple model were only intersublattice n_{AA} and intrasublattice n_{AB} couplings. When, only interactions between nearest neighbors are involved in the magnetism of the antiferromagnetic material, n_{AA}, $\Theta_P = -T_N$.

2.3.1 Antiferromagnetism under field

When a material is under magnetic field, another term has to be introduced to the magnetic Hamiltonian of the system, the Zeeman term, and equation (2.1) becomes:

$$\mathcal{H} = \mathcal{H}_{Coulomb} + \mathcal{H}_{S-O} + \mathcal{H}_{CristalField} + \mathcal{H}_{Zeeman} \tag{2.14}$$

where the Hamiltonian term for the Zeeman effect is written as:

$$\mathcal{H}_{Zeeman} = (\mu_0 \mu_B / \bar{h})(\hat{L} + 2\hat{S}) \cdot \mathbf{B} \tag{2.15}$$

The antiferromagnetic axis along which the two sub-lattice magnetizations lie is determined by magnetocrystalline anisotropy, and the magnetic response below T_N depends on the direction of H relative to this axis. If a small field is applied along its easy axis, a net induced magnetization will be twice as big as the difference of the magnetization in each sub-lattice δM,

$$\mathbf{M} = \mathbf{M}'_A + \mathbf{M}'_B = 2\delta M \tag{2.16}$$

and the magnetic susceptibility, along the easy axis can be derived assuming that the intrasublattice coupling is negligible, $n_{AA} = 0$, and using the Taylor series of the Brillouin function around $H_0 = 0$:

$$\chi_{\parallel} = \frac{\mathbf{M}'_A + \mathbf{M}'_B}{\mathbf{H}_0} = \frac{2\delta M}{\mathbf{H}_0} = \frac{2C'[3J/(J+1)]\mathcal{B}_{\mathcal{J}}{}'(x_0)}{T - n_{AB}C'[3J/(J+1)]\mathcal{B}_{\mathcal{J}}{}'(x_0)}. \tag{2.17}$$

When $T \to 0$ the susceptibility along the easy axis tends to zero,

$$\chi_{\parallel}(T \to 0) = 0, \tag{2.18}$$

and at T_N, where $M_{A,B} = 0$ and $\mathcal{B}_{\mathcal{J}}{}'(0) = \frac{J+1}{3J}$,

$$\chi_{\parallel}(T = T_N) = -\frac{1}{n_{AB}}. \tag{2.19}$$

If the same field is applied along the hard axis, then the magnetic moments of both sub-lattices tilt towards the external field making a δ angle with the easy axis, and the total magnetization is $M = 2M_A \sin\delta$. The moments of the sub-lattices will rotate until the molecular field equals the external field, and therefore $H = 2n_{AB}M_A \sin\delta$. Then,

$$\chi_{\perp} = -\frac{1}{n_{AB}}. \tag{2.20}$$

In this oversimplified model, the susceptibility along the hard axis does not depend on the temperature below the Néel temperature. In Fig. 2.3(a) are plotted $\chi_{\parallel}$ and $\chi_{\perp}$ of a simple antiferromagnet.

These results are obtained in the very simple case where only interactions between nearest neighbors are considered ($n_{AA} = 0$ and $n_{AB} \neq 0$) and the anisotropy constants, K_u in uniaxial systems, is considered to be $n_{AB} > \frac{K_u}{2M^2}$. However, often the behavior of the susceptibility in antiferromagnets is more complicated, and equations (2.18), (2.19) and (2.20) are no longer applicable. In the case of modulated structures, it has been seen that $\chi_{\parallel}(T \to 0) > 0$ and $\chi_{\perp}(T < T_N) < -\frac{1}{n_{AB}}$, see 2.3(b). This is the case of screw-type[2] structures [48–50]. In such cases and under a small external field parallel to the rotation plane, the magnetic susceptibility $\chi_{\parallel}^{screw}$ has a finite value at 0 K [see Fig. 2.3(b)]. If, on the contrary, the field is applied perpendicular to the rotation plane of the moments, the magnetic susceptibility $\chi_{\perp}^{screw}$ at 0 K is smaller to that of conventional collinear antiferromagnets, as depicted in Fig 2.3(b). Nevertheless, both $\chi_{\parallel}^{screw}$ and $\chi_{\perp}^{screw}$ have the same value at T_N.

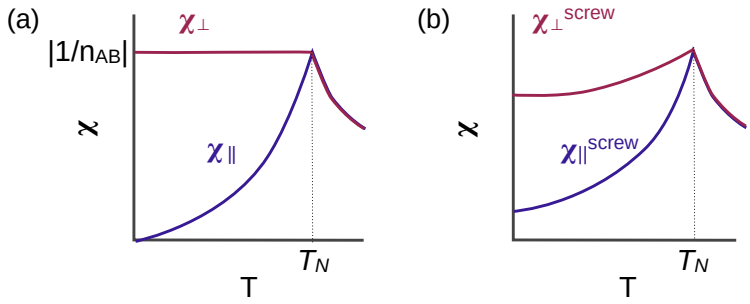

FIGURE 2.3: Magnetic susceptibility on an antiferromagnet along the easy and hard axes (a) within the molecular field theory and considering that $n_A A$ and K_u are negligible and (b) in more complicated systems such as magnetically modulated structures.

Magnetic structures can be modified/changed when high enough fields are applied to the magnetically ordered materials and hence, magnetic transitions can be induced. In principle, according to the Zeeman term [see equation (2.15)] the magnetization should be always perpendicular to the external field, but this will depend on the strength of the anisotropy field [equation (2.7)]. In the simplest case, when the field is applied along the easy axis, the moments will turn perpendicular to the field when the energies of the parallel and perpendicular configurations are

[2]Proper screws are the so-called helixes (**k** ⊥rotation plane) and improper screw structures are the so-called cycloidal structures (**k** ∥rotation plane)

the same, e. i. when

$$-\mu_0 M H_{an} - \mu_0 \chi_{\parallel} H_{sf}^2 = -\mu_0 \chi_{\perp} H_{sf}^2, \tag{2.21}$$

$$H_{sf} = \sqrt{\frac{M H_{an}}{\chi_{\perp} - \chi_{\parallel}}}. \tag{2.22}$$

When the spin-flop field, H_{sf}, is reached both sub-lattices are perpendicular to the field, they will rotated towards the field. This process is known as a *spin-flop* transition, and it is sketched in Figs 2.4(a), 2.4(b) and 2.4(c). Magnetization curves along easy axis is shown in Fig. 2.4(d). In spin-flop-like transitions, the magnetization ($M_{\parallel}$) increases very slowly, according to $\chi_{\parallel}$, until a threshold field when the moment become perpendicular to the field and then, it increases, according to $\chi_{\perp}$, until it saturates (moments parallel to the field). This saturated high field phase, in the western literature is termed "paramagnetic" while in the Russian literature a term "forced ferromagnetism" is used.

The situation is slightly different when the anisotropy is very strong. At low fields, magnetization increases with H according to the value of $\chi_{\parallel}$. Then, at a critical value H_{sflip}, the antiparallel spins flip over and become parallel, in other words, the situation jumps directly from Fig. 2.4(a) to Fig. 2.4(c), and the magnetization saturates. Since the magnetic anisotropy is very strong, the intermediate configuration Fig. 2.4 (b) is not stable. The spin-flip and spin-flop transitions are of metamagnetic type ones. Usually the critical field is rather high. The magnetization curves along easy and hard axis in this kind of transitions are shown in Fig. 2.4(e).

2.4 Inverse Dzyaloshinskii-Moriya mechanism

The Dzyaloshinskii-Moriya (DM) interaction is an antisymmetric, anisotropic exchange coupling between two spins on a lattice bond ij with no inversion center [24, 25]. For spins $\mathbf{S}_i$ and $\mathbf{S}_j$, a new term in the Hamiltonian is then given by

$$\mathcal{H}_{\mathcal{DM}} = \mathbf{D}_{ij} \cdot (\mathbf{S}_i \times \mathbf{S}_j) \tag{2.23}$$

where the Dzyaloshinskii-Moriya vector, $\mathbf{D}_{ij}$, is finite when the crystal field does not have inversion symmetry with respect to the center between $\mathbf{S}_i$ and $\mathbf{S}_j$. The effect of the DM interaction is often to provide a small canting of the moments in an antiferromagnetic structure, resulting in weak ferromagnetism. The DM interaction favors non-collinear spin ordering, as typically in the weak ferromagnet

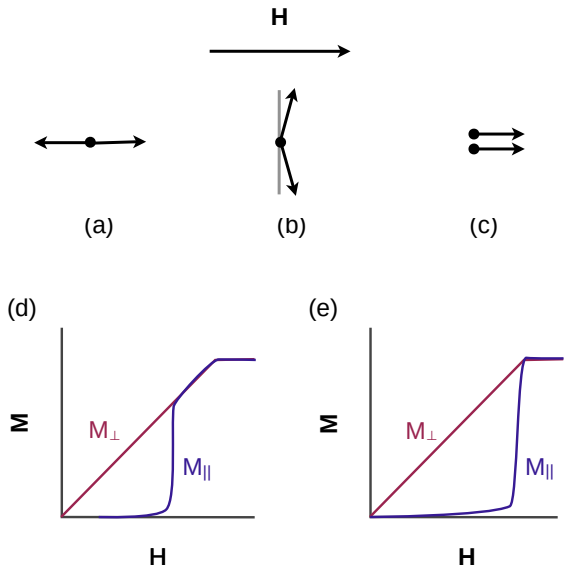

FIGURE 2.4: (a) Antiferromagnetic spin-configuration. (b) Spin-flop configuration. (c) Forced ferromagnetic (also called paramagnetic) configuration that describes the final stage in *metamagnetic* transitions. Magnetization curves with field parallel to the easy axis ($M_{\parallel}$) in (d) *spin-flop* and (e) *spin-flip* transitions. Magnetization curves with field perpendicular to the easy axis ($M_{\perp}$) are also shown.

R_2CuO_4 cuprates [52]. Generally, in DM weak ferromagnets the non-collinear order is not at the origin, but it is a consequence of the structural distortion.

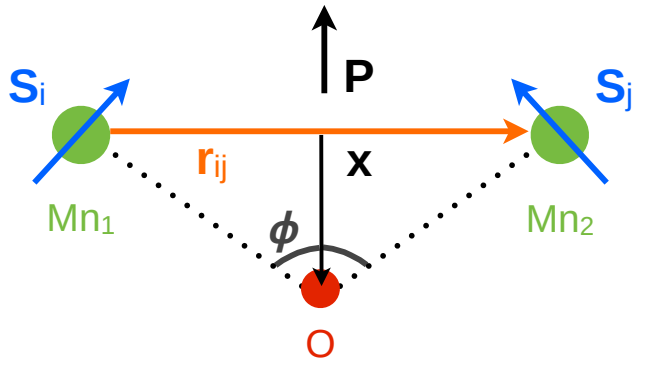

FIGURE 2.5: Electric polarization induced by the the displacement of the oxygen atoms due to the DM interaction.

Sergienko *et. al.* proposed a relationship between the DM interaction and the onset of ferroelectricity in systems, such us $TbMnO_3$ [26], where the electric

polarization appears together with a non-collinear spin order. That is the so-called Inverse Dzyaloshinskii-Moriya (IDM) mechanism. According to it, the magnetic coupling energy triggers a structural distortion resulting in a polar structure. In the IDM mechanism, $\mathbf{D}_{ij}$ is non-zero in the magnetically ordered phase, in contrast to the DM mechanism ($\mathbf{D}_{ij}$ can be non-zero above the transition to the weak ferromagnet phase). The vector $\mathbf{D}_{ij}$ shown in equation (2.23) is proportional to $(\mathbf{x} \times \mathbf{r}_{ij})$ and the spin-orbit coupling, where $\mathbf{x}$ is the displacement of the oxygen atom (see Fig. 2.5). The corresponding energy is therefore increased by pushing the oxygen anions away from the positively charged Mn ions, resulting in an electric polarization. As the displacement $\mathbf{x}$ of the oxygen atoms increases, the Mn-O-Mn bond angle ϕ decreases, suggesting an important relationship between ϕ and the existence of multiferroic properties. Goto *et. al.* suggested a relationship between the multiferroic properties seen in $TbMnO_3$ and $DyMnO_3$ and ϕ [51]. It was apparent that the cycloidal magnetic order was only seen for ϕ in the range $144.5^\circ \lesssim \phi \lesssim 145.8^\circ$, implying a strong relationship between the relative positions of neighboring Mn atoms and the magnetic frustration they experience.

2.5 Magnetic frustration

In frustrated magnets the magnetic interactions can not be satisfied simultaneously. In other words, the competing interactions in the Hamiltonian contribute in such way that the energy can not be minimized in a single ground state [53] and it becomes degenerated.

The geometry of the crystal or the competing interactions between different $\mathbf{S_i}$ and $\mathbf{S_j}$ couples may lead to complex structures.

To illustrate the case where a variety of J_i play an important role in the expression (2.2), lets imagine a square lattice where the interaction between the nearest neighbors is J_1 and between the next nearest neighbors is J_2, both being antiferromagnetic interactions. Depending on the relation between the strength of these two interactions either of the two spin configuration depicted in Figs. 2.6(a) and 2.6(b) will be stabilized. Thus, in the situation where the $|J_1| > |2J_2|$, first neighbors will be antiferromagnetically coupled whereas second neighbors will be forced to be parallel [Fig. 2.6 (a)]. On the other hand, if $|J_1| < |2J_2|$ the scenario would be the opposite, where first neighbors will be forced to be parallel and second neighbors antiparallel. There is a third possibility to take into account, and for us the most interesting: the situation where the interactions are comparable, $2J_2 \sim J_1$. In that

framework the structure becomes magnetically frustrated.

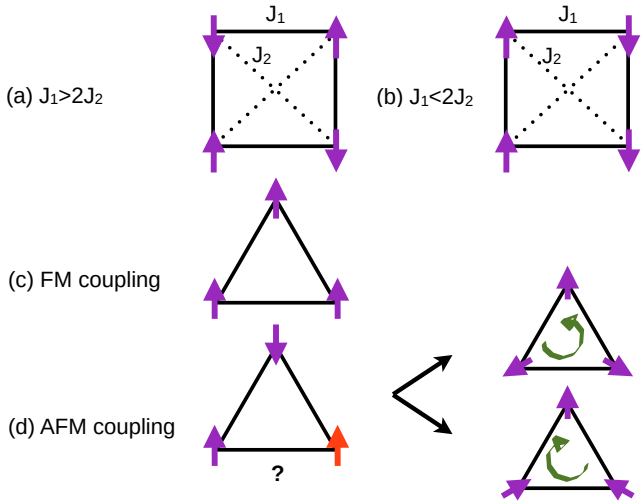

FIGURE 2.6: (a) and (b) show possible spin configurations depending on the relationship between first and second neighbors antiferromagnetic exchange interactions in a square lattice. If the interaction are comparable, $2J_2 \sim J_1$, then the system would be frustrated and the ground state degenerated. In (d) the frustration emerges from the geometry of the spin lattice even considering just first neighbors. Whereas a ferromagnetic coupling (c) is compatible with the lattice; (d) the antiferromagnetic it is not and this gives rise to different states. Adapted from reference [53].

In other cases, the origin of the frustration may be in the topology of the system, being all the exchange interactions equal. For instance, one can think about a triangular spin lattice, as shown in the Figs. 2.6(c) and 2.6(d). If the interaction between nearest neighbors are ferromagnetic, they can all be satisfied simultaneously [Fig. 2.6(c)] and the ground state is unique. However, if the interactions between the nearest neighbors is antiferromagnetic, as in Fig. 2.6(d), the system does not have a unique spin configuration that minimizes the energy and, hence, the ground state becomes degenerated and several spin structures may arise in the system.

There are distinct types of lattices and atomic configurations that favor the magnetic frustration, such as triangular lattices, the Kagomé lattice, pyrochlore lattice ...

In these systems $T_N = |\Theta_P|$ is no longer true because the interaction that play a role a not only those which concern between nearest neighbors. It has been

suggested that the $\frac{|\Theta_P|}{T_N}$ ratio could be used to characterize the degree of frustration, the more frustrated the system is the larger the value of the ratio is [55]. It does not mean that all the systems that show $T_N < |\Theta_P|$ are frustrated, as for example Mn [56].

2.6 Description of magnetic structures

As we have previously seen, very often it is not sufficient to say that a certain magnetic structure is either ferromagnetic, antiferromagnetic or ferrimagnetic, thus a complete and detailed description of the structure is mandatory.

In general, being the magnetic structure a periodic function, the orientation of the magnetic moment of an atom j in the unit cell l can be Fourier expanded and described by the following sum:

$$\mathbf{m}_{lj} = \sum_{\mathbf{k}} \mathbf{S}_{\mathbf{k}j} e^{-2\pi i \mathbf{k}\cdot\mathbf{R}_l} \tag{2.24}$$

where $\mathbf{S}_{\mathbf{k}j}$ stands the Fourier components of the distribution associated to the propagation vector $\mathbf{k}$.

As in conventional crystallography, magnetic structures are characterized by two features: the periodicity of the structure and the motif.

One the one hand, the first difficulty when dealing with magnetic structures arises from the fact that even if they are periodic, these structures do not necessarily have the same periodicity as the underlying crystallographic structures. In the three main cases seen in the previous section, ferromagnetic, antiferromagnetic or ferrimagnetic, the periodicity of the magnetic structure is equal or is an integral multiple of the nuclear one. However, this is not always the case and therefore, a more rigorous and better adapted method is used to describe magnetic structures: the propagation vector formalism, $\mathbf{k}$, see Section 2.6.1.

On the other hand, the magnetic *motifs* within the magnetic cell (propagated throughout the crystal according to $\mathbf{k}$) could correspond to any arrangement of the moments. However, as mentioned in the first chapter, the arrangement of the spins have to contain the symmetry of the crystal. Therefore, symmetry considerations can help to reduce the number of possible magnetic structures. These symmetry considerations can be done mainly through two formalisms: *representation analysis* (see Section 2.6.2) and *superspace* formalism (see Section 2.6.3). These

two formalisms impose sets of constraints that are closely related, but superspace symmetry is in general more restrictive and more comprehensive, as it affects all the degrees of freedom of the system.

2.6.1 Propagation vector

The propagation vector, **k**, is a mathematical object defined in the reciprocal space which describes the relation between the orientation of the equivalent atoms in different nuclear cells. Hence, from equation (2.24) it follows that **k** = (0, 0, 0) which means that the magnetic moments of equivalent atoms in two contiguous nuclear cell are parallel and consequently the magnetic cell coincides with the nuclear one. Let us assume that the situation is such that along a the moments are antiparallel, then **k** = ($\frac{1}{2}$, 0, 0) and the magnetic unit cell would be doubled along the a axis with respect to the nuclear, i. e. $a_{mag} = 2a_{nucl}$. In other words, **k** = (k_a, k_b, k_c) represent the wave vector that defines the phase difference between the moments of a magnetic modulation. When (k_a, k_b, k_c) are rational numbers, then the structure is *commensurable*, and if not, it is *incommensurable* with period 1.

Magnetic structures can be described not only by one propagation vector (single-**k** structures), but by various (multi-**k** structures). The most illustrative case of a multi-**k** structure is a canted one as represented in Fig. 2.2. This is a canted structure where it is mandatory to use two propagation vectors to completely describe the relation between magnetic moments in different cells: the antiferromagnetic coupling is described by **k** = ($\frac{1}{2}$, 0, 0)-like vector whereas the ferromagnetic one needs **k** = (0, 0, 0).

2.6.2 Representation analysis

This method is widely used. Once, the propagation vector is known, symmetry considerations and group theory can reduce the number of possible solutions. The magnetic modulations can be described by the representation analysis method (developed by Bertaut [57, 58]) which is based on the decomposition of the magnetic configuration space into basis modes transforming according to different physically irreducible representations, the so-called *irreps*, of the paramagnetic space group (regardless of their propagation vector being commensurate or incommensurate).

In the phase transitions that occur due to a break of the symmetry of the system and are characterized by an order parameter η, above the transition, the order parameter is zero and below a critical temperature, T_0, it can vary continuously or discontinuously (second and first order transitions, respectively) [59]. In second order transitions, in the paramagnetic state $\eta = 0$ and at T_0 it starts increasing smoothly. The number and types of order parameters can be derived from group theory since they are second-order invariants and group theory tells that second-order invariants are formed by components of basis vectors belonging to the same irreducible representation Γ_v of the paramagnetic group $\mathbf{G}_p$, which leaves the system invariant above the transition. Thus, if the magnetic transition is second order, only one irreducible representation Γ_v of $\mathbf{G}_p$ becomes critical at $T = T_0$.

The complete representation analysis of $MnWO_4$ is given in Appendix B.

2.6.3 Superspace formalism

In 1980 A. Janner and T. Janssen proposed the use of superspace formalism to describe incommensurate magnetic structures [60]. However, magnetic structures have not been studied in the light of this formalism until the program JANA2006 [61], which allows to perform refinements using symmetry constraints consistent with any magnetic superspace group [62, 63].

The tensor properties of a crystal are constrained by the magnetic point group. Superspace formalism provides, in a simple manner, not only the symmetry of the magnetic structures and their intrinsic restrictions, but also information about the tensor properties of each incommensurate phase, such as ferroelectricity or magnetostructural properties [64–67]. This fact makes the formalism very appropriate to study multiferroic properties, since it allows to rationalize the physical properties induced by the incommensurate magnetic order in the framework of a symmetry break.

Within the superspace formalism, a modulated magnetic structure with a single incommensurate propagation vector $\mathbf{k}$ is described by a periodic structure plus a series of atomic modulation functions that define the deviations of each atom from the periodic structure[3]. In general, a modulation function with period 1, $A_\mu(x_4)$, describes the variation of the property A_μ of an atom μ from one cell of the periodic structure to another, so that its value in the unit cell l is written the

[3]The basic concepts of this formalism are summarized from the review paper of Perez-Mato *et. al.* [66].

following manner:

$$A_{l\mu} = A_{\mu}(x_4 = \mathbf{k} \cdot \mathbf{r}_{l\mu}) \tag{2.25}$$

with the atom located in the basic position $\mathbf{r}_{l\mu} = \mathbf{l} + \mathbf{r}_{\mu}$ (l being a lattice translation of the basic structure).

These atomic modulation functions, with period 1, can be expanded in a Fourier series of the type:

$$A_{\mu}(x_4) = A_{\mu,0} + \sum_{n=1,...} [A_{\mu,ns} \sin(2\pi n x_4) + A_{\mu,nc} \cos(2\pi n x_4)] \tag{2.26}$$

By definition, if $(\mathbf{R}, \theta \mid \mathbf{t})$ is an operation of the magnetic space group Ω_b of the basic structure [4] it transforms the incommensurately modulated structure into a distinguishable incommensurate modulated structure: the same basic structure plus all its modulation functions changed by a common translation of the internal coordinate x_4. In other words,

$$(\mathbf{R}, \theta | \mathbf{t}) A_{\mu}(x_4) = A'_{\mu}(x_4) = A_{\mu}(x_4 + \tau). \tag{2.27}$$

The translation τ depends on each specific operation. This implies that the original modulated structure can be recovered by performing an additional translation τ along the so-called internal coordinate, i.e. the phase of the modulation functions. In this sense, one can speak of $(\mathbf{R}, \theta \mid \mathbf{t}, \tau)$ as a symmetry operation of the system defined in a four-dimensional mathematical space.

If $(\mathbf{R}, \theta \mid \mathbf{t}, \tau)$ belongs to the superspace group of an incommensurate magnetic structure with a single propagation vector, the action of $\mathbf{R}$ on its propagation vector $\mathbf{k}$ transforms this vector into a vector equivalent to either $\mathbf{k}$ or $-\mathbf{k}$.

$$\mathbf{k} \cdot \mathbf{R} = R_I \mathbf{k} + \mathbf{H}_{\mathbf{R}}, \tag{2.28}$$

where R_I is either +1 or -1 and $\mathbf{H}_{\mathbf{R}}$ is a reciprocal lattice vector of the basic structure that depends on the operation $\mathbf{R}$. And the atomic modulation functions of the symmetry-related ν and μ atoms ($(\mathbf{R} \mid \mathbf{t})\mathbf{r}_{\nu} = \mathbf{r}_{\mu} + l$) are restricted as follows:

$$A_{\mu}(R_I x_4 + \tau_0 + \mathbf{H}_{\mathbf{R}} \cdot \mathbf{r}_{\nu}) = Transf(\mathbf{R}, \theta) A_{\nu}(x_4), \tag{2.29}$$

where $\tau_0 = \tau + \mathbf{k} \cdot \mathbf{t}$ and $Transf(\mathbf{R}, \theta)$ is the operator associated with the transformation of the local quantity A_{μ} under the action of the point-group operation

[4] with $\mathbf{R}$ being a point-group operation, θ being -1 or +1 depending if the operation includes time reversal or not, and $\mathbf{t}$ a translation in 3d real space

$(\mathbf{R}, \theta)$. Thus, equation (2.29) introduces a relationship between the modulation functions of the magnetic moments of the two atoms:

$$M_\mu(R_I x_4 + \tau_0 + \mathbf{H_R} \cdot \mathbf{r}_\nu) = \theta det(\mathbf{R})\mathbf{R} \cdot \mathbf{M}_\nu(x_4). \tag{2.30}$$

The four elementary translations $(\mathbf{1}, +1\,|\,100, -k_x)$, $(\mathbf{1}, +1\,|\,010, -k_y)$, $(\mathbf{1}, +1\,|\,001, -k_z)$ and $(\mathbf{1}, +1\,|\,000, 1)$ generate the (3+1)-dim lattice and define a unit cell in the (3+1)-dim superspace. In this basis the symmetry operation $(\mathbf{R}, \theta\ |\,\mathbf{t}, \tau)$ can be expressed in the standard form of a space group operation in a 4-dim space, $(\mathbf{R}_s, \theta\ |\,\mathbf{t}_s)$, where $\mathbf{t}_s$ is a 4-dim translation and $\mathbf{R}_s$ a 4×4 integer matrix defining the transformation of a generic point x_1, x_2, x_3, x_4:

$$\mathbf{R}_s = \begin{pmatrix} R_{11} & R_{12} & R_{13} & 0 \\ R_{21} & R_{22} & R_{23} & 0 \\ R_{31} & R_{32} & R_{33} & 0 \\ H_{R1} & H_{R2} & H_{R3} & R_I \end{pmatrix}, \tag{2.31}$$

where R_{ij} are the matrix coefficients of the rotational 3-dim operation $\mathbf{R}$ belonging to Ω_b (expressed in the basis of the basic unit cell) and (H_{R1}, H_{R2}, H_{R3}) are the components of the vector $\mathbf{H_R}$ defined in equation (2.28). The superspace translation $\mathbf{t}_s$ in the 4-dim basis is given by (t_1, t_2, t_3, τ_0), where t_i are the three components of $\mathbf{t}$ in the basis of the basic unit cell.

Summarizing, an incommensurate magnetic structure can be fully described by specifying:

(i) its magnetic superspace group.

(ii) its periodic basic structure.

(iii) and a set of periodic atomic modulation functions that define the magnetic modulations for the atoms of the asymmetric unit of the basic structure.

Note that *the magnetic point group of the system is given by the set of all point-group operations present in the operations of this superpace group.*

Chapter 3

$Mn_{1-x}Co_xWO_4$

Zure iparrak noraezaren lekukoa hartu zuen

Mikel Urdangarin (1971 -)

The compounds studied in this thesis will be introduced to the reader in the following chapter. First, the properties of both $MnWO_4$ and $CoWO_4$, are described. Then, the reasons for studying the $Mn_{1-x}Co_xWO_4$ solid solution are summarized.

3.1 $MnWO_4$

Manganese Hübnerite, $MnWO_4$, was discovered in 1852 by A. Brelthaupt who named it as Megabslte. In 1865 it was renamed as Hubnerite in honor of the metallurgist Adolf Huebner. It is a dark, reddish, transparent mineral with one direction of easy cleavage [69]. It is a semiconducting material [70, 71], that has photoluminescence properties [72] and can be used as catalyst for H_2 generation [73] or humidity sensors [74–76]. Nevertheless, in the last decades the interest in $MnWO_4$ relies on its magnetic and electric properties and the interplay between them.

Even if it grows all over the world, it is a rather rare mineral and it usually grows embedded in pegmatites and high temperature quartz veins [Fig. 3.1(a)], hardly ever does it alone. Therefore, many methods have been developed to grow

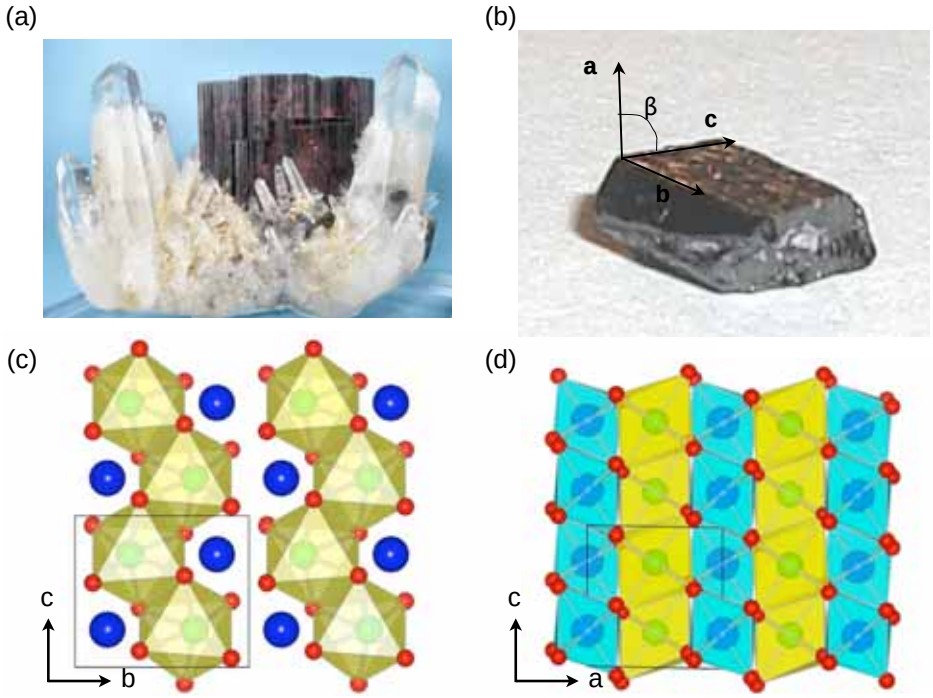

FIGURE 3.1: (a) A naturally grown $MnWO_4$ crystal found in Peru and photographed by Carles Millan. (b) Crystal (one of those used in our studies) grown in the laboratory. (c) Projection along the *a* axis of the crystal structure. Blue circles correspond to tungsten atoms, red ones to oxygen atoms and green ones to manganese. This color code will be maintained all along the manuscript. (d) Projection along the *b* axis where the Mn-W layered structure along *a* axis is visible.

crystalline samples of $MnWO_4$ in the laboratory [76–81].

The first recorded investigation in this compound dates back to 1957 [77], when Simanov and Kurshakova published the synthesis and X-ray experiments on $MnWO_4$. The crystal structure of Hübnerite has the symmetry $P2/c$ (No. 13, *b*-unique axis, standard setting) and it consists of alternative layers of Mn and W atoms along the [100] direction. Oxygen atoms form very distorted octahedra around Mn and W, and each octahedron shares two edges with the nearest ones, constructing zig-zag chains along the *c* axis [see Figs. 3.1(c) and 3.1(d)] [77, 82]. The crystallographic parameters (cell parameters and atomic positions) are gathered in Table 3.1.

In the sixties magnetic properties at low temperature were reported for the first time by Van Uitert and co-workers who revealed a magnetic order

Cell parameters:	a = 4.8238(7) Å, b = 5.7504(10) Å, c = 4.9901(8) Å, β = 91.18(1)^o			
Atoms	Wyckoff position	x	y	z
Mn	2f		0.6866(9)	
W	2e		0.1853(6)	
O1	4g	0.2132(5)	0.1026(5)	0.9394(4)
O2	4g	0.2524(4)	0.3707(6)	0.3918(5)
Volume:	138.3906 Å^3			

TABLE 3.1: The crystallographic parameters that describe the crystal structure of $MnWO_4$ which has $P2/c$ space-group symmetry are taken from Ref. [82].

below $\approx$ 16 K [83]. The antiferromagnetic nature of the compound was unveiled from the behavior of the magnetization as seen in Fig. 3.2(a), where a clear maximum of the magnetization appears around 16 K. The paramagnetic temperature Θ_P was extrapolated from their data, $\Theta_P \approx$ -72 K. The magnetic structure was investigated by Dachs and co-workers [84, 85] who made neutron diffraction, determined the magnetic propagation vector of the commensurate phase at 4.2 K [$\mathbf{k} = (\pm\frac{1}{4}, \frac{1}{2}, \frac{1}{2})$] and proposed spin arrangements to describe the magnetic structure. This magnetic structure was supposed to be the unique one below the Neél temperature. Nevertheless, specific heat measurements performed by C. P. Landee and E. R. Westrum [86] revealed three anomalies at 6.8(1) K, 12.57(5) K and 13.36(5) K [depicted in Fig. 3.2(b)], which were attributed to three consecutive magnetic transitions. The magnetic structures were named as AF3 (13.5 K $\lesssim$ T $\lesssim$ 12.5 K), AF2 12.5 K $\lesssim$ T $\lesssim$ 6.8 K) and AF1 (T $\lesssim$ 6.8 K).

The spin arrangements in AF1, AF2 and AF3 phases were studied in detail by Lautenschläger *et. al.* [87]. Just below the Néel temperature, $T_N \approx$ 13.5 K, moments order collinearly along a direction $\hat{u}$ within the *ac* plane with a sinusoidally modulated amplitude and an incommensurate propagation vector $\mathbf{k}$ = (-0.214, $\frac{1}{2}$, 0.457) [AF3 magnetic phase, Fig. 3.3(a)]. The $\hat{u}$ direction is in the *ac* plane, makes an angle of 35° with the a axis and is the magnetic easy-axis. The AF2 phase appears in the range 12.5 K $<$ T $<$ 7.5 K and presents an additional magnetic component along b, the propagation vector being the same. Thus, the magnetic ordering is an elliptical cycloidal spin structure as depicted in Fig. 3.3(b). Below 7.5 K the system is again collinear (along $\hat{u}$) and commensurate with $\mathbf{k}$ = ($\pm\frac{1}{4}$, $\frac{1}{2}$, $\frac{1}{2}$) [AF1, Fig. 3.3(c)]. Lautenschläger et. al. [87] managed to detect all the magnetic transitions by means of magnetic measurements done on powder samples [see Fig. 3.2(c)].

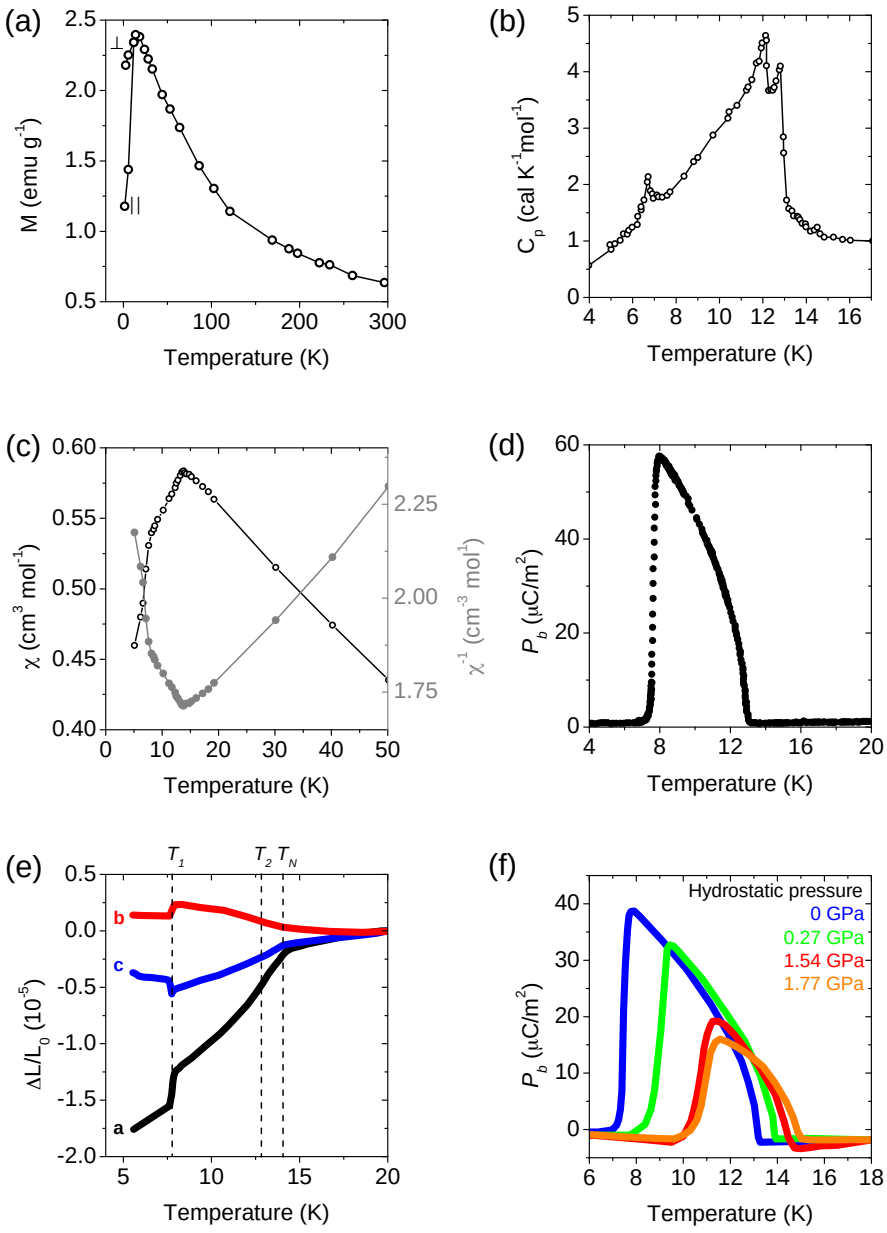

FIGURE 3.2: (a) Magnetization versus temperature along two different directions (easy and hard directions) done by Van Uitert *et. al.* where the antiferromagnetic nature of the crystal is reported [83]. (b) Specific heat by C. P. Landee *et. al.* [86]. (c) Magnetic susceptibility measured on powder samples (○) and its inverse (•) adapted from [87]. (d) Electric polarization along the *b* axis measured by Arkenbout *et. al.* [31]. (e) Thermal expansion reported in [95]. (f) Effect of hydrostatic pressure on the polarization along *b* axis adapted from Ref. [95].

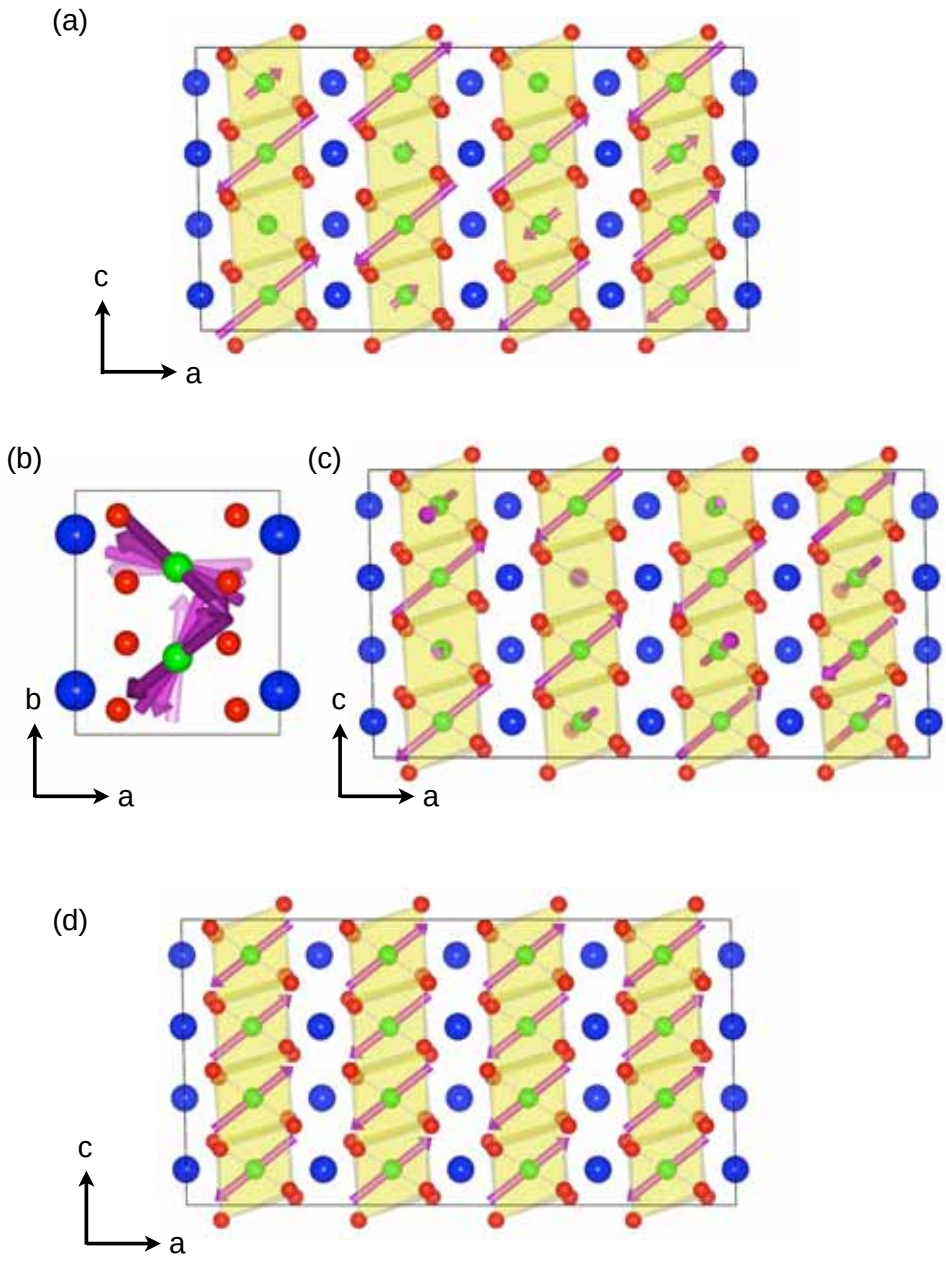

FIGURE 3.3: Magnetic structures of $MnWO_4$ determined by Lautenschläger *et. al.* [87]: (a) the AF3 magnetic structure projected along the *b* axis, (b) the AF2 magnetic structure projected along the *c* axis where the rotation of the moments is noticeable, (c) same structure projected along the *b* axis and (d) the commensurate AF1 spin arrangement.

The succession of magnetic phases together with the ratio between the Néel

and the paramagnetic temperature, $\frac{|\Theta|}{T_N} \gg 1$, is due to a strong competition and subtle balance among multiple magnetic interactions ($MnWO_4$ shows a small magnetic anisotropy which is comparable in energy to the Dzyaloshinskii-Moriya interactions, see Ref. [88]), i. e. magnetic frustration of the system, which was demonstrated by Feng and co-workers in 2011 by means of inelastic neutron scattering [89]. Figures 3.4(a) and 3.4(b) show manganese chains along the *c* axis and the magnetic interactions studied by Feng *et. al.*, and Table 3.2 summarizes the strength of the couplings. According to their results there are five main interaction (J_1, J_3, J_4, J_6 and J_8) that impose antiferromagnetic coupling between the involved atoms which can not be all satisfied simultaneously and hence, the structure becomes magnetically frustrated. Moreover, it turns out that these couplings implicate intrachain and interchain interactions along the *c* and *a* axes. This could explain the incommensurability of the propagation vector along these directions. On the other hand, the magnetic exchange along the *b* axis is rather weak.

Mn-Mn	J_1	J_2	J_3	J_4	J_5	J_6
Dist.	3.286	4.398	4.830	4.990	5.760	5.801
Interac.	-0.42(1)	-0.04(1)	-0.32(1)	-0.26(1)	0.05(1)	-0.43(1)
	J_7	J_8	J_9	J_{10}	J_{11}	
Dist.	5.883	6.496	6.569	6.875	7.013	
Interac.	-0.12(1)	0.02(1)	-0.26(1)	-0.15(1)	0.02(1)	

TABLE 3.2: Interatomic distances and corresponding magnetic interactions calculated by Feng and co-workers [89].

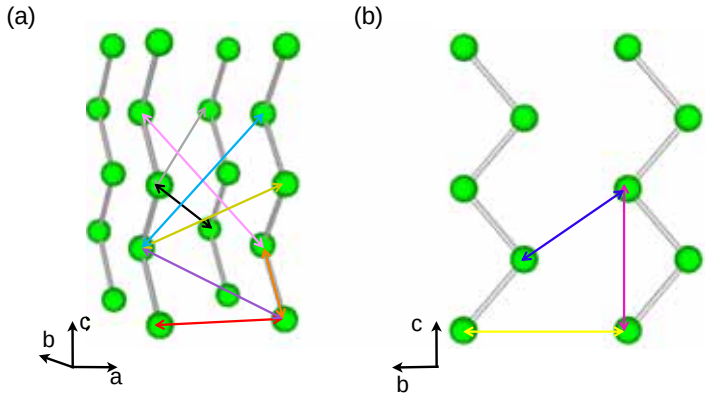

FIGURE 3.4: Two projections of the manganese chains and the intrachain and interchain magnetic interactions between them.

It is rather frequent that a crystal structure undergoes distortions through a magnetic transition, this is the so-called magnetoelastic effect or spin-lattice coupling [90–94]. In the case of $MnWO_4$ this phenomenon is very weak in the sense that the relative changes detected in the crystallographic axes are of the order of $\Delta L/L \sim 10^{-5}$ [95]. These very small changes were observed by thermal expansion measurements, which showed changes in the behavior of $\Delta L/L$ through the transitions, the a axis being the most sensitive to the transitions [see Fig. 3.2(e)].

The interest in this material considerably increased recently with the discovery of its ferroelectric nature at low temperatures [30, 31, 79, 80, 95–108], specially because this property was shown to be tightly linked to the magnetic order [30, 31]. An electric polarization was observed along the b axis in the temperature range where the AF2 magnetic structure exists [see Fig. 3.2(d)], and consequently, it turned out that the cycloidal AF2 structure is a type II multiferroic phase. Ever since then, the research on $MnWO_4$ has been focused on the study of this multiferroic phase.

Being a magnetically frustrated system, $MnWO_4$ tends to be very sensitive to external fields that can unbalance the subtle equilibrium between the magnetic interactions, giving rise to complex field-temperature phase diagrams [98, 109, 110]. On top of that, the fact that the ferroelectricity is somehow linked to the magnetic structure, any modification of the spin-arrangement could in principle change the orientation of the electric polarization or even erase it. As a consequence, the application of external fields can control not only the spin ordering but also the electric polarization (the case of the effect of hydrostatic pressure is depicted in Fig. 3.2(f) which is adapted from Ref. [95]). In this line, the effect of external magnetic field has been thoroughly investigated [31, 98–104, 109]:

- ◇ Applying a magnetic field along the easy axis (direction $\hat{u}$, in the ac plane) induces different magnetic phases depending on the temperature and the intensity of the field [98, 100]. The AF1 phase is suppressed and the multiferroic AF2 phase is stabilized at low temperatures and low magnetic field.

  However, if the field is increased above ≈ 12 T (below 8 K) the crystal undergoes a magnetic transition to a non-polar phase (HF).

  Very recently it has been observed that at very high fields along the easy axis, above ≈ 40 T, the HF phase is erased, the moments re-arrange in a polar structure where the electric polarization is parallel to the b axis [103]. This phase also appears at lower fields but higher temperatures, without going through the HF phase.

◇ If a relatively low magnetic field (about 11 T) is applied along the *b* axis, a new polar phase appears in a narrow temperature range, 10 K - 11 K, where the electric polarization flips from the *b* axis to *a* [99].

◇ On the other hand, if the field is applied along the *a* or the *c* axis, the behavior is similar to applying the field along the easy axis [100].

3.2 $CoWO_4$

Known as Krasnoselskite, this mineral is isomorphic to $MnWO_4$. Its crystal structure has $P2/c$ (No. 13, *b*-unique axis, standard setting) symmetry [82]. The structure is depicted in Fig. 3.5 and the parameters that describe the crystal structure are summarized in Table 3.3.

The first reported studies on $CoWO_4$ were done in the sixties [83, 111]. The magnetic properties were investigated by Van Uitert [83] who showed that this compound is antiferromagnetic below $\approx$ 55 K and that its paramagnetic temperature Θ_P is $\approx$ -85 K. Its magnetization as the temperature decreases exhibits a clear maximum at $\approx$ 55 K [Fig. 3.6(a)] which can be attributed to the Néel temperature. Neutron-diffraction experiments on powder and single crystal samples conclude that moments get ordered collinearly in the *ac* plane making $\approx$ 45° angle with the *c* axis as represented in Fig. 3.5(c) [112–116]. Figure 3.6(b) shows the evolution of the ordered magnetic moment measured by neutron diffraction. The magnetic transitions occurs together with a contraction of the volume of the unit cell as shown in Fig. 3.6(c) observed by Forsyth and co-workers in Ref. [116].

In $CoWO_4$, the strong single-ion anisotropy leads to a scenario where the anisotropic Dzyaloshinskii-Moriya interaction is too weak to cant the the magnetic moments, and therefore, the isotropic superexchange coupling minimizes the energy by aligning the spins along the easy axis [88].

On the contrary to $MnWO_4$, $CoWO_4$ does not show any electric polarization, it is paraelectric.

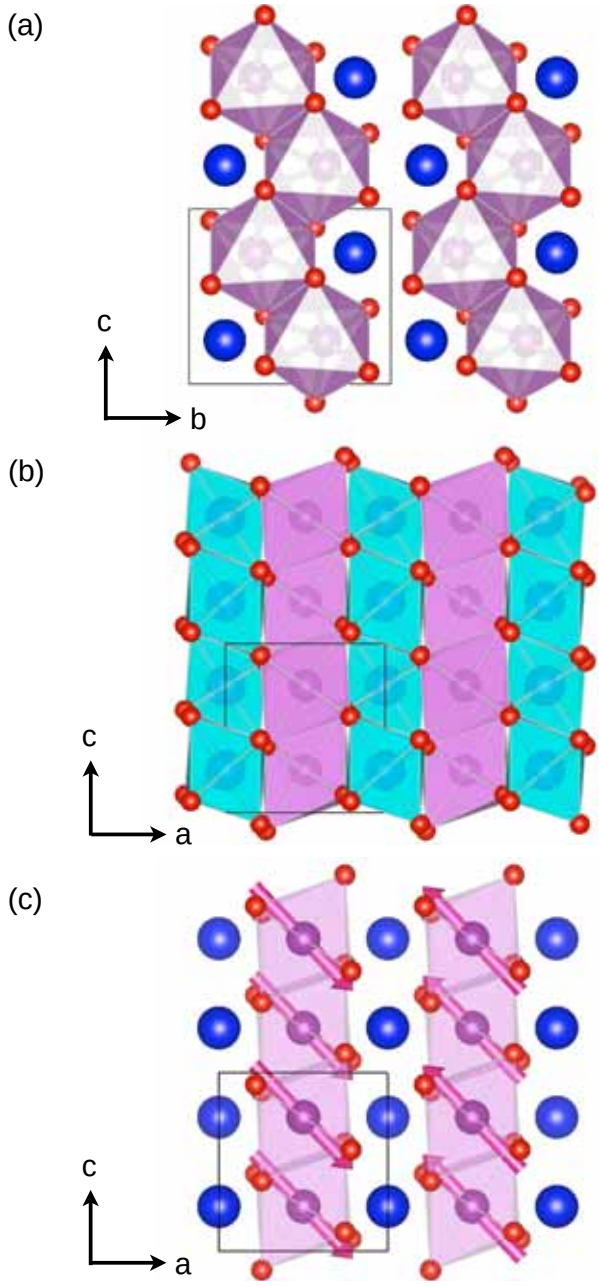

FIGURE 3.5: $CoWO_4$: projection of the crystal structure (a) along the *a* axis and (b) along the *b* axis. The color code is the following: Blue and biggest circles correspond to W atoms; smaller, purple circles inside the octahedra to Co and the smallest red atoms are O atoms. (c) Projection along the *b* axis of the magnetic structure determined at 15 K by Forsyth and co-workers [116].

Cell parameters:	a = 4.6698(9) Å, b = 5.6873(23) Å, c = 4.9515(17) Å, β = 90.(0)^o			
Atoms	Wyckoff position	x	y	z
Co	2f		0.6712(8)	
W	2e		0.1773(4)	
O1	4g	0.2176(3)	0.1080(4)	0.9321(3)
O2	4g	0.2540(3)	0.3757(4)	0.3939(3)
Volume:	131.501 Å^3			

TABLE 3.3: The crystallographic parameters that describe the crystal structure of $CoWO_4$ which has $P2/c$ space-group symmetry (taken from Ref. [82]).

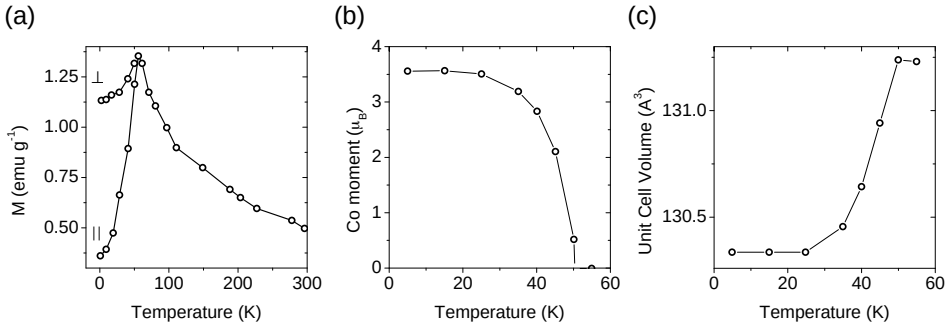

FIGURE 3.6: (a) Thermomagnetic curves of $CoWO_4$ reported by Van Uitert *et. al.*[83]. (b) Ordered Co magnetic moment measured by neutron diffraction and (c) contraction of the volume of the unit cell with decreasing the temperature below the magnetic transition observed by Forsyth and co-workers [116].

3.3 $Mn_{1-x}Co_xWO_4$

Like most of the frustrated multiferroic materials, $MnWO_4$ is extremely sensitive to small perturbations induced by an external agent such as magnetic field or pressure, and also to chemical substitution. One of the main challenges is to enlarge the temperature range where the multiferroic phase is stable. Thus, the objective is to modify the magnetic interactions between the atoms so that the multiferroic structure is favored. Chemical doping is the most promising method for such aim.

$MnWO_4$ has been doped with isovalent metal and nonmetal ions [117–131]. In 1969 Weitzel doped the material with iron for the first time and obtained the phase diagram for the $Mn_{1-x}Fe_xWO_4$ solid solution, the so called Wolframites [117]. In 2003 García-Matres and co-workers observed that the incommensurate magnetic structures disappear when substituting 16% of manganese by iron [118].

It turned out that the transition temperature to the commensurate AF1 increases. But with further doping this transition temperature decreases and another incommensurate phase is promoted which coexists with AF4 (collinear phase of $CoWO_4$). Nevertheless, the higher the doping is the higher the Néel temperature becomes. Some iron doped crystals have been studied under magnetic field. Ye *et. al.* and Chaudhury *et. al.* [121, 122] reported that applying a magnetic field along the easy axis stabilizes the multiferroic phase at low doping.

Other groups have tested nonmagnetic atoms as dopants and studied how the magnetic interactions are modified [123, 124]. It was found that Zn and Mg are good candidates to stabilize the multiferroic phase, although the Néel temperature rapidly decreases from $\approx$ 13 K to $\approx$ 7 K when 40 % of manganese is substituted by Zn. These studies demonstrated that the results obtained using nonmagnetic atoms were, in overall, independent of the dopant.

Very recently it was discovered that doping with Co^{2+} ions is particularly interesting since it strongly stabilizes the multiferroic phase at low temperatures and the transition temperatures do not decrease dramatically. According to preliminary data on powder samples by Song *et. al.* [125], the incommensurate multiferroic AF2 phase is expected to substitute the commensurate AF1 ordering at low temperature for cobalt doping above 3%. At higher doping the AF2 phase is supposed to transform into AF2′ magnetic phase having the same propagation vector but with different orientation of the moments. The proposed phase diagram is shown in Fig. 3.7. However the magnetic structures of the different compounds were not unambiguously determined from this work.

This was the state of the research in $Mn_{1-x}Co_xWO_4$ at the beginning of the thesis. Parallel to our work, other groups have also actively investigated this solid solution [125–131].

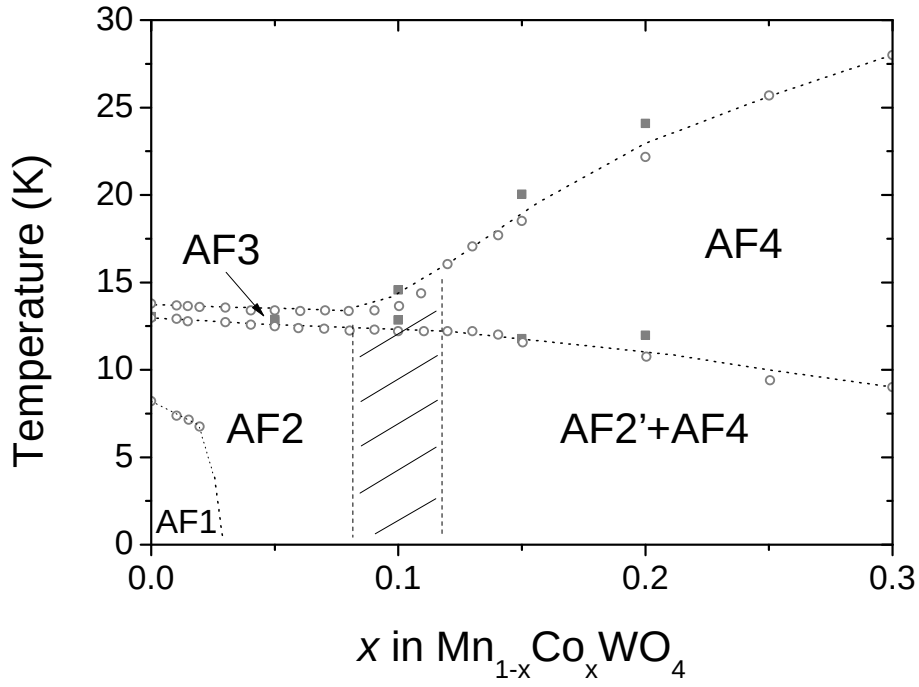

FIGURE 3.7: x-T phase diagram obtained by Song and co-workers on powder samples [125]. The empty circles were obtained from the temperature derivative of the susceptibility and the filled squares are neutron diffraction. The magnetic phases were unclear in the dashed area centered at $x = 0.10$.

Chapter 4

Experimental techniques

All the experimental techniques employed during the thesis are summarized in this chapter and a brief description of the instruments used for performing the experiments is also provided.

4.1 Diffraction

Even if technological advances allow the scientific community to investigate materials by means of a large variety of methods, it is still very difficult to see directly the atoms in a crystal. To see them we use indirect methods such as diffraction. By analyzing the diffraction pattern obtained by the interaction between a wave and the ordered atoms in the crystal, it is possible to reconstruct the structure of that crystalline material.

This technique was first studied in 1665 by Francesco Maria Grimaldi [132] who named this phenomenon as *diffringere* that in Latin means "break into pieces", referring to the scattering of the light when it founds an obstacle on its way [133]. This phenomenon occurs when any wave goes through an obstacle whose dimension is similar to the wavelength of the incoming wave. When the obstacles are located periodically, an interference phenomenon enters into play. The interference pattern is connected to the periodicity of the diffraction grating. In 1913, William Henry Bragg and his son William Lawrence Bragg deduced that if the diffraction grating is a crystal (three dimensional periodic structure), the condition

of constructive interference is given by the Bragg's law:

$$n\lambda = 2d\sin(\theta) \tag{4.1}$$

n being an integer number that corresponds to the order of the diffracted beam, λ the wavelength of the radiation, d the distance between the planes in the crystal and θ the angle of the diffracted wave with respect to the incoming one.

Within the Born approximation, the elastic scattering by a target of an incident wave vector $\mathbf{k}_i$ into a final state characterized by $\mathbf{k}_f$ is given by the differential cross section:

$$\frac{d\sigma}{d\Omega}(\mathbf{k}_i\sigma_i', \mathbf{k}_f\sigma_f') = \left(\frac{m}{2\pi\hbar^2}\right)^2 \mid < \mathbf{k}_f\sigma_f' \mid V(\mathbf{r}) \mid \mathbf{k}_i\sigma_i' > \mid^2 \tag{4.2}$$

where $V(\mathbf{r})$ is the potential felt by the beam (electrons, neutrons or X-rays) at $\mathbf{r}$ in the field of the scatterer. The σ parameter refers to any other property characteristic of each type of radiation. The potential describes the kind of interaction between the wave and the target. In the next sections neutron and X-ray diffraction will be discussed.

4.1.1 Neutron Diffraction

Neutrons have properties that make them unique for our purposes. Its mass gives to the neutron, once thermalized, a *de Broglie* wavelength comparable to the interatomic distances, which is a crucial condition for diffraction. Besides these, it is a neutral particle and, therefore, it does not interact with the electrons of the target but with its nuclei. Moreover, it can deeply penetrate in the sample giving information about the whole volume and not only about its surface. And, last but not least, this particle has a magnetic moment that undergoes a dipole-dipole interaction with the magnetic moments of the unpaired electrons in the material. Then, neutrons are suitable not only to study the crystal structure of crystalline materials but also their magnetic structure. In fact, up to now, they are a unique tool to study magnetic structures, even if other techniques such as Resonant X-Ray Magnetic Scattering provide details of these structures [134–136].

In the case of neutrons, σ_i and σ_f are the initial and final spin of the neutrons (σ is the Pauli spin matrix). The scattering due to the crystalline structure is ruled by the interaction of the neutrons and the nuclei of the atoms, which is assumed to be a δ-function,

$$V_n(\mathbf{r}) = \frac{2\pi\hbar^2}{m}\sum_{l,j} b_j\delta(\mathbf{r} - \mathbf{R}_{lj}) \tag{4.3}$$

where b_j is the scattering length[1]. The intensity of the reflections are proportional to

$$\frac{d\sigma_n}{d\Omega} = \frac{(2\pi)^3}{V} N \sum_{\mathbf{H}} |F_n(\mathbf{Q})|^2 \delta(\mathbf{Q} - \mathbf{H}) \tag{4.4}$$

where $\mathbf{R}_{lj}$ is the position of the atom j in the l unit cell, N is the number of unit cells, V is the volume, $\mathbf{Q} = \mathbf{k}_f - \mathbf{k}_i$ and $\mathbf{H}$ is a vector of the reciprocal lattice. The expression is nonzero when $\mathbf{H} = \mathbf{Q}$, and this is nothing else but the Bragg condition for reflection.[2] F_n is the nuclear structure factor and can be written as

$$F_n(\mathbf{Q}) = \sum_j b_j e^{i\mathbf{Q}\cdot\mathbf{r}_j} e^{W_j} \tag{4.5}$$

where e^{W_j} is the Debye-Waller factor which takes into account the thermal displacements around the equilibrium positions.

One of the advantages of using neutrons is, as mentioned before, that they do not interact with the electron cloud of the atoms but with the nuclei, by the scattering length b. This means that Mn^{2+} and Co^{2+} cations are easily distinguishable with neutron, since $b_{Mn^{2+}} = -3.75$ fm and $b_{Co^{2+}} = 2.49$ fm [137], whereas it is more difficult with X-rays.

4.1.1.1 Magnetic diffraction

In the case of magnetic scattering, the expression of the potential is more complicated. The magnetic moment of the neutron, μ_n, undergoes a dipole-dipole interaction with field created by the unpaired electrons of the atoms in the crystal:

$$V_m(\mathbf{r}) = -\mu_n \cdot \mathbf{B}(\mathbf{r}) = -\mu_n \cdot \sum_{i=1}^{N} \left(\nabla \times \left(\frac{\mu_i \times (\mathbf{r} - \mathbf{R}_i)}{|\mathbf{r} - \mathbf{R}_i|^3} \right) - \frac{2\mu_B \mathbf{p}_i \times (\mathbf{r} - \mathbf{R}_i)}{\hbar |\mathbf{r} - \mathbf{R}_i|^3} \right) \tag{4.6}$$

where $\mathbf{B}$ is the magnetic field arising from the unpaired electrons, μ_n is the magnetic moment of the neutron, μ_i is the moment of the unpaired electron, and $\mathbf{p}_i$, its momentum. With such a potential the scattering cross section from a magnetic crystal for unpolarized neutrons is the following:

$$\frac{d\sigma_m}{d\Omega}(\mathbf{Q}) = N \frac{(2\pi)^3}{V} \sum_{\mathbf{H}} \sum_{\mathbf{k}} |\mathbf{F}_{\mathbf{M}\perp}|^2 \delta(\mathbf{Q} - \mathbf{H} - \mathbf{k}) \tag{4.7}$$

[1] It depends on the isotope of the atom.

[2] Coherent elastic scattering occurs when the scattering vector coincides with a reciprocal lattice vector.

where $\mathbf{k}$ here is the propagation vector of the magnetic structure, and $\mathbf{F_M}$ is the magnetic structure factor. Note that only the component of the magnetic structure factor perpendicular to the scattering vector contributes to the magnetic scattering. Hence the intensity of the magnetic reflections are proportional to the square of $\mathbf{F_M}$.

$$\mathbf{F_M}(\mathbf{Q} = \mathbf{k} + \mathbf{H}) = pf(\mathbf{Q}) \sum_j \mathbf{S}_{\mathbf{k},j} e^{i\mathbf{Q}\cdot\mathbf{r}_j} e^{W_j} \tag{4.8}$$

p represents the scattering amplitude at $\mathbf{Q}$=0 for a single magnetic moment of $1\mu_B$ and $f(\mathbf{Q}) \propto \frac{1}{\mathbf{Q}}$ is the magnetic form factor. $\mathbf{S}_{\mathbf{k},j}$ is the Fourier component of the magnetic moment distribution.

Indeed, assuming that the magnetic atom j in the unit cell l carries a magnetic moment one can define a magnetic vector, $\mathbf{m}_{lj}$, for each of these atoms that gives the amplitude and the direction of each magnetic moment. This magnetic moment distribution can be Fourier expanded according to:

$$\mathbf{m}_{lj} = \sum_{\mathbf{k}} \mathbf{S}_{\mathbf{k}_j} e^{-2\pi i \mathbf{k}\cdot\mathbf{R}_l} \tag{4.9}$$

where $\mathbf{S}_{\mathbf{k}j}$ is the Fourier component of the distribution associated to the propagation vector $\mathbf{k}$.

The magnetic diffraction may occur at the same position of the nuclear peaks (if $\mathbf{k} = \mathbf{0}$) or at different places in the reciprocal space (if $\mathbf{k} \neq \mathbf{0}$), see equation (4.7).

Regarding the magnetic neutron-data refinements, except in Chapter 7, the magnetic structures have been studied based on the following expression, which is the expansion of equation (4.9) for a given magnetic propagation vector $\mathbf{k}$ (and the associated $-\mathbf{k}$):

$$\mathbf{m}_{lj}(\mathbf{k}) = \Re_j(m)\hat{u}_j \cos[2\pi(\mathbf{k}\cdot\mathbf{R}_l + \varphi_j)] + \Im_j(m)\hat{v}_j \sin[2\pi(\mathbf{k}\cdot\mathbf{R}_l + \varphi_j)], \tag{4.10}$$

where $\mathbf{m}_{lj}$ is the magnetic moment of the atom j in the unit cell l, $\mathbf{R}_l$ is the vector joining the arbitrary origin to the origin of unit cell l, and φ_j is a magnetic phase. The absolute value of each φ_j is completely arbitrary in the case of an incommensurate propagation vector. However, the difference of phases between the different Bravais sublattices in the unit cell is important. In the isostructural $Mn_{1-x}Co_xWO_4$ compositions there are two magnetic atoms in the unit cell, located at $Mn_{j=1}$ ($\frac{1}{2}$, y, $\frac{1}{4}$) and $Mn_{j=2}$ at ($\frac{1}{2}$, $1-y$, $\frac{2}{4}$). In what follows $\Delta\varphi_j$ stands for the difference $\varphi(Mn_2)-\varphi(Mn_1)$. This phase factor is given by representation analysis as developed in Ref. [62] and in Appendix B, and is equal to $\frac{k_z}{2}$, k_z being the component of the propagation vector along c^*.

For the description of the magnetic structures we use an orthonormal xyz coordinate system: x coincides with the crystallographic a axis, y belongs to the ab plane and z is perpendicular to the ab plane, along c^*. Therefore, in our case, $x = a$, $y = b$ and $z = x \times y \neq c$. The unitary vectors $\hat{u}$ and $\hat{v}$ are described in spherical coordinates: θ is the angle with the $z = c^*$ axis and ϕ the one with respect to the x axis of the projection in the xy plane.

Note that collinear structures are described by a unique direction, i. e. $\Im_j(m) = 0$.

4.1.1.2 Single-crystal diffraction versus powder diffraction

The main difference between powder diffraction and single-crystal diffraction, comes from the fact that for a powder pattern all the reciprocal space is projected onto one dimension as a function of 2θ. This means that all intensities located at the same 2θ angle contribute to a unique peak and consequently, the intensity is an average of all those peaks. Due to this averaging, neutron-powder-diffraction experiments do not provide in certain cases enough information to completely resolve the spin arrangement of magnetic structures. In a single crystal experiment each reflection is collected individually.

To illustrate the importance of having a single crystal to determine a magnetic structure, lets assume that the propagation vector associated to the magnetic structure is $\mathbf{k}$ = (0.21, $\frac{1}{2}$, 0), that the moments lay on the ab plane (so does the magnetic structure factor) and that the diffraction pattern of our material is the one shown in Fig. 4.1. Two magnetic reflections appear with the scattering vectors Q_1 = (1.21, -$\frac{1}{2}$, 0) and Q_2 = (1.21, $\frac{1}{2}$, 0). According to equation (4.7), only the perpendicular component of the magnetic structure factor to the scattering vector contributes to the intensity of each reflection. The green line of the plot represents the direction of the magnetic moments in the ab plane and α and β correspond to the angles that the scattering vectors make with the magnetic structure factors. As $\alpha \neq \beta$ the intensity of those reflection is different. However, both reflections, are located at the same 2θ and, therefore, in powder diffraction they would be added up in a unique peak. In that situation, it might occur that the analysis of the data could converge to different arrangements with equal values for the agreement factors.

Nevertheless, making the experiments on powder samples has certain advantages, such as the observation of all the reciprocal space in one shot, which is of great help when the propagation vector is not known. Actually, this is the main reason why the determination of the magnetic structures is usually first done on

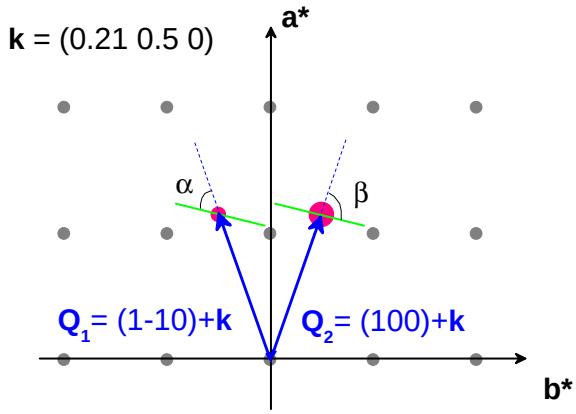

FIGURE 4.1: Sketch of a reciprocal space. Nuclear reflections are represented by grey dots and magnetic reflections by pink dots. For simplicity only two magnetic reflections are plotted. The green line stands for the direction of the magnetic moments. The scattering vectors, Q_1 and Q_2, make α and β angle with the direction of the moments, respectively.

polycrystalline samples. Moreover, obtaining a good single crystal, big enough to run a neutron experiment, is often not a trivial task.

In conclusion, the investigation of magnetic phase diagrams usually begins with the study of polycrystalline material. Once the propagation vectors are known and if the details of the magnetic structures are unclear, one should try to study single crystals. On the contrary, the effect of external fields on the behavior of the materials must be analyzed on single crystals, in order to apply the field in one fixed direction.

4.1.1.3 Larmor diffraction

This technique, which was developed by Rekveldt [138–140] 10 years ago, is based on the fact that a spin precesses around a magnetic field with a frequency equal to the Larmor one:

$$\omega_L = -\gamma B = -\frac{eg}{2m}B \tag{4.11}$$

where B is the magnitude of the magnetic field, g is the g-factor.

Within the classical model, lets assume that neutrons of velocity v and polarization σ_x enter a L_1 coil, hit the sample and go through another coil L_2. The neutrons spend a certain time in each coil, with a magnetic field perpendicular to

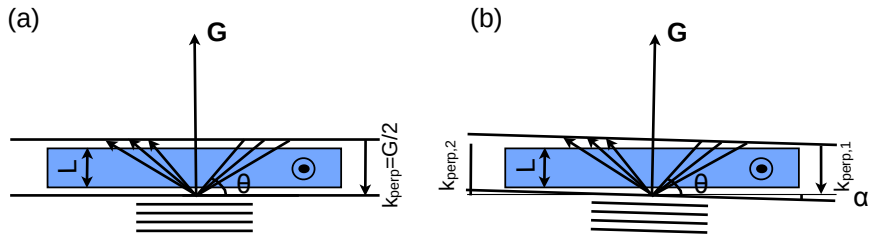

FIGURE 4.2: Larmor precession sketch.

their velocity and precess an angle

$$\phi = \frac{\omega_L L_i}{v_{i\perp}} \tag{4.12}$$

in each coil, where $i = 1, 2$ corresponds to the different coils.

Now, let us imagine the following set up. Neutrons go through a magnetic field, hit the sample and are diffracted according to the Bragg's law, $\mathbf{Q} = 2k \sin\theta_B \mathbf{u} = \mathbf{H}$, where $\mathbf{H}$ is a reciprocal lattice vector normal to the diffracting planes. In Fig. 4.2(a) the boundaries of the magnetic field are placed parallel to the diffracting planes, hence, neutrons that satisfy the diffraction condition will undergo an identical Larmor precession while they go through the same magnetic field, because the perpendicular component of the wave vector (or velocity) will be unchanged. If the boundaries of the magnetic field are not parallel to the diffracting planes, the path that neutrons will go through in each coil will not be the same anymore, and the precession of the neutrons will vary in each coil. The final precession angle can be expressed in terms of the cell parameters

$$\phi = \frac{4m}{\hbar H}\omega_L L\left(\frac{\cos\alpha}{\cos^2\alpha - \cot^2\theta_B \sin^2\alpha}\right) \propto aL, \tag{4.13}$$

where α is the tilting between the planes and the magnetic field boundary. By measuring the phase difference, variations of the lattice constants (due to thermal expansion/contraction for example) can be measured very accurately.

4.1.2 Synchrotron X-ray diffraction

Synchrotron X-ray radiation is produced by bending the trajectory of a relativistic charged particle. It is created artificially in synchrotrons through magnetic fields by means of bending magnets, undulators and wigglers. This radiation has certain

characteristics that makes it unique for many different kind of experiments. It's characteristics are the following: white light, very high flux, high brilliance, high stability, polarized beam and pulsed time structure. The high level of intrinsic collimation and high intensity of the source facilitates the construction of powder diffractometers with unrivaled resolution as ID31 at the ESRF. Taking profit of the pulsed time structure of the beam, experiments can be performed with good time resolution, even if this can not combined with ultrahigh resolution. Moreover, the beam can be tuned to use very shorts wavelengths, which allows to collect data at very high **Q** and at the same time to reduce the absorption in the crystal. The nature of the light provides diffractions patterns with very narrow peak-widths, of less than 0.05°, that can be modelled easily.

On the other hand, X-rays do not interact with the nucleus of the atoms but with the electron cloud that surrounds it. Using the proper potential function in equation (4.2), the nuclear structure factor of a crystal can be written as:

$$F_n(\mathbf{Q}) = \sum_j f_j e^{i\mathbf{Q}\cdot\mathbf{r}_j} e^{W_j} \tag{4.14}$$

where f_j is the form factor of each j atom and e^{W_j} is the Debye-Waller factor which takes into account the thermal displacements around the equilibrium positions. The form factor is the Fourier transform of the electron density, which is spread within a cloud, and therefore the Fourier transform depends on **Q**: it decreases as **Q** increases. These means that the intensity drops down at high **Q**.

4.1.3 Refinements and agreement factors

All diffraction data (crystal and magnetic) have been treated using Fullprof Suite package [141], except those treated by the superspace formalism in Chapter 7 for which the program JANA2006 [61] was used. The crystal and magnetic structures are refined/determined by minimizing the weighted squared difference between the observed data and calculated pattern. Depending on the initial data set, whether it is a powder profile or a set of integrated intensities, the quality of the agreement is measured by different parameters [141–143].

In the case of a powder pattern, where at each $2\theta_i$ the are y_i counts and the refinement of p parameters yields with a model for which the counts of each $2\theta_i$ is $y_{c,i}$:

◇ Profile Factor:

$$R_p = 100 \frac{\sum_{i=1,\ldots,n} |y_i - y_{c,i}|}{\sum_{i=1,\ldots,n} |y_i|} \tag{4.15}$$

◇ Weighted Profile Factor:

$$R_{wp} = 100 \left[\frac{\sum_{i=1,\ldots,n} [w_i |y_i - y_{c,i}|^2]}{\sum_{i=1,\ldots,n} w_i y_i^2} \right]^{\frac{1}{2}} \tag{4.16}$$

where the weight, w_i, is equal to $\frac{1}{\sigma_i}$ being σ_i the statistical error of y_i.

◇ Expected Weighted Factor: this is the expected value for R_{wp} considering that the profile function is perfect.

$$R_{exp} = 100 \left[\frac{n-p}{\sum_{i=1,\ldots,n} w_i y_i^2} \right]^{\frac{1}{2}} \tag{4.17}$$

begin n the total number of observed points, i. e. the amount of y_i; and p the number of refined parameters.

◇ χ^2: this value should tend to one.

$$\chi^2 = \left[\frac{R_{wp}}{R_{exp}} \right]^2 \tag{4.18}$$

This parameter is subject of many systematic errors, such as the underestimation of the standard deviations or large collection times with small steps that yield with small values of R_{exp} and therefore χ^2 results much bigger than 1.

In the cases where the diffraction information is recorded as integrated intensities, where F^2_{obs} are the observed integrated intensities, F^2_{calc} are the calculated ones, n runs over the observations from 1 to N_{obs}, w_n is the weight , M the function to be optimized, $M = \sum_n w_n \left(F^2_{obs,n} - \sum_k F^2_{calc,k} \right)^2$, k runs over the reflections that contribute to the observation n and p the number of refined parameters, the agreement factors given to measure the quality of the fitting are the following:

◇ R_{F^2}

$$R_{F^2} = 100 \frac{\sum_n [|F^2_{obs,n} - \sum_k F^2_{calc,k}|]}{\sum_n F^2_{obs,n}} \tag{4.19}$$

◇ R_{wF^2}

$$R_{wF^2} = 100 \sqrt{\frac{M}{\sum_n w_n F^2_{obs,n}}} \tag{4.20}$$

◇ R_{F^2}

$$R_{F^2} = 100\frac{\sum_n [|F_{obs,n} - \sqrt{\sum_k F^2_{calc,k}}|]}{\sum_n F_{obs,n}} \tag{4.21}$$

◇ χ^2

$$\chi^2 = \frac{M}{N_{obs} - p} \tag{4.22}$$

Very often, the best way to determine the goodness of a proposed model is to observe the observed intensities versus the calculated ones and to ensure that the result is physically acceptable.

4.1.4 Instrumentation

For diffraction experiments four different types of instruments were used: single-crystal neutron-diffractometers, a thermal-neutron spectrometer and a synchrotron-X-ray powder-diffractometer. Most of the neutron-diffraction experiments have been performed on D23 and therefore, a detailed description of this instrument is provided to the reader in the following.

D23: it is CEA/CRG a thermal-neutron two-axis diffractometer for single crystals [144]. It is installed on the thermal-neutron guide H25 at the Institut Laue Langevin (ILL) in Grenoble, France. The neutron guide is equipped with supermirrors and it is curved in such a way that no direct view of the reactor-core is possible: this means that there is not fast-neutron contamination and thus background levels are very low. D23 has been designed to work with or without polarized neutrons, in the incident wavelength range 1 Å - 3 Å.

As neutrons enter the instrument coming from the neutron-guide, they encounter either of the two monochromators that provide different wavelengths: a vertical focused pyrolythic graphite (PG) 002 (in reflection) with $\lambda \approx 1.3$ Å or a flat Cu 200 (in transmission) that provides $\lambda \approx 2.4$ Å. In the secondary shielding, another monochromator (a Heusler 111 in transmission) can be mounted when neutrons need to be polarized. The crystal is installed on the sample-table. The scattered neutrons are counted by a lifting detector mounted in an arc. The sketch of the instrument is shown in Fig. 4.3.

The diffractometer operates in normal-beam geometry which means that it has three angular motions: ω, γ and ν. The first corresponds to the rotation of the sample-table around the vertical axis and γ and ν are the angular motions

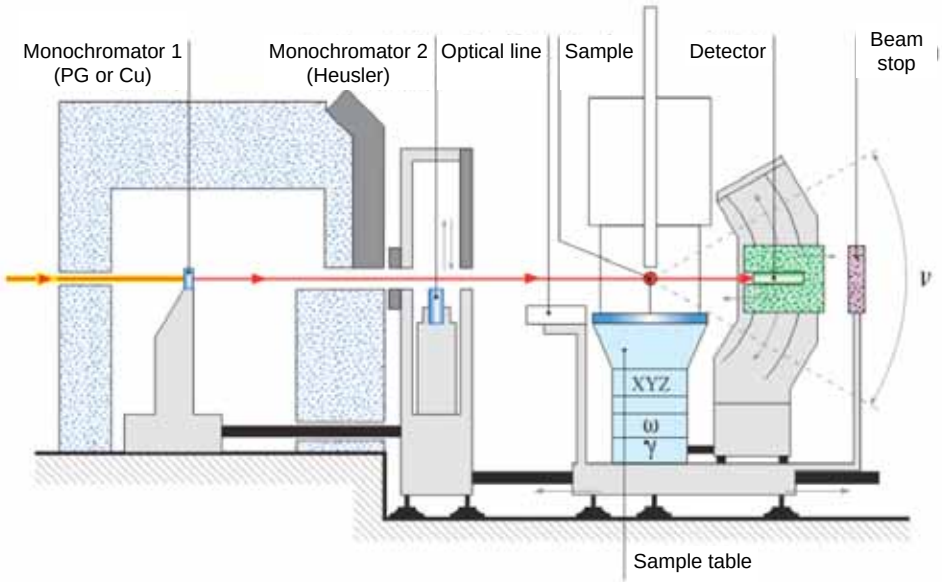

FIGURE 4.3: Sketch of the single-crystal thermal-neutron diffractometer D23. The figure has been adapted from [144].

of the detector, the rotation in the equatorial plane and out of the horizontal plane, respectively. The limitations on the angular motions restrain the maximum value of the Bragg angle ($2\theta_B \approx 130^\circ$). The lifting detector can cover a symmetric angular range $-29^\circ < \nu < 29^\circ$.

This instrument can hold different environments such as pressure cells, cryostats and cryomangets. The mechanics of the instrument is completely non magnetic which enables the instrument to support high field magnets. However the use of these sample environments introduces certain experimental restrictions. The following restrictions concern the cryomagnets used in this thesis:

(i) Smaller angular range: The magnets restrict the accessible ν range and can even reduce the reachable reflections to a single plane. The accessible ν angular range depends on each magnet, $-5^\circ < \nu < 20^\circ$ for the 6T-CNRS magnet and $-3^\circ < \nu < 10^\circ$ for the 12T-CEA-CRG magnet.

(ii) Blind regions: The mechanical structure of the magnet has columns which considerably reduce the neutron flux and hence, they produce

blind areas from the experimental point of view.

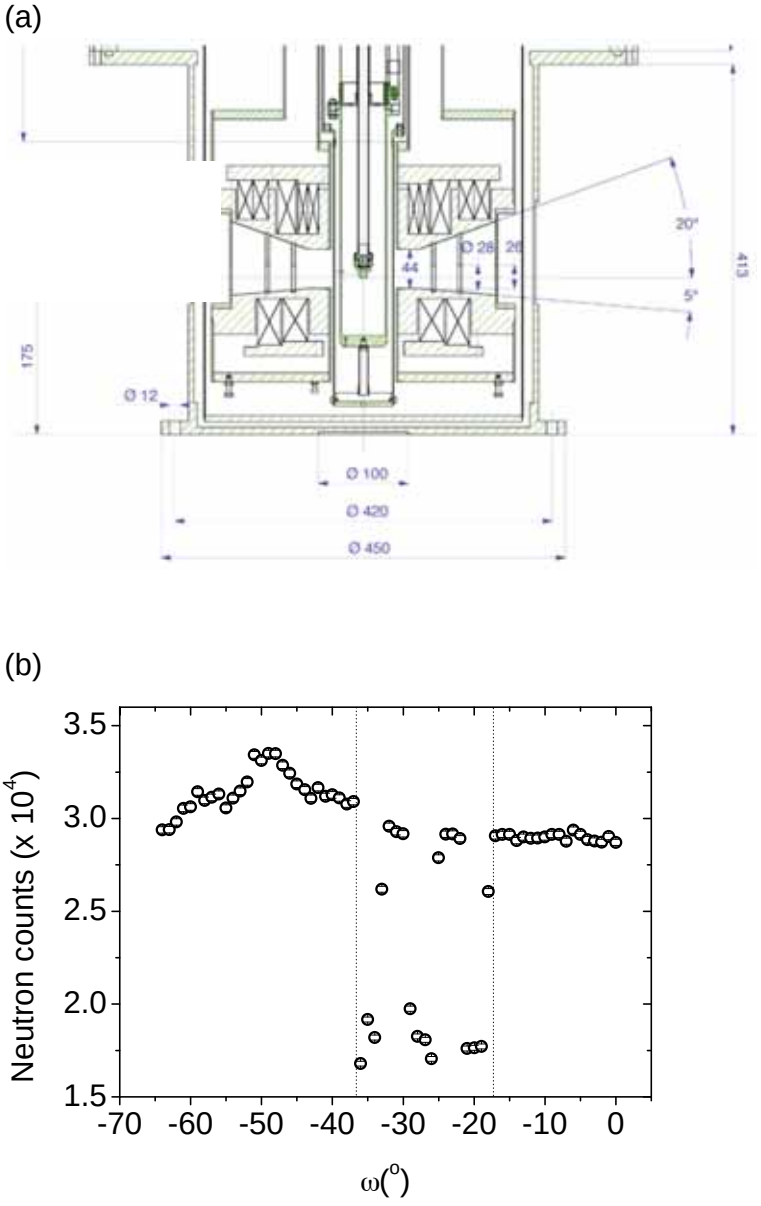

FIGURE 4.4: (a) Sketch of the 6T-CNRS vertical-field magnet that can be used on D23. (b) ω-scan of the direct beam which shows the influence of the pillars on the intensity of the beam.

D15: it was a thermal-neutron diffractometer for single crystals located at the ILL. It was installed on an inclined beam tube (IH4). Three wavelengths could

be set up, $\lambda \approx$0.85 Å, $\lambda \approx$1.17 Åand $\lambda \approx$1.54 Å. The instrument could be operated in either four-circle or normal-beam mode.

6T2: This diffractometer is a thermal-neutron four-circle diffractometer with lifting counter situated at the Laboratoire Léon Brillouin (LLB) at Saclay, France [146]. It is equipped with two vertically focusing monochromators: Cu 220 with $\lambda \approx 0.90$ Å and an Er filter and a PG 002 with $\lambda \approx 1.55$ Å and 2.35 Å (PG filter). Two types of geometries can be used: four-circle geometry with an Eulerian cradle for structural studies of large unit cells (cell volumes of more than 1000 Å) and high resolution studies (phase transitions, etc ...) or a lifting-counter geometry when using cryomagnet, dilution cryostat and high pressure cell for magnetic studies (normal-beam geometry).

IN22: this instrument is a three-axis spectrometer installed at the end position of the thermal supermiror guide H25 at the ILL [145]. It is equipped for full polarization analysis. The Heusler (111) provides a high flux of polarized neutrons. The sample, analyzer and detector are mounted on nonmagnetic modules with adjustable distances between them.

ID31: this beamline is devoted to high resolution powder-diffraction at the European Synchrotron Radiation Facility (ESRF) in Grenoble, France [147]. Three undulators produce X-rays with wavelengths 2.48 Åto 0.21 Å. A double-crystal monochromator is used to choose a unique λ: Si 111 crystals (for standard operation) or Si 311 crystals (for higher energy resolution). ID31 works with spinning capillaries or flat plate specimens. Nine detectors measure the diffracted intensity as a function of 2θ. Each detector is preceded by a Si 111 analyzer crystal. The flux at the sample is 1.5×10^{12} photons $mm^{-2}\ s^{-1}$ at 0.43 Å wavelength and 6.1×10^{12} photons $mm^{-2}\ s^{-1}$ at 0.85 Å. It can hold many sample environments: liquid-helium-cooled cryostat, Oxford Cryosystems Cryostream cold-nitrogen-gas blower, hot-air blower, mirror furnace, ...

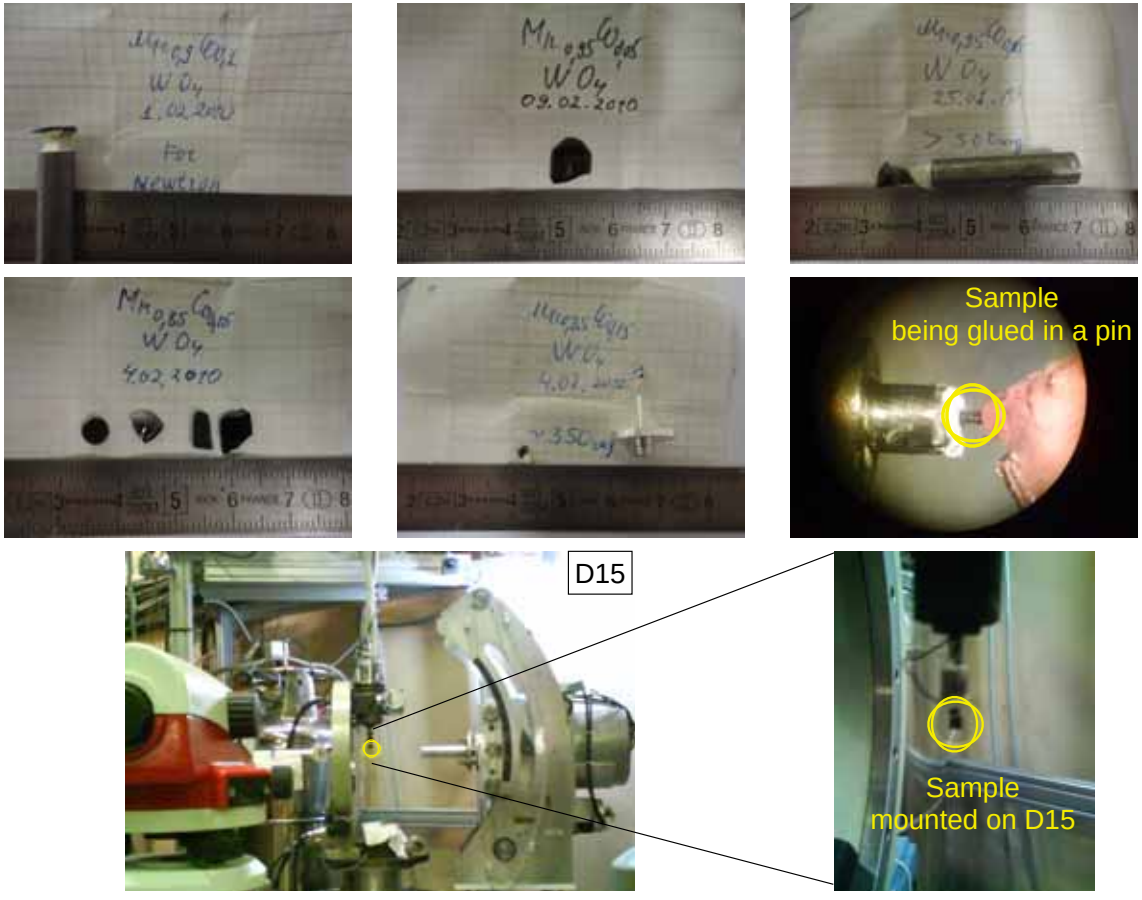

FIGURE 4.5: Pictures of single crystals of $Mn_{1-x}Co_xWO_4$. Some crystals appear unglued, one being glued and the last one already prepared on D15 ready for a neutron diffraction experiment.

Neutron-diffraction experiments were usually performed on big samples, which usually were not oriented. Thus, very often, the orientation was done on a neutron diffractometer. Usually big crystals are recommended because of the fact that neutrons hardly see materials and therefore, increasing the size of the sample helps to gain intensity. On the other hand, having a high quality single-crystal proper for neutron diffraction is sometimes rather difficult: often one finds reflections that are split in several reflections. It occurs if the crystal is slightly broken for example. The orientation of the pieces is a bit different and consequently, each piece diffracts in a different direction. So, even if for electric and magnetic measurements this misalignment is not important, it makes a neutron-diffraction experiment unfeasible. Coming upon a suitable crystal for a neutron-diffraction experiment requires testing a lot of crystals. Once a good crystal is found, usually it has to be oriented and glued in a pin. Figure 4.5 shows several pictures of unglued and glued crystals.

Once single-crystal data was collected the absorption in the sample was corrected using the Cambridge Crystallography Subroutine Library [148].

For synchrotron-X-ray powder-diffraction experiments, $\lambda = 0.40000(1)$ Å wavelength was selected. Powder samples were obtained from crushed single crystals and were enclosed in a borosilicate-glass capillary (with 0.5 mm $\varnothing$), and a good powder averaging was ensured by appropriate spinning of the capillary in the beam. The counting time was about 1.5 hours to have the desired statistics over the angular range 4° to 42° in 2θ.

The crystal and magnetic structures have been produced using program VESTA [149] and FullProf Studio [141].

4.2 Bulk magnetic measurements

The *magnetization* is defined as the magnetic moment of the material per unit volume (or per unit mass) and the *susceptibility* is defined as a proportionality between the magnetization and the applied magnetic field (it indicates the degree of magnetization of a material in response to an applied magnetic field).

When a dc field, H, is applied to a sample it gets magnetized and this state is characterized with a certain magnetization, M and magnetic susceptibility, χ, values. If an ac field is applied or superimposed to the dc field, the magnetic response

becomes time dependent. The fundamental difference between dc and ac measurements is that the former provides discrete information about the magnetization curve whereas the latter gives information about the slope of the magnetization curve at a certain point H. The ac susceptibility is given by

$$\chi_{ac} = \frac{dM}{dH}. \tag{4.23}$$

At low frequencies, where the measurement is more similar to dc magnetometry, the magnetic moment of the sample follows the $M(H)$ curve that would be measured in a dc experiment. As long as the ac field is small, the induced ac magnetization is

$$M_{ac} = \frac{dM}{dH} \cdot h_{ac}, \tag{4.24}$$

where h_{ac} is the time dependent applied magnetic field, and ω is the driving frequency:

$$h_{ac} = h \cos \omega t. \tag{4.25}$$

Changing the applied dc-magnetic-field, different parts of the $M(H)$ curve can be accessed. Since the ac measurement is sensitive to the slope of $M(H)$ and not to the absolute value, small magnetic changes can be detected even when the absolute magnetization is large.

At higher frequencies, the ac magnetization of the material does not follow the dc magnetization curve due to dynamic effects in the sample,

$$M_{ac} = M \cos(\omega t - \theta) \tag{4.26}$$

θ being the phase shift between the field and the magnetization. For this reason, the ac susceptibility is often known as dynamic susceptibility. In this case, the magnetization of the sample may lag behind the driving field. Thus, the ac-magnetic-susceptibility measurement yields two quantities: the magnitude of the susceptibility, χ, and the phase shift. Alternately, one can think of the susceptibility as having an in-phase, or real, component χ' and an out-of-phase, or imaginary, component χ''.

$$\chi_{ac} = \chi' \cos(\omega t) + \chi'' \sin(\omega t) \tag{4.27}$$

where,

$$\chi' = \chi \cos\theta \qquad \chi'' = \chi \sin\theta \qquad \theta = \arctan\frac{\chi''}{\chi'} \qquad \chi = \sqrt{\chi'^2 + \chi''^2}$$

The imaginary component, χ'', indicates dissipative processes in the sample. If there are any time-dependent relaxation processes in the system, the induced

magnetization cannot follow the field instantaneously and this leads to a non-zero θ and, therefore, to a non zero χ''. The imaginary component of the susceptibility, is also non zero if there are any non linearities or hysteresis in the dc magnetic response of the material. Besides that, both χ' and χ'' are very sensitive to thermodynamic phase changes, and are often used to measure transition temperatures.

Both dc- and ac-susceptibility measurements were used to obtain the magnetic phase-transition temperatures and the type of transitions of the handled materials during the thesis.

Superconducting quantum interference device (SQUID) magnetometer, a widely used instrument for magnetic measurements nowdays, is able to detect extremely tiny magnetic fields. This device is based on the tunneling of superconducting electrons across a very narrow insulating gap (known as a Josephson tunnelling junction) between two superconductors. Its high sensitivity is possible because it responds to changes of magnetic field associated with one flux quantum. The working principle of a SQUID is based on the possibility to convert magnetic flux into an electrical voltage.

In principle, a measurement is performed in the SQUID magnetometer by first moving the sample along the symmetry axis of superconducting detection coils and a magnet. Due to its movement, the magnetic moment of the sample induces an electric current in the detection coils. A change of magnetic flux in these coils changes the persistent current in the detection circuit. Hence, the change of the current in the circuit produces variation of output voltage in the SQUID, which is essentially proportional to the magnetic moment of the sample.

The detection coils are basically a single superconducting wire in the form of three counterwound coils configured as a second-order gradiometer. This configuration eliminates spurious signals caused by the fluctuations of the large magnetic field from the superconducting magnet, and also reduces noise from nearby magnetic objects in the surrounding environment.

Two commercial instruments from Quantum Design, Superconducting Quantum Interference Device (SQUID) and Physical Property Measurement System (PPMS), were used to measure bulk magnetic characteristics, namely ac-susceptibility and dc-susceptibility and magnetization. While the ASMS ac-susceptometer/dc-magnetomer option of the PPMS was used to obtain all ac-susceptibility and most of the magnetization data, the SQUID (model MPMS_LX) was used for low field magnetization measurements, to benefit from the specific characteristics of the two instruments:

- ◇ The superior sensitivity of the RSO[3] option of the SQUID $\approx 5 \times 10^{-8}$ emu ($\approx 5 \times 10^{-5}$ emu for the PPMS dc option).

- ◇ The possibility to get rid of the remnant field in the SQUID superconducting magnet by quenching it and also demagnetizing the shield screening the stray fields. No quenching option is provided in the PPMS and one could only minimize the remnant field of the type II superconducting magnet by periodically cycling the field when reducing it amplitude to zero.

- ◇ The PPMS maximum field of 9 T (7 T for the SQUID) and the possibility to study ac-susceptibility up to such high dc fields. Furthermore since the PPMS works as a dc-magnetometer based on the extraction technique, the measurements could be executed rather fast and also the maximum signal that could be measured is much bigger that the 0.3 emu upper limit for the RSO option of the SQUID.

The samples were generally mounted in clear plastic drinking straws within few degrees in respect of the magnetic field direction [see Fig. 4.6]. The specific conditions at which the data have been collected will be specified when presenting the results for each crystal.

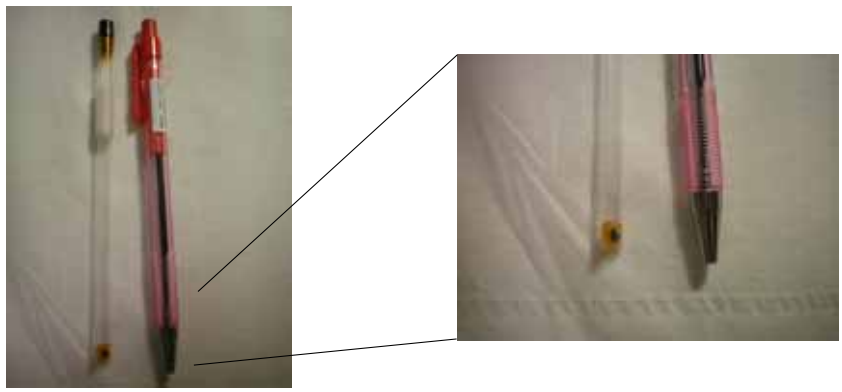

FIGURE 4.6: Single crystal located in a plastic straw. The red pen is provided as scale.

[3]When the sample is moved up and down it produces an alternating magnetic flux in the pick-up coil which leads to an alternating output voltage of the SQUID device. By locking the frequency of the readout to the frequency of the movement (RSO, reciprocating sample oscillation), the magnetometer system can achieve the extremely high sensitivity for ultra small magnetic signals as described above.

4.3 Pyroelectric measurements

Electric polarization measurements were kindly provided by Prof. A. A. Mukhin. The measurements of the electric polarization as a function of the temperature were performed by detecting the pyroelectric current by a Keithley 6517A electrometer. Samples were prepared with electrodes sputtered on opposite faces of the crystaland for different crystallographic orientations. In order to ensure a single domain ferroelectric state a poling field E_p up to $\pm$3000 V/cm was first applied in the paraelectric state, prior to cooling the sample down the lowest temperature, usually 1.9 K. At this point, the voltage was set to zero.

Since polarization measurements are concerned with the bulk polarization within the sample, it was important to remove the effect of surface charges which had built up due to the application of an electric field. A bleed resistor box was built for this purpose, which dissipated the surface charge when the voltage supply was disconnected. The sample was then connected to a Keithley 6517A electrometer, and the temperature of the sample was increased whilst measuring the pyroelectric current. The temperature dependence of the pyroelectric current typically shows a finite signal in the ferroelectric phase, with a sharp anomaly at T_{FE}. Above T_{FE}, the signal becomes flat, showing that electric polarization no longer exists in the system. In order to convert the data into a measure of the polarization (in Cm^{-2}), the following relationship is used:

$$P = \int \frac{Idt}{A} \tag{4.28}$$

Data are integrated with respect to time. This integration method ensures that zero polarization is calculated in the temperature range where the pyroelectric current is zero, i.e. above T_{FE}. The integral of the current is divided by the sample area (electrode area) to give the polarization, which can be plotted against temperature.

4.4 Crystal synthesis

I would like to stress that I did not participate in the synthsis of the crystals. They were all grown by Prof A. M. Balbashov from Moscow Power Engineering Institute and kindly provided to us by Prof. A. A. Mukhin. The single crystals were grown by a floating zone method using an FZ apparatus URN-2- ZM [150]. The crystal growth was performed in an air atmosphere at a linear speed of 8-10 mm/h with a counter-rotation of crystal and feed rod $\approx$ 20 min^{-1}. Finally the growing crystal

was annealed at T = 1100 °C. Small pieces of the crystal were cut for oriented by X-ray diffraction for bulk magnetic and electric polarization measurements.

Chapter 5

Interest and Objectives

Taking into consideration these previous work, it was worth studying the effect of doping the prototype multiferroic $MnWO_4$ with cobalt on single crystals. Experiments on powder samples evidenced that the phase diagram of this solid solution is very rich and interesting, however single crystal experiments were lacking to firmly establish the magnetic structures through the phase diagram.

The two main points that make this doping so interesting are the following:

- ◇ The multiferroic phase is stabilized when doping above 3%.
- ◇ The transition temperature to the multiferroic phase does not decrease drastically.

The *principal objective* of this thesis was to contribute to the field of multiferroics by studying this highly frustrated family. Namely, we would like to shed light on the following points:

(i) The effect of substituting Mn^{2+} by the anisotropic Co^{2+} ion on the magnetic frustration.

(ii) The interplay between the magnetic structure and the induced electric polarization.

(iii) The existence of new multiferroic phases varying the cobalt content: the magnetic structures and the orientation of the induced electric polarization. The

ultimate aim was to complete the $x - T$ phase diagram of the $Mn_{1-x}Co_xWO_4$ family of compounds.

(iv) The spin-lattice coupling, specially at the multiferroic transition.

(v) Magnetic-field-induced transitions.

(vi) Magnetic field effects, depending on the direction along which it is applied, on the magnetic structures and on the electric polarization: $H - T$ phase diagrams.

(vii) How the magnetic and electric phase transitions occur.

Part II

Magnetic, ferroelectric and structural properties of $Mn_{1-x}Co_xWO_4$ under zero magnetic field

Chapter 6

Crystal Structure of the $Mn_{1-x}Co_xWO_4$ family

The study of the crystal structure of the $Mn_{1-x}Co_xWO_4$ family are presented in this chapter, where the influence of both, the temperature and the cobalt content, are investigated.

The study of the interplay between magnetic transitions and the crystal structure is crucial for the investigation of multiferroic materials. In fact, the structural changes across the magnetic transitions are usually the clue to ascribe the origin of the concomitant appearance of electric polarization. Nevertheless, in some materials, those structural variations are so small that their detection is very difficult. This is usually the case of the magnetic oxides that belong to the type II multiferroics where the inverse Dzyaloshinskii-Moriya interaction induces small displacements of oxygen atoms that are located between magnetic atoms, producing a charge distribution that yields a macroscopic electric polarization. $MnWO_4$ being a prototype of type II multiferroics, is of high interest to search for structural changes that occur at its magnetic transitions, specially at the multiferroic transition.

With this aim, the crystal structure of all the compositions were determined by means of single-crystal neutron-diffraction. Note that with X-ray diffraction there could be some problems to locate light atoms beside heavy ones, that is the case of oxygen atoms close to manganese/cobalt and tungsten atoms (X-rays basically see the electron cloud and not the nuclei, and small atoms such as oxygen can be shadowed by bigger atoms). The study done on the pure compound at different

temperatures allows us to observe the spin-lattice coupling, whereas the analysis of the crystal structure of the distinct species of the series will permit us to establish a relationship between the structural changes induced by the cobalt and the distinct magnetic structures in the phase diagram.

A careful study of the cell parameters of all compositions has been done at room temperature by means of high resolution synchrotron-X-ray powder-diffraction because this technique provides very accurate values for the cell parameters. All the samples were measured in the same conditions (environment, wavelength, ...) and therefore, the systematic errors that those factors could introduce in the determination of the cell parameters is the same. This allows a precise comparison and to see very small relative differences with high precision.

6.1 The crystal structure of $MnWO_4$ across the magnetic transitions investigated by single-crystal neutron-diffraction

The crystalline structure of the pure $MnWO_4$ was carefully studied by means of neutron-diffraction experiments on the D15 diffractometer at the Institute Laue-Langevin (ILL) in Grenoble operating in a four-circle geometry.

Crystal structures were refined at T = 2 K, 5 K, 8 K (magnetically ordered state) and T = 16 K (paramagnetic state). The cell parameters (a, b, c and β) were obtained at these temperatures from the centering of 63 strong reflections and are listed in Table 6.1. No significant changes in the cell parameters were observed.

In addition to the cell variation, modifications in the crystallographic structure may occur at magnetic transitions, i. e. atomic displacements linked to the orientation of the moments. To check this, 290 independent reflections [symmetry averaged from 818 reflections with R_{int}(16 K) = 1.21%, R_{int}(8 K) = 1.21%, R_{int}(5 K) = 1.24% and R_{int}(2 K) = 1.30%] were collected at each temperature. From the refinements it was not possible to see any difference in the structure at those temperatures. Figure 6.1 shows the nuclear structure as refined, where blue circles represent tungsten atoms, green ones are manganese atoms and red circles correspond to oxygen atoms. This color code will be maintained throughout the manuscript. The agreement plots of the refinements at each temperature are also given in Fig. 6.1. Table 6.1 summarizes the refined atomic positions which are the

Temperature		T = 16 K	T = 8 K	T = 5 K	T = 2 K
Magnetic phase		Paramaganetic	AF2	AF2-AF1	AF1
a/Å		4.824(2)	4.823(2)	4.824(2)	4.824(2)
b/Å		5.755(3)	5.755(3)	5.757(2)	5.756(2)
c/Å		5.002(2)	5.001(3)	5.004(2)	5.004(2)
β/°		91.08(3)	91.10(4)	91.09(2)	91.06(3)
Volume/Å^3		138.83(3)	138.79(4)	138.98(2)	138.95(3)
Mn	y	0.6841(2)	0.6841(2)	0.6842(2)	0.6841(2)
	B_{iso}/Å^2	0.27(2)	0.27(2)	0.26(3)	0.26(3)
W	y	0.1803(1)	0.1802(1)	0.1803(1)	0.1802(1)
	B_{iso}/Å^2	0.17(2)	0.17(1)	0.17(2)	0.16(2)
O1	x	0.2108(1)	0.2108(1)	0.2108(1)	0.2108(1)
	y	0.1023(1)	0.1024(1)	0.1024(1)	0.1024(1)
	z	0.9423(1)	0.9422(1)	0.9423(1)	0.9422(1)
	B_{iso}/Å^2	0.29(2)	0.29(1)	0.29(1)	0.29(1)
O2	x	0.2510(1)	0.2511(1)	0.2511(1)	0.2511(1)
	y	0.3746(1)	0.3746(1)	0.3746(1)	0.3746(1)
	z	0.3933(1)	0.3933(1)	0.3933(1)	0.3933(1)
	B_{iso}/Å^2	0.33(2)	0.32(1)	0.32(1)	0.32(1)
R_F/%		3.04	3.03	3.10	3.06
R_{F^2}/%		4.46	4.47	4.60	4.64
R_{F^2w}/%		6.13	5.79	5.90	5.92
χ^2		55.2	59.8	61.9	62.7

TABLE 6.1: The crystal-structure parameters of $MnWO_4$ refined at 16 K, 8 K, 5 K and 2 K from single-crystal neutron-diffraction. Atomic coordinates are given relative to the cell. All the experiments were performed in a four-circle geometry on D15.

same, within the errors bars, for all the temperatures.

The distances between Mn-O atoms and the angles between O-Mn-O atoms that form the octahedra are summarized in Table 6.2 and Table 6.3 respectively, and the sketch of the octahedra is plotted in Fig. 6.2. Within the accuracy of the experiment, there is no clear evidence of any structural change in $MnWO_4$. The octahedra are very distorted, but this distortion is not influenced by the magnetic ordering.

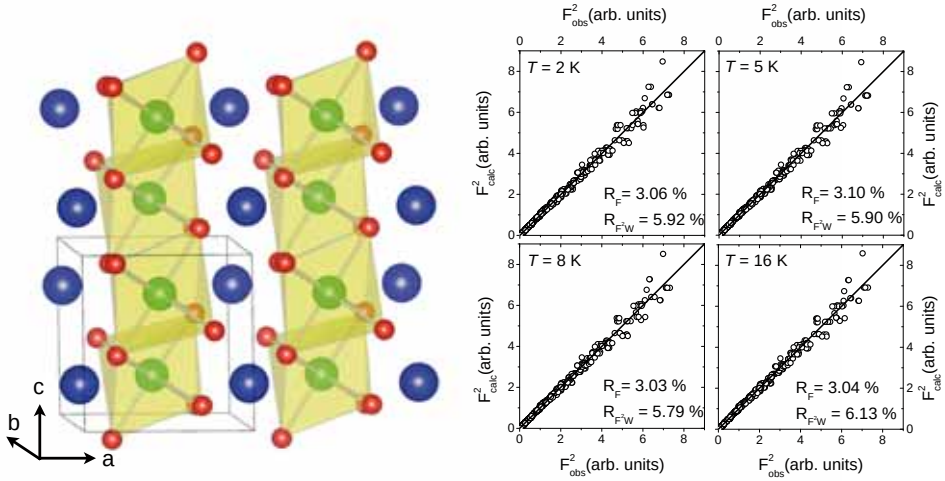

FIGURE 6.1: Nuclear structure at 16 K, 8 K, 5 K and 2 K in the pure $MnWO_4$ compound together with the calculated versus observed integrated-intensities from the refinements.

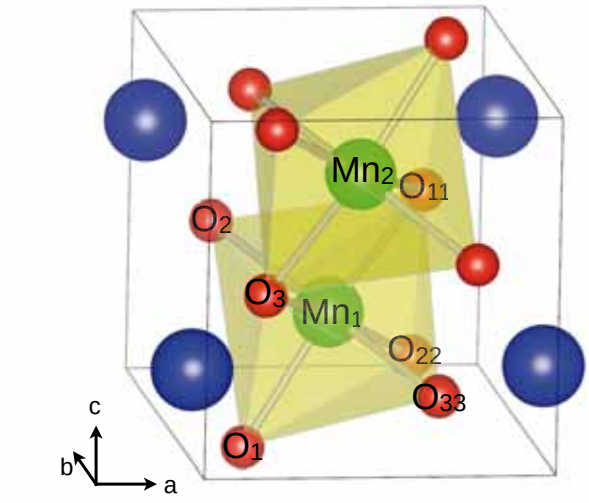

FIGURE 6.2: Sketch of the distorted octahedra. O_i and O_{ii} are equivalent in the octahedra. The atoms are labeled as in Tables 6.2 and 6.3.

Temp.	Angle/°					
	O_1-Mn_1-O_{11}	O_1-Mn_1-O_2	O_1-Mn_1-O_3	O_2-Mn_1-O_{22}	O_2-Mn_1-O_3	O_3-Mn_1-O_{33}
T = 16 K	161.98(5)	96.08(5)	81.31(5)	108.56(5)	87.41(5)	76.74(5)
T = 8 K	161.97(4)	96.09(4)	81.31(4)	108.58(4)	87.41(4)	76.73(4)
T = 5 K	161.97(5)	96.10(5)	81.32(5)	108.59(5)	87.40(5)	76.72(5)
T = 2 K	161.98(5)	96.09(5)	81.32(5)	108.57(5)	87.42(5)	76.72(5)

TABLE 6.3: Angle between O-Mn-O at distinct temperatures in $MnWO_4$.

Temperature	Distance/Å				
	Mn_1-O_1	Mn_1-O_2	Mn_1-O_3	Mn_1-Mn_2	<Mn-O>
T = 16 K	2.1584(5)	2.1054(8)	2.2717(9)	3.2780(9)	2.1785(4)
T = 8 K	2.1576(5)	2.1050(8)	2.2720(9)	3.2781(9)	2.1782(4)
T = 5 K	2.1591(5)	2.1057(8)	2.2728(8)	3.2799(9)	2.1792(4)
T = 2 K	2.1594(5)	2.1052(8)	2.2723(9)	3.2795(9)	2.1790(4)

TABLE 6.2: Interatomic distance between manganese and oxygen atoms and the average distance for the Mn-O bond in $MnWO_4$.

6.1.1 Larmor-diffraction study of the spin-lattice coupling

Chaudhury and co-workers [95] found a weak but non-zero spin-lattice coupling by means of thermal-expansion measurements, see Fig. 6.3. According to their results, a and c parameters decrease across the paramagnetic-to-AF3 transition at $T_1 \approx T_N$, whereas the monoclinic axis, b, increases. At the AF3-to-AF2 magnetic transition, where a new magnetic component arises along the b axis [87], no evidence of any change in the behavior of the cell parameters was seen. However, at the AF2-to-AF3 (T_2) a sharp change of the evolution of a, b and c was found. The a and b parameters undergo a sharp decrease, whereas c suffers an abrupt increase. The overall evolution of the cell parameters from 20 K to 4 K yields with slightly higher value of b and smaller c and a parameters, a being the one that presents the biggest change. So, with the aim of detecting such small changes of the cell parameters, we turned to a spin-echo experiment in the *Larmor-diffraction* configuration.

The *Larmor diffraction* is a neutron-diffraction technique very sensitive to the relative changes of the cell parameters, $\Delta l/l \sim (10^{-5} - 10^{-6})$. We had the opportunity to perform a test experiment on IN22 with the help from N. Martin and L. P. Regnault. The crystal was mounted on the triple-axis IN22 in the *Larmor-diffraction* configuration. The obtained variations of the a and b parameters are shown in Fig. 6.4 (c and β parameters have not been investigated during this experiment). b was recorded when decreasing temperature, whereas a was measured on increasing. The variation of a and b is very small ($\Delta a/a \sim 10^{-5}$ and $\Delta b/b \sim 10^{-6}$), however clear changes in the evolution of these parameters can be observed at the temperatures which coincide with the magnetic transitions: $T_1 \approx T_N$ and $T_2 \approx T_{AF2-to-AF1}$. The observed evolution of both parameters agrees well with the evolution reported in Ref. [95]: whilst temperature decreases, b slightly increases and a decreases, the relative change of b being much smaller. Though there is a discrepancy with the work of Chaudhury *et. al.* concerning the absolute change

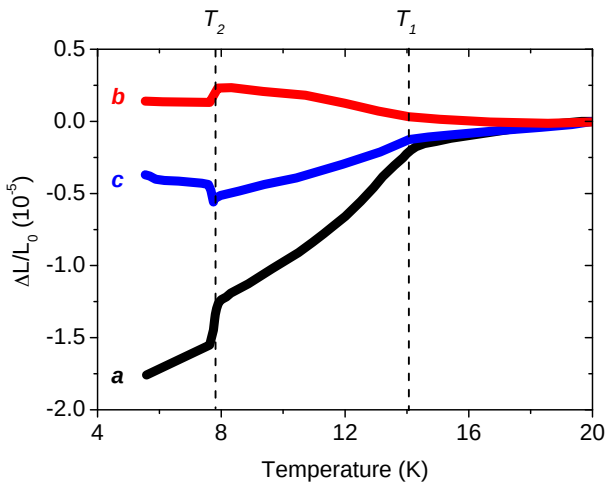

FIGURE 6.3: Thermal expansion of a, b and c parameters observed by Chaudhury and co-workers in Ref. [95].

of the parameters. Nevertheless, this small change of the cell parameters confirms the fact that there is a small magnetoelastic coupling and that conventional experiments of single-crystal neutron-diffraction, like the one performed on D15, are not sensitive enough to detect such effects in this compound.

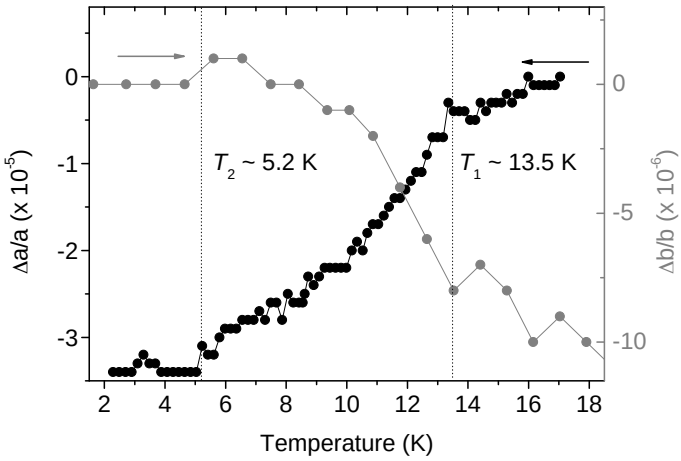

FIGURE 6.4: Relative variation of a and b parameters observed by Larmor diffraction.

6.2 Influence of the Co on the crystal structure of the $Mn_{1-x}Co_xWO_4$ family (x = 0.05, 0.10, 0.15 and 0.20)

Substituting Mn^{2+} by Co^{2+} induces changes in the magnetic behavior of the material [125]: the AF1 phase disappears and the multiferroic AF2 phase takes its place (at $x \approx 3\%$). With increasing the amount of cobalt up to about $x = 10\%$, the multiferroic phase undergoes distortions which results in a different orientation of the electric polarization [126]. When the amount of cobalt is around 15% coexisting magnetic phases arise. Some phases are only observed in these composition [127]. At higher doping the coexistence of phases disappears [125]. The magnetic structures of all this compositions will be discussed in Chapter 8. Seeing such differences on the magnetic behavior depending on the cobalt concentration, it is important to make a careful study of the crystal structures and find out the differences between the compositions that could modify the magnetic interactions.

To search for variations of the nuclear structure of the crystals investigated during the thesis, the nuclear structures of all them have been checked by single-crystal neutron-diffraction. All the compositions are isoestructural to the pure $MnWO_4$, with space group $P2/c$. All the structural parameters are summarized in Table 6.4. The difference between the neutron scattering-lengths of Mn (-3.75 fm) and Co (2.49 fm) permitted us to refine of the concentrations of these two species in all the compositions. There are some parameters that were not refined when the experimental environments used for some experiments did not allow to collect a proper set of reflections for that task. Those parameters are marked by a star (*) in Table 6.4. In the case of the 5% Co-doped composition, several experiments were needed to completely refine the structure. However, the agreement factors demonstrate that the quality of the refinements in all cases was good enough.

Even if there are not significant variations of the relative positions of the atoms in the crystallographic unit cell, the absolute vales of the distances variy noticeably with the Co concentration. Tables 6.5 and 6.6 contain the Mn-O distances and the O-Mn-O bond angles, respectively. Note that O_i and O_{ii} are equivalent in the octahedra. This information is given only for $x = 0.05$, 0.10 and 0.20 due to the fact that the 15% Co-doped composition was not completely refined because of the experimental conditions[1]. All the compositions were not investi-

[1] $x = 0.15$ was studied inside a magnet. The angular aperture did not allow to collect reflections with $l \neq 0$ and thus none of the parameters related to this direction could be refined.

		$\mathbf{Mn_{0.95}Co_{0.05}WO_4}$	$\mathbf{Mn_{0.90}Co_{0.10}WO_4}$	$\mathbf{Mn_{0.85}Co_{0.15}WO_4}$	$\mathbf{Mn_{0.80}Co_{0.20}WO_4}$
Temperature		2 K	17 K	2 K	25 K
Instrument		6T2	D23	D23	D23
Orientation		*a* and *b* axis	*c* axis	*c* axis	*a* axis
λ/Å		0.900	1.2832	1.2773	1.2773
a/Å		4.816(7)	4.8068(9)	4.7982(7)	4.784(2)
b/Å		5.751(2)	5.744(1)	5.742(1)	5.731(2)
c/Å		4.997(2)	4.983(5)	4.98*	4.976(2)
β/°		90.99(7)	90.91(5)	90.8*	90.80(7)
Volume/Å^3		138.3906	137.5633	136.337*	137.2635
Mn	y	0.6839(7)	0.6847(2)	0.6860(9)	0.6847(5)
	Occ.	96.0(1)%	90.6(2)%	85(1)%	82.0(6)%
	B_{iso}	0.5(2)	0.20(3)	0.36(5)	0.31(7)
Co	y	0.6839(7)	0.6847(2)	0.6860(9)	0.6847(5)
	Occ.	4.0(1)%	9.4(2)%	15(1)%	18.0(6)%
	B_{iso}	0.5(2)	0.20(3)	0.36(5)	0.31(7)
W	y	0.1799(6)	0.1802(1)	0.1809(5)	0.1807(3)
	B_{iso}	0.4(1)	0.16(1)	0.20(6)	0.08(3)
O1	x	0.2111(5)	0.21142(9)	0.2115(4)	0.2124(8)
	y	0.1022(4)	0.10290(7)	0.1026(3)	0.1031(1)
	z	0.9416(4)	0.9410(4)	0.9410*	0.9401(2)
	B_{iso}	0.5(1)	0.29(1)	0.40(5)	0.24(2)
O2	x	0.2510(5)	0.25150(9)	0.2515(4)	0.2522(8)
	y	0.3747(4)	0.37507(7)	0.3751(3)	0.3752(1)
	z	0.3933(4)	0.3941(4)	0.3939*	0.3928(2)
	B_{iso}	0.5(1)	0.29(1)	0.40(5)	0.24(2)
R_F/%		5.99 and 6.59	2.39	4.44	3.65
R_{F^2}/%		8.12 and 8.78	3.09	6.45	5.65
R_{F^2w}/%		3.91 and 4.99	4.99	9.63	6.78
χ^2		25.7 and 29.3	11.2	97.3	52.0

TABLE 6.4: Structural parameters of the $Mn_{1-x}Co_xWO_4$ family ($x = 0.05, 0.10, 0.15$ and 0.20). All the experiments were performed in normal-beam geometry. Those parameters were used for the refinement of the magnetic structures.

gated at the same temperature, but the study of the pure $MnWO_4$ showed us that no drastic changes were occurring between 2 K and 25 K. The nuclear structure of the 10% Co-doped material was check at different temperature below 17 K and indeed, it did not suffer any modification within the experimental resolution. The results show that the distances between atoms shrink with increasing the amount of cobalt, which turns in a smaller volume of the octahedra. The Mn-O-Mn angle increases, however the Mn-Mn interatomic distance becomes smaller at high Co doping. The angles between the oxygens in the basal plane of the octahedra also undergo small variations: the angle between O_2-Mn_1-O_3 grows at expenses of the

one between O_2-Mn_1-O_{33}. The modifications of the octahedra do not affect their orientation with respect to the c axis. If one draws a plane that contains the oxygen atoms in the equatorial plane of the octahedra, and another one that contains the apical ones, see Fig. 6.5, the orientation of those planes does not vary within the experimental resolution. The equatorial plane of the octahedra is about 134.5° far from c and the apical plane is basically perpendicular to it.

Concentration	Distance/Å				
	Mn_1-O_1	Mn_1-O_2	Mn_1-O_3	Mn_1-Mn_2	<Mn-O>
x = 0%	2.1584(5)	2.1054(8)	2.2717(9)	3.2780(9)	2.1785(4)
x = 5%	2.157(2)	2.101(4)	2.267(5)	3.274(5)	2.175(2)
x = 10%	2.150(2)	2.089(1)	2.265(2)	3.272(1)	2.168(1)
x = 20%	2.146(2)	2.074(3)	2.255(3)	3.267(3)	2.159(2)

TABLE 6.5: Interatomic distances between manganese and oxygen atoms and the average distance for the Mn-O bond in the $x = 0.05$, 0.10 and 0.20 compositions. The pure compound has been included for making easier the comparisons.

Concen.	Angle/°						
	O_1-Mn_1-O_{11}	O_1-Mn_1-O_2	O_1-Mn_1-O_3	O_2-Mn_1-O_{22}	O_2-Mn_1-O_3	O_3-Mn_1-O_{33}	Mn_1-O_3-Mn_2
x = 0%	161.98(5)	96.08(5)	81.31(5)	108.56(5)	87.41(5)	76.74(5)	95.42(5)
x = 5%	162.00(9)	96.0(1)	81.30(9)	108.3(1)	87.5(1)	76.74(9)	95.4(1)
x = 10%	161.6(1)	96.02(8)	81.22(4)	108.5(1)	87.52(9)	76.57(7)	95.62(7)
x = 20%	161.58(4)	96.2(1)	81.34(8)	108.22(9)	87.8(1)	76.31(1)	95.8(2)

TABLE 6.6: Angle between O-Mn-O in $x = 0.05$, 0.10 and 0.20 compositions. $x = 0$ has been included to complete the view of the effect of the Co.

6.2.1 Influence of the Co doping on the crystal unit-cell

To obtain the cell parameters with better accuracy, all the compositions were investigated at room temperature by means of high resolution synchrotron-X-ray powder-diffraction, at the ultra-high resolution ID31 diffractometer of the European Synchrotron Radiation Facility (ESRF) in Grenoble, France. Figure 6.6 shows the evolution of the cell parameters a, b, c and β as a function of the cobalt concentration, gathered in Table 6.7. The corresponding diffraction pattern and the fits are depicted in Fig. 6.7. The sample with 15 % of cobalt contained very little impurity, which most likely comes from the crystal surface that was scratched to obtain the powder. This explains why a small range in 2θ has been erased for the profile matching and why the reliability factors are slightly worse for this composition

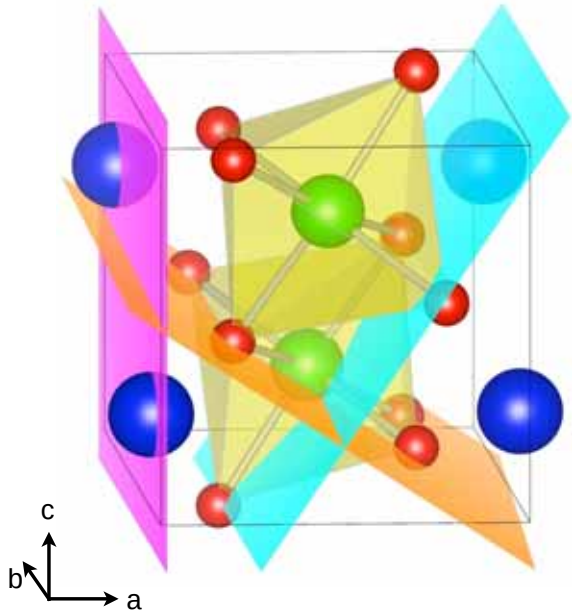

FIGURE 6.5: Sketch of the planes used to calculate the orientation of the octahedra: pink plane correspond to the (001) plane, the blue one contains the apical oxygens of the octahedra and the orange one the oxygens in the equatorial plane of the octahedra.

than for the rest.

As expected from Vegard's law [151], the lattice parameters decrease as the concentration of cobalt increases, because Co^{2+} ions are smaller in size than Mn^{2+}; the ionic radii of Co^{2+} ions with coordination six is 0.745 Å, whereas that of Mn^{2+} ions in the same configuration is 0.83 Å (both in high spin state) [152]. Thus, the decrease of the cell parameters is linear, a being the one which decreases more rapidly, $\frac{\Delta a}{\Delta x} \approx -0.16$ Å$/x_{\%Co}$. By fitting the data, the cell parameters of the complete family could be predicted. In particular, the values predicted for the pure $CoWO_4$ agree very well with the ones given in Table 3.3. Indeed, the cell parameters for the pure $CoWO_4$ extrapolated from the linear fits are the following: $a \approx 4.669(1)$ Å, $b \approx 5.690(1)$ Å, $c \approx 4.950(1)$ Å and $\beta \approx 90.05(1)^\circ$, that should be compared to the observed values (a = 4.6698(9) Å, b = 5.6873(23) Å, c = 4.9515(17) Å, β = 90.(0)$^\circ$ measured by Weitzel in Ref. [82]).

	$MnWO_4$	$Mn_{0.95}Co_{0.05}WO_4$	$Mn_{0.90}Co_{0.10}WO_4$	$Mn_{0.85}Co_{0.15}WO_4$	$Mn_{0.80}Co_{0.20}WO_4$
a/Å	4.83242(1)	4.82445(1)	4.81621(1)	4.80785(2)	4.79984(2)
b/Å	5.76211(1)	5.75871(1)	5.75494(1)	5.75174(2)	5.74768(2)
c/Å	4.99986(1)	4.99751(1)	4.99481(1)	4.99256(2)	4.99000(2)
β/°	91.1514(1)	91.0970(1)	91.0418(1)	90.9900(2)	90.9300(2)
Volume/Å^3	139.193(1)	138.818(1)	138.418(1)	138.042(1)	137.646(1)
R_p/%	7.61	7.11	7.08	12.8	7.72
R_{wp} /%	9.79	9.36	9.37	17.4	9.87
R_{exp}/%	3.61	3.37	4.09	4.91	3.28
χ^2	7.34	7.69	5.25	12.5	9.48

TABLE 6.7: Cell parameters of the $Mn_{1-x}Co_xWO_4$ family ($x = 0, 0.05, 0.10, 0.15$ and 0.20) determined by profile matching of powder-diffraction patterns obtained on ID31 at room temperature.

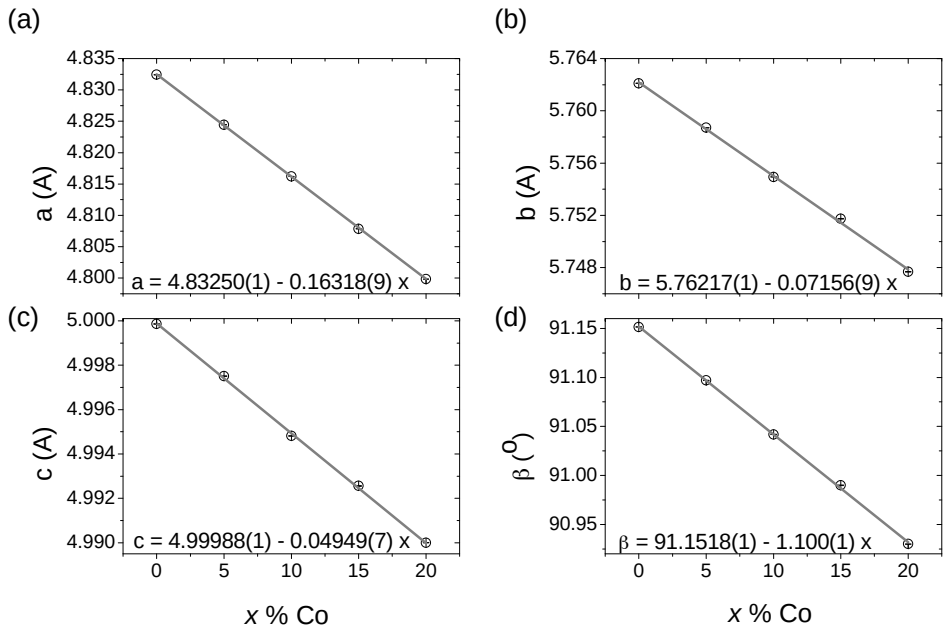

FIGURE 6.6: Evolution of the cell parameters with the amount of Co, x. In panels (a), (b), (c) and (d) are given the evolution of a, b, c and β, respectively. Empty circles correspond to the profile-matching results (errors inside the symbols) and the grey line is a linear fitting.

6.3 Summary and conclusions

To summarize, the substitution of Mn^{2+} by Co^{2+} reduces the volume of the unit cell, which in turn provokes the contraction of the oxygen-made octahedra but not

any tilt of them. The length of Mn-O and Mn-Mn bonds become shorter and the angle between O_2-Mn_1-O_3 gets bigger at expenses of the one between O_2-Mn_1-O_{33}, see Fig. 6.2 and Tables 6.5 and 6.6. The result that there is not systematic rotation of the MO_6 octahedra with increasing the cobalt content is an important one. This fact allows us to conclude that not only the average basal plane is not systematically rotating but, much more important, locally the specific basal plane of a given octahedra can be considered constant with increasing the Co content.

Given the complexity of this system (not less than ten exchange coupling interactions competing) it is not possible to establish a direct relationship between the evolution of the structure with x and the magnetic properties. Nevertheless, these small but clear modifications of the atom positions should be at the origin of the cobalt-induced changes in the magnetic and polar phase diagram, as it will be discussed further in the thesis.

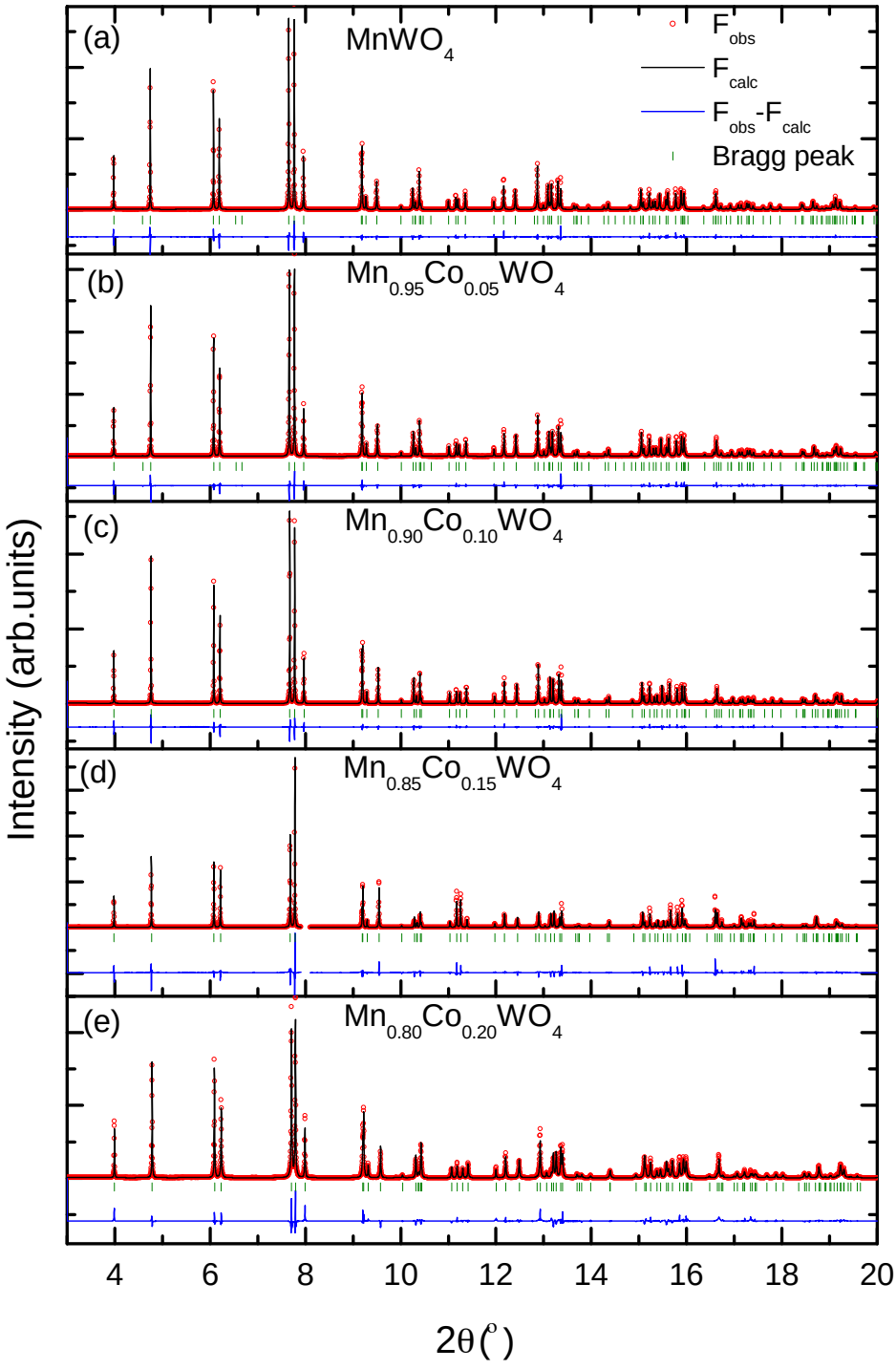

FIGURE 6.7: High resolution X-ray powder-diffraction patterns fitted by the profile-matching method. Data were collected at room temperature.

Chapter 7

Detailed description of the magnetic structures of $MnWO_4$

The truth of the story lies in the details.

Paul Auster (1947 -)

In this chapter, the incommensurate magnetic structures of $MnWO_4$ are analyzed using the superspace-symmetry formalism.

The magnetic structures of the multiferroic $MnWO_4$, see Chapter 3, have been previously analyzed using the representation analysis method [87] and the Landau theory of phase transition [107, 108]. In this chapter, the incommensurate structures of $MnWO_4$ are re-determined, ascribing to each phase its corresponding superspace group, that determine the possibility of having electric polarization or not and hence, multiferroicity.

7.1 Symmetry analysis

Since only first order magnetic reflections have been observed in pure $MnWO_4$, one can describe its magnetic modulation with a single harmonic. Hence, the magnetic moments of a magnetic atom μ in the position $\mathbf{r}_\mu$, inside the cell $\mathbf{l}$ of

the crystal, can be expressed as follows:

$$\mathbf{M}_{\mu,l} = \mathbf{M}_{\mu} e^{-2\pi i \mathbf{k}\cdot(\mathbf{l}+\mathbf{r}_{\mu})} + \mathbf{M}_{\mu}^{*} e^{2\pi i \mathbf{k}\cdot(\mathbf{l}+\mathbf{r}_{\mu})} \tag{7.1}$$

The introduction of the superspace formalism essentially reduces to:

(i) The introduction of a modulation function for each magnetic atom μ, defined along a continuous coordinate x_4, which is directly related to the previous expression:

$$\mathbf{M}_{\mu}(x_4) = \mathbf{M}_{\mu} e^{-2\pi i x_4} + \mathbf{M}_{\mu}^{*} e^{2\pi i x_4} \tag{7.2}$$

This simply means that the value of the magnetic moment $\mathbf{M}_{\mu,l}$ of the atom μ at any unit cell $\mathbf{l}$ is given by the value of the corresponding $\mathbf{M}_{\mu}(x_4)$ modulation function for $x_4 = \mathbf{k}\cdot(\mathbf{l}+\mathbf{r}_{\mu})$.

(ii) The definition of a set of symmetry operations (the superspace group) that in general constrain the possible form of these modulation functions and correlate the modulation functions of symmetry related atoms within the unit cell, such that only some of them are independent. In this way, an asymmetric unit for both atomic positions and modulation functions can be defined. The symmetry operations $\{\mathbf{R},\theta|\mathbf{t},\tau\}$ of the relevant superspace group (θ = -1 or +1 labels the inclusion or not of time reversal respectively) are ordinary space group operations $\{\mathbf{R},\theta|\mathbf{t}\}$ belonging to the grey space group[1] of the paramagnetic phase, but followed by some specific translation related with τ along the internal coordinate x_4 of all atomic modulation functions.

In the simplest case of a purely incommensurate propagation vector (see Ref. [66] for the general expressions or the summary given in Chapter 2 Section 2.6.3), the symmetry relation between the magnetic modulation functions of two atoms related by a superspace symmetry operation $\{\mathbf{R},\theta|\mathbf{t},\tau\}$ is given by :

$$\mathbf{M}_{\mu}(R_I x_4 + \tau) = \theta\ det(\mathbf{R})\mathbf{R}\cdot\mathbf{M}_{\nu}(x_4) \tag{7.3}$$

with the average position of atom μ being related with that of atom ν by the space group operation $\{\mathbf{R}|\mathbf{t}\} : \{\mathbf{R}|\mathbf{t}\}\mathbf{r}_{\nu} = \mathbf{r}_{\mu} + \mathbf{l}$. Here, R_I is $+1$ or -1 if $\mathbf{R}$ keeps $\mathbf{k}$ invariant or transforms $\mathbf{k}$ into $-\mathbf{k}$, respectively. For $\mu = \nu$, equation (7.3) defines a

[1] Magnetic space groups combine the crystallographic space-groups with the time reversal operator. If an symmetry operator contains the time inversion, $\theta = -1$, it is known as *black* and if it does not, $\theta = +1$, it is named *white*, a *grey* space group combines all spatial operator with both $\theta = -1$ and $\theta = +1$ doubling the number of operator in the space group.

constraint on the form of the modulation. Note that the symmetry relations defined in the superspace formalism, in contrast with the traditional Bertaut representation method, include in general rotational or roto-inversion transformations that change the sign of the propagation vector. These symmetry transformations have been previously considered using a so-called "non-conventional use" of the co-representations [153] or within the frame of Landau theory [107, 108]. As explained in Ref. [66], the use of the superspace formalism introduces automatically and in a simple form the whole set of symmetry constraints associated to these operations, for any degree of freedom of the structure, including non-magnetic ones.

The space group of the paramagnetic phase of $MnWO_4$ is $P2/c$. In the crystallographic unit cell there is one independent manganese atom located at the $2f$ Wyckoff position: Mn_1 at $(\frac{1}{2},\ y,\ \frac{1}{4})$. The symmetry related atom Mn_2 within the unit cell is at $(\frac{1}{2},\ -y+1,\ \frac{3}{4})$. In general, for the symmetry analysis of a magnetic structure, the parent symmetry has to be taken into account, which in this case corresponds to the grey magnetic space-group $P2/c1'$ of the paramagnetic phase, where $1'$ refers to the time inversion operation. This space group consists of all the symmetry operations of the ordinary $P2/c$ space group, plus an equal number of operations obtained by multiplying all of them by time reversal $\{1'\,|\,0\,0\,0\,0\}$ (which is also a symmetry operation of the paramagnetic phase). The incommensurate propagation vector, $\mathbf{k} = (-0.214, \frac{1}{2}, 0.457)$, lies on the symmetry line G ($\alpha\ \frac{1}{2}\ \gamma$) of the Brillouin Zone [154]. The corresponding little group, formed by the symmetry operators that leave $\mathbf{k}$ invariant, is $Pm1'$. There are two possible magnetic irreducible representations (*irreps*) of this little group. They are both one-dimensional and are defined by the corresponding *irreps* of the little co-group $m1'$ (see Table 7.1).

irrep	1	m	$1'$	Superspace group	Generators
mG_1	1	1	-1	$P2/c1'(\alpha\frac{1}{2}\gamma)00s$	$\{m_y\,\vert\,0\,0\,\frac{1}{2}\,0\}$,$\{\bar{1}\,\vert\,0\,0\,0\,0\}$, $\{1'\,\vert\,0\,0\,0\,\frac{1}{2}\}$
mG_2	1	-1	-1	$P2/c1'(\alpha\frac{1}{2}\gamma)0ss$	$\{m_y\,\vert\,0\,0\,\frac{1}{2}\,\frac{1}{2}\}$, $\{\bar{1}\,\vert\,0\,0\,0\,0\}$, $\{1'\,\vert\,0\,0\,0\,\frac{1}{2}\}$

TABLE 7.1: *Irreps* of the little co-group, $m1'$, which define the two possible magnetic *irreps* of the paramagnetic group $P2/c1'$ with $\mathbf{k} = (\alpha, \frac{1}{2}, \gamma)$. The label of the resulting superspace group as well as its generators are provided in each case.

As explained in Ref. [66], if the magnetic order is realized according to a single one dimensional *irrep*, a unique superspace group can be assigned to the resulting magnetic structure. All the operations of the little group are kept in this superspace group, but a $(0\ 0\ 0\ \frac{1}{2})$ translation (along the internal space) has to be added to those operators that have -1 character. In addition, all operations transforming

k into $-\mathbf{k}$ are also maintained: its chosen representative (for instance the space inversion) can be chosen with zero translation along the internal space by a convenient choice of the phase of the magnetic modulation, while the remaining operations can be obtained from the application of the internal product of the group. Following these rules, the two possible superspace groups corresponding to the two possible active *irreps* at the G line can be derived (the program JANA2006 [61] has also an option to derive them automatically). According to the notation usually employed, they can be labeled as $P2/c1'(\alpha\frac{1}{2}\gamma)00s$ and $P2/c1'(\alpha\frac{1}{2}\gamma)0ss$, and their generators are listed in Table 7.1. It is important to stress that these superspace groups include operations that transform **k** into $-\mathbf{k}$. In both cases, the corresponding magnetic point-group is $2/m1'$, which implies the absence in such phases of any induced ferroelectricity and of any linear magnetoelectric response. It is also worth mentioning that the magnetic superspace groups associated to magnetic *irreps* can also be obtained using the program ISODISTORT [155], but in this case the symmetries are given in standard settings, which are not the settings used here.

Centered unit cells are used to simplify the description of crystal symmetry in standard crystallography. This can also be done in the case of incommensurate superspace symmetry. The propagation vector $(\alpha, \frac{1}{2}, \beta)$ is not purely incommensurate, as it includes a component $\frac{1}{2}$ along y. Because of this commensurate component, the symmetry relations and constraints of the modulations are given by an equation more complex than equation (7.3) (the symmetry relations and constrains imposed by $P2/c1'(\alpha\frac{1}{2}\gamma)00s$ and $P2/c1'(\alpha\frac{1}{2}\gamma)0ss$ superspaces are developed in Appendix C). This complication can however be avoided, and equation (7.3) can be applied, by using a unit cell doubled along y, so that the propagation vector in its reciprocal basis becomes $\mathbf{k}' = (\alpha, 0, \beta)$. The effect of the $(0, \frac{1}{2}, 0)$ component of the modulation propagation vector is maintained by the introduction of an appropriate centering translation in superspace. More specifically, one considers a cell a, $2b$, c such that now there are four Mn atoms per unit cell. The $(0, \frac{1}{2}, 0)$ component of the original modulation only means that the atoms within this unit cell related by a translation b have modulations with a π phase shift. This is ensured by including in the superspace group a centering translation $(0\ \frac{1}{2}\ 0\ \frac{1}{2})$. Indeed, according to equation (7.3), if the atoms in the doubled cell are labeled as $Mn_1 = (\frac{1}{2}, \frac{y_1}{2}, \frac{1}{4})$, $Mn_2 = (\frac{1}{2}, \frac{-y_1+1}{2}, \frac{3}{4})$, $Mn_{11} = (\frac{1}{2}, \frac{y_1+1}{2}, \frac{1}{4})$ and $Mn_{22} = (\frac{1}{2}, \frac{-y_1+2}{2}, \frac{3}{4})$, the modulations of the atoms Mn_{11} and Mn_{22} are $\frac{1}{2}$ shifted

with respect to those of the other two atoms:

$$\begin{aligned}\mathbf{M}_{Mn_{11}}(x_4) &= \mathbf{M}_{Mn_1}(x_4 + \tfrac{1}{2}) \\ \mathbf{M}_{Mn_{22}}(x_4) &= \mathbf{M}_{Mn_2}(x_4 + \tfrac{1}{2}).\end{aligned} \tag{7.4}$$

The description of a superspace group with this optional centered unit cells is usually indicated in the superspace group label by means of an "X". Thus $P2/c1'(\alpha\frac{1}{2}\gamma)0ss$ becomes $X2/c1'(\alpha0\gamma)0ss$ and $P2/c1'(\alpha\frac{1}{2}\gamma)00s$ becomes $X2/c1'(\alpha0\gamma)00s$. The symmetry operations of the superspace groups are described in detail in Table 7.2. The apparent new reflections introduced by the duplication of the basic unit cell are canceled out due to the centering $(0\ \frac{1}{2}\ 0\ \frac{1}{2})$, as depicted in Fig. 7.1. In the following, we will use this X-centered description of any relevant superspace group.

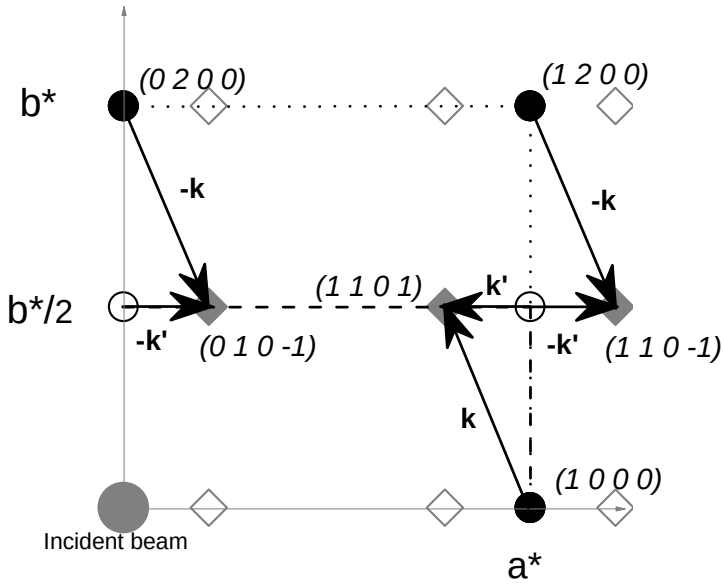

FIGURE 7.1: Scheme of the indexation $(hklm)$ of diffraction peaks according to a, $2b$, c supercell and a propagation vector $\mathbf{k}' = (\alpha\ 0\ \beta)$ together with a $(0\ \frac{1}{2}\ 0\ \frac{1}{2})$ centering translation (X-centering). Full circles and grey rhombuses correspond to nuclear and magnetic reflections, respectively. Magnetic reflections are projected on the plane $(hk0)$. Empty circles and empty rhombuses represent systematic extinctions caused by the X-centering, which forces that both magnetic and nuclear reflections obey the $k + m = 2n$ reflection condition.

A magnetic phase can result from the activation of several primary *irrep* modes. In this case, if the propagation vector is incommensurate, its superspace

$P2/c1'(\alpha\frac{1}{2}\gamma)0ss$					
$\{1\|0000\}$	x_1	x_2	x_3	x_4	m
$\{2_y\|00\frac{1}{2}\frac{1}{2}\}$	$-x_1$	x_2	$-x_3+\frac{1}{2}$	$x_2-x_4+\frac{1}{2}$	m
$\{\bar{1}\|0000\}$	$-x_1$	$-x_2$	$-x_3$	$-x_4$	m
$\{m_y\|00\frac{1}{2}\frac{1}{2}\}$	x_1	$-x_2$	$x_3+\frac{1}{2}$	$-x_2+x_4+\frac{1}{2}$	m
$\{1'\|000\frac{1}{2}\}$	x_1	x_2	x_3	$x_4+\frac{1}{2}$	-m
$X2/c1'(\alpha 0\gamma)0ss$					
$\{1\|0000\}$	x_1	x_2	x_3	x_4	m
$\{2_y\|00\frac{1}{2}\frac{1}{2}\}$	$-x_1$	x_2	$-x_3+\frac{1}{2}$	$-x_4+\frac{1}{2}$	m
$\{\bar{1}\|0000\}$	$-x_1$	$-x_2$	$-x_3$	$-x_4$	m
$\{m_y\|00\frac{1}{2}\frac{1}{2}\}$	x_1	$-x_2$	$x_3+\frac{1}{2}$	$x_4+\frac{1}{2}$	m
$\{1'\|000\frac{1}{2}\}$	x_1	x_2	x_3	$x_4+\frac{1}{2}$	-m
$\{1\|0\frac{1}{2}0\frac{1}{2}\}$	x_1	$x_2+\frac{1}{2}$	x_3	$x_4+\frac{1}{2}$	m

$P2/c1'(\alpha\frac{1}{2}\gamma)00s$					
$\{1\|0000\}$	x_1	x_2	x_3	x_4	m
$\{2_y\|00\frac{1}{2}0\}$	$-x_1$	x_2	$-x_3+\frac{1}{2}$	x_2-x_4	m
$\{\bar{1}\|0000\}$	$-x_1$	$-x_2$	$-x_3$	$-x_4$	m
$\{m_y\|00\frac{1}{2}0\}$	x_1	$-x_2$	$x_3+\frac{1}{2}$	$-x_2+x_4$	m
$\{1'\|000\frac{1}{2}\}$	x_1	x_2	x_3	$x_4+\frac{1}{2}$	-m
$X2/c1'(\alpha 0\gamma)00s$					
$\{1\|0000\}$	x_1	x_2	x_3	x_4	m
$\{2_y\|00\frac{1}{2}0\}$	$-x_1$	x_2	$-x_3+\frac{1}{2}$	$-x_4$	m
$\{\bar{1}\|0000\}$	$-x_1$	$-x_2$	$-x_3$	$-x_4$	m
$\{m_y\|00\frac{1}{2}0\}$	x_1	$-x_2$	$x_3+\frac{1}{2}$	x_4	m
$\{1'\|000\frac{1}{2}\}$	x_1	x_2	x_3	$x_4+\frac{1}{2}$	-m
$\{1\|0\frac{1}{2}0\frac{1}{2}\}$	x_1	$x_2+\frac{1}{2}$	x_3	$x_4+\frac{1}{2}$	m

TABLE 7.2: Representative operations of the space groups $P2/c1'(\alpha\frac{1}{2}\gamma)0ss$ and $P2/c1'(\alpha\frac{1}{2}\gamma)0ss$ described in primitive setting and in the X-centered one. Both generalized Seitz-type notation (left column) and symmetry cards as used in JANA2006 are listed. The labels -m or m indicate whether the operation includes the time inversion (-m) or not (m). The remaining operations are obtained by the internal product of the group.

symmetry is described by the intersection of the superspace groups associated with each individual *irrep*. This intersection depends on the relative phases of

the corresponding modulations. When two primary incommensurate *irrep* modulations are superimposed, only one of the two modulation phases can be arbitrarily chosen. This is done by associating to a representative operation of its superspace group transforming $\mathbf{k}$ into $-\mathbf{k}$ a null translation along the internal space. For the calculation of the intersection of the superspace groups associated with different *irrep* modulations, one has to consider that if a magnetic modulation is phase shifted by a quantity ϕ the symmetry operators of its superspace group that leave invariant $\mathbf{k}$ do not change, whereas the operations that transform $\mathbf{k}$ into $-\mathbf{k}$ acquire an additional $(0\ 0\ 0\ 2\phi)$ translation along the internal space [66]. If we consider the superposition of two primary modes transforming according to any of the two possible mG_1 and mG_2 *irreps*, taking into account all possible relative phase shifts, several different superspace groups are possible and can be readily calculated following these rules. They are listed in Table 7.3 (Appendix D shows how to build Table 7.3). One can see that the superposition of two modes mG_1 or two modes mG_2 reduce the magnetic point-group symmetry to $m1'$, i. e. a polar group that allows a spontaneous electric polarization in the *ac* plane, while the superposition in quadrature of a mode mG_1 and a mode mG_2 implies a $21'$ point-group symmetry, i. e. a polar symmetry that allows the build-up of electrical polarization along *b*.

$\Delta\phi = 0, \frac{1}{2}$	$mG_1 + mG_1$	$X2/c1'(\alpha 0\gamma)00s$	$2/m1'$
	$mG_2 + mG_2$	$X2/c1'(\alpha 0\gamma)0ss$	$2/m1'$
	$mG_1 + mG_2$	$X\bar{1}1'(\alpha 0\gamma)0s$	$-11'$
$\Delta\phi = \frac{1}{4}, \frac{3}{4}$	$mG_1 + mG_1$	$Xc1'(\alpha 0\gamma)0s$	$m1'$
	$mG_2 + mG_2$	$Xc1'(\alpha 0\gamma)ss$	$m1'$
	$mG_1 + mG_2$	$X21'(\alpha 0\gamma)0s$	$21'$
$\Delta\phi$ = arbitrary	$mG_1 + mG_1$	$Xc1'(\alpha 0\gamma)0s$	$m1'$
	$mG_2 + mG_2$	$Xc1'(\alpha 0\gamma)ss$	$m1'$
	$mG_1 + mG_2$	$X11'(\alpha 0\gamma)0s$	$11'$

TABLE 7.3: Superspace groups resulting from the superposition of two *irrep* magnetic modulations with a phase shift $\Delta\phi$ between them. The magnetic point-group of each superspace group is in the last column.

7.2 Paraelectric AF3 magnetic phase

If we assume that the paraelectric magnetic structure of the AF3 phase corresponds to a single active *irrep* modulation, described in Table 7.1, its magnetic symmetry should be described by either the $X2/c1'(\alpha 0\gamma)00s$ or $X2/c1'(\alpha 0\gamma)0ss$ superspace groups. Both symmetries include the inversion operation $\{\bar{1}|0\frac{1}{2}0\frac{1}{2}\}$ that relates atoms Mn_1 and Mn_2. According to equation (7.3) this means that, the magnetic modulations of both atoms are in both cases related in the form:

$$\mathbf{M}_{Mn_2}(-x_4+\frac{1}{2}) = \mathbf{M}_{Mn_1}(x_4) \tag{7.5}$$

which implies that only the modulation of one atom, say Mn_1, is independent, while the two atoms Mn_2 and Mn_1 have, in both superspace groups, identical modulations but with opposite chirality. The distinction between the two possible symmetries comes from the operation $\{2_y|00\frac{1}{2}\tau\}$ (see Table 7.2), which keeps atom Mn_1 invariant and therefore constrains the form of its modulation. According to equation (7.3):

$$\mathbf{M}_{Mn_1}(-x_4+\tau) = 2_y \cdot \mathbf{M}_{Mn_1}(x_4) \tag{7.6}$$

If we call $[M_{1x}(x_4), M_{1y}(x_4), M_{1z}(x_4)]$ the three components of the magnetic modulation function of Mn_1 along the three crystallographic directions, in the first superspace group $\tau = 0$, according to equation (7.6), the modulation of the x, z components of the magnetic moment should be sine-like, while the y component cosine-like.

$$\tau = 0 \rightarrow M_{1\alpha}(x_4) = M^s_{1\alpha}\sin(2\pi x_4) \qquad (\alpha = x,z) \tag{7.7}$$

$$M_{1y}(x_4) = M^c_{1y}\cos(2\pi x_4). \tag{7.8}$$

On the other hand, for $X2/c1'(\alpha 0\gamma)0ss$, $\tau = \frac{1}{2}$ and the constraint of sine and cosine forms are exchanged, so that:

$$\tau = \frac{1}{2} \rightarrow M_{1\alpha}(x_4) = M^c_{1\alpha}\cos(2\pi x_4) \qquad (\alpha = x,z) \tag{7.9}$$

$$M_{1y}(x_4) = M^s_{1y}\sin(2\pi x_4) \tag{7.10}$$

while according to equation (7.5), the spin modulation of atom Mn_2 is given by

$$\tau = 0 \rightarrow M_{2\alpha}(x_4) = M^s_{1\alpha}\sin(2\pi x_4) \qquad (\alpha = x,z) \tag{7.11}$$

$$M_{2y}(x_4) = -M^c_{1y}\cos(2\pi x_4) \tag{7.12}$$

$$\tau = \frac{1}{2} \rightarrow M_{2\alpha}(x_4) = -M^c_{1\alpha}\cos(2\pi x_4) \qquad (\alpha = x,z) \tag{7.13}$$

$$M_{2y}(x_4) = M^s_{1y}\sin(2\pi x_4) \tag{7.14}$$

Thus, the real amplitudes sets (M^s_{1x}, M^c_{1y}, M^s_{1z}) or (M^c_{1x}, M^s_{1y}, M^c_{1z}) fully describe the magnetic structure.

It is important to stress that, even if the modulation of Mn_1 were reduced to the plane *ac*, the choice of cosine or sine functions for its description does not represent a mere phase shift in the global spin wave, because equation (7.5) is also included in the model, and it implies a completely different choice for the correlation with the spins of Mn_2 atoms, if one or the other superspace group is chosen. In both alternative symmetries three parameters are required to describe the magnetic structure.

It is worth to compare with the usual representation approach. As it is usually used, the representation analysis only introduces the *irrep* restrictions corresponding to the symmetry operations of the little group, which keeps **k** invariant. Atoms Mn_1 and Mn_2 in the unit cell are related in the paramagnetic phase by the space group operation $\{m_y|01\frac{1}{2}\}$, belonging to the little group. Thus, the representation method introduces a relation between the spin modulations of the two Mn atoms corresponding to this symmetry operation. This relation is equivalent to the one resulting from the superspace operation $\{m_y|0\frac{1}{2}\frac{1}{2},\frac{1}{2}+\tau\}$ (*X*-setting) with $\tau = 0$ for mG_1 and $\tau = \frac{1}{2}$ for mG_2, which is present in their respective superspace group. However, no restriction equivalent to the one of equation (7.6) is considered, and therefore, in the representation approach, the spin modulation of one of the atoms is fully free [87]. This means that the relative phases between the modulations of the three spin components are free parameters. As in an incommensurate modulation, one of the phases can be fixed arbitrarily, the number of refinable parameters of the model is five, compared with only three parameters when using the superspace group description. In fact, the model considered in Ref. [87], applying the standard representation analysis method, is equivalent to using the minimal superspace groups $Xc1'(\alpha 0\gamma)0s$ or $Xc1'(\alpha 0\gamma)ss$ corresponding to the superposition of at least two phase-shifted *irrep* modes of the same *irrep* symmetry (see Table 7.3). Note that this model for the magnetic structure would imply a magnetic point-group $m1'$, and therefore polarity within the *xz* plane. As it happens in many other studies, the additional restrictions necessary to increase the symmetry of the model and to reduce the modulations to a single *irrep* mode were subsequently introduced in Ref. [87] by means of intuitive arguments based on the search for simple modulations (collinear, spiral, etc.). In general, the structures described applying the representation approach (as normally used) are compatible with those obtained using the superspace formalism, but less constraints are introduced, and are less symmetric.

Both superspace groups, $X2/c1'(\alpha 0\gamma)00s$ and $X2/c1'(\alpha 0\gamma)0ss$, were tried alternatively to refine the magnetic structure from the single crystal data obtained on D23. The 166 observed magnetic reflections resulted after averaging into 66 independent ones with R_{int} = 8.67. From the refinement it can be clearly concluded that the magnetic symmetry of the AF3 phase is $X2/c1'(\alpha 0\gamma)0ss$. The refined parameters that describe the possible magnetic structure with different symmetry as well as the agreement factors are given in Table 7.4 and the structure is depicted in Fig. 7.2 according to the $X2/c1'(\alpha 0\gamma)0ss$ symmetry. The refined value of the amplitude M_y^s describing the symmetry-allowed sine modulation along the y-direction is very small, although larger than its standard deviation. It was then fixed to zero, and Table 7.4 also shows the result of this second refinement. This latter refinement, with the weak M_y^s component neglected, reduces the model to a sinusoidally-modulated collinear magnetic modulation in the ac plane, with the direction of the moments (the so-called $\hat{u}$ direction) making approximately a 39(1)$^\circ$ angle with the a axis and 1.88(4) μ_B amplitude. This approximate model is directly comparable and agrees with the magnetic structure proposed in Ref. [87], where amplitude is 2.1 μ_B and the angle is 35°.

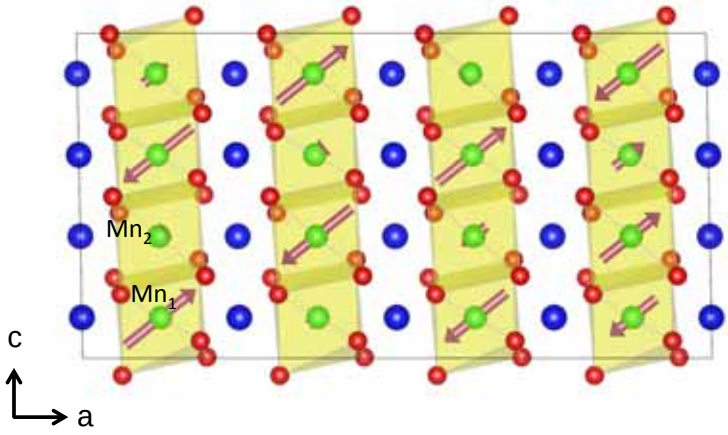

FIGURE 7.2: Projection along b axis of the AF3 phase of $MnWO_4$ at 13 K (Table 7.4). Only the non-periodic modulation within a region $4a \times 2b \times 2c$ is represented.

It is important to stress that the structure of the AF3 phase is not forced by symmetry to be collinear. A Hamilton test [156] indicates that the weak non-zero value of the amplitude M_y^s is statistically significant. This non-zero modulation for the y spin component makes the spin waves helical, but of opposite chiralities in the two Mn atoms. This situation is represented in Fig. 7.3, where for clarity reasons an artificially large component M_y^s has been introduced in the model. The two modulations are related by space inversion [see equation (7.5)], which forbids

	M^s_{1x}	M^s_{1y}	M^s_{1z}	M^c_{1x}	M^c_{1y}	M^c_{1z}	$\|m_{max}\|$	$\|m_{min}\|$
$X2/c1'(\alpha 0\gamma)00s$								
	0.5(2)	0.000*	0.2(2)	0.000*	1.8(1)	0.000*	1.8(1)	0.5(1)
	R_F(obs)= 40.45%, R_{wF}(obs)= 43.64%, R_{wF^2}(obs)= 70.86%							
$X2/c1'(\alpha 0\gamma)0ss$								
	0.000*	0.05(3)	0.000*	1.46(3)	0.000*	1.18(2)	1.88(4)	0.05(3)
	R_F(obs)= 7.15%, R_{wF}(obs)= 5.51%, R_{wF^2}(obs)= 10.59%							
$X2/c1'(\alpha 0\gamma)0ss$								
	0.000*	0.00**	0.000*	1.47(2)	0.000**	1.17(2)	1.88(3)	
	R_F(obs)= 7.23%, R_{wF}(obs)= 5.63%, R_{wF^2}(obs)= 10.86%							
* Constrained by symmetry. ** Fixed manually.								

TABLE 7.4: Refined parameters (μ_B) that describe the magnetic structure of $MnWO_4$ at 13 K with constrains imposed by the $X2/c1'(\alpha 0\gamma)00s$ and $X2/c1'(\alpha 0\gamma)0ss$ superspace group, the latter including or not a y-component in the magnetic modulation. Maximum and minimum values of the ordered moments are given in the last two columns, i. e. the semi-major and semi-minor axes of the helix in the first two models and the amplitude of the modulation in the second model. Parameters are defined in the text.

any induced net electric polarization.

7.3 AF2 multiferroic phase

The propagation vector does not change at the transition from the AF3 phase to the multiferroic AF2 phase, but the symmetry is clearly broken, as a spontaneous polarization appears. In the simplest scenario, one can consider that this symmetry breaking is due to the activation of an additional *irrep* magnetic mode. Table 7.3 contains all possible superspace groups that can result from the superposition of two primary *irrep* magnetic modes. One can see that there are three magnetic symmetries in the table that could in principle describe a multiferroic structure, as their magnetic point-groups are $21'$, $m1'$ and $11'$. Those point-groups allow the appearance of electric polarization along the b axis, in the xz plane, or along an arbitrary direction, respectively. It is known that the polarization in $MnWO_4$ arises along the b axis [30, 31, 96]. Hence, according to Table 7.3 the superspace group symmetry that must correspond to phase AF2 is $X21'(\alpha 0\gamma)0s$ (the symmetry operations of the space group are described in Table 7.5). The inversion and the glide plane that relate Mn_1 and Mn_2 in the AF3 phase are therefore lost at the transition, and these two manganese atoms become symmetry-independent. The

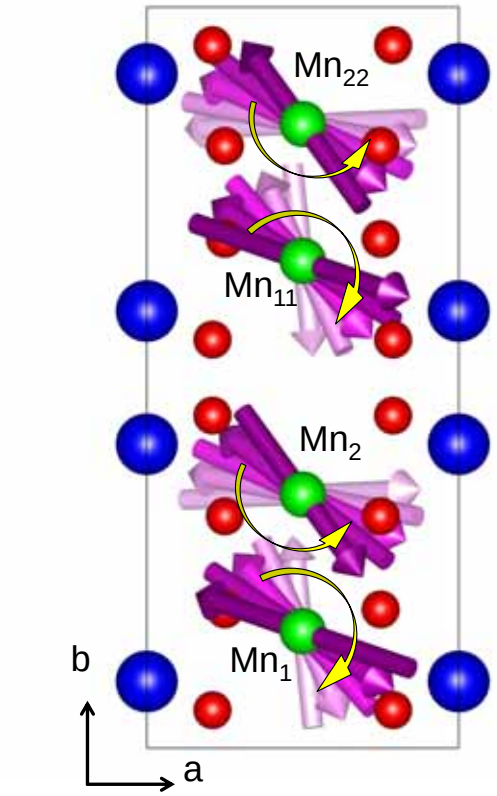

FIGURE 7.3: Projection along c axis of the AF3 phase with an arbitrarily large amplitude of the symmetry-allowed y-component of the magnetic modulations. The symmetry of the AF3 phase allows a cycloidal component in the Mn modulations but of opposite chirality for Mn_1 and Mn_2.

symmetry $X21'(\alpha 0\gamma)0s$ keeps however the operation $\{2_y|00\frac{1}{2}\frac{1}{2}\}$ [2]. This means that the spin modulations of both atoms Mn_1 and Mn_2 atoms maintain the symmetry constraints imposed by equations (7.9) and (7.10), but with amplitudes that are no longer symmetry-related. There are therefore six parameters to refine, three for each manganese atom: $(M^c_{1x}, M^s_{1y}, M^c_{1z})$ and $(M^c_{2x}, M^s_{2y}, M^c_{2z})$.

$$M_{1\alpha}(x_4) = M^c_{1\alpha}\cos(2\pi x_4) \qquad (\alpha = x, z) \tag{7.15}$$

$$M_{1y}(x_4) = M^s_{1y}\sin(2\pi x_4) \tag{7.16}$$

$$M_{2\alpha}(x_4) = M^c_{2\alpha}\cos(2\pi x_4) \qquad (\alpha = x, z) \tag{7.17}$$

$$M_{2y}(x_4) = M^s_{2y}\sin(2\pi x_4) \tag{7.18}$$

[2] The $\frac{1}{2}$ shift of this operation along the internal variable could be made zero by a convenient shift of the origin of the x_4 coordinate, but we prefer to keep the origin considered in the AF3 phase, to allow a more direct comparison with this phase.

$P21'(\alpha\frac{1}{2}\gamma)0s$					
$\{1\|0000\}$	x_1	x_2	x_3	x_4	m
$\{2_y\|00\frac{1}{2}\frac{1}{2}\}$	$-x_1$	x_2	$-x_3+\frac{1}{2}$	$x_2-x_4+\frac{1}{2}$	m
$\{1'\|000\frac{1}{2}\}$	x_1	x_2	x_3	$x_4+\frac{1}{2}$	-m
$X21'(\alpha0\gamma)0s$					
$\{1\|0000\}$	x_1	x_2	x_3	x_4	m
$\{2_y\|00\frac{1}{2}\frac{1}{2}\}$	$-x_1$	x_2	$-x_3+\frac{1}{2}$	$-x_4+\frac{1}{2}$	m
$\{1'\|000\frac{1}{2}\}$	x_1	x_2	x_3	$x_4+\frac{1}{2}$	-m
$\{1\|0\frac{1}{2}0\frac{1}{2}\}$	x_1	$x_2+\frac{1}{2}$	x_3	$x_4+\frac{1}{2}$	m

TABLE 7.5: Representative operations of the space group $P21'(\alpha\frac{1}{2}\gamma)0s$ described in primitive setting and in the X-centered one. Both generalized Seitz-type notation (left column) and symmetry cards as used in JANA2006 are listed. The labels -m or m indicate whether the operation includes the time inversion (-m) or not (m). The remaining operations are obtained by the internal product of the group.

The refinement from 162 independent magnetic reflections (averaged from 246 reflections collected on D23 at 9 K with $R_{int} = 2.50$) confirmed the superspace symmetry $X21'(\alpha0\gamma)0s$ for AF2 phase, and therefore a spin modulation according to a superposition in quadrature of mG_2 and mG_1 modes [Table 7.3 shows that the $X21'(\alpha0\gamma)0s$ results from combining mG_1 and mG_2 with $\Delta\phi = \frac{1}{4}, \frac{3}{4}$]. The refined parameters are listed in Table 7.6 and a scheme of the magnetic structure is plotted in Fig. 7.4. The moments rotate according to an ellipse in the ub plane, where $\hat{u}$ is the easy direction in the ac plane. In this case, in contrast with the AF3 phase, the chirality of the two Mn_1 and Mn_2 spin chains is the same, see Fig. 7.4 (a), giving rise to a net electrical polarization by some mechanism such as the spin-orbit driven inverse Dzyaloshinskii-Moriya effect. As it can be seen in Table 7.6 the deviation from a circular spiral of the modulations of both Mn atoms is very significant. The elliptical orbits have semi-axes of [4.1(1) μ_B, 3.26(7) μ_B] and [3.6(1) μ_B, 2.97(6) μ_B], for Mn_1 and Mn_2 respectively. The direction $\hat{u}$ of the magnetic moments also differs between the two atoms, forming an angle with the a axis of about 37(2)° for Mn_1 and of 30(2)° for Mn_2. These differences between the two modulations are basically due to the strong difference of the modulation amplitude along the z axis (see Table 7.6). While the x and y modulation amplitudes have similar magnitude for both atoms, the amplitude along z differs substantially, and changes both the spiral plane and the elliptical orbit of the magnetic moments.

Table 7.6 also shows the results of a refinement where the amplitudes of the modulations along the three crystallographic directions of the two atoms were

$\mathbf{Mn}_i$	M_x^s	M_y^s	M_z^s	M_x^c	M_y^c	M_z^c	$\lvert m_{max}\rvert$	$\lvert m_{min}\rvert$
$i=1$	0.0*	3.26(7)	0.0*	3.28(8)	0.0*	2.49(6)	4.1(1)	3.26(7)
$i=2$	0.0*	-2.97(6)	0.0*	-3.11(8)	0.0*	-1.78(6)	3.6(1)	2.97(6)
R_F(obs)= 3.54%, R_{wF}(obs)= 3.45%, R_{wF^2}(obs)= 6.20%								
$i=1$	0.0*	3.14(3)	0.0*	3.21(4)	0.0*	2.14(5)	3.86(8)	3.14(3)
$i=2$	0.0*	-3.14**	0.0*	-3.21**	0.0*	-2.14**	3.86(8)	3.14(3)
R_F(obs)= 3.94%, R_{wF}(obs)= 3.75%, R_{wF^2}(obs)= 6.71%								
* Constrained by symmetry. ** Constrained manually.								

TABLE 7.6: Refined parameters of the magnetic modulations (μ_B) of the multiferroic phase of pure $MnWO_4$ (9 K) in the superspace group $X21'(\alpha 0\gamma)0s$. The results of constrained refinement forcing the two symmetry-independent atoms to have equal spiral modulation is also included. Maximum and minimum values of the ordered moments are given in the last two columns, i. e. the semi-major and semi-minor axes of the helixes.

forced to be, respectively, of equal magnitude but with opposite sign. These restrictions make equal the elliptical helix modulations of the two atoms, except for a π phase shift, and reduces the number of refinable parameters to three. This is the model of phase AF2 that was proposed in Ref. [87]. In this constrained refinement, the obtained elliptical helix, forced to be common to both atoms, has 3.86(5) μ_B and 3.14(3) μ_B as semi-axes and its plane forms an angle of 34(2)$^\circ$ with the a axis, in agreement with the values reported in Ref. [87]. In this constrained model the two superimposed magnetic modes are such that the mG_2 mode is restricted to the plane xz, while the mG_1 mode is limited to the y direction. In this way, the sign correlation of neighboring spins is the same for the two modes. This model neglects those degrees of freedom in the spin arrangement that, although allowed by symmetry, have sign correlations of neighbouring spins which are not favored by the exchange coupling.

The simplification included in the model proposed in Ref. [87] is consistent with the prevailing role of the isotropic exchange energy, but the better results of the refinement of a non-constrained model, only restricted by the superspace symmetry of the phase, demonstrates that the modulations of the two Mn atoms have significant differences, due to some non-negligible contribution of spin-mode components with unfavourable exchange energies. Anisotropic effects beyond the exchange interaction, although weak, are an essential ingredient of multiferroics, and this feature of the magnetic structure of the AF2 phase, demonstrated by the present study, can be considered one of them. This is similar to what happens

in weak ferromagnets, where the magnetic ordering exhibits ferromagnetic correlations along some directions, despite being unfavourable from the viewpoint of exchange energy. They appear as secondary effects because they are permitted by symmetry. The application of superspace symmetry allows to predict similar effects in incommensurate magnetic phases, distinguishing the rigorous restrictions coming from symmetry, from those that are only approximate and are associated with the overwhelming role of the isotropic exchange interactions.

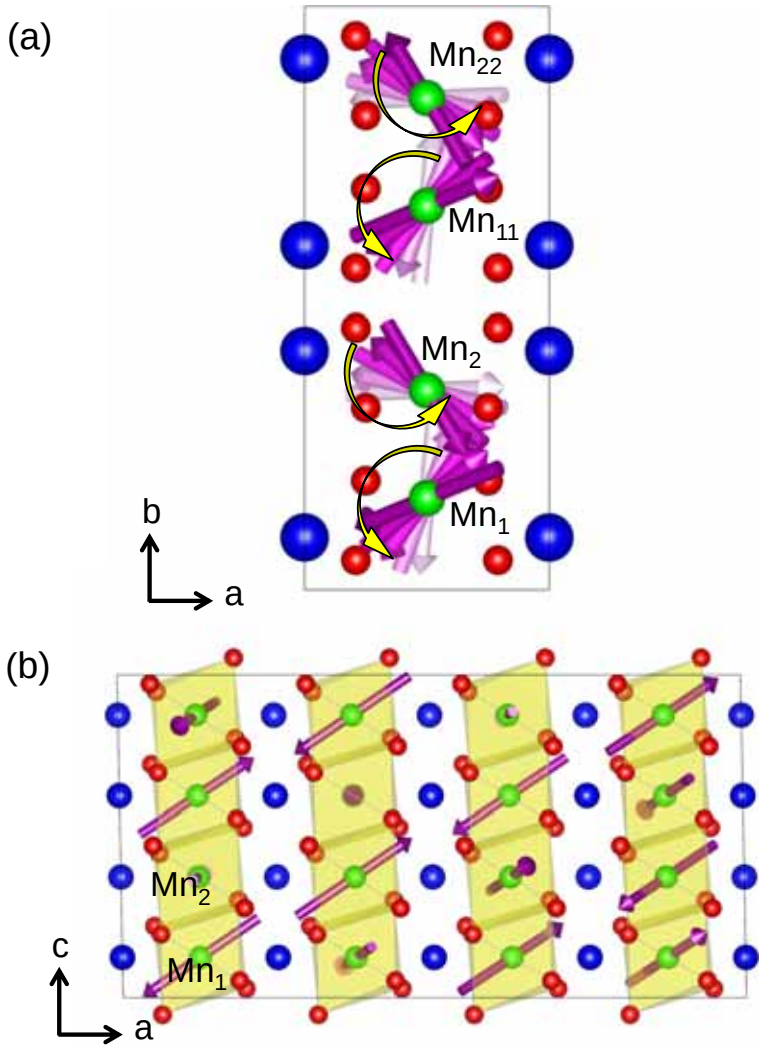

FIGURE 7.4: AF2 multiferroic magnetic structure of $MnWO_4$ at 9 K. (a) Projection along c axis showing the chirality of the structure. (b) Projection along the b axis. Only the non-periodic modulation within a region $4a \times 2b \times 2c$ is represented.

7.4 Atomic modulations

Apart from the constraints on the magnetic modulations, the superspace symmetry of an incommensurate magnetic phase also provides information on the possible displacement modulations of the atoms positions.

Although the structural modulations induced by magnetostructural coupling are very weak (as discussed in Chapter 6), and have not been considered in the measurements reported in this chapter, it is important to have in mind their possible existence and their expected characteristics. The ferroelectric behavior observed in $MnWO_4$ is in fact part of this induced structural distortion resulting from the magnetic symmetry break, and corresponds to a $\mathbf{k} = 0$ polar structural modulation. In this section we present the symmetry constraints of the atomic structures of the AF3 and AF2 magnetic phases.

The structural distortions that result from magnetostructural coupling with the magnetic ordering are subject to the same symmetry than the actual magnetic ordering. This means that the atomic positions can in principle become modulated, but their modulations will be restricted by the same superspace group operations as the magnetic modulations. Their effect is however different due to the invariance of the structural modulation for time reversal. Hence, the atomic modulation functions $\mathbf{u}_\nu(x_4)$ and $\mathbf{u}_\mu(x_4)$ that describe the atomic displacements of the symmetry related ν and μ atoms from their basic positions $\mathbf{r}_{l_\nu}$ and $\mathbf{r}_{l_\mu}$ are related as:

$$\mathbf{u}_\mu(R_I x_4 + \mathbf{H}_\mathbf{R} \cdot \mathbf{r}_\nu) = \mathbf{u}_\nu(x_4) \tag{7.19}$$

and thus, the symmetry operation $\{1'|000\frac{1}{2}\}$, common to both phases, force the possible displacive modulations of any atom to the condition:

$$\mathbf{u}_i(x_4 + \frac{1}{2}) = \mathbf{u}_i(x_4) \tag{7.20}$$

This means that any possible induced structural modulation is limited to even harmonics. Remember that in Chapter 2 the atomic modulation functions were Fourier expanded, being periodic with period 1:

$$A_\mu(x_4) = A_{\mu,0} + \sum_{n=1,\ldots} [A_{\mu,ns}\sin(2\pi n x_4) + A_{\mu,nc}\cos(2\pi n x_4)] \tag{7.21}$$

and taking into account equation (7.20) it is straight forward that the atomic mod-

ulations are related to even harmonics.

$$\begin{aligned} \sum_{m=1,\ldots} [\mathbf{u}_{i,ms}\sin(2\pi m(x_4+\frac{1}{2}))+\mathbf{u}_{i,mc}\cos(2\pi m(x_4+\frac{1}{2}))] & \\ = \sum_{n=1,\ldots} [\mathbf{u}_{i,ns}\sin(2\pi n x_4)+\mathbf{u}_{i,nc}\cos(2\pi n x_4)] & \quad (7.22) \\ \rightarrow n = 2m & \quad (7.23) \end{aligned}$$

This is a quite general feature of single-**k** incommensurate magnetic phases (see Ref. [66]), restricting possible satellite structural diffraction peaks to even n indices, while magnetic ones are necessarily odd ones[3] if the modulation becomes anharmonic. Second order satellites due to induced structural modulations, although weak, are indeed quite common [23, 100, 157, 158], and they have been also found in $MnWO_4$ by synchrotron X-ray diffraction [100].

Note that equation (7.20) implies that the non-magnetic atomic modulations of Mn_1 and Mn_{11} (as those of Mn_2 and Mn_{22}), related by the centering X, are identical. In principle, provided that second order satellites are strong enough to be measurable, the atomic modulated structure could be determined separately from the magnetic one using the non-magnetic superspace group (with modulation wave vector 2**k**), resulting from substituting the operation $\{1'|000\frac{1}{2}\}$ by $\{1|000\frac{1}{2}\}$, and applying then the usual procedures that have become standard for non-magnetic incommensurate structures. This is however not necessary and could be misleading, because magnetic superspace symmetry provides an unified framework that constrains all degrees of freedom, and clarifies the correlation between the constraints imposed upon magnetic and non-magnetic degrees of freedom.

The Mn and W atoms are kept invariant by the symmetry operation $\{2_y|00\frac{1}{2}\frac{1}{2}\}$, which is common both to AF3 and AF2 phases, and this implies, according to the analogous of equation (7.3) that their displacive modulations must satisfy:

$$\mathbf{u}_i(-x_4+\frac{1}{2}) = 2_y\cdot\mathbf{u}_i(x_4) \quad (7.24)$$

[3] $\{1'|000\frac{1}{2}\}$ forces the magnetic modulations to odd harmonics

$$\begin{aligned} \mathbf{M}_i(x_4+\frac{1}{2}) &= -\mathbf{M}_i(x_4) \\ \sum_{n=1,\ldots} [\mathbf{M}_{i,ns}\sin(2\pi n(x_4+\frac{1}{2}))+\mathbf{M}_{i,nc}\cos(2\pi n(x_4+\frac{1}{2}))] &= -\sum_{m=1,\ldots} [\mathbf{M}_{i,ms}\sin(2\pi m x_4)+\mathbf{M}_{i,mc}\cos(2\pi m x_4)] \\ \sum_{n=1,\ldots} [\mathbf{M}_{i,ns}\sin(2\pi n(x_4+\frac{1}{2}))+\mathbf{M}_{i,nc}\cos(2\pi n(x_4+\frac{1}{2}))] &= \sum_{m=1,\ldots} [\mathbf{M}_{i,ms}\sin(2\pi m x_4+\pi))+\mathbf{M}_{i,mc}\cos(2\pi m x_4+\pi)] \\ \rightarrow n &= 2m+1 \end{aligned}$$

with i any Mn or W atom in the paramagnetic unit cell.

Hence, the x and z components of these modulations are restricted to sine terms while the y component can only contain cosine terms:

$$\mathbf{u}_{i\alpha}(x_4) = \mathbf{u}^1_{i\alpha}\sin(4\pi x_4) \qquad (\alpha = x, z) \tag{7.25}$$

$$\mathbf{u}_{iy}(x_4) = \mathbf{u}^o_{iy} + \mathbf{u}^1_{iy}\cos(4\pi x_4) \tag{7.26}$$

being $i =$ Mn, W and $\mathbf{u}^o_{iy}$ being related to $\mathbf{k} = 0$.

The displacive modulations that can happen to W and Mn atoms by any kind of magnetostructural coupling are therefore $\frac{\pi}{2}$ shifted with respect to the magnetic modulation of the Mn atoms, see equation (7.9) and (7.10), independently of the specific mechanism at play.

In the AF3 phase, any pair of atoms $i = 1, 2$, related by $\{\bar{1}|0\frac{1}{2}0\frac{1}{2}\}$, as Mn_1 and Mn_2, have their structural modulations related by:

$$\mathbf{u}_2(-x_4 + \frac{1}{2}) = -\mathbf{u}_1(x_4) \tag{7.27}$$

which according to equations (7.25) and (7.26) implies equal amplitudes for the x, z sine terms, and opposite ones for the y amplitudes. Mn and W are allowed to have homogeneous ($\mathbf{k} = 0$) displacements along y, see equation (7.26), but equation (7.27) implies that in the AF3 phase each pair of atoms related by inversion will have opposite homogeneous displacements, consistently with the centrosymmetric point-group symmetry $2/m$ of this phase. Something similar happens for the more general modulations of the oxygen atoms in general positions that can have an homogeneous components along the three crystallographic directions. In contrast, in the AF2 phase, as the inversion symmetry operation is no longer valid, the constraint limiting the homogeneous displacements along y of inversion-related atoms to opposite values disappears and a polar distortion mode is allowed.

Summarizing both AF3 and AF2 phases may exhibit a magnetic induced structural modulation with $2\mathbf{k}$ as primary modulation wave vector. In the AF3 phase this structural modulation maintains an average structure with $P2/c$ symmetry, i. e. the same space group as in the paramagnetic phase, while the structural modulation in the AF2 phases looses some of its constraints and has only as symmetry for the average structure the space group $P2$.

7.5 Summary and conclusions

The two incommensurate magnetic phases of the multiferroic $MnWO_4$ have been re-analyzed using the superspace formalism. The superspace group corresponding to each phase has been identified, and the structures have been re-determined under these symmetries, using single-crystal non-polarized neutron-diffraction data. The spin modulations of the Mn atoms have been fully determined, distinguishing those features forced by symmetry and fulfilled exactly, from those only approximate and essentially caused by the strong weight of the isotropic exchange interaction. The study shows that in the antiferromagnetic phase AF3, the modulations of the two Mn atoms in the unit cell can have a small cycloidal component, exactly equal but with opposite chiralities in the two atoms, such that their effect cancel and they cannot induce any electric polarization. In contrast, in the AF2 phase, the addition of a second magnetic mode to the spin modulations breaks the symmetry relation between the two manganese atoms, the two modulations have then chiralities of the same sign, and their effect add up giving rise an electric macroscopic polarization.

The superspace group of each phase also determines the magnetic point-group governing its tensor properties. The ferroic properties of the multiferroic AF2 phase can then be characterized by the point-group symmetry break $2/m1' \rightarrow 21'$, i. e. by the ferroic species $2/m1'F21'$ [159]. This ferroic species implies that there can only be two types of ferroic domains in the AF2 phase, related by the space inversion lost in the symmetry break or equivalently by the mirror plane. Thus, the correlated switching properties of electric polarization and magnetic modulations in phase AF2 can be readily predicted: space inversion switches polarization, while it keeps invariant the amplitude of the mG_2 *irrep* mode and changes sign of the amplitude of the mG_1 *irrep* modulation. This means that the two domains with opposite polarization have also spin modulations of opposite chirality related by inversion.

The application of superspace formalism to the analysis of incommensurate magnetic phases is a promising new development with yet few examples in the literature. We explain here its application on $MnWO_4$ and demonstrate how a powerful it is to describe and use systematically the symmetry properties of incommensurate magnetic structures.

Chapter 8

Magnetic structure determination and ferroelectric properties of $Mn_{1-x}Co_xWO_4$ (x = 0.05, 0.10, 0.15 and 0.20)

Chapter 8 is devoted to the determination of the magnetic structures, the study of the ferroelectricity and the inter-relation between the magnetic and electric properties of the $Mn_{1-x}Co_xWO_4$ series at zero field. For that purpose we have used bulk magnetic measurements, neutron scattering and pyroelectric measurements on single crystals. The results for each composition are presented first, followed by a summary of the results, our contribution to the magnetic phase-diagram and a preliminary electric phase-diagram.

By the time the work on this thesis began, there was a single publication by Song and co-workers [125] discussing the influence of cobalt substitution for manganese in $MnWO_4$. However, since the proposed magnetic structures were based on neutron-powder-diffraction data, the refined structures were not unambiguously determined and important details of them were not provided (as already mentioned in Chapter 4, neutron powder-diffraction sometimes is not enough for the determination of magnetic structures). That is why, in the conclusions of this first paper on the Co substitution the authors called for "further work using single crystal samples to resolve the uncertainties" of the analyses of their powder-diffraction data.

During this years, new important features of the magnetic phase diagram emerged from the work by other groups [126–131] which were published in parallel with the results obtained during the work on this thesis. At the end of this chapter there is a section devoted to the comparison and discussion about the results obtained by other groups and ours.

8.1 $Mn_{0.95}Co_{0.05}WO_4$

8.1.1 Bulk magnetic response

The temperature variation of the susceptibilities along the b axis and along the magnetically easy and hard axes (confined within the ac plane as determined below) are presented in Fig. 8.1(a). The easy axis is called α, whereas the hard axis is called $\alpha + 90^\circ$. For all orientations the susceptibilities have the highest value at $T_N = 13.2(2)$ K. At lower temperature, there is an anomaly in the susceptibility along b at T_{N2} = 12.2(2) K which can be attributed to a magnetic transition. No evidences of this transition are observed in the susceptibilities along α and $\alpha + 90^\circ$, within experimental resolution. The magnetic anisotropy is confirmed by measuring the angular dependence of the magnetic susceptibility by rotating the crystal around the b axis, see Fig. 8.1(b). According to these measurements, the minimum of the susceptibility, which indicates the easy axis, occurs at 15(1)$^\circ$ from a, and the hard axis, $\alpha + 90^\circ$, is located approximately 107(1)$^\circ$ from a.

The difference of susceptibilities along the different directions at high temperatures (in the paramagnetic region) is found to be zero within experimental resolution. Figure 8.1(c) shows the inverse of the magnetic susceptibilities along the crystallographic axes, a, b and c: they follow the Curie-Weiss law with an effective magnetic moment μ_{eff} = 5.88(8) μ_B, which is in a very good agreement with the expected contribution from the Mn^{2+} and the effective spin only moment of the Co^{2+} ions (5.83 μ_B). The paramagnetic Curie temperature Θ_P = -64(3) K is practically the same for all the directions. The latter, together with the negligible orbital contribution is in agreement with the lack of anisotropy in the paramagnetic region [43–45].

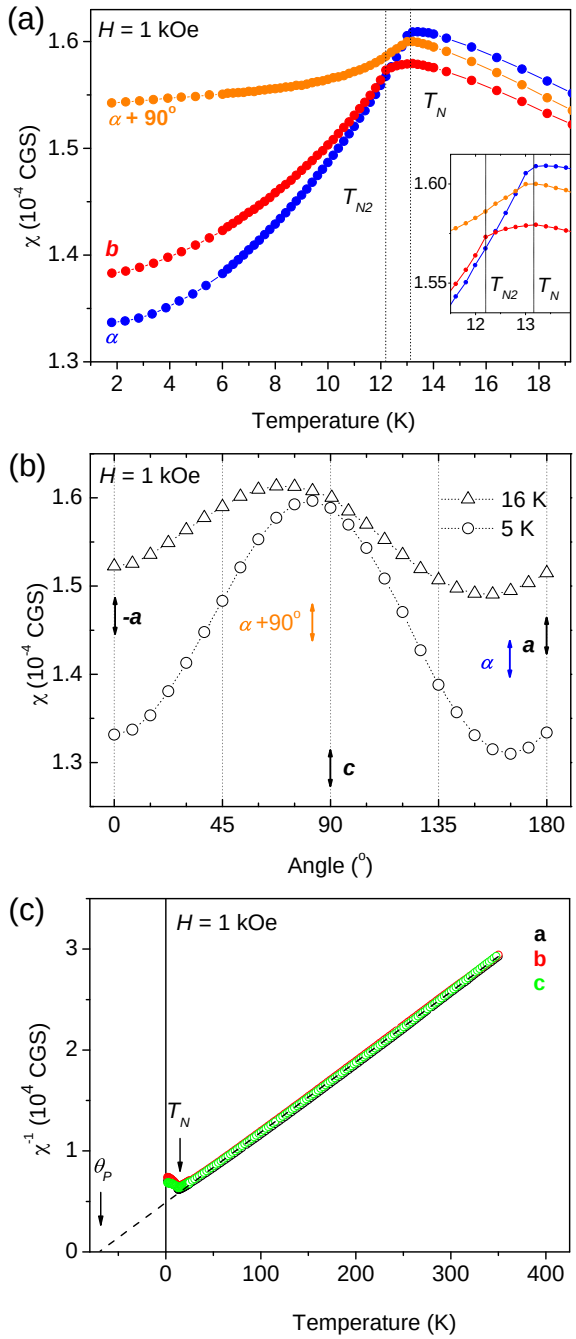

FIGURE 8.1: (a) Temperature dependence of dc susceptibility of $Mn_{0.95}Co_{0.05}WO_4$ along the b axis and along two distinctive directions within the ac plane, namely at an angle α of about 15° with respect to the a axis and perpendicular to it $\alpha + 90°$. (b) Angular dependencies of susceptibility within the ac plane (measurement done in collaboration with the group leaded by Prof. A. A. Mukhin). (c) Inverse of the susceptibility along the a, b and c (no difference was found also between α and $\alpha + 90°$ in the paramagnetic region, data not shown).

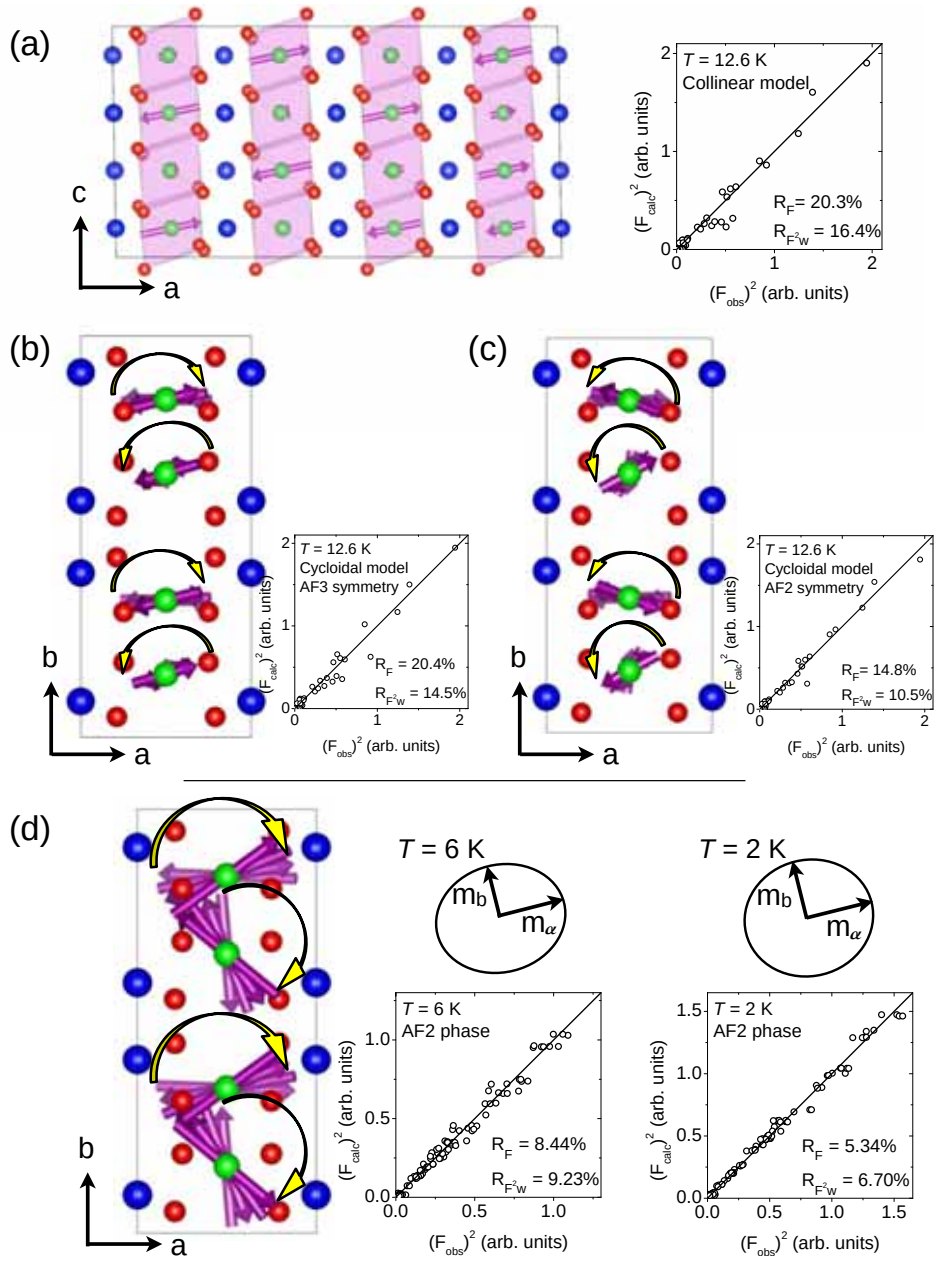

FIGURE 8.2: Magnetic models for $Mn_{0.95}Co_{0.05}WO_4$ for data collected at 12.6 K: (a) model 1 (sinusoidal AF3); (b) model 2 (cycloidal AF2), with opposite chirality for Mn_1 and Mn_2 and (c) model 3 (cycloidal AF2), with equal chirality for Mn_1 and Mn_2. (d) Magnetic model for data collected at 6 K and 2 K. The yellow arrows sign the chirality of the spins. All the models are accompanied by their corresponding agreement plots. A unique model is given for the data at 6 K and 2 K, the ellipse that envelops the amplitudes is drawn above the agreement plots.

8.1.2 Neutron diffraction

The magnetic structures of $Mn_{0.95}Co_{0.05}WO_4$ were studied on two instruments: 6T2 in the Laboratoire Léon Brillouin (LLB) at Saclay and D23 in the Institut Laue Langevin (ILL) in Grenoble (in both cases the sample was mounted inside a magnet). The propagation vector that describes the periodicity of the magnetic phases was refined from centering about thirty magnetic reflections at 2 K and resulted in $\mathbf{k}$ = [-0.216(1), $\frac{1}{2}$, 0.461(1)].

The temperature evolution of several magnetic reflections appearing below T_N = 13.2 K did not show any anomaly which could be related to a magnetic phase transition at $\sim$ 12.2 K, expected from the bulk magnetic data. Since the temperature range for the high temperature magnetic phase is only 1 K wide (12.2 K - 13.2 K) and furthermore, it is close to the Néel temperature (weak magnetic reflections), collecting data at the appropriate temperature and refining those data is a rather difficult task. We collected data at 12.6 K (this refers to the thermometer used in the neutron experiment, and might be few tents of degree different from the temperature read in the magnetic measurements). Three following models have been tested to explain the collected data, and their details are given in Table 8.1:

(i) Model 1 (Sinusoidal AF3): It is a collinear structure with the moments in the *ac* plane at about 11(2)$^\circ$ from the *a* axis and sinusoidally modulated. This structure is similar to the AF3 phase of the pure compound and agrees with the model proposed by Song and co-workers in Ref. [126]. The structure is plotted in Fig. 8.2(a).

(ii) Model 2 (Cycloidal AF3): It corresponds to a cycloidal structure with opposite chirality for Mn_1 and Mn_2. The moments rotate in the *ub* plane, where *u* is a direction in the *ac* plane 15(2)$^\circ$ from *a*. The chirality of the Mn_1 and Mn_2 atoms is opposite which maintains the symmetry of the AF3 phase as explained in Chapter 7. Figure 8.2(b) depicts this structure. This structure is an analogue of the alternative antiferroelectric AF3 structure of $MnWO_4$, as suggested by the superspace analysis provided in Chapter 7.

(iii) Model 3 (Cycloidal AF2): This model is similar to the one of the multiferroic phase of the pure compound. The differences with respect to that structure are related to the amplitudes of the moments and the inclination of the rotation plane within the *ac* plane. Thus, the structure is cycloidal, with the spins rotating in the *ub* plane, *u* being within the *ac* plane 15(2)$^\circ$ from *a*. Both manganese atoms in the crystallographic unit cell have the same chirality, and

therefore, they break the spacial inversion. The spin arrangement is plotted in Fig. 8.2(c).

The magnetic *sinusoidal AF3* (model 1) and *cycloidal AF3* (model 2) spin arrangements have the same symmetry as the AF3 phase of the pure compound and therefore they take its name (even if the model 2 has more freedom than the model 1, in the sense that more parameters are refined to describe the structure). The same reasoning is applied to model 3, which has the symmetry of the so-called AF2 phase. Although among those plausible models the AF2 fits the data slightly better, its validity should be taken with some precautions since the residual factors of all the proposed models are not very good. This may be due to the fact the experiment was done close to the Néel temperature and inside a magnet, which introduces noise to the data. The magnetic models are accompanied by their corresponding agreement plots. The compatibility of the models with polarization results should be compared to try to choose one model among them.

Temperature		T = 12.6 K	T = 12.6 K	T = 12.6 K	T = 6 K	T = 2 K
Magnetic phase		(i) AF3	(ii) AF3	(iii) AF2	AF2	AF2
Instrument		D23	D23	D23	6T2	6T2
k				[-0.216(1), 0.5, 0.461(1)]		
Mn_1	$\Re(m)(\mu_B)$	2.72(3)	2.63(3)	2.38(4)	4.26(6)	4.67(4)
	ϕ_u	0°	0°	0°	0°	0°
	θ_u	79(2)°	75(2)°	80(2)°	73(2)°	77(2)°
	$\Im(m)(\mu_B)$		0.78(9)	1.24(6)	-3.51(6)	-4.20(5)
	ϕ_v		90°	90°	90°	90°
	θ_v		90°	90°	90°	90°
Mn_2		$\mathbf{u}_2^{x,z} = -\mathbf{u}_1^{x,z}$ $\mathbf{v}_2 = \mathbf{v}_1 = 0$	$\mathbf{u}_2^{x,z} = -\mathbf{u}_1^{x,z}$ $\mathbf{v}_2^{y} = \mathbf{v}_1^{y}$	$\mathbf{u}_2^{x,z} = -\mathbf{u}_1^{x,z}$ $\mathbf{v}_2^{y} = -\mathbf{v}_1^{y}$	$\mathbf{u}_2^{x,z} = -\mathbf{u}_1^{x,z}$ $\mathbf{v}_2^{y} = -\mathbf{v}_1^{y}$	$\mathbf{u}_2^{x,z} = -\mathbf{u}_1^{x,z}$ $\mathbf{v}_2^{y} = -\mathbf{v}_1^{y}$
$R\Delta\varphi$		$\frac{k_z}{2}$	$\frac{k_z}{2}$	$\frac{k_z}{2}$	$\frac{k_z}{2}$	$\frac{k_z}{2}$
$R_{F^2}/\%$		20.3	20.4	14.8	8.44	5.26
$R_{F^2w}/\%$		16.4	14.5	10.5	9.23	6.58
$R_F/\%$		26.9	26.4	22.0	5.46	3.65
χ^2		12.8	10.2	5.34	9.79	7.03

TABLE 8.1: Parameters that describe the magnetic structures of $Mn_{0.95}Co_{0.05}WO_4$. Magnetic atoms Mn_1 and Mn_2 are located in the crystallographic unit cell at $[\frac{1}{2}, 0.6839(7), \frac{1}{4}]$ and $[\frac{1}{2}, 0.3161(7), \frac{3}{4}]$, respectively. Three models are given to describe the magnetic structure at 12.6 K: (i) model 1 (sinusoidal AF3), (ii) model 2 (cycloidal AF3) and (iii) model 3 (cycloidal AF2).

Regarding the low temperature magnetic phase, the refinements were done from the integrated intensities of about a hundred reflections at 6 K and 2 K, respectively. The details of the structure are given in Table 8.1. The low temperature

phase corresponds to a cycloidal structure that has the same symmetry as the AF2 phase of the pure $MnWO_4$, so, accordingly this phase is named AF2. The moments are rotating in the ub plane and the amplitudes are enveloped by an ellipse. The orientation of the direction u changes a few degrees from 73(2)° to 77(2)° when temperature decreases from 6 K to 2 K. The main difference concerns their amplitudes of the ordered magnetic moments; the lower the temperature is, the bigger the amplitudes are. It is worth to pay attention on the way the amplitudes increase and how the eccentricity of the ellipse evolves. If the eccentricity is defined as

$$\epsilon = \sqrt{1 - \frac{\Im(m)^2}{\Re(m)^2}}, \tag{8.1}$$

then, it changes from ϵ(6 K) = 0.54(3) to ϵ(2 K) = 0.44(3). The development of the magnetic component along the b axis, makes the ellipse more circular as temperature decreases and therefore, the magnetic anisotropy within the ub plane decreases. Figure 8.2(d) shows the magnetic structures model for the multiferroic phase and a plot of the ellipses that envelop the amplitudes of the magnetic moments at $T = 6$ K and $T = 2$ K, respectively.

8.1.3 Electric polarization

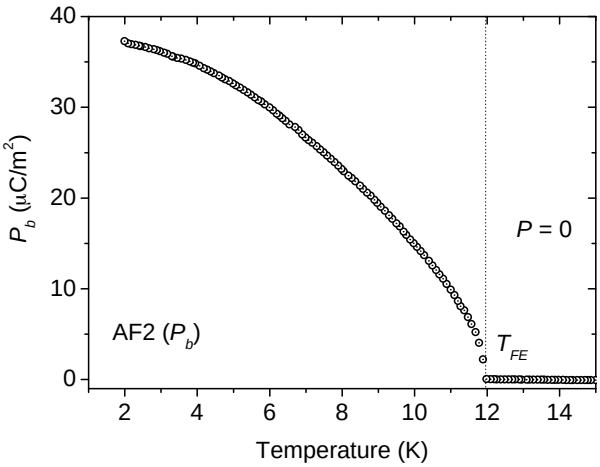

FIGURE 8.3: Temperature dependence of the spontaneous electric polarization along the b axis.

Spontaneous electric polarization appears only along the b axis below T_{FE} = 12.0(1) K and increases up to about 37 $\mu C/m^2$ at 2 K as shown in Fig. 8.3.

The temperature at which the polarization arises, T_{FE}, coincides with the temperature where the anomaly in the magnetic susceptibility along the b axis is observed, T_{N2}, see Fig. 8.1(a), that is, when entering the AF2 phase.

The fact that the polarization arises below 12.0(1) K can help us to discard the polar Model 3 to describe the magnetic structure at 12.6 K. So, we are left with the sinusoidal collinear structure and the cycloidal structure with opposite chirality for Mn_1 and Mn_2. Anyway, as mentioned before, the data refinement is not conclusive.

The polarization along the b axis could be indeed predicted from the symmetry of the AF2 magnetic structure [$X21'(\alpha 0\gamma)0ss$], as it is the case for the pure $MnWO_4$ (see Chapter 7).

8.2 $Mn_{0.90}Co_{0.10}WO_4$

8.2.1 Bulk magnetic response

The temperature dependence of the dc susceptibility with field applied along the principal crystallographic directions is given in Fig. 8.4(a). A clear maximum, which could be associated to the Néel temperature, is seen at T_N = 13.2(1) K for all the three directions. It is worth noting that the a- and c-axis susceptibilities have a similar value at T_N, which is bigger than the one for the b axis. With further decrease of the temperature another small change in the susceptibility slope takes place at T_{N2} = 11.4(1) K, more visible along the c axis, signaling a second magnetic transition. The two characteristic temperatures are in a good agreement with the data reported in Ref. [126] and are associated with the appearance of the AF3 phase below T_N and with the so-called AF2' phase below T_{N2}. Though below T_N the a-axis susceptibility decreases faster than the one along the c axis, they both change in a similar fashion and in disparity with the relatively small decrease of the b-axis susceptibility.

Above T_N, the a- and c-axis susceptibilities are very close and higher than the b-axis susceptibility. The observed anisotropy is rather different from the one reported in Ref. [126]. However, this discrepancy and the magnitude of the measured anisotropy itself should be taken with some precautions until careful measurements on a crystal with similar dimensions along the three directions are reported, or after proper corrections for sample shape and size are made [160]. At temperatures above 30 K, the susceptibilities along all the three directions fol-

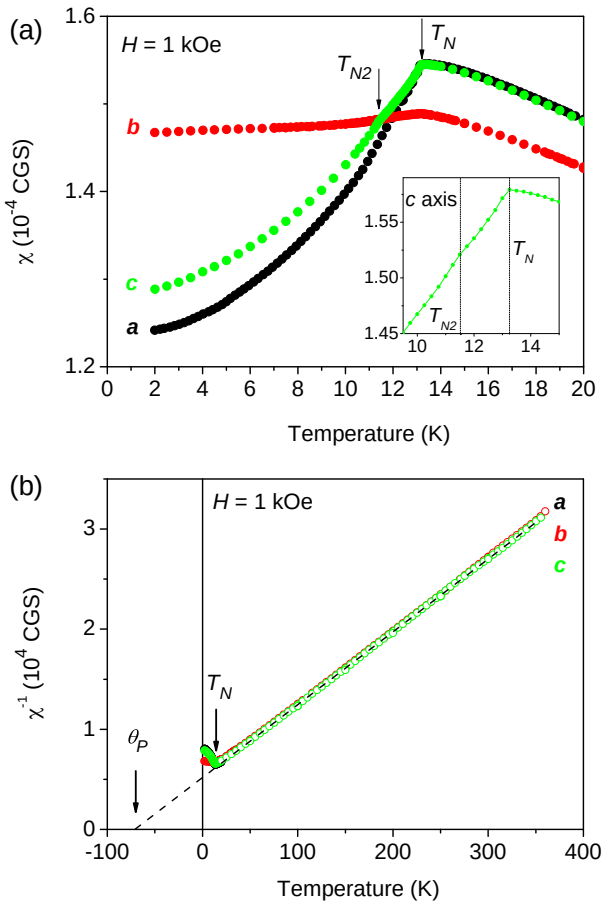

FIGURE 8.4: (a) Temperature dependence of dc susceptibilities at field of 1 kOe applied along the principal crystallographic directions. (b) Temperature dependence of the inverse susceptibilities along the same directions. T_N and θ_P stand for Néel and asymptotic paramagnetic temperatures respectively, while T_{N2} refers to the small change in the susceptibility slope, tentatively ascribed to a second transition.

low the Curie-Weiss law, see Fig. 8.4(b), with an effective magnetic moment of μ_{eff} = 5.74(1) μ_B, which is in a very good agreement with the expected contribution from the Mn^{2+} and the effective spin only moment of the Co^{2+} ions (μ_{eff} = 5.75 μ_B). The paramagnetic Curie temperature Θ_P = -71(3) K is practically the same for all the crystallographic directions.

8.2.2 Neutron diffraction

The two magnetically ordered states in $Mn_{0.90}Co_{0.10}WO_4$, evidenced by the susceptibility measurements, are reflected in the variation of the integrated intensities of two representative magnetic reflections shown in Fig. 8.5(a). Below $T_N \sim 13$ K it orders in the so-called AF3 phase. Then at $T_{N2} \sim 11$ K, a second transition occurs towards the so-called AF2' phase [125, 126], as revealed by the accident in the curves of Fig. 8.5(a) and in agreement with magnetic susceptibility measurements.

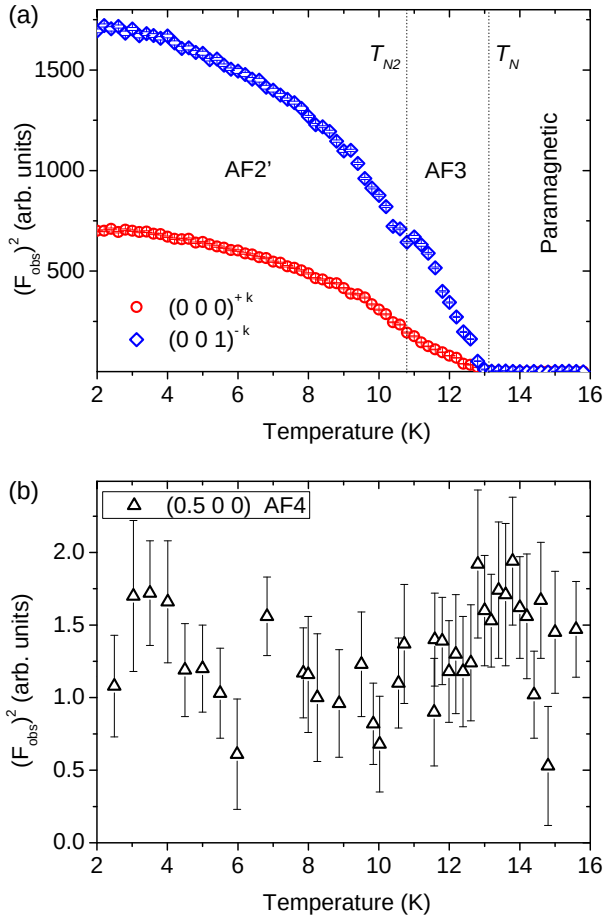

FIGURE 8.5: Integrated intensities of magnetic reflections in zero applied field monitored as the temperature increases. (a) Magnetic satellites that correspond to **k** = [-0.222(1), $\frac{1}{2}$, 0.472(1)]. The error bars are inside the symbols. Vertical lines indicate the two magnetic transitions. (b) The ($\frac{1}{2}$00) reflection characteristic of the AF4 commensurate phase.

Temperature		T = 12 K	T = 12 K	T = 9 K	T = 2 K
Magnetic phase		AF3	AF3	AF2′	AF2′
k			[-0.222(1), $\frac{1}{2}$, 0.472(1)]		
Mn_1	$\Re(m)(\mu_B)$	2.53(7)	2.55(7)	3.71(1)	4.45(2)
	ϕ_u	0°	0°	0°	0°
	θ_u	124.7(5)°	123.3(5)°	115.5(8)°	99(2)°
	$\Im(m)(\mu_B)$		-0.13(2)	2.80(1)	4.03(2)
	ϕ_v		90°	0°	0°
	θ_v		90°	25.5(8)°	9(2)°
Mn_2		$\mathbf{u}_2^{x,z} = -\mathbf{u}_1^{x,z}$ $\mathbf{v}_2^{y} = \mathbf{v}_1^{y} = 0$	$\mathbf{u}_2^{x,z} = -\mathbf{u}_1^{x,z}$ $\mathbf{v}_2^{y} = \mathbf{v}_1^{y}$	$\mathbf{u}_2^{x,z} = -\mathbf{u}_1^{x,z}$ $\mathbf{v}_2^{x,z} = -\mathbf{v}_1^{x,z}$	$\mathbf{u}_2^{x,z} = -\mathbf{u}_1^{x,z}$ $\mathbf{v}_2^{x,z} = -\mathbf{v}_1^{x,z}$
$\Delta\varphi$		$\frac{k_z}{2}$	$\frac{k_z}{2}$	$\frac{k_z}{2}$	$\frac{k_z}{2}$
R_{F^2}/%		15.7	15.3	6.51	5.67
R_{F^2w}/%		13.6	12.6	6.94	6.16
R_F/%		17.6	17.3	8.49	6.65
χ^2		5.53	4.82	7.00	7.14

TABLE 8.2: Parameters that describe the magnetic structures of $Mn_{0.90}Co_{0.10}WO_4$. Mn_1 and Mn_2 are located in the crystallographic unit cell at [$\frac{1}{2}$, 0.6847(2), $\frac{1}{4}$] and [$\frac{1}{2}$, 0.3153(2), $\frac{3}{4}$], respectively.

After centering 20 magnetic reflections and refining the propagation vector at 12 K, 9 K and 2 K (**k** = [-0.222(1), $\frac{1}{2}$, 0.472(1)]), which within error bars is temperature independent, 680 magnetic peaks were collected at each temperature. The details of the refined magnetic structures are given in Table 8.2. The spin arrangements are depicted in Fig. 8.6 together with the observed and calculated squared structure factors. As for the pure and 5%-Co-doped compositions, two models can fit the data in the AF3 phase: a collinear structure with sinusoidally modulated amplitudes or a cycloidal order with different chirality for Mn_1 and Mn_2. In the collinear structure the moments lay in the *ac* plane, along a direction $\hat{u}$ making an angle ψ = 34.7(5)° (θ_u - 90°) with the *a* axis, with maximum amplitude of 2.53(3) μ_B. They are confined in the equatorial plane of the MO_6 octahedra and perpendicular to the *b* axis, see Fig. 8.6(a). In the cycloidal model the moments have an additional component along the *b* axis of $-0.13(2)$ μ_B, see Fig. 8.6(b). Even if the latter structure is a cycloidal one, both Mn atoms in the crystallographic unit cell have opposite chirality and hence, the structure is non-polar. Nevertheless, below 10.8 K another component ($\hat{v}$) appears perpendicular to the existing one ($\hat{u}$). Both $\hat{u}$ and $\hat{v}$, are in the *ac* plane. As a consequence, the structure becomes an elliptical helix in this *ac* plane, see Fig. 8.6(c), the so-called AF2′ phase [a brief superspace analysis is provided in Appendix E, where it is proved that the symmetry of the structure corresponds to $Xm1'(\alpha 0\gamma)ss$]. From the analysis of the magnetic

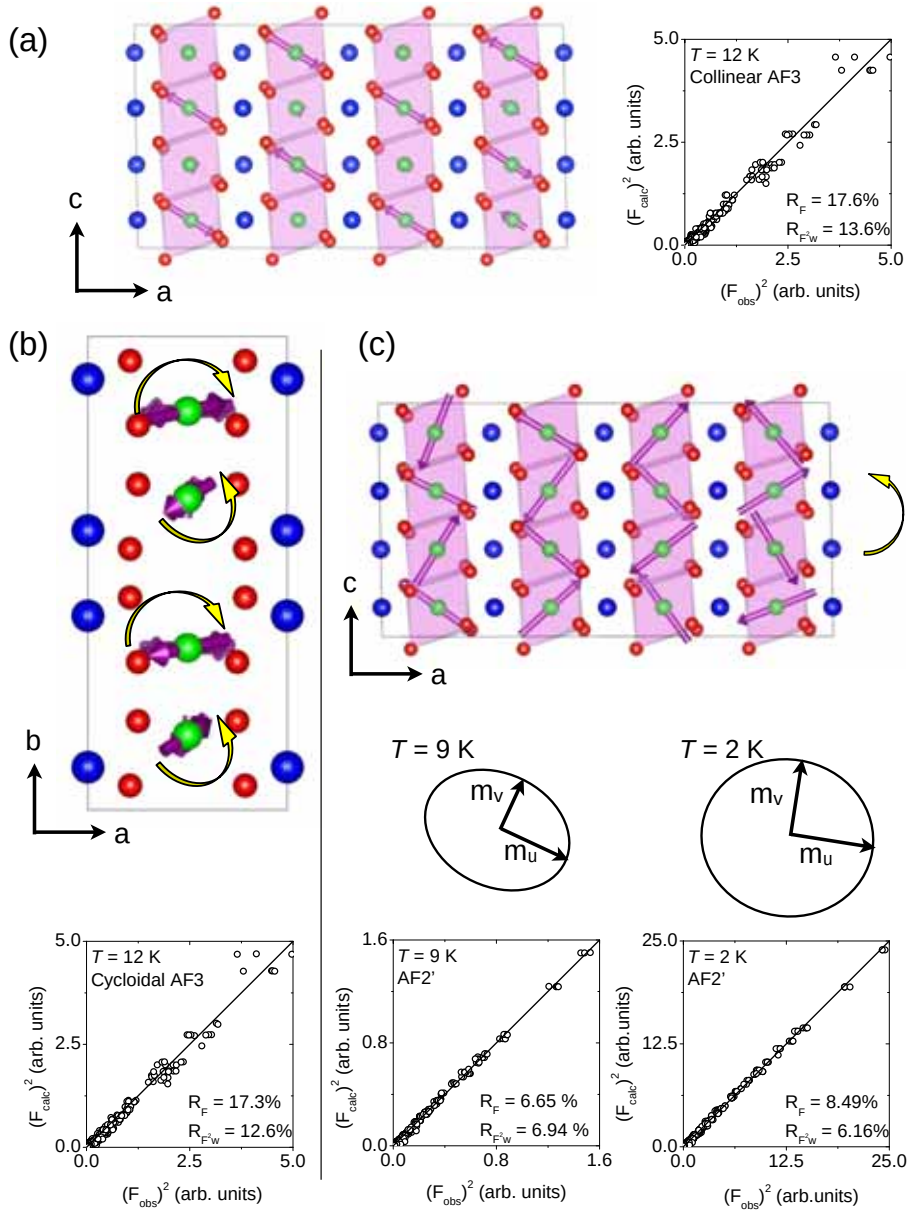

FIGURE 8.6: Magnetic structure models of $Mn_{0.90}Co_{0.10}WO_4$ in zero field with their corresponding agreement plots. (a) the collinear and (b) cycloidal models for the AF3 magnetic phase at 12 K and (c) the cycloidal model for the multiferroic AF2′ phase. The ellipses that envelop the amplitudes of the moments in the multiferroic phase are plotted at 9 K and 2 K. The yellow arrow mark the chirality of the moments. The corresponding magnetic models are described in the text and Table 8.2.

intensities we can appreciate a change in the orientation of the principal axes of the ellipse within the *ac* plane when decreasing the temperature. The angle that the semi-major axis of the ellipse makes with the c^* axis decreases from 124.8(5)° down to 99(2)° on cooling from 12 K to 2 K. Moreover, in the AF2′ multiferroic phase there is an apparent evolution of the eccentricity of the ellipse, defined as in equation (8.1), with temperature. From 9 K to 2 K the eccentricity changes from $\epsilon = 0.66(1)$ to 0.42(1). The fast development of the magnetic component perpendicular to $\hat{u}$ as the temperature decreases in the AF2′ phase, results in a more circular cycloid. Figure 8.6(c) shows the shape and orientation of the ellipses that envelop the magnetic moments.

We did not observe any sign of the collinear AF4 phase with propagation vector $\mathbf{k} = (\frac{1}{2}, 0, 0)$, see Fig. 8.5(b). Traces of this phase were reported by Song *et. al.* [125] for powder samples of $Mn_{0.90}Co_{0.10}WO_4$. Its possible presence in our sample was carefully examined. Our conclusion is that this commensurate phase characterized by $\mathbf{k} = (\frac{1}{2}, 0, 0)$ requires higher doping and does not appear in the 10 % Co-doped crystal. The presence AF4 in powder samples may be due to some inhomogeneities in the composition.

8.2.3 Electric polarization

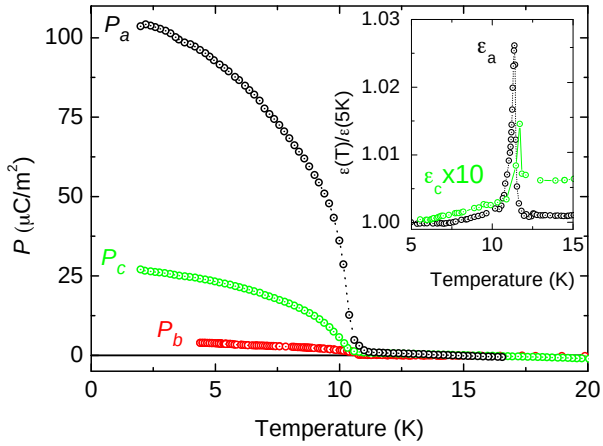

FIGURE 8.7: Temperature dependence of the spontaneous electric polarization along the principal crystallographic directions which appeared below T_{N2}, in the AF2′ cycloidal phase. Insert shows the anomalies of the dielectric constants along *a* and *c* axes at T_{N2} (measured at 16 kHz).

The temperature dependence of the electric polarization along a, b and c axes in zero magnetic field is shown in Fig. 8.7. Below $T_{N2} \sim 11$ K electric polarization is observed along both a and c axes, which increase up to $P_a \sim 100\ \mu C/m^2$ and $P_c \sim 30\ \mu C/m^2$ at low temperatures. The polarization along the b axis does not exceed 3 $\mu C/m^2$ and is probably due to a small misalignment from the b axis. Insert in Fig. 8.7 shows the temperature variation of the dielectric constant along a and c axes, which reveals peaks at T_{N2} where the spontaneous polarization appears; the peak's amplitude along a axis is significantly higher than along c axis. These results unambiguously show that spins in the cycloidal ferroelectric phase AF2' are aligned in the ac plane in agreement with our results from neutron diffraction and with Refs. [125, 126]. However we observe polarization not only along the a axis, as expected for the predominated Mn-Mn exchange in zigzag chains along the c axis, but also a noticeable P_c component, the value of which is beyond possible misalignment in the measurement direction and thus, suggests a contribution from the exchange along the a axis. This component of the polarization ($\sim 20\ \mu C/m^2$) was also observed in Ref. [126]. This contribution from the exchange along the a axis is supported by the spin-wave excitations studies in $MnWO_4$ [118] that confirmed that the exchange coupling between chains along the a axis is as strong as along the c axis and similarly strongly frustrated.

8.3 $Mn_{0.85}Co_{0.15}WO_4$

8.3.1 Bulk magnetic response

The temperature dependence of the magnetic susceptibilities along b and along two particular directions are plotted in Fig. 8.8. The latter two directions are located within the ac plane, one at about 35° from the -c axis (named α) and the other perpendicular to it (called $\alpha + 90°$). The angular dependence of the susceptibility at room temperature presented in Fig. 8.9(a), exhibits its maximum value along α, and a minimum at $\alpha + 90°$. On the contrary, when the crystal is magnetically ordered, the maximum and minimum values are switched.

The α-axis susceptibility shows a clear maximum at 16.7(2) K, whereas along $\alpha + 90°$ and b axes there is a less visible accident that slightly changes the slope of the curve. This singularity could be attributed to the Néel temperature, T_N. Several anomalies occur below T_N which are evident for all the orientations, and suggest changes in the magnetic order. The first occurs at T_2 = 10.4(2) K, temper-

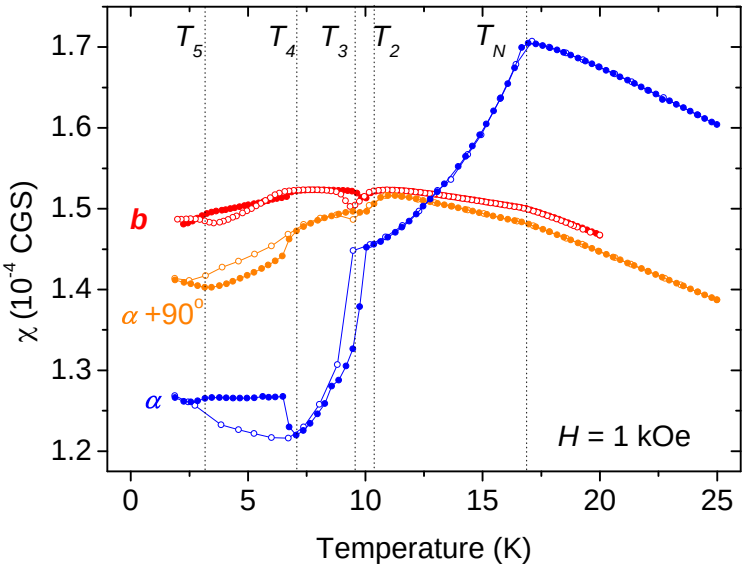

FIGURE 8.8: (a) Temperature dependencies of magnetic susceptibilities of $Mn_{0.85}Co_{0.15}WO_4$ along b, α (easy-axis) and $\alpha + 90^\circ$ (hard-axis) directions. Full circles (•) are recorded during heating of the sample and empty circles (○) are recorded while the sample was cooled down. Dotted lines mark the anomalies of the susceptibilities during heating of the sample.

ature at which the $\alpha + 90^\circ$- and b-axis susceptibilities have their maximum value. However, at about 9.4(2) K, χ_b recovers its value and $\chi_{\alpha+90^\circ}$ increases a bit. At this point α-axis susceptibility significantly decreases until they reach a linear behavior. The next anomaly happens at T_4 = 7.0(2) K where the slope of all the curves change smoothly during cooling (○), while on the contrary, with increasing the temperature (•) the change occurs in a step-like fashion along α and $\alpha + 90^\circ$ axes. Finally, there is a small change in the susceptibility at T_5 = 3.5(2) K which marks another transition. All the low temperature transitions are highly hysteretic, depending on whether the temperature increases or decreases, thus implying a first-order phase-transition and phase coexistence.

A magnetic anisotropy in the paramagnetic region is clearly observed in Fig. 8.9(b), where the inverse susceptibilities along b, α and $\alpha + 90^\circ$ are plotted. The χ^{-1} become parallel straight lines at high temperatures and follow the Curie-Weiss law. The asymptotic paramagnetic temperatures, Θ_P, obtained for the three directions differ considerably: Θ_P = -74(2) K along the b axis, Θ_P = -56(2) K for the α orientation, and Θ_P = -80(2) K for the orientation perpendicular to α within the ac plane. Furthermore, the effective magnetic moment was found to be 5.88(5) μ_B,

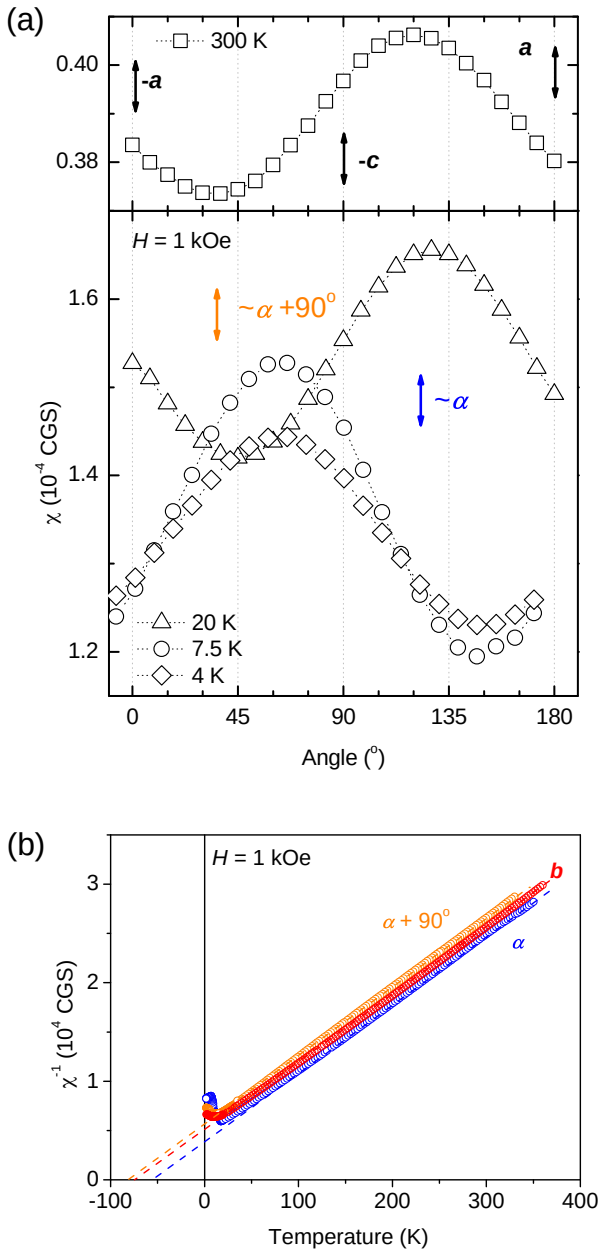

FIGURE 8.9: (a) Angular dependence of $\chi_{\perp b}$ at 300 K, 20 K, 7.5 K and 4 K measured in collaboration with Prof. A. A. Mukhin. (b) Inverse of χ along b, α and $\alpha + 90^\circ$ of $Mn_{0.85}Co_{0.15}WO_4$.

higher than the one expected from the Mn^{2+} ions and the spin only contribution from the Co^{2+} ions (5.66 μ_B) and therefore suggests that the Co orbital moment is

not completely frozen [43–45]. The anisotropy in Θ_P and the fact that the effective magnetic moments suggest orbital contribution from the cobalt, fully support the magnetic anisotropy in the paramagnetic region of the 15%-Co-doped composition.

8.3.2 Neutron diffraction

Magnetic reflections were recorded as a function of the temperature in order to follow magnetic transitions and to determine the propagation vectors present in each phase. In this case, magnetic reflections were monitored by performing scans along specific directions in the reciprocal space instead of integrated intensities.

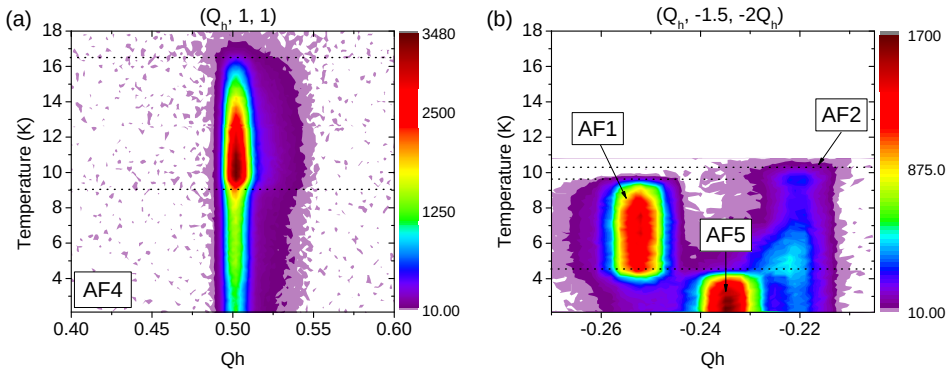

FIGURE 8.10: Scans of the magnetic reflections as a function of the temperature. (a) Q_h scan centered on the (0.5 1 1) reflection. (b) Scan along (Q_h, -1.5, -2Q_h) direction in the reciprocal space that shows reflections that correspond to three incommensurate propagation vectors. Black dashed lines are guides to observe the magnetic transitions.

Figure 8.10(a) shows Qh scan of the (0.5 1 1) magnetic reflection characteristic of the AF4 phase as a function of the temperature, whereas, Fig. 8.10(b) shows the temperature variation of the scans along (Q_h, -1.5, -2Q_l) direction in the reciprocal space. Along this latter direction reflections characteristic of AF1, AF2 and AF5 phases are visible. Four propagation vectors are thus observed below T_N: $\mathbf{k}_{AF1}$ = ($\frac{1}{4}$, $\frac{1}{2}$, $\frac{1}{2}$); $\mathbf{k}_{AF2}$ = [-0.22(1), $\frac{1}{2}$, 0.45(1)]; $\mathbf{k}_{AF4}$ = (-$\frac{1}{2}$, 0, 0) and $\mathbf{k}_{AF5}$ = [-0.23(1), $\frac{1}{2}$, 0.48(1)]. The values of the incommensurate propagation vectors were refined from the scans along Q_h and Q_l directions. The lower accuracy with respect to the other compounds comes from the coexistence of the reflections and therefore, the difficulty to center them due to their overlapping.

As it can be observed in Fig. 8.10(a) the magnetic phase AF4 exists below the

Néel temperature down to the lowest investigated temperature, 2 K. That magnetic peak appears at T_N, then its intensity increases up to about 9 K, where it drops down to a third of its value to become almost constant down to 2 K. In Fig. 8.10(b) one can observe that the commensurate AF1 phase exists in the 9.5 - 4 K temperature range, while the intensity of the AF5 peak emerges below 4.5 K and grows down to 2 K. The incommensurate peak that corresponds to the AF2 multiferroic phase exhibits the most complex behavior. It shows up at about 10.5 K, slightly before the AF1 phase, and when the latter appears the intensity of the AF2 reflection decreases, but it does not vanish. This AF2 phase recovers some intensity when the AF1 peak starts loosing it, as if it was replacing it. On the other hand, at about 4.5 K AF5 emerges with a subsequent disappearance and decrease of the AF1- and AF2-peak's intensity, respectively. Taking into account this information we can associate the characteristic temperatures obtained from magnetic susceptibility data with the magnetic phases:

- T_2 = 10.4(2) K: Emergence of AF2.
- T_3 = 9.4(2) K: Appearance of AF1 phase and modification of AF2 (eventually disappearance).
- T_4 = 7.0(2) K: Change in the AF1 phase and reappearance of AF2.
- T_5 = 3.5(2) K: There is not any clear evidence of any change in the evolution of the studied magnetic peaks.

Note that even if the AF5 peak vanishes abruptly at about 4.5 K [see Fig. 8.10(b)] there is not any trace of this transition in the evolution of the magnetic susceptibility, and this suggests that the AF5 phase could be somehow similar to the underlying AF2.

Intensity maps in the reciprocal space at several temperatures are depicted in Fig. 8.11, where the overlap of the reflections is very clear at 4.6 K and 1.6 K. Maps on Figs. 8.11(a), 8.11(b), 8.11(c), 8.11(d) and 8.11(e) were recorded consecutively and partially unveil the magnetic behavior that depend on whether the sample is cooled or heated, as seen in the susceptibility data. The comparison between Figs. 8.11(c) and 8.11(e) demonstrate that AF5- and AF1-peak's intensities are different at the same temperature (4.6 K in this case) depending whether the sample is further cooled down between both measurements or not. The magnetic hysteresis could be related to the martensitic nature of the transition.

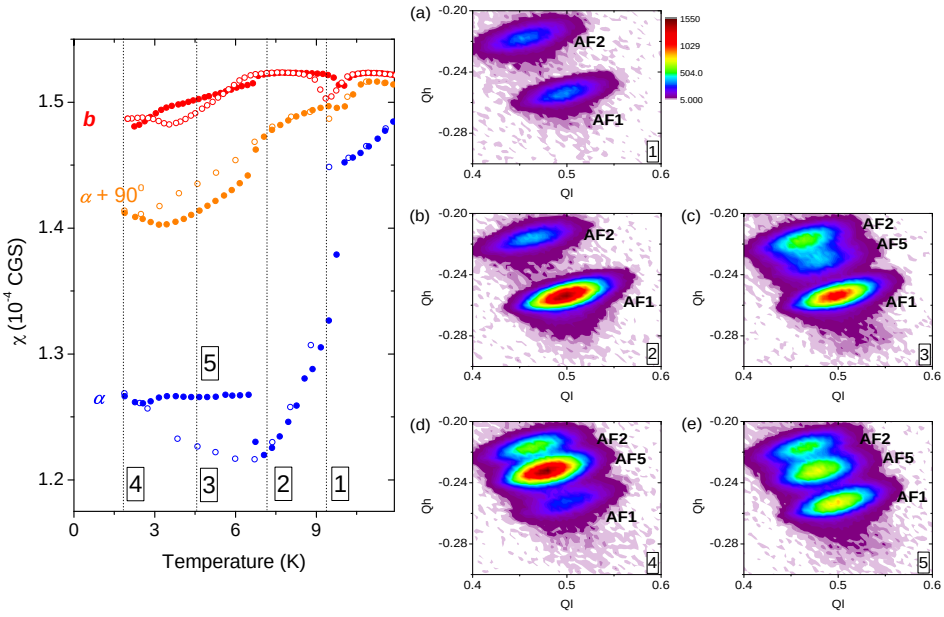

FIGURE 8.11: Intensity maps of $(Q_h, -1.5, -2Q_h)$ reciprocal plane at different temperatures, where $-0.30 < Q_h < -0.20$. Magnetic reflections of AF1, AF2 and AF5 magnetic phases are visible in this cut of the reciprocal space. Each mapping has a number which refers to the temperature at which it has been measured, marked in the susceptibility graph.

The strong peak-overlap is the reason why AF1 and AF4 are the only phases for which details were obtained by collecting magnetic reflections. The AF4 phase was studied at two temperatures, 11.5 K and 3 K, while data corresponding to the AF1 phase were only collected at 9 K. The refined parameters that describe those magnetic structures are summarized in Table 8.3 and they were obtained from the least square fitting of about 60 reflections of the AF4 phase and about 210 of the AF1 one. The spin arrangements are depicted in Fig. 8.12 together with their correspondent agreement plot. The AF4 phase of the 15%-Co-doped compound is similar to the one of the $CoWO_4$, in the sense that the moments are antiferromagnetically coupled along the a axis and they are located within the ac plane. Nevertheless, due to the experimental configuration (the sample was mounted in a cryomagnet), only the $l = 0$ plane was available, and therefore the treatment of these data yields two undistinguishable solutions that are $\theta_u = 32(2)^\circ$ and $\theta_u = -32(2)^\circ$, which means that the moments are $58(2)^\circ$ from a towards c or -c. This occurs because, as explained in the introductory chapters, magnetic neutron-diffraction is sensitive to the perpendicular component of the

Magnetic phase		(AF4)	(AF4)	(AF1)
Temperature		T = 11.5 K	T = 3 K	T = 9 K
k		$(\frac{1}{2}, 0, 0)$	$(\frac{1}{2}, 0, 0)$	$(\frac{1}{2}, \frac{1}{4}, \frac{1}{4})$
Mn_1	$\Re(m)(\mu_B)$	2.08 (2)	1.14 (1)	3.67 (2)
	ϕ_u	0°	0°	0°
	θ_u	32 (2)° or -32 (2)°	32 (2)° or -32 (2)°	142 (2)°
Mn_2		$\mathbf{u}_2 = \mathbf{u}_1$	$\mathbf{u}_2 = \mathbf{u}_1$	$\mathbf{u}_2 = \mathbf{u}_1$
$\Delta\varphi$		0	0	0
$R_{F^2}/\%$		11.9	15.3	21.9
$R_{F^2w}/\%$		11.3	12.7	15.6
$R_F/\%$		10.7	14.4	30.9
χ^2		8.78	2.93	3.60

TABLE 8.3: Parameters that describe the AF1 and the AF4 commensurate magnetic structures of $Mn_{0.85}Co_{0.15}WO_4$ at different temperatures.

magnetic moment with respect to the scattering vector. As the crystal was mounted with c axis vertical, and only $l = 0$ plane was accessible, both θ_u and $-\theta_u$ angles explain the data. However, as magnetic measurements show that the easy axis is located about 55° from the a axis toward -c, one can conclude that the real value of θ_u is -32(2)°=148(2)°. The solution is depicted in Fig. 8.12(a). The amplitude of the moments decreases with decreasing temperature as revealed by the refinement at 3 K.

Regarding the AF1 phase, it is pretty similar to the AF1 phase of the pure $MnWO_4$ compound [87]. The structure is collinear in the ac plane and the magnetic moments are arranged in a $++--$ configuration. Unlike the pure compound where moments are about 35° far from a towards c, in $Mn_{0.85}Co_{0.15}WO_4$ spins are located at θ_u = 142(2)° from the c axis (52° from a, towards -c), see Fig. 8.12(b).

These results obtained for $Mn_{0.85}Co_{0.15}WO_4$ give additional details compared to the model proposed by Song *et. al.* [125] from powder samples with the same nominal composition and agrees quite well with the results obtained by Chaudhury and co-workers in Ref. [127]. However, there are some discrepancies: concerning the transition temperatures to the AF2 and AF1 phases, Chaudhury *et. al.* ascribe a single temperature whereas in our data there is a narrow, but clear, temperature gap between both transitions (T_2 and T_3). Besides that, decreasing temperature, the intensity of the AF1 peak does not vanish in their sample whilst in ours it does. In addition, the intensity of the AF2 peak keeps on increasing whereas

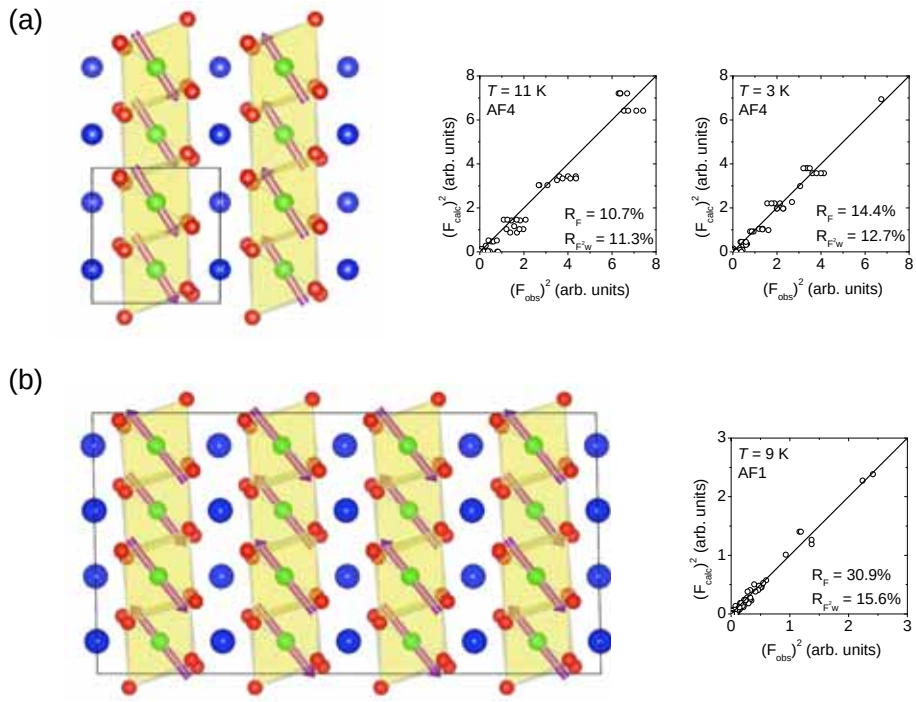

FIGURE 8.12: Magnetic models associated with the commensurate wave vectors in $Mn_{0.85}Co_{0.15}WO_4$: (a) Magnetic model for the AF4 magnetic phase with $\mathbf{k} = (\frac{1}{2}, 0, 0)$. (b) AF1 spin arrangement with $\mathbf{k} = (\frac{1}{4}, \frac{1}{2}, \frac{1}{2})$. The observed intensities compared to calculated intensities with parameters given in Table 8.3 are shown next to each model.

our data does not show such evolution. All these differences between our results and those reported in Ref. [127] can be related to the strong frustration in the compound, and show how small modifications (such us for example tiny variations of the cobalt concentration around its nominal value) can derive in somewhat distinct responses.

In summary, neutron diffraction has suggested the high degree of magnetic frustration of $Mn_{0.85}Co_{0.15}WO_4$ as evidenced by the existence of several coexisting magnetic phases. As the temperature decreases the collinear structure associated with $\mathbf{k}_4$ arises (characteristic for $CoWO_4$ parent compound), but with further decreasing the temperature new magnetic reflection related to $\mathbf{k}_1$, $\mathbf{k}_2$ and $\mathbf{k}_5$ emerge and compete.

8.3.3 Electric polarization

Figure 8.13 presents the polarization along the a and b axes measured on cooling. Polarization along b arises at about 10.0(1) K, has its maximum at 9.3(1) K and disappears at about 8.5(1) K. This temperature range coincides with the one where the AF2 phase exists (on cooling) and confirms that its propagation vector describes the periodicity of the AF2 multiferroic phase instead of the paraelectric AF3's. In contrast with the lower doped compositions, $Mn_{0.85}Co_{0.15}WO_4$ exhibits another multiferroic phase between 6.0(1) K and 3.0(1) K with maximum polarization along b at 3.9(1) K. The polarization in this range must come from the reappearance of the AF2 magnetic phase. The continuous increase of the polarization below 3.0(1) K is still unclear. Note that the polarization along a undergoes the same accidents as P_b, but in a smaller scale, that can be due to a small misalignment of the sample.

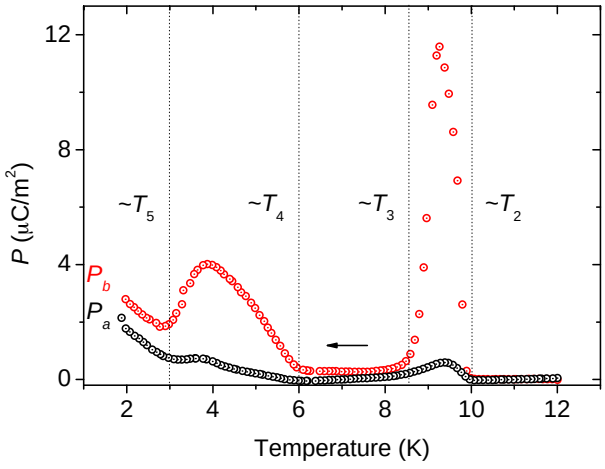

FIGURE 8.13: Temperature dependence of spontaneous electric polarization along the principle crystallographic directions measured while the temperature was decreasing.

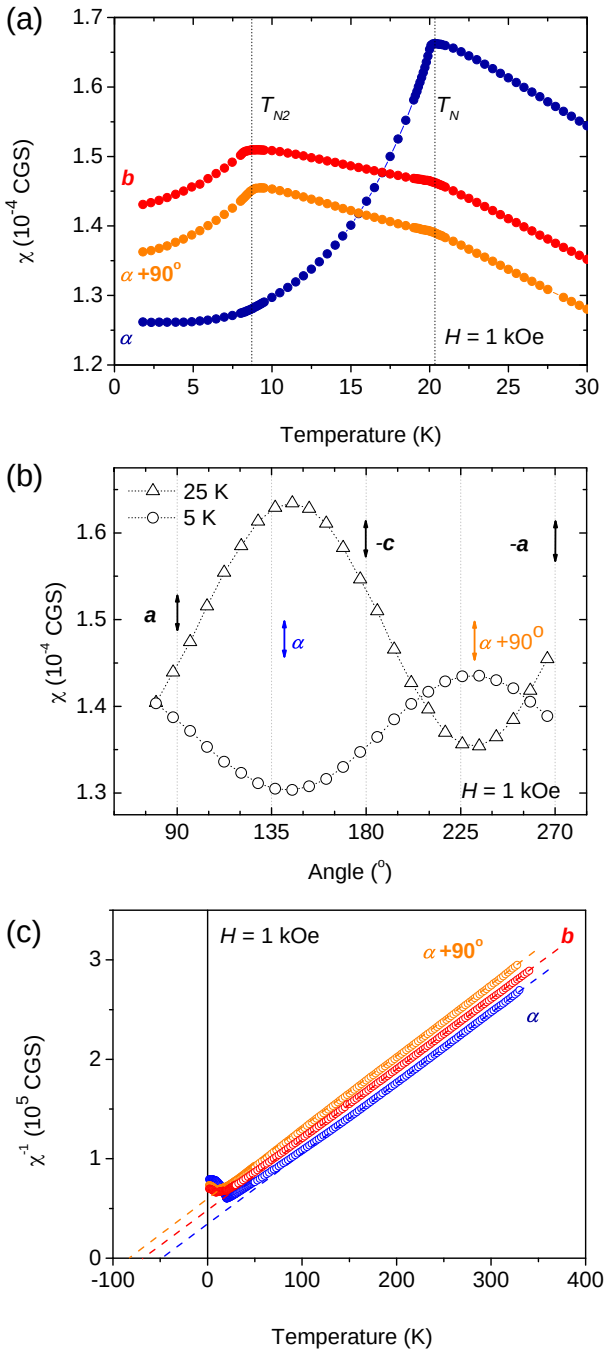

FIGURE 8.14: (a) Temperature dependence of susceptibility along the b axis and along two particular directions within the ac plane, namely for field applied at an angle α of about 37° with respect to the c axis and for field perpendicular to it; (b) angular dependencies of susceptibility in $H = 1$ kOe within the ac plane, at 25 K and 5 K; (c) temperature dependence of the inverse susceptibility.

8.4 $Mn_{0.80}Co_{0.20}WO_4$

8.4.1 Bulk magnetic response

Figure 8.14(a) presents the temperature variation of dc susceptibilities along the *b* axis and along two particular directions within the *ac* plane, namely for field applied at an angle α of about 143° with respect to the *c* axis (named α axis) and for field perpendicular to it. For those two orientations it was found that the susceptibilities at $\sim$ 20 K have the highest and the lowest values, respectively. This is confirmed by the angular dependencies of the susceptibility measured in magnetic field of 1 kOe rotating within the *ac* plane, shown in Fig. 8.14(b). At 25 K, above T_N, the angular dependency of the magnetic susceptibility along the easy (α) and hard (α+90°) directions exhibits its maximum and minimum, respectively, whereas below T_N the situation is inverted. The difference of the susceptibilities in Figs. 8.14(a) and 8.14(b) is due to the small contribution from the rotator. The susceptibility along any other direction in the crystal was found to be a superposition of the three orientations presented in Fig. 8.14(a). The peculiarity at 20.2(2) K, clearly visible in the susceptibility along all the directions, could be naturally attributed to the Néel temperature, T_N. Another susceptibility anomaly at 8.6(3) K, which is evident for the two orientations perpendicular to the α axis, evidences a change in the magnetic structure. Within the experimental resolution no unambiguous fingerprint of this transition was detected in the susceptibility along the α direction.

As seen from Fig. 8.14(c), the anisotropy observed at T_N persists in the paramagnetic region with all the three inverse susceptibilities becoming parallel straight lines at high enough temperatures where the Curie-Weiss law applies. This results in significant differences in the asymptotic paramagnetic temperatures, Θ_P, obtained for the three directions: Θ_P = -70(2) K along the *b* axis, Θ_P = -48(2) K for the α orientation, and Θ_P = -83(2) K for the orientation perpendicular to α within the *ac* plane. Within the experimental errors, the effective magnetic moment was found to be the same for all the orientations 5.78(5) μ_B, a value which is somewhat higher than the one expected from the Mn^{2+} ions and the spin only contribution from the Co^{2+} ions (5.57 μ_B) and thus, suggests that the Co orbital moment is not completely quenched [43–45].

8.4.2 Neutron diffraction

Below the Néel temperature, T_N = 20 K, two magnetically ordered phases were found, one of which is characterized by a single propagation-vector, $\mathbf{k}_1$, and the other one by two vectors, $\mathbf{k}_1$ and $\mathbf{k}_2$. The centering of 20 reflections at 2 K concluded that $\mathbf{k}_2$ = [-0.211(1), $\frac{1}{2}$, 0.452(2)] is an incommensurate propagation vector, while on the contrary $\mathbf{k}_1$ = ($\frac{1}{2}$, 0, 0) is commensurate from T_N down to the lowest temperature. Figure 8.15(a) shows the evolution of two magnetic reflections characteristic of $\mathbf{k}_1$ and $\mathbf{k}_2$ with the temperature. When decreasing temperature, below 20 K the reflection related to $\mathbf{k}_1$ appears. Its intensity increases down to 8.5 K where there is a change in its evolution. At this point new reflections associated to $\mathbf{k}_2$ emerge. With further decreasing of the temperature, the intensity of the latter reflection increases whereas the intensity of the commensurate reflection slightly decreases.

Data collections were made in order to determine the magnetic structures at 2 K and 11 K. The parameters of the obtained magnetic structures are given in Table 8.4, the spin arrangements are plotted in Figs. 8.15(b) and 8.15(c) and the agreement plots are depicted below each magnetic model. The magnetic structure at 11 K is a collinear one, the so-called AF4 [125, 127]. The moments lay in the *ac* plane, along the easy-axis α that makes an angle θ_u = 142(2)$^\circ$ with the c^* axis, see Fig. 8.15(b). In the collinear AF4 order, the magnetic moments in the zigzag chains of octahedra running along the *c* axis are ferromagnetically coupled. Chains form ferromagnetic layers which extend parallel to the *bc* plane, and the adjacent layers along the *a* axis are antiferromagnetically coupled. The ordered moment observed at 11 K is 3.17(7) μ_B per magnetic atom.

The same set of reflections related to $\mathbf{k}_1$ revealed no difference (within the error bars) in the magnetic component associated to $\mathbf{k}_1$ at 2 K. However at that temperature there is an additional propagation vector and new magnetic reflections of the type $(hkl) \pm \mathbf{k}_2$ arise. The refinement of the 212 latter type of reflections let us conclude that the incommensurate part is an elliptical cycloid, the eccentricity of which is $\epsilon = 0.61$ according to the definition given in equation 8.1. The main axes of the cycloid are along the *b* axis and a direction in the *ac* plane that makes and angle ω = 55(1)$^\circ$ with the c^* axis ($\omega = \alpha + 90^\circ$). Therefore, the incommensurate part of the magnetic structure is rotating in a plane ($b\omega$) which is perpendicular to α (direction of the moments of the collinear component). The coexistence of two propagation vectors can thus be explained by a conical structure, as sketched in Fig. 8.15(c). Below T_{N2}, $\mathbf{m}_{conical} = \mathbf{m}_{AF2} + \mathbf{m}_{AF4}$ at each Mn/Co site. At 2 K the two components

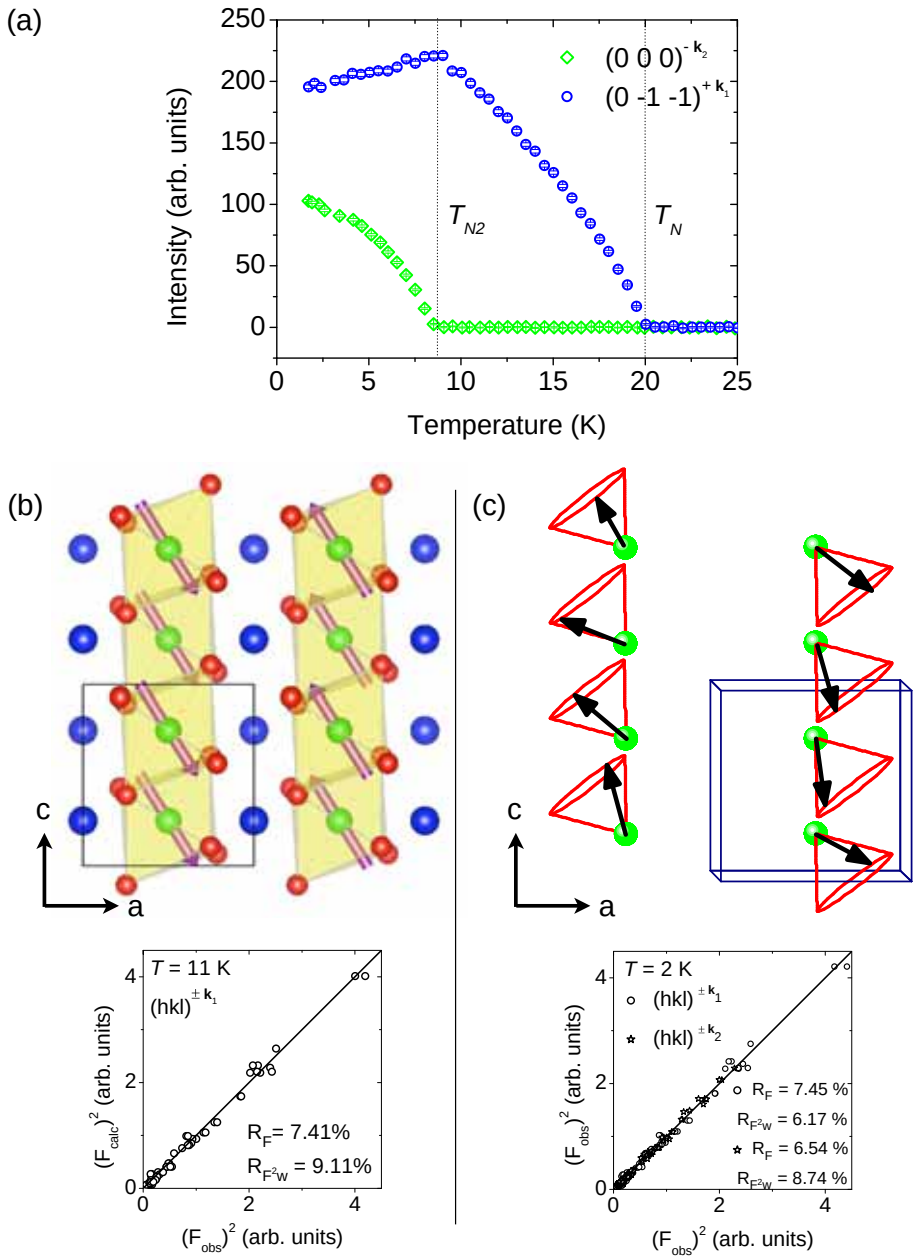

FIGURE 8.15: (a) Integrated intensities of two magnetic reflections as a function of the temperature (the error bars are smaller than the symbols). (b) and (c) show the magnetic structures of $Mn_{0.80}Co_{0.20}WO_4$ at 11 K and 2 K, respectively. The corresponding agreement plots of the refinements are plotted below each model.

are rather similar: m_{AF4} = 3.23 μ_B and 2.42$\mu_B \leqslant m_{AF2} \leqslant$ 3.05μ_B (since $\mathbf{m}_{AF2}$ is an elliptical helix). As a result, the maximum amplitude on the Mn/Co site is 4.44 μ_B. This value is practically the theoretical saturation moment expected [4.6 μ_B per (Mn,Co) site in $Mn_{0.80}Co_{0.20}WO_4$, having both Mn^{2+} and Co^{2+} in high-spin state].

Temperature		T = 11 K	T = 2 K	T = 2 K
Magn. phase		AF4	Conical	Conical
k		$(\frac{1}{2}, 0, 0)$	$(\frac{1}{2}, 0, 0)$	[-0.211(1), $\frac{1}{2}$, 0.452(2)]
Mn_1	$\Re(m)(\mu_B)$	3.15(2)	3.23(6)	3.05(3)
	ϕ_u	0°	0°	0°
	θ_u	142(2)°	143(2)°	55.0(9)°
	$\Im(m)(\mu_B)$			-2.42(4)
	ϕ_v			90°
	θ_v			90°
Mn_2		$\mathbf{u}_2^{x,z} = \mathbf{u}_1^{x,z}$ $\mathbf{u}_2^{y} = \mathbf{u}_1^{y} = \mathbf{v} = 0$	$\mathbf{u}_2^{x,z} = \mathbf{u}_1^{x,z}$ $\mathbf{u}_2^{y} = \mathbf{u}_1^{y} = \mathbf{v} = 0$	$\mathbf{u}_2 = -\mathbf{u}_1$ $\mathbf{v}_2 = -\mathbf{v}_1$
$\Delta\varphi$		0	0	$\frac{k_z}{2}$
R_{F^2}/%		8.90	8.37	6.86
R_{F^2w}/%		9.11	8.74	6.17
R_F/%		7.41	6.54	7.45
χ^2		26.2	25.4	4.37

TABLE 8.4: Parameters that describe the magnetic structures of $Mn_{0.80}Co_{0.20}WO_4$. Magnetic atoms Mn_1 and Mn_2 are located in the crystallographic unit cell at [$\frac{1}{2}$, 0.6847(5), $\frac{1}{4}$] and [$\frac{1}{2}$, 0.3153(5), $\frac{3}{4}$], respectively.

The alternative scenario that could also result in two coexisting propagation vectors, namely the one based on phase separation with distinct volume fractions, can be ruled out since, according to the experimental intensities, the atomic magnetic moment of one of the hypothetic phases would be unrealistically high. Indeed, if we assume that there are two equal volumes for the two phases, the collinear and the cycloidal structures, $V_{Tot} = 2V_{\mathbf{k}_1} = 2V_{\mathbf{k}_2}$, the magnetic moments should be multiplied by $\sqrt{2}$, resulting in a too large total moment at 2 K.

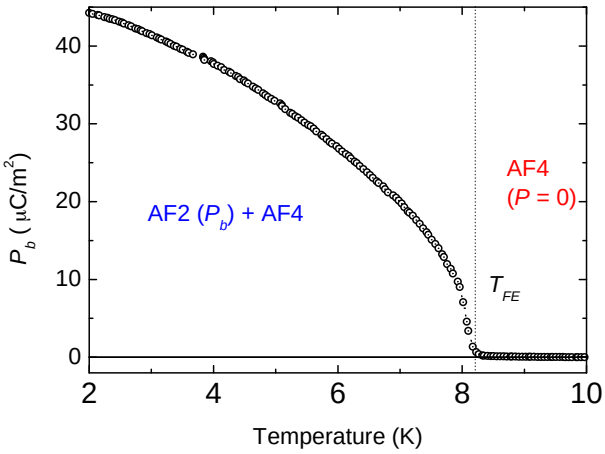

FIGURE 8.16: Temperature dependence of spontaneous electric polarization along b axis in $E = 0$. Data was collected while heating, after cooling the sample from the paraelectric state down to 1.9 K in poling field $E_p = 1.8$ V/cm.

8.4.3 Electric polarization

Spontaneous electric polarization was observed only along the b axis. It arises below $T_{FE} \approx 8.2$ K and increases up to 45 $\mu C/m^2$ at 2 K as shown in Fig. 8.16. The onset in the temperature dependence of the electric polarization corresponds to the observed anomalies in the magnetic susceptibility along the b axis and perpendicular to the easy axis at $\approx$ 8.6 K [Fig. 8.14(a)] as well as the onset of the incommensurate $(0\ 0\ 0)^{-\mathbf{k}_2}$ magnetic reflection [Fig. 8.15(a)]. Thus the observed conical spin structure can be also identified as a ferroelectric state with $\mathbf{P} \| b$ which is likely driven by the inverse Dzyaloshinskii-Moriya magnetoelectric interaction.

At first glance the existence of the $\mathbf{P} \| b$ polarization makes the cycloid part of the composed conical phase similar to the cycloidal ferroelectric phase AF2 in pure and slightly doped (Co 5%) $MnWO_4$ [87, 125, 126]. However, there is a principal difference between them. In $Mn_{0.80}Co_{0.20}WO_4$ the cycloidal component of the composed spin structure is developed below T_{FE} on top of the already existing and more stable collinear AF4 phase in which spins are oriented along the easy direction in the ac plane (142° with respect to the c^* axis). So, the appearance of the competing incommensurate cycloid AF2 ($\mathbf{k}_2$) spin order along easy direction is suppressed at low temperatures and it occurs in the directions being orthogonal to the spins in the existing AF4 spin order. Thus the AF2 spin order can appear only in the magnetically hard directions. This is clearly seen from our neutron

data revealing the main cycloid axes along b and perpendicular to the easy direction in the ac plane (ω axis at 55° from c^* axis). This circumstance, i. e. the competition between the magnetic anisotropy and the isotropic exchange interactions stabilizing the cycloidal structure, could explain the observed decreasing of the ferroelectric transition temperature from $\approx$ 12.5 K in pure $MnWO_4$ down to $\approx$ 8.5 K in $Mn_{0.80}Co_{0.20}WO_4$ and likely its further suppression and disappearance with increasing Co concentration.

8.5 $x-T$ phase diagram

Summarized below are the features that we have found in the x = 0.05, 0.10, 0.15 and 0.20 compositions of the $Mn_{1-x}Co_xWO_4$ family:

- $Mn_{0.95}Co_{0.05}WO_4$: Two magnetic transitions were detected by bulk magnetic measurements at T_N = 13.2(2) K and T_{N2} = 12.2(2) K that separate three distinct magnetic phases: the paramagnetic, the AF3, and the cycloidal AF2 phase. The two transition temperatures are very similar to T_{N2} and T_N in the pure composition (12.3 and 13.5 K, respectively). Both magnetic orders have the same periodicity, $\mathbf{k}$ = [-0.216(1), $\frac{1}{2}$, 0.461(1)]. At this low cobalt doping the collinear commensurate AF1 phase, characteristic of the ground state in pure $MnWO_4$ [87], is suppressed. The stability range of the AF3 order is so narrow and the ordered magnetic moments so small that after several attempts it was difficult to ensure that the sample was in the AF3 phase during the neutron data-collection and also to safely ascribe a magnetic model to describe the data. The AF2 magnetic structure is a cycloidal spin-arrangement in the ub plane, where u is within the ac plane about 13° from a (towards c). We observed that whilst temperature decreases, the magnetic anisotropy in the ub plane effectively diminishes as indicated by the decrease of the eccentricity of the elliptical envelope of the moments. This magnetic structure has the same symmetry as the AF2 phase of $MnWO_4$, and consequently has a unique polar axis, the b axis. Accordingly, the emergence of the cycloidal structure is linked to the appearance of the electric polarization along b.

- $Mn_{0.90}Co_{0.10}WO_4$: Bulk magnetic measurements revealed two magnetic transitions: T_N = 13.2(1) K and T_{N2} = 11.4(1) K. As for $Mn_{0.95}Co_{0.05}WO_4$ the AF3 phase is present in the crystal. In the collinear model for the AF3 phase the spins are located within the ac plane, about 34° from a towards -c, in contrast

to lower doped compositions. Our data refinement concluded that an additional spin component along the *b* axis is also plausible in the AF3 phase of this composition, even if its amplitude is rather small. Below T_{N2}, the multiferroic phase emerges, the symmetry of which differs from AF2-structure's, and does not allow any polarization along *b*, but within the *ac* plane. Therefore, the multiferroic phase of $Mn_{0.90}Co_{0.10}WO_4$ is named AF2′ instead of AF2. The latter is confirmed by the polarization measurements that show both P_a and P_c components of spontaneous electric-polarization below T_{N2} down to the lowest temperatures ($\sim$ 2 K).

◇ $Mn_{0.85}Co_{0.15}WO_4$: The magnetic behavior of this composition is the most complicated among the studied ones. The numerous and complex magnetic transitions below T_N = 16.7(2) K demonstrated the strong competition between distinct magnetic phases. In this case, the easy axis is located within the *ac* plane about 58° from *a* towards -*c*. Due to the strong peak overlap, only two collinear structures were studied in detail: AF1 and AF4. The former is similar to the AF1 of the pure compound but the moments are closer to *c*, close to the easy axis. Regarding the AF4 phase, it is a simple antiferromagnetic structure along *a* with the moments in the *ac* plane parallel to the magnetic easy-axis. In the paramagnetic region there is magnetic anisotropy found that is attributed to the substitution of Mn by the anisotropic Co.

◇ $Mn_{0.80}Co_{0.20}WO_4$: This crystal displays a coexistence of commensurate-collinear AF4 and incommensurate-cycloidal AF2 structures, which produces a ferroelectric ground state characterized by a conical antiferromagnetic spin order. The translational symmetry of the double-**k** magnetic structure is determined by two wave vectors $\mathbf{k}_1$ = ($\frac{1}{2}$, 0, 0) and $\mathbf{k}_2$ = [-0.211(1), $\frac{1}{2}$, 0.452(2)]. First, the collinear AF4 phase ($\mathbf{k}_1$) (similar to pure $CoWO_4$'s structure) appears at $T_N \approx$ 20 K and then, decreasing temperature below $T_{N2} \approx$ 8.5 K, this collinear phase coexists with the cycloidal AF2 spin structure ($\mathbf{k}_2$). This second modulation is accompanied by the appearance of ferroelectric polarization along *b* axis. We have found that spins in the AF4 phase are ordered along the easy direction in the *ac* plane, at an angle of 52° with respect to the *a* axis (towards -*c*) and does not change down to the lowest temperature reached (2 K). The collinear order is clearly reminiscent of the antiferromagnetic order in $CoWO_4$ (AF4, T_N = 55 K, $\alpha \approx 137°$) [116]. In the cycloidal AF2 structure observed below T_{N2} the spin ordering occurs perpendicular to the easy-axis α of AF4, i. e. in magnetically hard directions that makes this structure different compared to the pure cycloidal AF2 phase at lower cobalt concentrations. As in $Mn_{0.85}Co_{0.15}WO_4$, the magnetic anisotropy found in

the paramagnetic region is attributed to the substitution of manganese by the anisotropic cobalt.

The results obtained for the 5%-Co-doped crystal agree rather well with the description given by Song and co-workers in Ref. [126]. However, our results reveal more and new details. Following our superspace-formalism-backed idea for an alternative description of the AF3 structure of $MnWO_4$, we propose for first time a cycloidal but antiferroelectric magnetic structure for the AF3 phase not only for this 5%-Co composition but also for $Mn_{0.90}Co_{0.10}WO_4$. In Ref. [126], the magnetic structure and the electric polarization of $Mn_{0.90}Co_{0.10}WO_4$ were shown but, again, the details of the structure ($\mathbf{u}_{1,2}$ and $\mathbf{v}_{1,2}$ components of the magnetic moments) were not provided. Anyhow, their results are qualitatively consistent with ours. Regarding the $Mn_{0.85}Co_{0.15}WO_4$, the phase diagram proposed by Song *et. al.* in Ref. [125] ascribed just two magnetic phases to this material: one associated to $\mathbf{k}_4$ wave vector and the other one to the co-existence of $\mathbf{k}_2$ and the former. On the contrary the number of propagation vectors that we found is four ($\mathbf{k}_1$, $\mathbf{k}_2$, $\mathbf{k}_4$ and $\mathbf{k}_5$) coinciding with those detected by Chaudhury *et. al.* in Ref. [127], but not with the five found by Feng and co-workers in Ref. [130]. Nevertheless, we have seen up to five characteristic temperatures that could be ascribed to magnetic transitions instead of just three as observed in Ref. [127].

The recent work done by Feng *et. al.* [130] and Liang *et. al.* [131] consider that the AF5 structure is the so-called AF2′ of the $Mn_{0.90}Co_{0.10}WO_4$. The AF2′ gives rise to the polarization within the *ac* plane. Though, in $Mn_{0.85}Co_{0.15}WO_4$, where both $\mathbf{k}_2$ and $\mathbf{k}_5$ exist, there is not evident polarization within the *ac* plane. Nevertheless, they suggest neutron-diffraction experiments to really verify their proposal. In the lack of any neutron data, we consider that the AF2′ and the AF5 magnetic phases are independent. From our measurements the temperature range for the AF1 phase in the 15%-Co-doped sample is slightly bigger than that given in Ref. [131]. The AF4 and AF1 phases of $Mn_{0.85}Co_{0.15}WO_4$ have also been determined in this work. Last but not least, the magnetic structures of $Mn_{0.80}Co_{0.20}WO_4$ have been studied for the first time and the results have been corroborated by Feng *et. al.* in Ref. [130].

This work is limited to the study of just five family members of the $Mn_{1-x}Co_xWO_4$ solid solution. For that reason, the borders between magnetic phases (in the x direction of the phase diagram) are not definitely established. Nevertheless, the phase diagram plotted in Fig. 8.18 shows the temperatures at which each composition undergoes a magnetic transition (red circles) obtained from our

bulk magnetic data and the points at which the magnetic structures have been refined (black crosses). This information is on top of the $x - T$ phase diagram proposed for $Mn_{1-x}Co_xWO_4$ by Liang *et. al.* in Ref. [131].

8.6 Evolution of the easy axis

The evolution of the orientation of the easy magnetization directions within the *ac* plane with Mn^{2+} substitution by the anisotropic Co^{2+} ions is summarized in Fig. 8.17. One can observe how the increase of cobalt in the composition changes the direction of the easy axis. In the extreme cases, i. e. in $MnWO_4$ and $CoWO_4$, the easy axis is located about 35° from *a* axis (towards *c*) and about 45° from *a* axis (towards -*c*) respectively, see Refs. [87, 116]. From our investigation we have seen that just 15% of cobalt is enough to fix the easy axis about 10° from its location in the pure $CoWO_4$.

The observed finite values of the susceptibility along the easy directions of all the compositions at low temperature differ qualitatively from those of the simple collinear antiferromagnet (where parallel susceptibility vanishes at low temperature) and are somewhat reminiscence of the susceptibility behavior in screw-type magnetic structures [48–50].

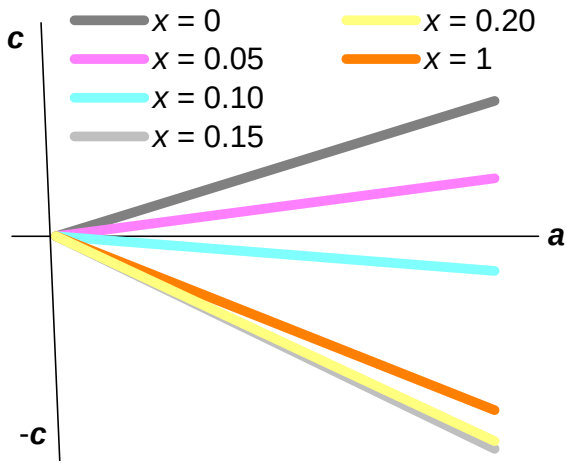

FIGURE 8.17: Magnetic easy-axes of the $Mn_{1-x}Co_xWO_4$ family plotted in the *ac* plane.

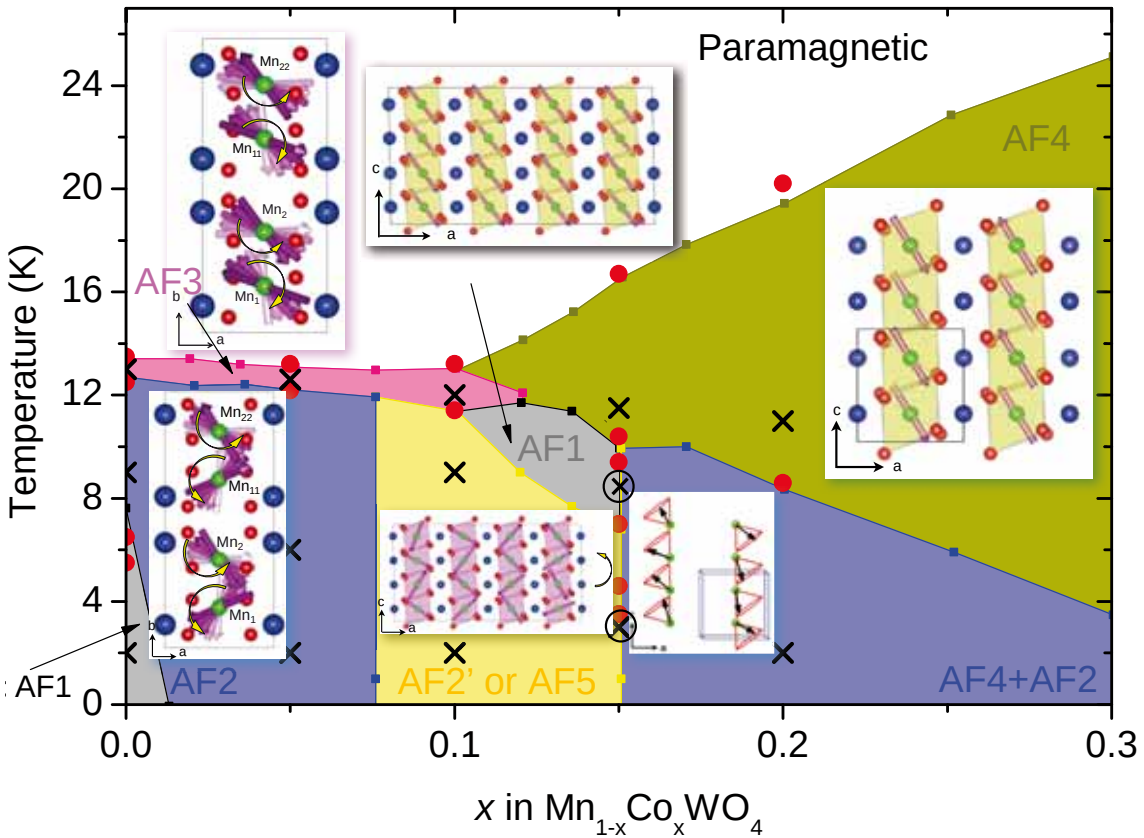

FIGURE 8.18: Phase diagram proposed by Liang *et. al.* in Ref. [131]. Red circles (transition temperatures) and black crosses (magnetic structure determined) are our contribution. Circles crossed mean that there is coexistence of phases as found in our data.

8.7 Evolution of the orientation of the electric polarization

Within the microscopic scheme of spin current or inverse Dzyaloshinskii-Moriya model, the expected electric polarization can be expressed as

$$\mathbf{P} \sim \mathbf{r}_{ij} \times (\mathbf{S}_i \times \mathbf{S}_j) \tag{8.2}$$

where $\mathbf{r}_{ij}$ is the vector between two neighboring spins, $\mathbf{S}_i$ and $\mathbf{S}_j$. Note that, in the multiferroic phase of the studied compounds, two neighboring atoms along the b axis do not contribute to the polarization because the spins are antiparallel and thus, $\mathbf{S}_i \times \mathbf{S}_j$ is zero. Lets then calculate the contribution of the coupling between two neighboring Mn atoms in the chains (parallel to c), $\mathbf{P}_1$, and between two neighboring Mn atoms in distinct chains parallel to a, $\mathbf{P}_2$, in the multiferroic AF2 phase. For this calculation it is assumed that the unit cell is orthogonal for simplicity ($\beta = 90^\circ$). The orientation of each Mn_i magnetic moment in the unit cell can be expressed in the following way (see the relation between $\mathbf{m}_u$ and $\mathbf{m}_y$ in the refinement tables):

$$\begin{aligned}
\text{Case 1} \quad &\rightarrow \quad \text{Calculation within the chains along } c \\
i = 1 \quad &\rightarrow \quad \mathbf{S}_1 = m_{1u}\cos(2\pi\mathbf{k}\cdot\mathbf{R})\mathbf{u} + m_{1y}\sin(2\pi\mathbf{k}\cdot\mathbf{R})\mathbf{y} \qquad (8.3) \\
i = 2 \quad &\rightarrow \quad \mathbf{S}_2 = m_{1u}\cos[2\pi(\mathbf{k}\cdot\mathbf{R} + \frac{k_z}{2}) + \pi]\mathbf{u} + m_{1y}\sin[2\pi(\mathbf{k}\cdot\mathbf{R} + \frac{k_z}{2}) + \pi]\mathbf{y} \qquad (8.4)
\end{aligned}$$

$$\begin{aligned}
\text{Case 2} \quad &\rightarrow \quad \text{Contribution of the interchain interaction along } a \\
i = 1 \quad &\rightarrow \quad \mathbf{S}_1 = m_{1u}\cos(2\pi\mathbf{k}\cdot\mathbf{R})\mathbf{u} + m_{1y}\sin(2\pi\mathbf{k}\cdot\mathbf{R})\mathbf{y} \qquad (8.5) \\
i = 2 \quad &\rightarrow \quad \mathbf{S}_2 = m_{1u}\cos[2\pi(\mathbf{k}\cdot\mathbf{R} + k_x)]\mathbf{u} + m_{1y}\sin[2\pi(\mathbf{k}\cdot\mathbf{R} + k_x)]\mathbf{y} \qquad (8.6)
\end{aligned}$$

Taking into account that the direction u in the AF2 phase is within the ac plane ($\phi = 0$) and that the vectorial product of the spins is parallel to the normal of the rotation plane of the moments, $\hat{n}$,

$$\begin{aligned}
\mathbf{S}_1 \times \mathbf{S}_2 \quad &= \quad |\mathbf{S}_i \times \mathbf{S}_j|\hat{n} \\
\text{Case 1} \quad &\rightarrow \quad m_{1u}m_{1y}\sin(\pi k_z)(\sin\theta\hat{i} + \cos\theta\hat{k}) \qquad (8.7) \\
\text{Case 2} \quad &\rightarrow \quad m_{1u}m_{1y}\sin(2\pi k_x)(\sin\theta\hat{i} + \cos\theta\hat{k}) \qquad (8.8)
\end{aligned}$$

We will focus on Case 1. To calculate the electric polarization induced by the antisymmetric coupling of the spins, we have to take into account the $\mathbf{r}_{12}$ vector that

goes from Mn_1 to Mn_2

$$\mathbf{r}_{12} = -y\hat{j} + \frac{c}{2}\hat{k} \tag{8.9}$$

$$P_1 = C_1 m_{1u} m_{1y} \sin(\pi k_z)(-y\hat{j} + \frac{c}{2}\hat{k}) \times (\sin\theta\hat{i} + \cos\theta\hat{k}) \tag{8.10}$$

$$= C_1 m_{1u} m_{1y} \sin(\pi k_z)(-y\cos\theta\hat{i} + \frac{c}{2}\sin\theta\hat{j} + y\sin\theta\hat{k}) \tag{8.11}$$

where C_i is related to the spin-orbit coupling. Note that the contribution of the next Mn_2 Mn_{11} couple in the chain will be

$$P_1 = C_1 m_{1u} m_{2y} \sin(\pi k_z)(-y\cos\theta\hat{i} + \frac{c}{2}\sin\theta\hat{j} - y\sin\theta\hat{k}) \tag{8.12}$$

and therefore, the contribution of the Mn atoms within the zigzag chains is parallel to the b axis.

$$P_1 \parallel b = C_1 m_{1u} m_{1y} c \sin(\pi k_z)\sin\theta\hat{j} \tag{8.13}$$

On the other hand, the contribution of the interchain coupling results in

$$\mathbf{r}_{12} = a\hat{i} \tag{8.14}$$

$$P_2 = C_2 m_{1u} m_{1y} \sin(2\pi k_x)(a\hat{i}) \times (\sin\theta\hat{i} + \cos\theta\hat{k}) \tag{8.15}$$

$$P_2 \parallel b = -C_2 m_{1u} m_{1y} a \sin(2\pi k_x)\cos\theta\hat{j} \tag{8.16}$$

In conclusion, the total electric polarization will come from the sum of both P_1 and P_2, at least.

$$P = P_1 + P_2 = m_{1u} m_{1y}(C_1 c \sin(\pi k_z)\sin\theta - C_2 a \sin(2\pi k_x)\cos\theta)\hat{j} \tag{8.17}$$

When the rotation plane gets close to the ac plane θ becomes smaller and hence, the electric polarization too, see Fig. 8.20(a). According to Sagayama *et. al.* in Ref. [96] there is a critical value for θ that makes unstable the polarization along b, and therefore it flops to the ac plane, the so-called AF2' phase (or AF5 in [130, 131]). This critical value, θ_c, corresponds to certain cobalt concentration x_c, which should be $0.05 < x_c < 0.10$ ($x_c = 0.075$ according to Refs. [130, 131]).

If we consider that the $\hat{n}$ vector it is not restricted to the ac plane ($\sin\theta\cos\phi\hat{i} + \sin\theta\sin\phi\hat{j} + \cos\theta\hat{k}$), then P_1 and P_2 have a more general expression:

$$P_1 = C_1 m_{1u} m_{1y} c \sin(\pi k_z)(-\sin\theta\sin\phi\hat{i} + \sin\theta\cos\phi\hat{j}) \tag{8.18}$$

$$P_2 = C_2 m_{1u} m_{1y} a \sin(2\pi k_x)(-\cos\theta\hat{j} + \sin\theta\sin\phi\hat{k}). \tag{8.19}$$

Note that for 10%-Co-doped composition $\hat{n} = b$ ($\theta = 90$ and $\phi = 90$) and therefore P is constrained to the ac plane.

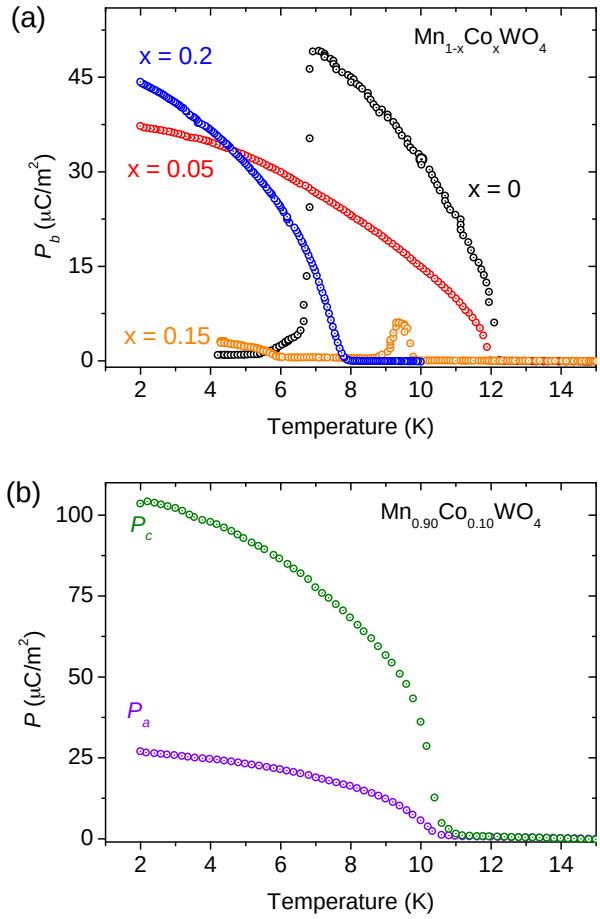

FIGURE 8.19: Electric polarization of the x = 0, 0.05, 0.10, 0.15 and 0.20 compositions of the $Mn_{1-x}Co_xWO_4$ family.

In Refs. [130, 131] it is suggested that once the polarization is within the *ac* plane (AF2′ or AF5), with increasing the concentration of cobalt the rotation plane of the moments rotate continuously around the a axis so that the electric polarization does it too ($\theta < 90^\circ$ or/and $\phi < 90^\circ$). Hence, P_a and P_c decrease with increasing x. However, if it was so, the polarization along b should increase and the latter is not observed, which is attributed to an accidental cancelation of the contribution to P_b coming from P_1 and P_2. Anyhow, according to Feng and Liang the decrease of the P_a and P_c components, again makes the AF5 phase unstable flipping the electric polarization towards b at concentrations of cobalt above $x_{c2} \sim 0.135$. These two groups locate the $x = 0.15$ compound just in the boundary, and therefore they consider that the AF5 phase that appears should give rise to

very small (even not measurable) electric polarization within the ac plane, assuming that $\theta << 90^\circ$ or/and $\phi << 90^\circ$.

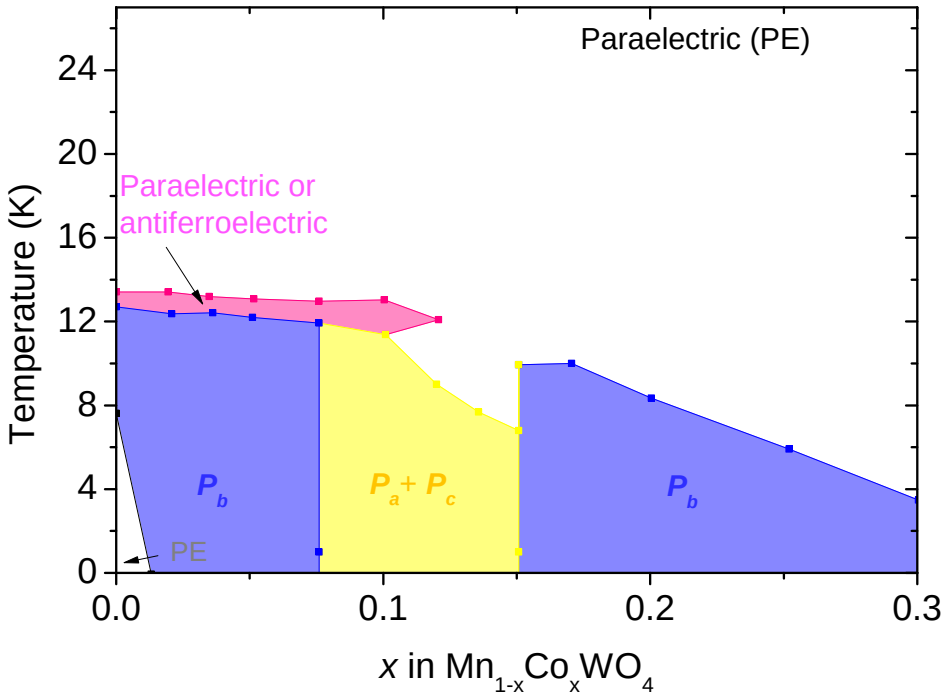

FIGURE 8.20: Phase diagram of $Mn_{1-x}Co_xWO_4$ taking into account the electric order, based on the phase diagram proposed by Liang *et. al.* in Ref. [131] to locate the boundaries.

From our point of view, it is not clear the AF2′ and AF5 phase are the same. The point symmetry of the AF2′ phase (present in $Mn_{0.90}Co_{0.10}WO_4$) is $m1'$, since the data can be refined using the superspace group $Xc1'(\alpha 0\gamma)ss$ that arises from the superposition of two mG_2 magnetic modes, see Appendix E. This phase is not allowed to give rise to macroscopic electric polarization along the b axis. So, if the rotation plane of the spins would rotate around a as suggested by Liang in Ref. [131], the polarization along b must be compensated for every θ and ϕ values in equations (8.18) and (8.19). Otherwise, the coexistence of polarization along a, b and c axes requires either a phase separation, or the point symmetry $11'$, situation in which the number of parameters free for the refinement would be doubled. Then, if there is any rotation of the plane as suggested by Liang *et. al.* [131] the symmetry of the system would change and consequently the multiferroic AF2′ phase and AF5 phases would not be equal.

8.8 Summary and conclusions

We have contributed to precise the $x - T$ phase diagram of $Mn_{1-x}Co_xWO_4$. Detailed descriptions of the magnetic structures of several concentrations have been provided together with a careful study of the bulk magnetic properties and the electric polarization. Our main contributions to the $x - T$ phase diagram are:

(i) Complete description of all the investigated magnetic structures, giving the Fourier components of moments of the magnetic atoms in the unit cell.

(ii) New cycloidal model which describes the AF3 phase.

(iii) Evolution of the cycloidal phase with decreasing temperature in x = 0.05 and 0.10: the eccentricity and the amplitude of the mayor and minor semi-axes.

(iv) Detection of the phase transitions of x = 0.15 and the low-temperature hysteresis.

(v) Antiferromagnetic-conical structure proposed for the first time in this family for the x = 0.20 composition.

(vi) Based on the symmetry considerations, we claim that the AF2' phase and the AF5 phases are not equal.

Therefore, we have confirmed the existence of new multiferroic phases varying the cobalt content, which give rise to electric polarization either along b axis or within the ac plane.

Apart from the contributions to the $x - T$ diagram, it has been found that the orientation of the easy-magnetic axis is close to the pure $CoWO_4$'s one with just 15% of cobalt. At this doping the AF4 phase (proper of $CoWO_4$) is already very stable, however at low temperatures competing phases emerge and coexist due to high degree of magnetic frustration. Indeed, we have observed that increasing the cobalt content increases the magnetic frustration, being 15%-cobalt-doped composition the most frustrated one of the series. Though, with further increasing the amount of cobalt, $x > 0.15$, the frustration decreases.

Chapter 9

Lattice anomalies at the ferroelectric and magnetic transitions in cycloidal $Mn_{0.95}Co_{0.05}WO_4$ and conical $Mn_{0.80}Co_{0.20}WO_4$ multiferroics

In this chapter we present a study of the thermal evolution of the cell parameters and a description of the lattice anomalies detected in the vicinity of the successive magnetic transitions of two multiferroic $Mn_{1-x}Co_xWO_4$ compounds ($x = 0.05$ and 0.20).

These two systems have been chosen for the study because they have different magnetic ground states, unlike magnetic transitions, but similar ferroelectric state. We have observed remarkable differences in the thermal evolution of the lattice parameters below 30 K. The comparison with the magnetic features provides evidence of distinct directional effects depending on the characteristics and symmetry of the magnetic order parameters at the paraelectric-ferroelectric transition.

Synchrotron X-ray powder-diffraction data were collected at ultra-high resolution ID31 diffractometer of the European Synchrotron Radiation Facility (ESRF, Grenoble). To reduce the absorption, a short wavelength was selected (λ = 0.40000(1) Å). The finely grounded samples were enclosed in a 0.5 mm di-

ameter borosilicate glass capillary, and a good powder averaging was ensured by appropriate spinning of the capillary in the beam. To collect low temperature patterns the capillary was placed in a continuous liquid-helium flow cryostat with rotating sample rod. Diffraction patterns down to 5 K were recorded at different temperatures (on cooling) after appropriate waiting time for a good thermal stabilization. The counting time was about 1.5 hours to have the desired statistics over the angular range 4° to 42° degrees in 2θ.

9.1 Lattice evolution in $Mn_{0.95}Co_{0.05}WO_4$

As it has been discussed in Chapter 8, magnetic susceptibility measurements performed in $Mn_{0.95}Co_{0.05}WO_4$ single crystal [plotted in Fig. 9.1 for the field applied along *b* axis] indicate only two transitions (at T_N = 13.2 K and T_{N2} = 12.2 K), which separate three distinct magnetic phases: paramagnetic (PM), AF3, and the cycloidal AF2. The two latter with $\mathbf{k}$ = [-0.216(1), $\frac{1}{2}$, 0.461(1)]. We have observed that at this low Co doping the collinear commensurate order (AF1) characteristic of the ground state in pure $MnWO_4$ is suppressed and that the transition temperatures in $Mn_{0.95}Co_{0.05}WO_4$ are very similar to T_{N2} and T_N in the pure composition (12.3 K and 13.5 K, respectively).

The low temperature cycloidal phase of $Mn_{0.95}Co_{0.05}WO_4$ displays the same characteristics as AF2 phase in $MnWO_4$. The main difference between AF2 in $Mn_{0.95}Co_{0.05}WO_4$ and $MnWO_4$ is the decrease of the angle between the easy plane and *a* axis in the former, see either Chapter 8 or Ref. [126]. Namely, the cycloidal plane is parallel to the *b* axis and the angle between the plane and the *a* axis is of about 15° in $Mn_{0.95}Co_{0.05}WO_4$, smaller than in $MnWO_4$ ($\approx 34^\circ$). Two projection of the cycloidal order are depicted in Fig. 9.1. Remember that the ground state of the 5%-Co sample is ferroelectric with the electric polarization along *b* axis, as predicted by the point symmetry of the superspace group, see Chapter 8.

Figure 9.2(a) depicts the evolution of *a*, *b*, and *c* parameters of the 5%-Co crystal obtained in the profile matching. As seen in Fig. 9.2(a), as temperature decreases approaching the transition into the incommensurate AF3 order, a magnetoelastic anomaly appears in the paramagnetic region at the vicinity of the transition temperature of T_N ($\approx$ 13.3 K), as signaled by the small but clear downturn in the evolution of *a*, *b*, and *c*. These parameters suddenly contract below 14 K, apparently in a rather isotropic manner. Note that this spin induced strain disappears exactly at T_N, and cell parameters sharply relax at entering of the AF3 magnetic order,

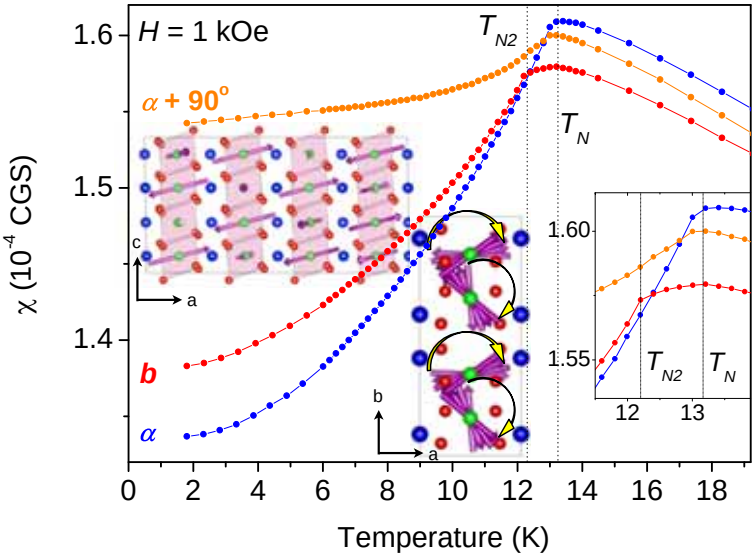

FIGURE 9.1: Magnetic susceptibility of $Mn_{0.95}Co_{0.05}WO_4$ single crystal (cooling and heating cycle, 1 kOe), measured with the magnetic field applied along a, b and c axes. The multiferroic structure present below T_{N2} is projected along b and c axes.

recovering approximately their (larger) values. From data in Fig. 9.2(a), the spin induced changes in cell parameters correspond to $\Delta a \approx \Delta c \approx -1.3(4) \times 10^{-4}$ Å and $\Delta b \approx -1.7(4) \times 10^{-4}$ Å. Despite the fact that, within our experimental accuracy, these lattice anomalies associated to the order-disorder magnetic transition look rather similar along the three axes, a certain degree of anisotropy in the observed lattice strain cannot be discarded. Decreasing further the temperature no clear effects on the lattice were detected across T_{N2} ($\approx$ 12.5 K) or down to the lowest temperature.

The evolution of $\beta(T)$ (the angle characteristic of the monoclinic $P2/c$ cell) is shown in Fig. 9.2(b) together with the behavior of the unit cell volume. The angle β in this compound evolves linearly in the temperature range shown in the figure, increasing with temperature at a rate $2.4 \times 10^{-4\circ}/K$. Therefore, within experimental errors, we do not appreciate any anomaly or deviation related to the successive magnetic phases. An anomalous volume contraction within the paramagnetic regime precedes the AF3 spin order. Concomitant with the onset of this magnetic order, the strain energy accumulated in the compressed cell is released and the volume abruptly expands to achieve again its normal size. Finally, we have not detected apparent volume anomalies on going from the AF3 to the AF2 phase, at T_{N2}. In the AF2 phase (below T_{N2}) Fig. 9.2(a) shows that thermal con-

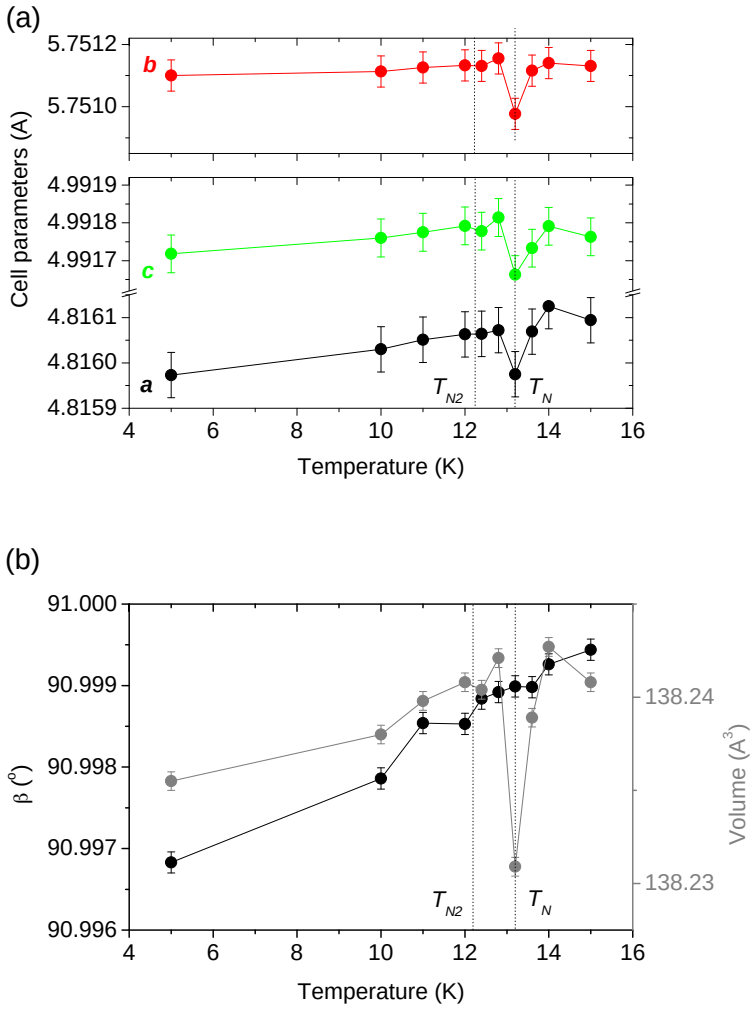

FIGURE 9.2: Evolution of the cell parameters of $Mn_{0.95}Co_{0.05}WO_4$ as a function of the temperature: (a) a, b and c, (b) β and unit cell volume.

traction on cooling is bigger for a and c axis than for b axis. This difference is reminiscent of the distinct behavior of b reported from thermal expansion measurements on $MnWO_4$ by Chaudhury *et. al.* [95]: they observed a weak negative expansion of b between T_{N1} and T_N. But the evolution of β was not determined and its contribution to these thermal expansion data obtained using a capacitance dilatometer is unknown. In $MnWO_4$ these authors reported a variation of the expansion coefficients at T_N and anisotropic step-like changes at T_{N1} = 7.5 K [95] ($\Delta a/a = -3 \times 10^{-5}$, $\Delta c/c = 1 \times 10^{-5}$, $\Delta b/b = -1 \times 10^{-5}$ at the entering of the reentrant paraelectric AF3, which has been suppressed in $Mn_{0.95}Co_{0.05}WO_4$).

9.2 Lattice evolution in $Mn_{0.80}Co_{0.20}WO_4$

Increasing the cobalt content from $x = 0.05$ to 0.20 in $Mn_xCo_{1-x}WO_4$ produces remarkable changes in the magnetic and lattice behavior of the system. According to the discussion in Chapter 8, the dc susceptibility of the $Mn_{0.80}Co_{0.20}WO_4$ single crystal along the b axis (χ_b), plotted in Fig. 9.3(a), signals two magnetic transitions at about T_N = 20.3 K and T_{N2} = 8.5 K. A simple collinear antiferromagnetic order with $\mathbf{k}_{AF4} = (\frac{1}{2}, 0, 0)$ sets below the Néel temperature, the so called AF4 structure, whereas at T_{N2} another incommensurate propagation vector arises $\mathbf{k}_{AF2} \approx (-0.21, \frac{1}{2}, 0.45)$, similar to the one of the pure $MnWO_4$ and $Mn_{0.95}Co_{0.05}WO_4$ composition. Accompanying the latter wave vector, spontaneous electric polarization appears along the b axis, i. e. in the same direction as in the ferroelectric phase of $Mn_{0.95}Co_{0.05}WO_4$ (below T_{N2} = 12.2 K). However, it is important to note that, increasing Co doping from x = 0 the polarization first reorients from the b axis to the ac plane in vicinity of x = 0.10. With further doping it flips again to the b axis for x = 0.20. Namely at $x \sim 0.10$ the cycloidal plane of spins flops by 90° from parallel to perpendicular to b axis, and then for $x \sim 0.20$ it returns back to the b axis. In addition, an important difference between magnetic orders in the ferroelectric phases of low (x = 0.05) and high (x = 0.20) doping states is that in $Mn_{0.80}Co_{0.20}WO_4$ the collinear commensurate $\mathbf{k}_{AF4}$ modulation (characteristic of the paraelectric phase at $T_{N2} < T < T_N$) coexists with the cycloidal magnetic modulation $\mathbf{k}_{AF2} \approx (-0.21, \frac{1}{2}, 0.45)$ that appears below T_{N2}. The coexistence of this two propagation vectors below T_{N2} produces a conical antiferromagnetic spin order in $Mn_{0.80}Co_{0.20}WO_4$ (Fig. 9.3).

The evolution of a, b and c parameters determined from profile matching procedure in this compound are shown in Fig. 9.4(a) and they exhibit a non-monotonous evolution below 30 K. Two separate small anomalies are perceived coinciding with the magnetic transitions at T_N and T_{N2}. These three parameters increase slightly on cooling across the paramagnetic-to-AF4 transition, and the observed changes are very isotropic: $\Delta a/a \approx 1.5 \times 10^{-5}$, $\Delta c/c \approx 2.2 \times 10^{-5}$, $\Delta b/b \approx 1.7 \times 10^{-5}$. Other changes were observed on further cooling across the ferroelectric temperature T_{N2}. There is a sudden change of slope below 9 K indicating a superior thermal contraction: a and b parameters decrease faster, whereas the change in c seems smaller. Figure 9.4(b) plots both the volume of the unit cell in $Mn_{0.80}Co_{0.20}WO_4$ across the two magnetic transitions and the obtained evolution of the monoclinic angle $\beta(T)$. Small but clear magnetoelastic effects are apparent when looking at the evolution of the β angle and the cell volume. The characteristic

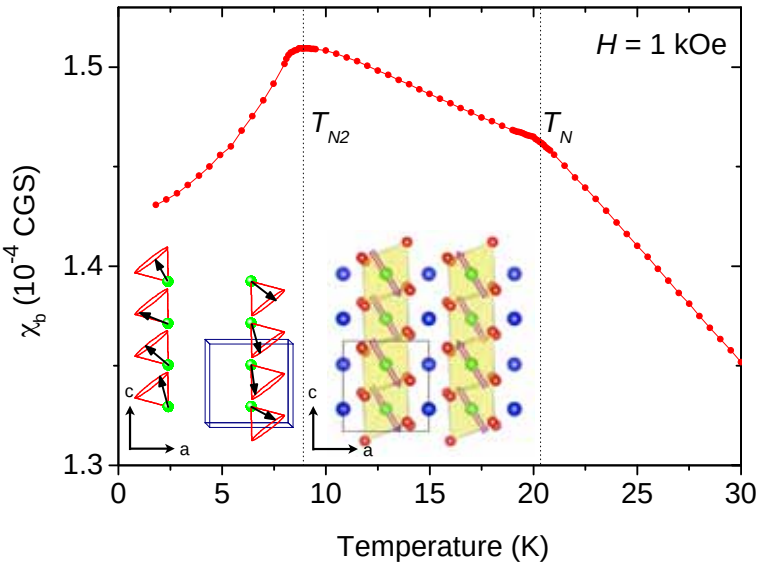

FIGURE 9.3: Evolution of the cell parameters of $Mn_{0.95}Co_{0.05}WO_4$ as a function of the temperature: (a) a, b and c, (b) β and unit cell volume.

volume of the intermediate AF4 phase (in the interval $\approx 10-20$ K) is bigger than in both the paramagnetic and the ferroelectric conical phases, respectively above T_N and below T_{N2}. So, a small ($\Delta V/V \approx 7.3 \times 10^{-5}$) but sharp volume expansion takes place at T_N (at the entering of the AF4 phase). By further cooling the extra volume of the intermediate phase seems to be released by appearing the conical ferroelectric phase.

9.2.1 Influence of the spiral plane on β at the ferroelectric transition

The monoclinic distortion described by angle β decreases with increasing the cobalt content. The β value at 5 K is 90.9968(2)° for $x = 0.05$ and 90.8353(2)° for $x = 0.20$. The monoclinic angle shows a very different thermal evolution in these two multiferroics. They are compared in Fig. 9.5 below 30 K. Although the origin of the left and right axes differs in the figure, the scale of both y axis is exactly the same. The evolution above 10 K displays a very similar slope in both samples ($2.3 \times 10^{-4\circ}/K$ and $2.4 \times 10^{-4\circ}/K$, respectively). Regarding $Mn_{0.80}Co_{0.20}WO_4$ there are two visible anomalies coinciding with the successive magnetic orders. The first is seen as a small step across T_N ($\Delta\beta \approx -1 \times 10^{-3\circ}$ entering the AF4 phase). But more ap-

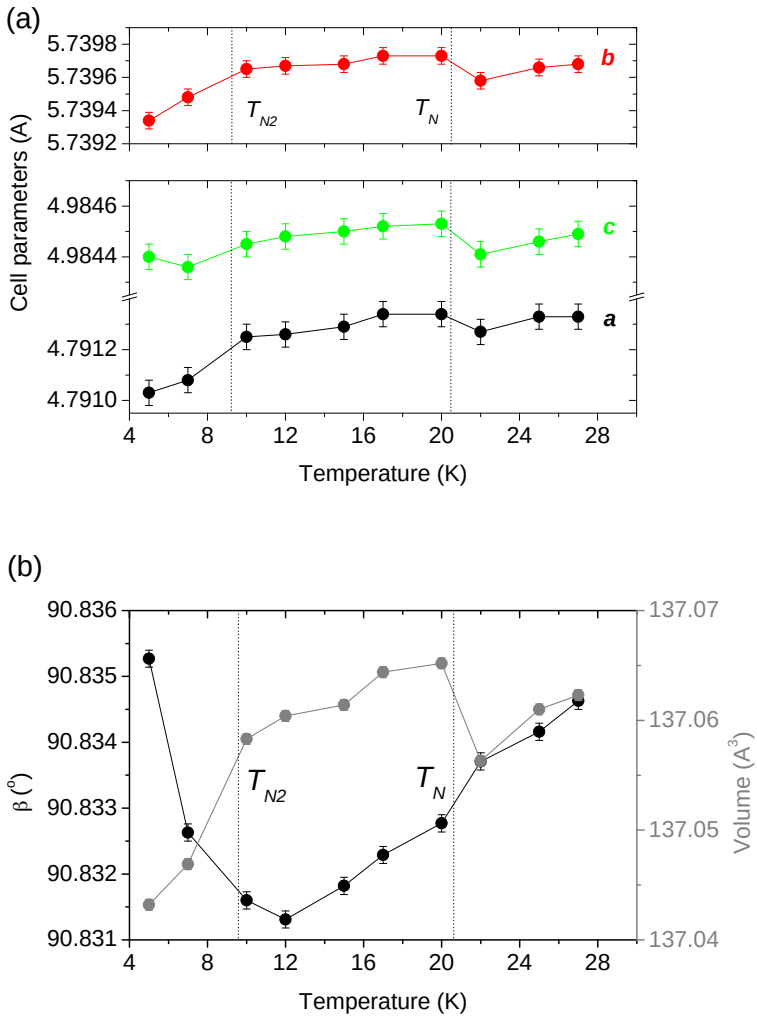

FIGURE 9.4: Evolution of the cell parameters of $Mn_{0.80}Co_{0.20}WO_4$ as a function of the temperature: (a) a, b and c, (b) β and unit cell volume.

pealing is the anomaly of β angle detected in $Mn_{0.80}Co_{0.20}WO_4$ when it enters the incommensurate magnetic order below 9 K. In spite of the normal thermal contraction (which acts decreasing β upon cooling), this angle suddenly starts increasing below T_{N2}. So, Fig. 9.5 shows that β (5 K) $> \beta$(25 K). In absolute terms the atypical augment is small ($\Delta\beta$ =0.0040(2)$^\circ$ in the interval 5 K - 12 K), but remarkable because this anomalous evolution should be forced by the exchange mechanism responsible for the P_b polarization below 9 K, and was not observed in the ferroelectric AF2 phase of $Mn_{0.95}Co_{0.05}WO_4$.

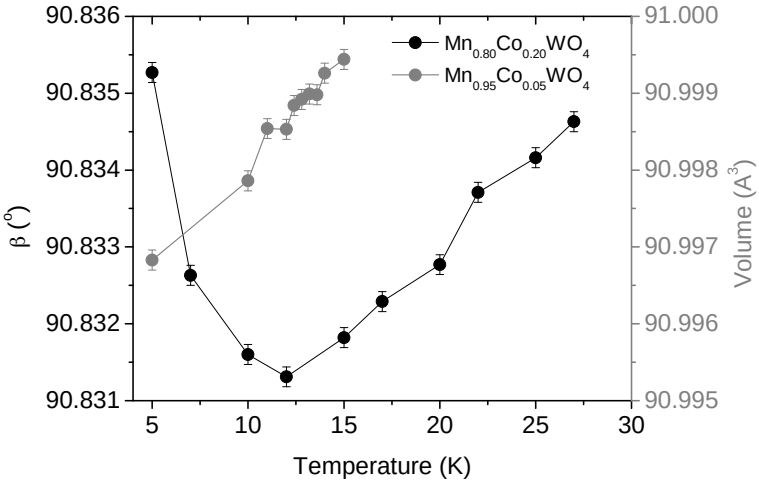

FIGURE 9.5: Evolution of the β of both $Mn_{0.95}Co_{0.05}WO_4$ and $Mn_{0.80}Co_{0.20}WO_4$.

9.3 Summary and conclusions

We have observed distinct lattice anomalies associated to some of the magnetic transitions in two selected compositions. The anomalies detected were rather small ($\Delta l/l \approx 10^{-5}$) but prove that the spin-lattice coupling in this family of materials is weak. The observed anisotropy of the lattice strain is also weak. We did not observe strongly anisotropic step-like changes of *a*, *b* and *c* parameters in any of the two compositions. In addition to changes of slope in the thermal evolution of the lattice, sudden modifications in the cell dimensions at some of the magnetic transitions were observed.

In $Mn_{0.95}Co_{0.05}WO_4$, the three *a*, *b* and *c* parameters abruptly contract below 14 K preparing the appearance of magnetic order. This anomalous volume contraction within the paramagnetic regime precedes the paraelectric AF3 spin order. At T_N = 13.2 K the spin induced strain energy accumulated in the compressed cell is released and the volume abruptly expands to adopt its normal size. In this compound we have not detected lattice anomalies on going from the AF3 to the AF2 phase.

Distinct small but unambiguous anomalies were observed in the lattice evolution of $Mn_{0.80}Co_{0.20}WO_4$ associated to the magnetic transitions at T_N = 20.3 K and T_{N2} = 9.1 K. In the first (at the paramagnetic-to-AF4 transition) there is an isotropic cell expansion on cooling. The volume of the intermediate AF4 phase (in the interval $\approx 10 - 20$ K) is bigger than in both the paramagnetic and low tempera-

ture phases. The temperature evolution of the monoclinic angle β in $Mn_{0.80}Co_{0.20}WO_4$ completely differs from the monotonous behavior of $\beta(T)$ in $Mn_{0.95}Co_{0.05}WO_4$. Surprisingly, the monoclinic angle β in $Mn_{0.80}Co_{0.20}WO_4$ systematically increases on cooling below T_{N2}.

The different behavior of the lattice found in the ferroelectric phases of these two compounds seems related to their distinct magnetic structures. In the AF2 structure of $Mn_{0.95}Co_{0.05}WO_4$ the spiral plane contains the b axis, and it is close to the a axis (about 15° to the a axis). The AF2 phase is developed from the AF3 order [$\mathbf{k} \approx (-0.22, \frac{1}{2}, 0.47)$], simply by a new magnetic component parallel to b which adopts the same modulation vector $\mathbf{k}_{AF2}$. The magnetic order in the ferroelectric phase of $Mn_{0.80}Co_{0.20}WO_4$ is a conical antiferromagnetic order, composed of a cycloidal component [$\mathbf{k}_{AF2} \approx (-0.21, \frac{1}{2}, 0.45)$] and a collinear AF4 component perpendicular to it [$\mathbf{k}_{AF4} = (\frac{1}{2}, 0, 0)$]. The rotation plane of the cycloidal component is parallel to b and forms an angle of about 35° with the a axis, see Chapter 8. It is important to notice that in the ferroelectric phase of the $x = 0.05$ sample the cycloidal plane contains the easy magnetic axis (defined by the collinear modulated AF3 order in this composition). However, for $x = 0.20$ the cycloidal plane is perpendicular to the magnetic anisotropy axis (defined by the collinear commensurate AF4 order). The emergence of a cycloid perpendicular to the easy magnetic axis of $Mn_{0.80}Co_{0.20}WO_4$, with a second propagation vector (incommensurate), and its strong interaction with the preexisting collinear commensurate AF4 component parallel to the easy axis can explain the qualitatively different lattice anomalies observed at the ferroelectric transition in the two compositions. In particular, the observed change at T_{N2} of the monoclinic angle β related to the non-diagonal (i. e. shift) u_{xz} component of the deformation tensor could be associated with the magnetoelastic coupling which include contributions from isotropic exchange and anisotropic interactions. Among latter there are anisotropic terms proportional to $u_{xz}L^x_{k_4}L^z_{k_4}$ and $u_{xz}L^x_{k_2}L^z_{k_2}$, where $L^{x,z}_{k_4}$ and $L^{x,z}_{k_2}$ are x, z ($a*$, $c*$) components of the order parameters in the AF4 and AF2 phases, respectively, which are determined by linear combinations of the corresponding Fourier components of Mn/Co spins in two sites of the crystallographic unit cell. Due to the orthogonality of $\mathbf{L}_{k_4}$ and $\mathbf{L}_{k_2}$ in the combine (AF4+AF2) conical structure the products $L^x_{k_4}L^z_{k_4}$ and $L^x_{k_2}L^z_{k_2}$ have different signs that could result in a bend of the $\beta(T)$ at T_{N2}. One cannot exclude the contribution to the $\beta(T)$ anomaly of exchange magnetoelastic terms such as $u_{xz}L^2_{k_4}$ and $u_{xz}L^2_{k_2}$ whose difference determines also the bend in the $\beta(T)$ at T_{N2}. Further studies are required to clarify the role of different mechanisms of the magnetoelastic coupling.

Part III

Magnetic-field-induced transitions

Chapter 10

Magnetic-field-induced transition on $MnWO_4$ with field applied along b axis

In this Part we will study the effects of the applied magnetic field on the magnetic structures. We begin with the parent $MnWO_4$. In particular, the magnetic structure of the so called "X phase" with a flopped electric polarization emerging from the zero-field cycloidal structure of $MnWO_4$ at high magnetic field applied along the b axis has been characterized.

The evolution of the magnetic and polar phase-diagrams of $MnWO_4$ under application of magnetic field have been explored in number of studies including neutron diffraction, ultrasound, polarization and magnetization experiments in pulsed high magnetic fields, see Refs. [103, 161–163]. This evolution naturally depends on the direction in which the field is applied (note that the magnetic principle axes are different from the crystallographic ones). It includes new high field phases and reveals remarkable magnetoelectric effects.

The evolution of the polar AF2 phase under magnetic field applied along the b axis is perhaps of highest interest and has been the most studied part of the phase diagram [31, 99–102, 108, 161]. It has been found [99] that the magnetic field stabilizes the AF1 and AF3 phases at the expense of the polar AF2 phase and most importantly that a new magnetic phase in which the spontaneous polarization changes from b to a axis emerges in a narrow temperature range, at fields

higher than about 11 T, see Fig. 10.1. Though as soon as the demonstration of this magnetoelectric effect took place, the determination of the magnetic structure of the new phase was anticipated [99], to the best of our knowledge up to now this has not been done and the term "X phase" continues to be in use [161].

We have characterized the magnetic structure of the so called X phase and tried also to shed some light on how it emerges from the zero-field AF2 phase. Some intriguing features of the field-induced transition from the AF2 to the neighboring AF1 and AF3 phases will be also presented.

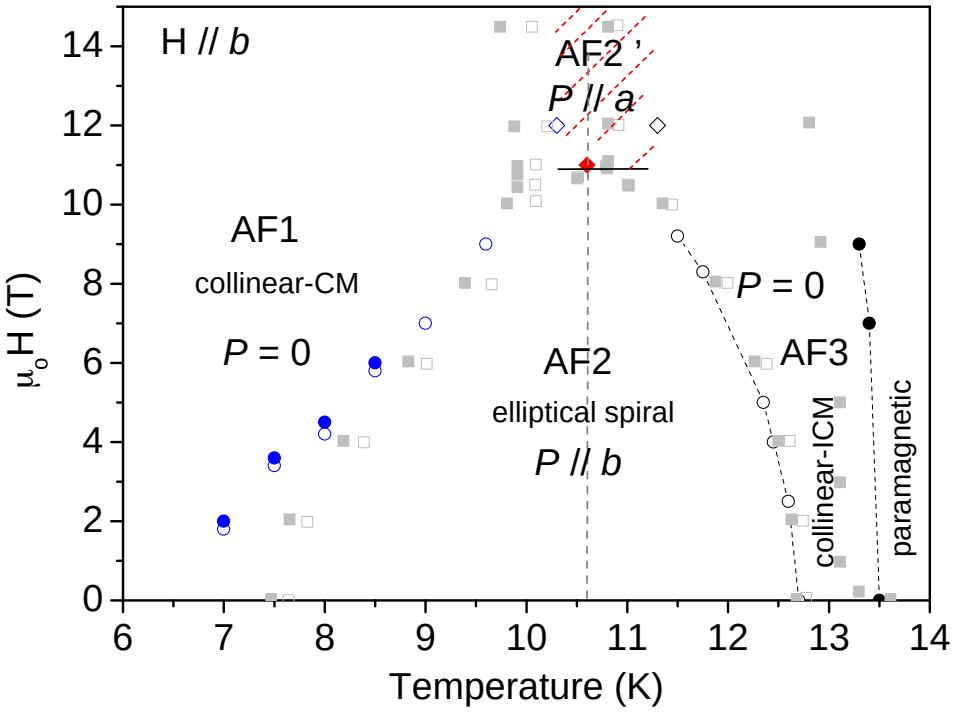

FIGURE 10.1: Magnetic phase diagram in magnetic field applied along the *b* axis as determined in this work (blue and dark circles are obtained from susceptibility data; rhombs from neutron diffraction) and from the polarization measurements reported in Ref. [99] (grey quadratic symbols).

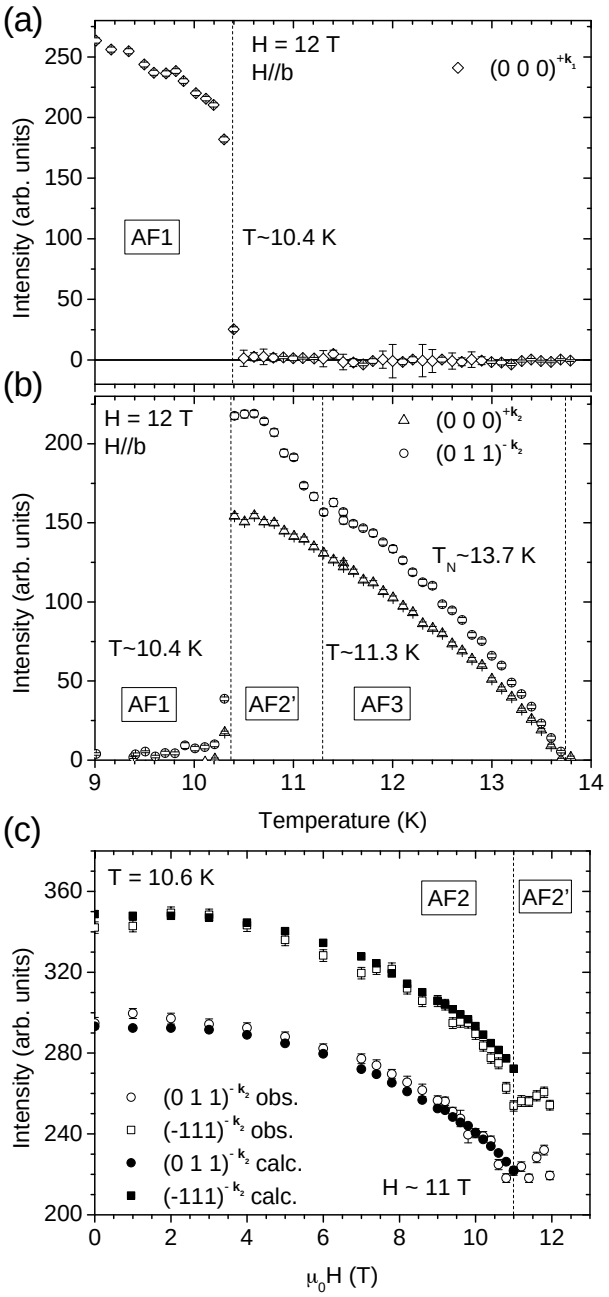

FIGURE 10.2: Temperature dependence of the integrated intensities of magnetic satellites at 12 T applied along the b axis. (a) commensurate reflection with $\mathbf{k}_1 = (\frac{1}{4}, \frac{1}{2}, \frac{1}{2})$ and (b) incommensurate reflections with $\mathbf{k}_2$ = [-0.221(1), $\frac{1}{2}$, 0.462(1)]; (c) Integrated intensities of magnetic satellites characteristic of the AF2 phase at 10.6 K as a function of magnetic field applied along b axis. Empty and full symbols are the experimental and the simulated data, respectively.

The neutron-diffraction experiment on a single crystal of $MnWO_4$ was performed on the CEA-CRG D23 diffractometer.

In order to explore the phase boundaries at high magnetic field three magnetic reflections were followed as a function of the temperature at 12 T (maximum field available): one commensurate reflection indexed as $(0\,0\,0)^{+\mathbf{k}_1}$ with $\mathbf{k}_1 = (\frac{1}{4}, \frac{1}{2}, \frac{1}{2})$ and two incommensurate indexed as $(0\,0\,0)^{+\mathbf{k}_2}$ and $(0\,1\,1)^{-\mathbf{k}_2}$ with $\mathbf{k}_2$ = [-0.221(1), $\frac{1}{2}$, 0.462(1)]. Figures 10.2(a) and 10.2(b) show the evolution of those magnetic reflections as a function of temperature and reveal three magnetic transitions. Upon increasing temperature, the first transition occurs at about 10.4 K, a point at which the intensity of the commensurate peak vanishes and incommensurate peaks emerge. At higher temperatures (about 11.3 K) the evolution of the incommensurate peaks changes, signaling another transition. Finally, above 13.7 K the intensity of all magnetic peaks becomes zero indicating the paramagnetic state. These magnetic transitions should be related to AF1, X and AF3 phases [99]. $T = 10.6$ K was chosen as an optimum temperature to collect data and determine the magnetic structure of the X phase. At this temperature, the integrated intensities of two magnetic reflections characteristic of AF2 and X phases were followed as a function of the magnetic field [Fig. 10.2(c)]. Both monitored peaks behave in a different manner in fields above and below 11 T, pointing a transition between the AF2 and X phases.

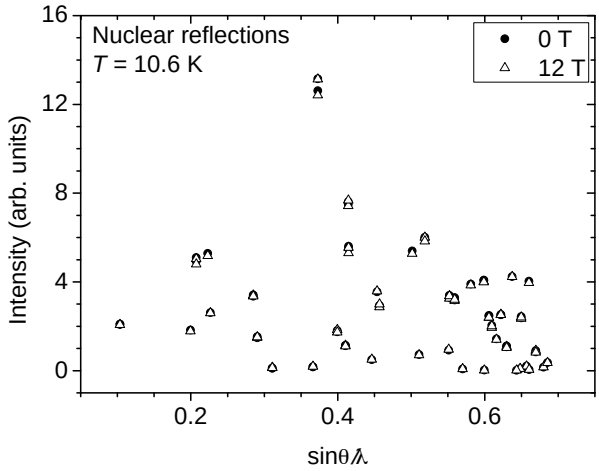

FIGURE 10.3: Integrated intensities of nuclear reflections collected at 0 T and 12 T (10.6 K). There is not any evidence of structural change nor ferromagnetic contribution.

Nuclear reflections were collected at 10.6 K at both, zero- and 12 T fields. From the refinement of the nuclear data at zero field it was found that the crystal

structure agrees with the one given in Ref. [87]. High field data does not unveil any change within the experimental error (see Fig. 10.3), indicating that the magnetic component aligned parallel to the field is negligible or not reflected in the bunch of collected reflections.

Then, 39 magnetic reflections were centered at 12 T and 10.6 K. The refinement of the propagation vector confirms that the modulation of the high field phase corresponds to a slightly different $\mathbf{k}_2$ = [-0.221(1), $\frac{1}{2}$, 0.462(1)] compared to the zero field $\mathbf{k}$ = [-0.216, $\frac{1}{2}$, 0.457]. The refined parameters are gathered in Table 10.1. The zero field structure (refined to check the data) agrees with the description given by Lautenschlager *et. al.* in Ref. [87], see Fig. 10.4(a). The high field magnetic structure is again an elliptical helix but oriented perpendicular to the external field, i. e. in the *ac* plane, as depicted in Fig. 10.4(c). The major semi-axis of the helix remains along the magnetic easy-axis. Note that, for sake of simplicity, in the above description of the magnetic structures we have omitted additional fine components determined by anisotropic (relativistic) interactions and allowed by the symmetry according to analysis presented in the Chapter 7.

Temperature		10.6 K	10.6 K	10.6 K	11.8 K
Field ($\mathbf{H} \parallel \mathbf{b}$)		0 T	9.5 T	12 T	12 T
Magnetic phase		AF2	AF2	X	AF3 (collinear)
$\mathbf{k}$		(-0.216, $\frac{1}{2}$, 0.457)	(-0.216, $\frac{1}{2}$, 0.457)	[-0.221(1), $\frac{1}{2}$, 0.462(1)]	(-0.216, $\frac{1}{2}$, 0.457)
Mn_1	$\Re(m)(\mu_B)$	-3.02(6)	-3.22(3)	-3.28(4)	-2.77(2)
	ϕ_u	0	0	0	0
	θ_u	59(1)°	58(1)°	56(1)°	56(1)°
	$\Im(m)(\mu_B)$	2.56(6)	1.78(4)	-1.23(4)	
	ϕ_v	90°	90°	0	
	θ_v	90°	90°	146(1)°	
Mn_2		$\mathbf{u}_2$ = - $\mathbf{u}_1$	$\mathbf{u}_2$ = - $\mathbf{u}_1$	$\mathbf{u}_2$ = - $\mathbf{u}_1$	$\mathbf{u}_2$ = - $\mathbf{u}_1$
		$\mathbf{v}_2$ = - $\mathbf{v}_1$	$\mathbf{v}_2$ = - $\mathbf{v}_1$	$\mathbf{v}_2$ = - $\mathbf{v}_1$	$\mathbf{v}_2$ = $\mathbf{v}_1$ = 0
$\Delta\varphi$		$\frac{k_z}{2}$	$\frac{k_z}{2}$	$\frac{k_z}{2}$	
R_{F^2}/%		8.89	7.90	9.20	14.1
R_{F^2w}/%		9.22	6.43	7.34	8.78
R_F/%		9.43	9.22	9.89	22.9
χ^2		11.4	4.64	4.67	2.17

TABLE 10.1: Parameters that describe the magnetic structures of $MnWO_4$ at zero field and under field applied along *b*. Magnetic atoms Mn_1 and Mn_2 are located in the crystallographic unit cell in [$\frac{1}{2}$, 0.68414(2), $\frac{1}{4}$] and [$\frac{1}{2}$, 0.3154(2), $\frac{3}{4}$], respectively.

In order to shed light on the way the high field phase evolves from the AF2 phase, data were collected at an intermediate field of 9.5 T. In this case, the structure is qualitatively the same as in AF2, however the component along the *b* axis

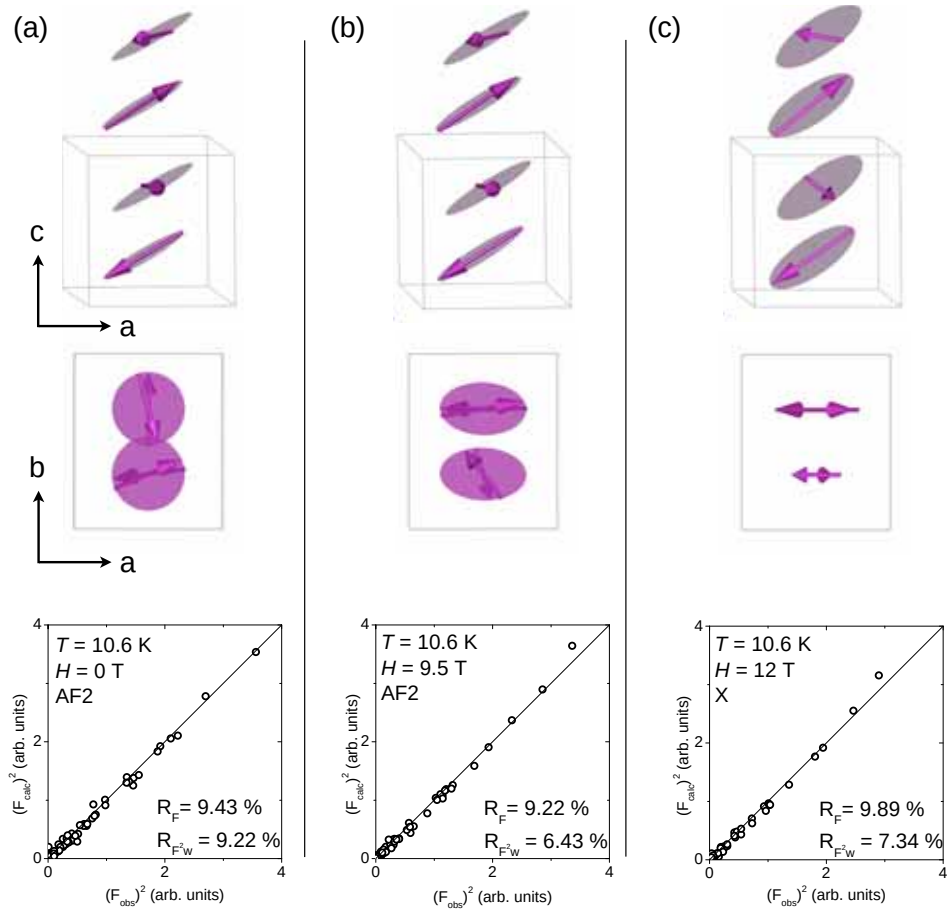

FIGURE 10.4: Magnetic structures under (a) zero field; (b) 9.5 T; and (c) 12 T field applied along b axis at 10.6 K.

(m_b) is considerably smaller than at zero field and the component along u is a little bit bigger. Therefore, the eccentricity of the helix becomes bigger with increasing field. The magnetic structure is sketched in Fig. 10.4(b). These results suggest that the transition under field occurs in an abrupt manner, in the sense that the main effect of the field on the magnetic structure is that m_b decreases with increasing field until a threshold value (achieved at about 10.5 T) where m_b flops to the ac plane. The evolution of the magnetic peaks with the field has been simulated under the former assumption and is reproduced in Fig. 10.2(c). Though we can not completely rule out a rotation of the plane in a narrow field interval between 9.5 T and the threshold field, if the transition would occur by a smooth rotation of the plane around the easy axis, the intensity of those peaks should first decrease and then increase, which is at odd with our experimental data. The suggested

way in which the high field phase evolves from the AF2 phase is reflected in the polarization changes observed upon the transition. As seen from Fig. 10.5, the P_b spontaneous polarization continuously decreases and P_a only slightly increases up to at least 10 T, followed by a rapid change in both components in the vicinity of the threshold field. It is believed [108] that the transition is of first order. The observed continuous decrease of the P_b, which has to be proportional to a b-spin component, is in good agreement with the observed decrease of m_b. The lack of clear discontinuity in P (Fig. 10.5) might be due to a small misalignment between the applied magnetic field and b axis. It is worth noting that, as demonstrated in Ref. [101], the polarization after the transition into the high field phase should be zero unless the field is slightly tilted.

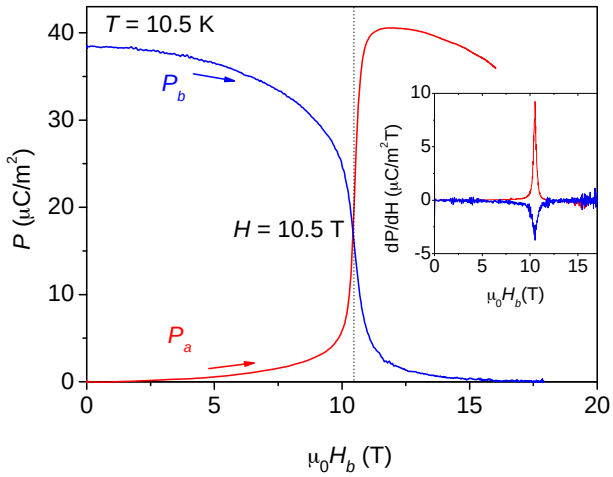

FIGURE 10.5: Polarization P along a and b crystallographic directions at 10.5 K as a function of field applied along the b axis and corresponding derivatives (insert).

With respect to the effect of the field applied along b axis in the AF3 sinusoidally modulated collinear structure, the refinement shows that this structure reminds basically invariant up to 12 T with respect to the zero field structure [87], with slightly more saturated magnetic moment.

Complimentary to the neutron diffraction study, ac-magnetic susceptibility has been recorded in superimposed dc-magnetic fields applied along the b axis. Though the maximum strength of the available dc-field (9 T) is below the threshold field (11 T), those bulk magnetic measurements helped us to further characterize the evolution of the AF2 upon application of magnetic field. The incremental susceptibility (plotted for better appreciation either as a function of temperature at a constant dc-field or as a function of dc-field at constant temperature) given

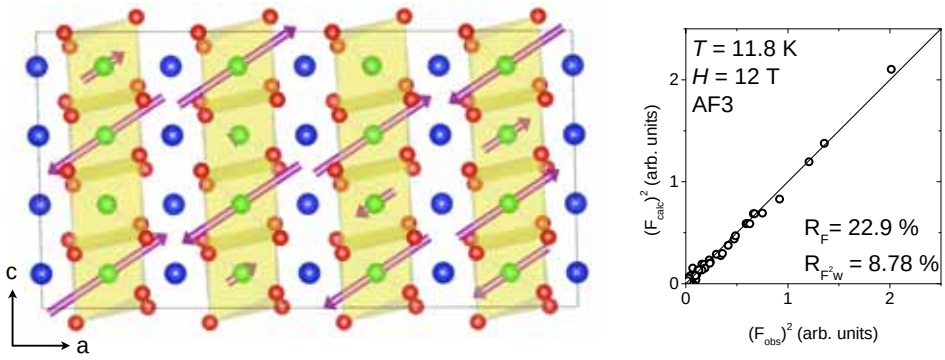

FIGURE 10.6: AF3 magnetic structure at 11.8 K under 12 T field along *b*.

in Fig. 10.7 confirms that magnetic field stabilizes the AF1 and AF2 phases at the expense of the polar AF1 phase, narrowing the temperature range in which the later exists. While the susceptibility of the AF1 and AF3 phases changes smoothly and almost linearly with the field (Fig. 10.7(b), the curves at 6.5 K and 13.5 K respectively) the susceptibility of the AF2 phase evolves in a non linear manner. The high field susceptibility at temperatures from the upper part of the zero field region of the AF2 phase (between about 11.5 K and 12.5K) cross the AF3 susceptibility, form a maximum and finally merge the AF3 susceptibility. This behavior is compatible with AF2 to AF3 field-induced transition. On the other hand, the high field susceptibility at temperatures from the lower part of the zero field region of the AF2 phase (between about 7 K and 9.5 K) merge the AF1 phase susceptibility, reflecting field-induced transition from AF2 to AF1 phase. The corresponding transitions determined as the point at which the incremental susceptibility merge the corresponding AF1 or AF2 curves, Fig. 10.7, are plotted on the phase diagram shown in figure 10.1 for increasing/decreasing field. It should be noted that while no measurable hysteresis was observed at the AF2 to AF3 transition, the field induced AF2 to AF1 transformation is clearly hysteretic implying that in this case a first order transition takes place. It is worth to point out the "open hysteresis loop" at 7 K (see the inset in Fig. 10.7). At this temperature the initial zero-field susceptibility value is not recovered after magnetic field was increased beyond the field needed for the AF2 to AF1 transformation and then reduced to zero. Further cycling the field reflects in minor hysteresis loops reminiscent of magnetic material with martensite type structural phase transition. The observed peculiarity in the susceptibility is consistent with the magnetoelectric memory effect attributed to the existence of small ferroelectric embryos [102, 164, 165] of the AF2 phase at temperatures below the transition into the non-polar AF1 phase. The origin of the

above phase separation at this stage is uncertain and further studies are needed to clarify whether it is of structural or other types. The data extracted from Fig. 10.7 together with the neutron diffraction data let us to construct the magnetic phase diagram presented in Fig. 10.1. Our results are in good agreement with previously published polarization data [99] (also plotted) apart from the smaller field effect on the Néel temperature documented by us, and most importantly the low temperature tail of AF2 expanded into the AF1 phase. This tale could be regarded as a support for the existence of AF2 "embryos" leading to the previously reported polarization memory effect [102, 164, 165].

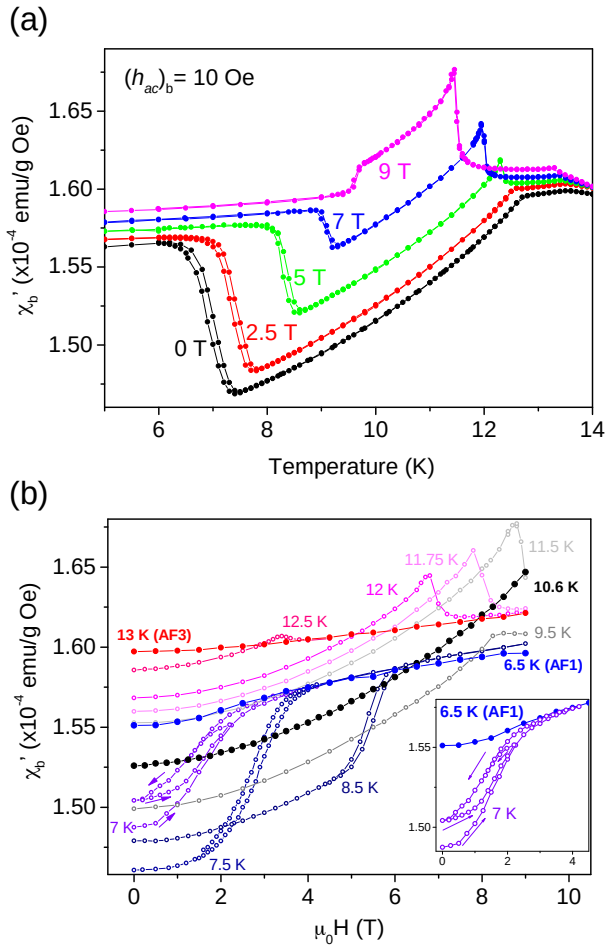

FIGURE 10.7: Incremental susceptibility plotted for better appreciation either (a) as a function of temperature at constant dc-field or (b) as a function of dc-field at constant temperature.

10.1 Summary and conclusions

To summarize, the X phase of the pure $MnWO_4$ has been determined by neutron diffraction experiments. The X phase has been named as AF2' since it has the same symmetry as the multiferroic phase of $Mn_{0.90}Co_{0.10}WO_4$.

An abrupt transition has been proposed to describe the AF2-to-AF2' transition: a decrease of the eccentricity upon increasing field until the rotation plane of the spins flops perpendicular to the field.

The electric polarization aligned parallel to b in the AF2 phase, continuously decreases and P_a slightly increases, followed by a rapid change in both components in the vicinity of the threshold field. The observed continuous decrease of the P_b, is in good agreement with the observed decrease of m_b. Small misalignments between the applied magnetic field and the b axis can result in the lack of clear discontinuity in P.

Evidence for coexistence of the nonpolar collinear commensurate magnetic phase, AF1, and the polar cycloidal structure, AF2, during the field-induced AF2-to-AF1 transition in $MnWO_4$ is provided based on incremental-magnetic-susceptibility results. These data also suggest that a trace of AF2 domains exist at temperature lower than the AF2-AF1 boundary of the zero magnetic-field phase-diagram (this observation could be regarded as a support for existence of AF2 embryos being responsible for the recently published polarization memory effect).

Chapter 11

Magnetic-field-induced transitions in $Mn_{0.95}Co_{0.05}WO_4$

Various magnetic-field-induced phase-transitions observed in $Mn_{0.95}Co_{0.05}WO_4$ will be presented in this chapter, depending on the direction of the magnetic field with respect to the crystal orientation, namely along the *b* axis and along the particular direction α, the easy axis.

It is worth recalling the results obtained in Chapter 8 for this composition. It was concluded that $Mn_{0.95}Co_{0.05}WO_4$ has two magnetic phases in zero field, the AF3 phase between 13.2 K and 12.2 K and the AF2 multiferroic phase below 12.2 K. The AF2 phase is a cycloidal structure with the moments rotating within the $b\alpha$ plane, α being the easy-magnetic axis located at about 15° from *a* towards *c*. For the AF3 phase, it was concluded that most likely the structure corresponds to a cycloidal structure with opposite chirality of the magnetic moments in the unit cell.

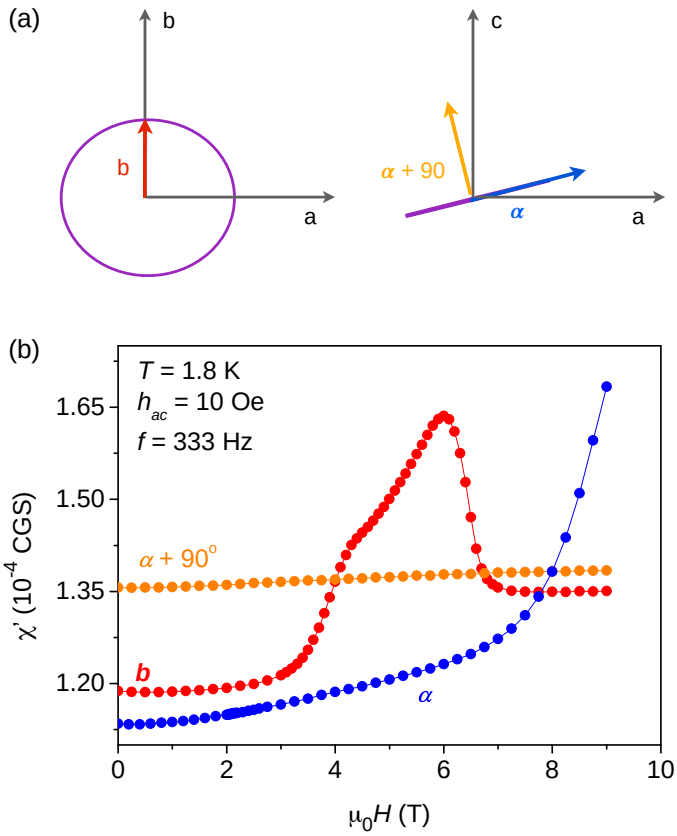

FIGURE 11.1: (a) Sketch of the direction along which the field was applied with respect to the orientation of the magnetic moments. In purple the ellipse that envelops the magnetic moments. (b) Real component of the ac susceptibility versus superimposed dc field along the easy (α) and hard ($\alpha + 90^\circ$) directions within the ac plane, and along the b axis, obtained at 1.8 K.

11.1 Probing field-induced transitions by incremental-magnetic susceptibility

To detect field-induced transitions in those magnetic phases, ac-susceptibility was measured along b, α and $\alpha + 90^\circ$[1] directions at fixed temperatures and varying the amplitude of the dc-field which was superimposed in the same direction as the ac-field. Figure 11.1(a) shows a sketch of the direction of the field with respect to the spin arrangement projected along c and b axes. In the former the ellipse that

[1] As previuously defined in Chapter 8, $\alpha + 90^\circ$ is the magnetic hard-axis which is located within the ac plane 90° from α.

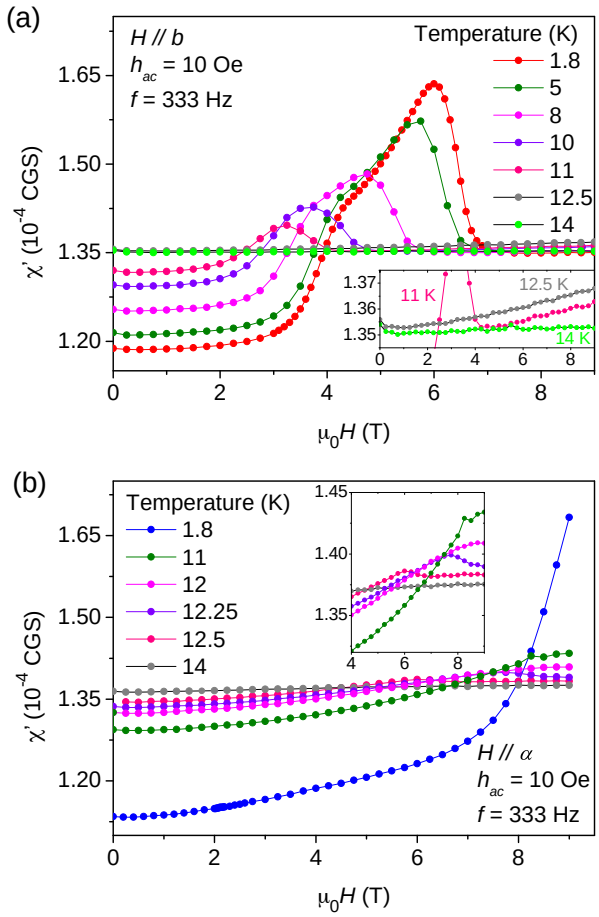

FIGURE 11.2: Real component of the ac susceptibility along the b and a axes versus superimposed dc field, at different temperatures in (a) and (b) respectively. The inset are zooms.

envelops the magnetic moments is plotted in purple and the b axis is drawn in red. In the projection along b, the ellipse is a line at about 14° away from a (the so-called a axis) and 90° far from it within the ac plane is located the $a + 90°$ axis. The evolution of the incremental susceptibility at 1.8 K shown in Fig. 11.1(b), reveals a field-induced transition along the b direction and suggests a beginning of such transition along a, while no indication of any transition is seen along the hard axis up to the highest applied field of 9 T.

The transition along b starts at fields as low as 3.5 T, indicated by the increase of the real component of the ac susceptibility in Fig. 11.1(b), and ends at about 7 T. The susceptibility evolution suggests that this transition is completed in

two stages (and presumably composed of two consecutive transitions), evidenced by the susceptibility increase from the almost constant low field value, followed by an almost linear increase and then a decrease to an almost constant high field value. The higher the temperature is, the lower the fields needed to induce the transition are and the narrower the transition itself is, see Fig. 11.2(a). The two consecutive stages seem to merge into a single one at temperatures above 8 K. In the AF3 phase, between about 12.1 K and 13.2 K, the peak in the ac susceptibility completely disappears and the slope of the curves is similar to the slope at about 2 T that coincides with the slope of the high-field phase of the AF2 structure. In the paramagnetic region (14 K), as expected, the ac-susceptibility is practically flat.

Field-induced transition takes place also along the α direction. As seen from Fig. 11.1(b), at 1.8 K, the susceptibility initially increases almost linearly up to about 7 T followed by much faster increase at higher fields indicating the beginning of the transition, which however reminds uncompleted to the highest field available of 9 T. The susceptibility maxima observed on the 12 K, 12.25 K and 12.5 K curves (AF3 phase region) should be related to the crossing from AF3 to the paramagnetic region rather than to a spin-flop-type transition expected for the AF2 phase.

11.1.1 Incremental-magnetic susceptibility along intermediate orientations between α and $\alpha + 90^\circ$

The incremental susceptibility was also measured at intermediate orientations between the b axis and the easy- and the hard-magnetic axes, see Figs. 11.3(a) and 11.3(b) respectively. The crystal was cautiously oriented by hand using a protractor and put back in the magnetometer for each measurement. Figure 11.3(a) shows how the transitions evolve when the field is applied further from b and closer to α. In such cases, higher fields are necessary to produce changes in the magnetic structure compared to the case where $H \parallel b$, and the transitions are broader. However the *two-stage* shape is maintained until the field is about 60° from b, where the second stage fully vanishes. Then, the ac susceptibility strongly increases and forms a rather a sharp peak. As one approaches the α direction the maximum value of the susceptibility increases considerably as well as the critical field.

On the contrary, if the field is tilted towards the hard axis starting from b, the transition is broadened very fast and also the *two-stage* shape disappears at angles as low as 13° from the b axis [see 11.3(b)].

With the aim of clarifying the nature of these transitions neutron diffraction experiments were performed applying the field along b and α. Furthermore, the effect of the external field on the electric polarization was also investigated. We will first discuss the influence of applying the field along b, $H \parallel b$, and then we will make a similar discussion when the field is applied along α, $H \parallel \alpha$.

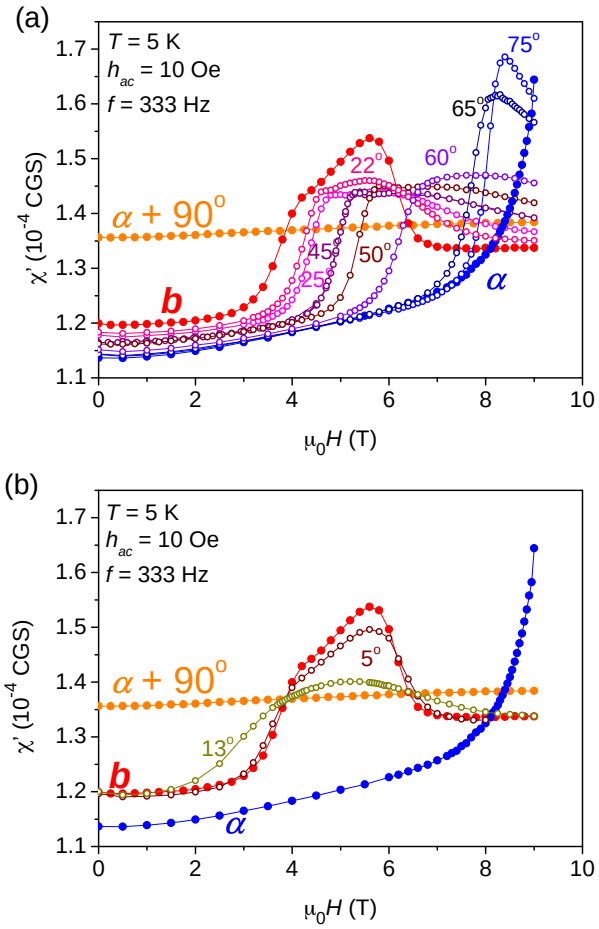

FIGURE 11.3: Real component of the ac susceptibility versus superimposed dc field at 5 K, (a) at different angles between the easy direction within the *ac* plane and the *b* axis; and (b) at different angles between the hard direction within the *ac* plane and the *b* axis. In (a) and (b) the angles increase with the deviation from the *b* axis.

11.2 Continuous rotation of the magnetic structure and of the electric polarization with field aligned parallel to b

11.2.1 Magnetic order

The neutron experiment started by measuring two magnetic reflections on D23 while an external magnetic field was applied along the b axis. The field increased from 0 T to 10 T. The integrated intensities of those two reflections, depicted in Fig. 11.4, exhibit changes in the field range 2.5 T - 7 T, which agrees with the field-induced transition observed by means of ac-susceptibility measurements with $H \| b$. The $(0\ 0\ 0)^{+\mathbf{k}}$ shows a evolution characterized by a maximum and a minimum value that occur at the fields where the $(0\ 0\ 1)^{-\mathbf{k}}$ starts increasing and has a maximum, respectively.

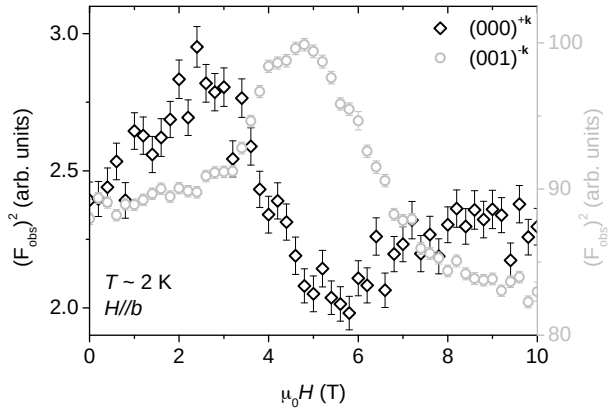

FIGURE 11.4: Integrated intensities of $(0\ 0\ 0)^{+\mathbf{k}}$ and $(0\ 0\ 1)^{-\mathbf{k}}$ reflections as a function of the external field applied along b at about 2 K.

Then, the centering of roughly 20 magnetic reflections at 5 T and 10 T showed that the propagation vector does not vary with the application of such fields compared to the one found at zero field, $\mathbf{k}$ = [-0.216(2), $\frac{1}{2}$, 0.460(2)]. The magnetic structures were refined from the integrated intensities of about 130 reflections, at 5 T (within the transition) and 10 T (above the transition). The parameters that describe the proposed spin arrangements are gathered in Table 11.1, the corresponding structures are depicted in Figs. 11.5(a), 11.5(b), 11.5(c) and 11.5(d), together with their corresponding observed intensities compared to the calculated ones. The data treatment concluded that the high-field structure ($\mu_0 H$ = 10 T) is a

cycloidal structure in the *ac* plane, perpendicular to the external field, as expected for an antiferromagnetic material above the spin-flop transition. The treatment of the data recorded at 5 T, i. e. in an intermediate field, revealed that the magnetic structure is such that the rotation plane of the moments is in between the initial and final orientations, and hence, suggests that the transition occurs in a continuous manner. Taking into account the refinement at 5 T, the plane where the moments rotate tilts around the easy axis; one can observe in the Table 11.1 that by fixing the easy axis and leaving the rest of the parameters free for the refinement, the plane rotates around α towards the *ac* plane making an angle of $\kappa = 32(4)^\circ$ with the *ac* plane. However, if we give more freedom to the structure, and refine the parameters associated to α too, there is a small reorientation of the easy axis, it tilt towards *c*. In this last model the angle κ is bigger, 46(4)°.

Temperature		T = 2 K	T = 2 K	T = 2 K	T = 2 K
Magnetic field ($H \| b$)		0 T	5 T	5 T	10 T
Instrument		D23	D23	D23	D23
k		$\mathbf{k}_0$	$\mathbf{k}_b$	$\mathbf{k}_b$	$\mathbf{k}_b$
Mn_1	$\Re(m)(\mu_B)$	3.83(7)	3.88(3)	3.86(4)	3.91(6)
	ϕ_u	0°	0°	0°	0°
	θ_u	77(2)°	77°	64(4)°	86(2)°
	$\Im(m)(\mu_B)$	-3.89(6)	-3.43(4)	-3.35(4)	-3.30(4)
	ϕ_v	90°	106(3)°	124(4)°	180°
	θ_v	90°	32(3)°	46(4)°	-4(2)°
Mn_2			$\mathbf{u}_2$ = - $\mathbf{u}_1$		
			$\mathbf{v}_2$ = - $\mathbf{v}_1$		
$\Delta\varphi$		$\frac{k_z}{2}$	$\frac{k_z}{2}$	$\frac{k_z}{2}$	$\frac{k_z}{2}$
κ		90°	32(4)°	37(4)°	0°
R_{F^2}		11.8	12.3	11.5	14.5
R_{F^2w}		10.0	9.58	8.71	13.1
R_F		16.1	17.2	16.8	19.0
χ^2		10.2	8.40	7.00	4.01

TABLE 11.1: Parameters that describe the magnetic structures of the $Mn_{0.95}Co_{0.05}WO_4$ at 2 K at zero field, 5 T and 10 T ($H \parallel b$). For simplicity the following notation has been used: $\mathbf{k}_0$ = [-0.216(1), $\frac{1}{2}$, 0.461(1)] and $\mathbf{k}_b$ = [-0.216(2), $\frac{1}{2}$, 0.460(2)]. The parameter κ is the angle between the plane where moments lay and the *ac* plane; it is not refined but derived from ϕ_v and θ_v.

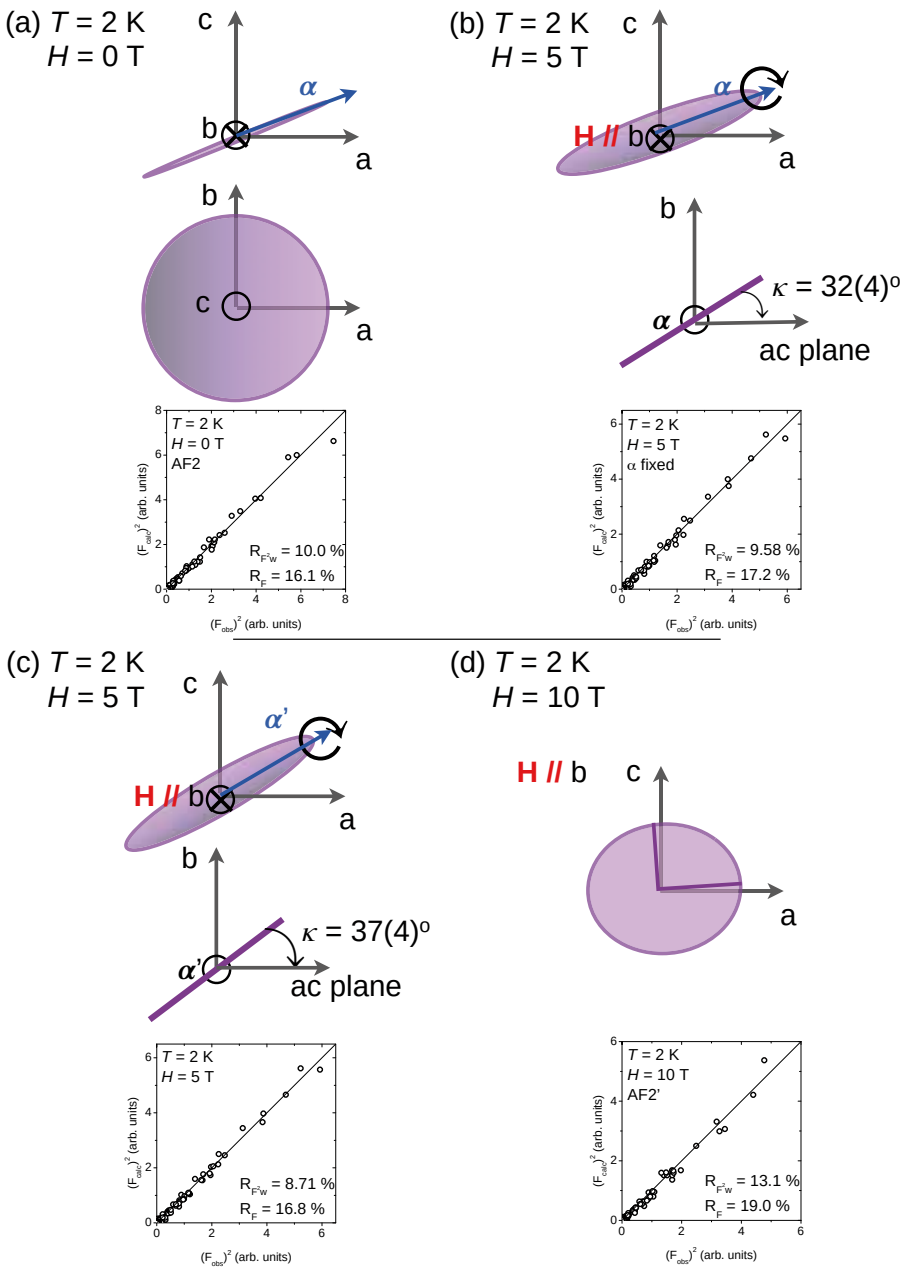

FIGURE 11.5: Sketch of the magnetic structures of $Mn_{0.95}Co_{0.05}WO_4$ at 2 K, only the ellipse that envelops the moments is given: (a) projection along *b* and *c* axes at zero field; (b) and (c) projections along *b* and α under 5 T field, the latter refining the direction of α and (d) projection along *b* of the high-field phase (10 T). κ is the angle of the rotation plane with respect to the *ac* plane.

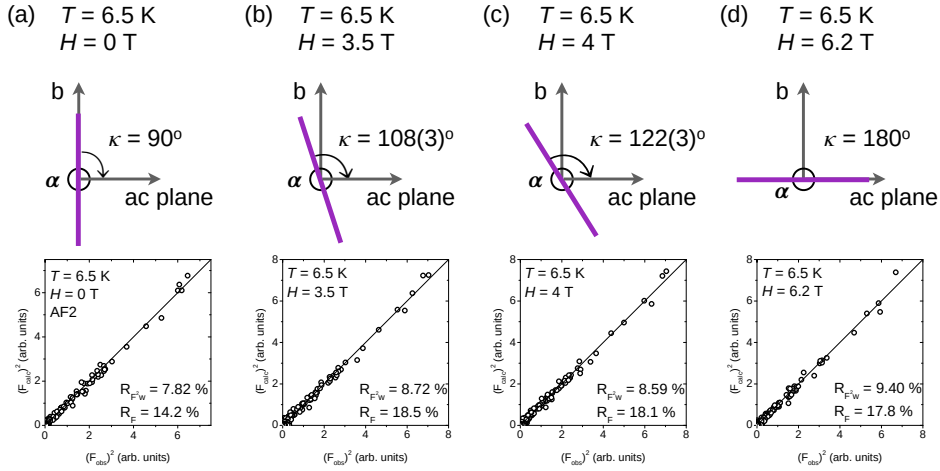

FIGURE 11.6: Evolution of the rotation plane of the moments with increasing the magnetic field applied along b.

Temperature		T = 6.5 K	T = 6.5 K	T = 6.5 K	T = 6.5 K
Magnetic field ($H \| b$)		0 T	3.5 T	4 T	6.2 T
Instrument		6T2	6T2	6T2	6T2
k		$\mathbf{k}_0$	$\mathbf{k}_b$	$\mathbf{k}_b$	$\mathbf{k}_b$
Mn_1	$\Re(m)(\mu_B)$	4.74(5)	4.87(4)	4.85(5)	4.86(3)
	ϕ_u	0°	0°	0°	0°
	θ_u	70(2)°	69(2)°	65(2)°	66(2)°
	$\Im(m)(\mu_B)$	-3.56(5)	-3.59(4)	-3.60(5)	-3.62(3)
	ϕ_v	90°	80(2)°	73(2)°	0°
	θ_v	90°	106(2)°	118(2)°	156(2)°
Mn_2			$\mathbf{u}_2$ = - $\mathbf{u}_1$		
			$\mathbf{v}_2$ = - $\mathbf{v}_1$		
$\Delta\varphi$		$\frac{k_z}{2}$	$\frac{k_z}{2}$	$\frac{k_z}{2}$	$\frac{k_z}{2}$
κ		90°	108(3)°	122(3)°	180° = 0°
R_{F^2}/%		10.2	12.3	11.6	11.8
R_{F^2w}/%		7.82	8.72	8.59	9.40
R_F/%		14.2	18.5	18.1	17.8
χ^2		2.83	1.38	1.36	1.58

TABLE 11.2: Parameters that describe the magnetic structures of the $Mn_{0.95}Co_{0.05}WO_4$ at 6.5 K under 0 T, 3.5 T, 4 T and 6.2 T field ($H \parallel b$). For simplicity the following notation has been used: $\mathbf{k}_0$ = [-0.216(1), $\frac{1}{2}$, 0.461(1)], $\mathbf{k}_b$ = [-0.216(2), $\frac{1}{2}$, 0.460(2)]. The parameter κ is not refined but deduced from ϕ_v and θ_v, and corresponds to the angle between the spin-rotation plane and the ac plane.

According to the experiment performed on D23, the transition occurs continuously by the rotation around the easy axis of the plane where spins lay. The rotation of the plane was better studied at 6.5 K on 6T2 in another experiment, see Table 11.2. In that experiment four data collections were done: zero field, 3.5 T, 4 T and 6.2 T. The refinements of the data clearly conclude that indeed the plane rotates from the αb plane to the ac plane around α. Note that the rotation takes place in the opposite direction compared to the experiment performed on D23. This may be because in one experiment the field was probably along b whereas in the other it was along -b. The amplitudes of the ordered magnetic moments barely change along the transition, and therefore, neither does the eccentricity.

If one simulates the evolution of the magnetic peaks in Fig. 11.4 with the proposed model for the transition, i. e. by considering that the plane rotates around α, the pattern that follow those magnetic reflections is reproduced rather well. Figure 11.7 presents the experimental integrated intensities of the $(0\ 0\ 0)^{+\mathbf{k}}$ and $(0\ 0\ 1)^{-\mathbf{k}}$ reflections (represented by empty symbols) as a function of the external field and the calculated intensities (full symbols) for those reflections as a function of κ. There is an offset between the field and κ, however the way how the transition occurs is relatively well reproduced. Note that the second order effects revealed by the refinements, such us the small re-orientation of the easy axis or the variation of the amplitudes, were not taken into account in the simulation.

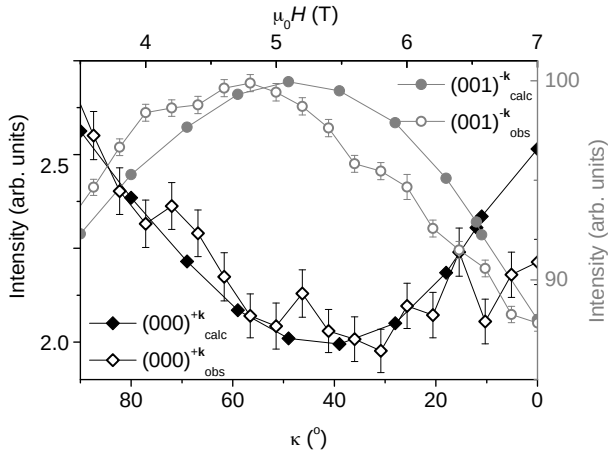

FIGURE 11.7: Observed integrated intensities of the $(0\ 0\ 0)^{+\mathbf{k}}$ and $(0\ 0\ 1)^{-\mathbf{k}}$ reflection as a function of the field along b represented by ($\diamond$) and ($\circ$) respectively. The simulated intensities of those two peaks as a function of κ have ($\blacklozenge$) and ($\bullet$) symbols.

The ferromagnetic component that may appear at high fields was also investigated. A bunch of nuclear peaks were recorded under the different fields, they

were carefully compared, but none of them showed any observable change which could be safely attributed to a ferromagnetic component. Moreover, the structure does not suffer any distortion, within experimental resolution.

11.2.2 Polarization

Figures 11.8(a) and 11.8(b) show the field dependence of the a, b and c components of the electric polarization at different temperatures, in $H \parallel b$ configuration. A smooth decrease of P_b is observed starting at about $H \sim 3.5$ T and finishing at about 7.5 T (2 K), in good agreement with the other techniques. As observed in the susceptibility measurements, the width of the transition decreases with increasing temperature and this is also reflected in the polarization measurements (note that at 10 K P_b disappears within 3 T-field range). Polarization measurements exhibit a small hysteresis with the field. a and c components of the polarization arise at about 3 T and reach their maximum at about 6.5 T (4.2 K). This results agree with the continuous flop of the rotation plane of the moments. In the initial and final stages, the polarization is either along b or in the ac plane, whereas in the intermediate stages the electric polarization has non-zero components along the 3 directions. One may think that this can be due to a phase separation and therefore, the result of the contribution of two elliptical-magnetic structures each of which producing polarization either along b or in the ac plane. However, the magnetic-diffraction data refinement concluded that there is a unique phase and that hypothesis can be ruled out.

Electric polarization along the a axis was measured as a function of the temperature at fixed fields. The first conclusion is that the T_{FE} does not feel the presence of the external field, within the experimental resolution: it is unchanged at least up to 5 T fields. The behavior of the polarization is rather peculiar: at low fields, it has a maximum value close to T_{FE} and decreases at low temperatures. A recent work by Liang *et. al.* [129] associates this interesting response of P_a to the temperature at fields between 2 T and 5 T to the rotation of the spin-plane around the easy axis. According to Liang in that field range and right below T_{FE}, the spin plane is parallel to ac, and then, with decreasing temperature the plane rotates. The temperature range where the reorientation of the plane takes place depends on the field; for example at 2 T, P_a tends to zero within 2 K. On the contrary, at 4 T none of the components of the polarization is zero and therefore, at that field, the rotation of the spin plane is not completed.

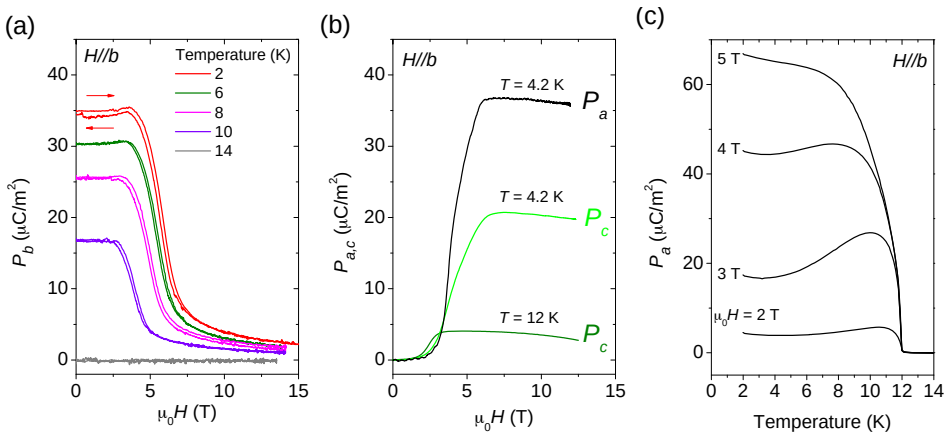

FIGURE 11.8: Field dependence of the components of the electric polarization for $H \| b$, (a) P_b component at several temperatures and (b) P_a and P_c components at 4.2 K. (c) Temperature dependence of P_a at different fields.

11.3 Magnetic transitions with $H \parallel \alpha$

Ac susceptibility measurements suggest a beginning of field-induced transition with magnetic field along the easy axis (see Fig. 11.1) that is probably completed slightly above the maximum available field for this measurements (9 T). The usual procedure was followed to perform the experiment on D23 and first, two magnetic reflections were monitored at 2 K as the field increased, from 0 T to 12 T. The integrated intensity of those two reflections display a clear and sharp transition at 10 T, see Fig. 11.9. The intensity of the $(0\ 0\ \text{-}1)^{+\mathbf{k}}$ reflection gradually decreases until the transition occurs, then, it remains constant up to 12 T field. On the contrary, the intensity of the $(\text{-}1\ 1\ 1)^{-\mathbf{k}}$ reflection increases and has a maximum value at 10 T, then it decreases and above 11 T it becomes constant too.

Magnetic data were collected at 8 T (before the transition), 10 T and 11.75 T (above the transition). Unfortunately, the collected data at both high field and intermediate fields did not allow us to determine unambiguously the corresponding magnetic phases. Most likely, due to the geometrical restrictions imposed by the magnet, the set of collected reflections was not enough to give a definitive answer, and therefore this experiment should be repeated.

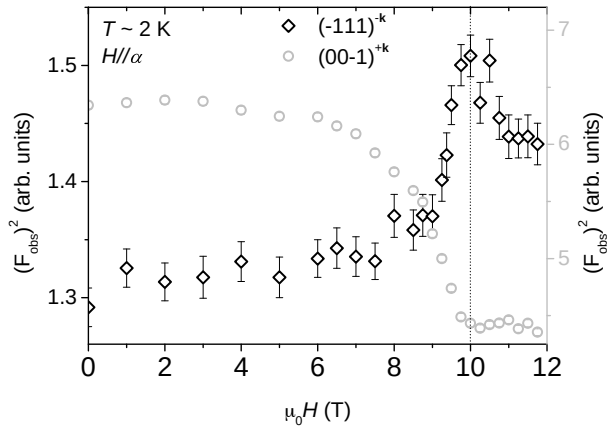

FIGURE 11.9: Integrated intensities of (0 0 -1)$^{+\mathbf{k}}$ and (-1 1 1)$^{-\mathbf{k}}$ reflections as a function of the external field applied along α at 2 K.

11.4 Summary and conclusions

To summarize, the effect of a magnetic field applied along the b axis of $Mn_{0.95}Co_{0.05}WO_4$ has been investigated and this study consistently reveals that, the ferroelectric phase with spin-cycloid structure in the αb plane and with polarization along b undergoes a continuous transition from the αb plane to the $w\alpha$ plane, with $w = \alpha + 90^\circ$ being the hard direction. Such evolution of the plane rotation was suggested by Liang *et. al.* [129] but only our neutron diffraction study unambiguously confirmed it. The electric polarization undergoes a similar behavior: it rotates continuously from the b axis to the ac plane. Indeed, as expected from the rotation of the spin-plane. As a result, we propose a complete phase diagram that gathers all the results we obtained, see Fig. 11.10.

Although both, bulk magnetic measurements and the evolution of certain magnetic reflections clearly demonstrate a field-induced transition, with $H \parallel \alpha$, neutron-diffraction experiments were not conclusive about the spin arrangement.

By comparing the $H - T$ phase diagrams with $H \parallel b$ of the $MnWO_4$ and $Mn_{0.95}Co_{0.05}WO_4$ compositions it becomes evident that doping $MnWO_4$ with only 5% of cobalt does not only to destabilize the AF1 phase. The influence of an external magnetic field along the monoclinic-b axis in both compounds is radically different. In the parent compound the m_b component of the magnetic moment decreases with increasing field until it becomes unstable and flops to the ac plane. This is not the case in $Mn_{0.95}Co_{0.05}WO_4$, where the rotation happens in a continu-

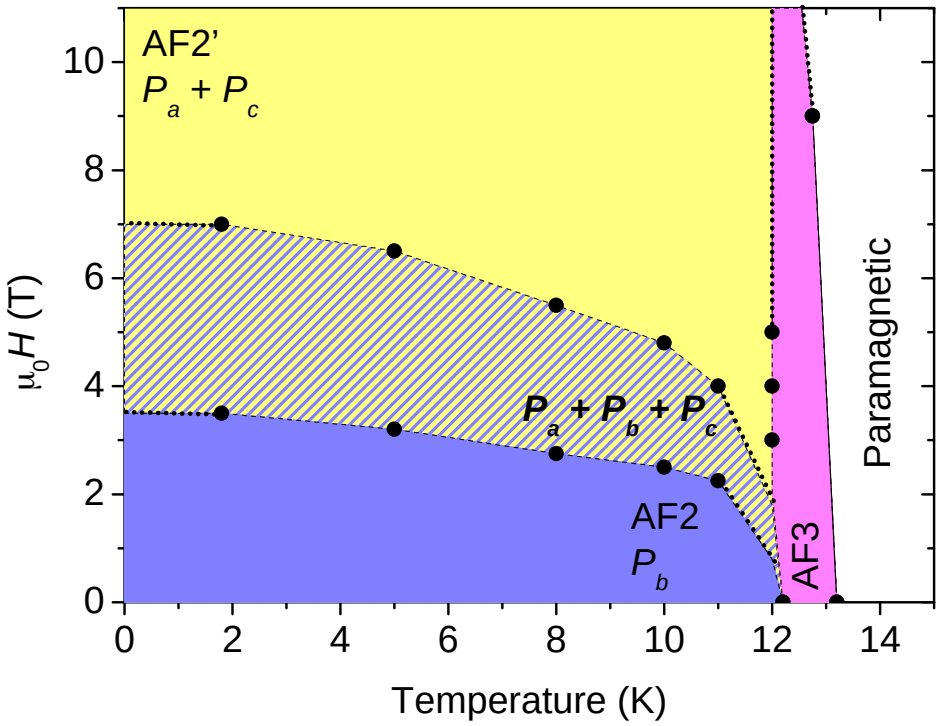

FIGURE 11.10: $H \parallel b$ phase diagram proposed for $Mn_{0.95}Co_{0.05}WO_4$.

ous manner. One main consequence is that in the $MnWO_4$, P_b and P_a do not coexist whereas in the doped composition they do.

Chapter 12

Magnetic-field-induced transitions in $Mn_{0.90}Co_{0.10}WO_4$

Various magnetic-field-induced phase transitions will be presented in this chapter, which were studied by means of magnetic and magnetoelectric measurements, and neutron diffraction.

Two magnetic structures appear below T_N in $Mn_{0.90}Co_{0.10}WO_4$: AF3 and AF2'. The AF3 is described as a cycloidal structure with the magnetic moments located basically within the basal plane of the octahedra. The AF2' phase, the multiferroic one, corresponds to a cycloidal order within the *ac* plane. The magnetic symmetry of the latter structure is different to that of the multiferroic phases of the rest of the studied compositions. So, applying a magnetic field along different directions could give rise to effects that may only happen to this composition.

Please note, that this was the first under-field-study done in this thesis. We made the mistake of applying the field along the crystallographic axes instead of applying it along the magnetically characteristic ones. Nevertheless, the easy axis is 9° from *a* at 2 K, and consequently the field has been applied rather close to the magnetic-easy axis.

12.1 Bulk magnetic response

The field dependence of the magnetization at 2 K along the principle crystallographic directions is shown on Fig. 12.1. Up to fields as high as 9 T the magnetization along *b* and *c* axis reminds higher than along the *a* axis. While the later changes linearly up to about 7.5 T, it turns concave upwards at higher fields signalling a spin reorientation process, presumably of spin-flop type. More careful inspection of the *c* axis magnetization reveals similar but less pronounced peculiarity at fields of about 2 T, see the calculated derivative of the magnetization in the insert of Fig. 12.1. No coercivity was observed in any orientation.

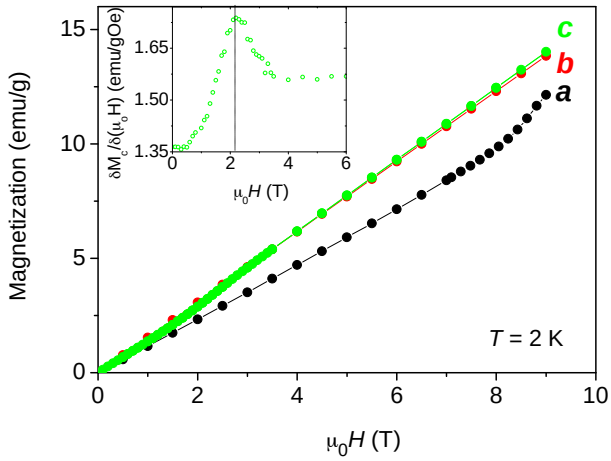

FIGURE 12.1: Magnetization curves along the principle crystallographic directions. In the insert, the derivative of the *c*-axis magnetization with respect to the applied field.

To better monitor the above field-induced departure from the linear variation of magnetization with field applied along *a* and *c* directions, we studied the ac-susceptibility at fixed temperatures as a function of the amplitude of the dc-field, superimposed in the same direction as the ac-field. As illustrated on Fig. 12.2(a), at 2 K the field-induced transition along the *a* direction starts at fields as low as 6.5 T as evidenced by the increase of the real component of the ac-susceptibility, which forms a peak at 8.7 T. This critical field should correspond to the maximum slope in the magnetization curve depicted on Fig. 12.1. As suggested by Fig. 12.2(a), the field-induced transition is not completed up to the highest applied field of 9 T. The critical field slightly decreases with increasing temperature (to about 8.3 T at 10 K). A small but noticeable hysteresis is seen depending on the way the field is ramped, see the inset of Fig. 12.2(a). No clear maximum of ac-susceptibility is observed between T_{N2} and T_N. However, one should keep in mind that this narrow temper-

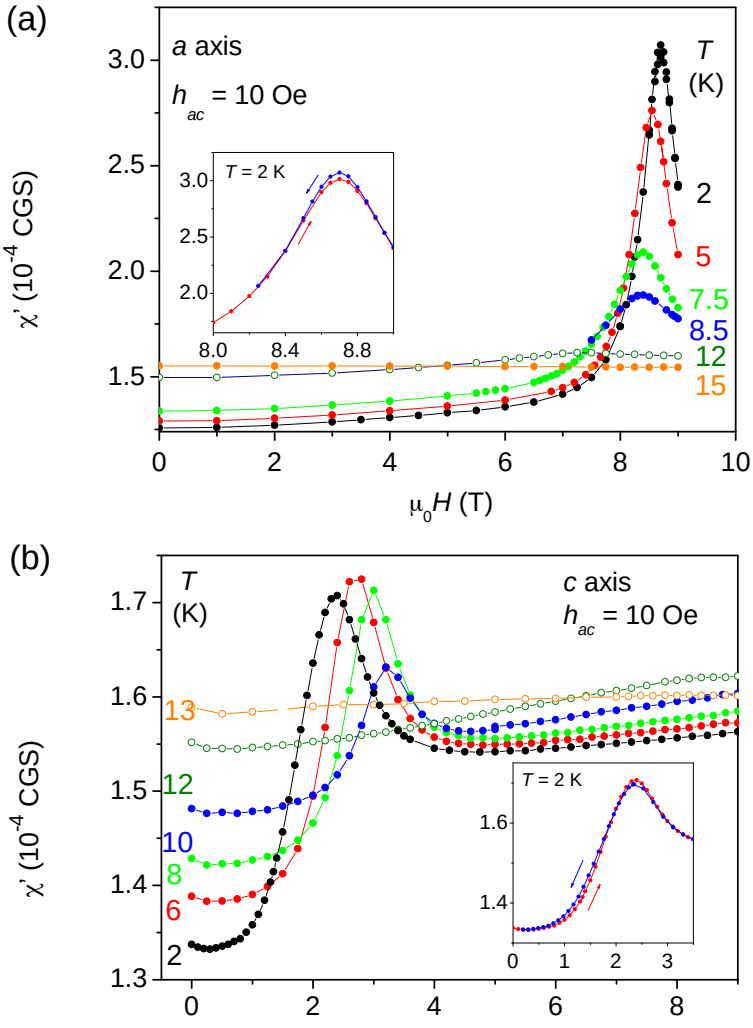

FIGURE 12.2: (a) Real component of ac-susceptibility along *a*-axis as a function of superimposed dc field amplitude. (b) The same for the *c* axis. The insets are zooms of the susceptibility maxima. The arrows indicate the direction of changing the field.

ature region is too close to the paramagnetic transition, which might be affected by the relatively high magnetic field. Figure 12.2(b) focuses on the hardly seen magnetization anomaly along *c* direction, depicted on Fig. 12.1, and demonstrates the versatility of the used approach in studying small changes in the magnetization curve. At 2 K a clear maximum of the ac-susceptibility is observed at about 2.4 T (as also manifested on from the derivative of the magnetization), suggesting a field-induced transition. Such transition was not reported in the previous studies [126]. The width of the peak implies that this transition is accomplished in a rela-

tively broad range of fields between about 1 to 3.5 T. A very narrow but noticeable hysteresis is visible on the inset of 12.2(b). The peak position is strongly affected by temperature and it shifts to 3.2 T at 10 K. Importantly the susceptibility peak disappears above T_{N2}.

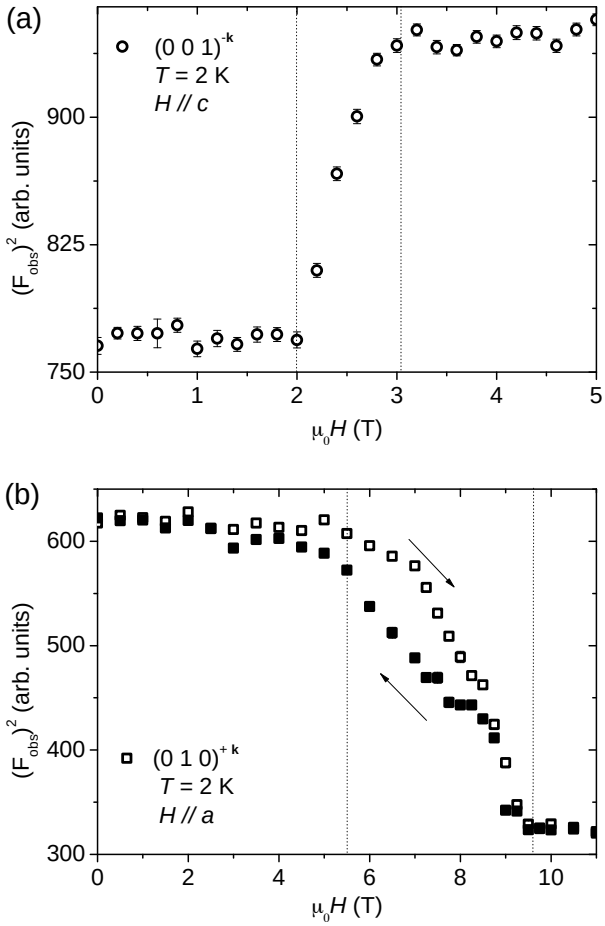

FIGURE 12.3: (a) Evolution of the integrated intensity of $(0\,0\,1)^{-\mathbf{k}}$ magnetic satellite with the magnetic field applied parallel to the c axis ($H \| c$). (b) Similar plot for the $(0\,1\,0)^{+\mathbf{k}}$ satellite when the magnetic field is applied parallel to the a axis ($H \| a$).

12.2 Neutron diffraction

12.2.1 Field along the c axis

In an experiment performed on the diffractometer D15, where the sample was mounted with the c axis parallel to the field we have followed the $(0\ 0\ 1)^{-\mathbf{k}}$ magnetic satellite as a function of the applied field at T = 2 K. The variation of its integrated intensity is depicted in Fig. 12.3(a). The field-induced transition suggested by the magnetization and ac-susceptibility measurements with $H \| c$ is apparent. The transition starts at fields around 2 T and is completed at about 3 T, in agreement with those measurements. Data were then collected at 5 T. First, the propagation vector was refined by centering 35 magnetic peaks which revealed that it is nearly unchanged compared to the zero field value: $\mathbf{k}(H = 5\text{T})$ = [-0.220(1), $\frac{1}{2}$, 0.469(2)].

Temperature		T = 2 K	T = 2 K	T = 2 K	T = 2 K
Magnetic field		0 T	2.2 T $\| c$	5 T $\| c$	11 T $\| a$
$\mathbf{k}$		$\mathbf{k}_0$	$\mathbf{k}_c$	$\mathbf{k}_c$	$\mathbf{k}_a$
Mn_1	$\Re(m)(\mu_B)$	4.45(2)	3.21(8)	4.41(2)	3.67(3)
	ϕ_u	0°	0°	-7(2)°	90°
	θ_u	99(2)°	87(3)°	95(1)°	-21(2)°
	$\Im(m)(\mu_B)$	4.03(2)	4.10(8)	3.78(2)	4.19(3)
	ϕ_v	0°	0°	83(2)°	83(1)°
	θ_v	9(2)°	-3(3)°	93(1)°	69(2)°
Mn_2		$\mathbf{u}_2$ = - $\mathbf{u}_1$	$\mathbf{u}_2$ = - $\mathbf{u}_1$	$\mathbf{u}_2$ = - $\mathbf{u}_1$	$\mathbf{u}_2$ = - $\mathbf{u}_1$
		$\mathbf{v}_2$ = - $\mathbf{v}_1$	$\mathbf{v}_2$ = - $\mathbf{v}_1$	$\mathbf{v}_2$ = - $\mathbf{v}_1$	$\mathbf{v}_2$ = - $\mathbf{v}_1$
$\Delta\varphi$		$\frac{k_z}{2}$	$\frac{k_z}{2}$	$\frac{k_z}{2}$	$\frac{k_z}{2}$
R_{F^2}/%		5.67	9.89	5.81	9.53
R_{F^2w}/%		6.16	10.5	5.86	7.33
R_F/%		6.65	11.9	5.39	17.0
χ^2		7.14	32.1	8.37	8.30

TABLE 12.1: Parameters that describe the magnetic structures of the $Mn_{0.90}Co_{0.10}WO_4$ at 2 K under 5 T field along the c axis and 11 T field along the a axis. Zero field structure from Chapter 8 is also included for comparison. For simplicity the following notation has been used: $\mathbf{k}_0$ = [-0.222(1), $\frac{1}{2}$, 0.472(1)], $\mathbf{k}_c$ = [-0.220(1), $\frac{1}{2}$, 0.469(2)] and $\mathbf{k}_a$ = [-0.206(3), $\frac{1}{2}$, 0.465(1)].

The integrated intensities of 135 independent magnetic peaks were collected and refined first at 2.2 T and then at 5 T. The obtained parameters are gathered

in Table 12.1 and the corresponding structures are depicted in Figs. 12.4(a) and 12.4(b). At 2.2 T, the data can be explained with relatively good agreement as a cycloidal structure with the spins in the *ac* plane. This structure keeps the symmetry of the zero field AF2' phase, with the small differences such as a small change in the orientation of the principal axes of the ellipse and the amplitude of the moments closer to *a* and an eccentricity $\epsilon(H\|c = 2.2\ \mathrm{T}) = 0.62$ (the direction perpendicular to the field). At higher fields, the scenario is completely different. Compared to the zero-field structure, there is a flip of the plane where the moments rotate from the *ac* plane towards the *ab* plane. The refinements improve if we consider that the rotation plane is not parallel to the *ab* plane but slightly tilted, as the parameters in Table 12.1 show. That plane is forced by the field to be as perpendicular as possible to the direction of the external field. In addition, the eccentricity of the ellipse in the new structure has increased, from $\epsilon(H = 0) = 0.42$ to $\epsilon(H\|c = 5\ \mathrm{T}) = 0.51$.

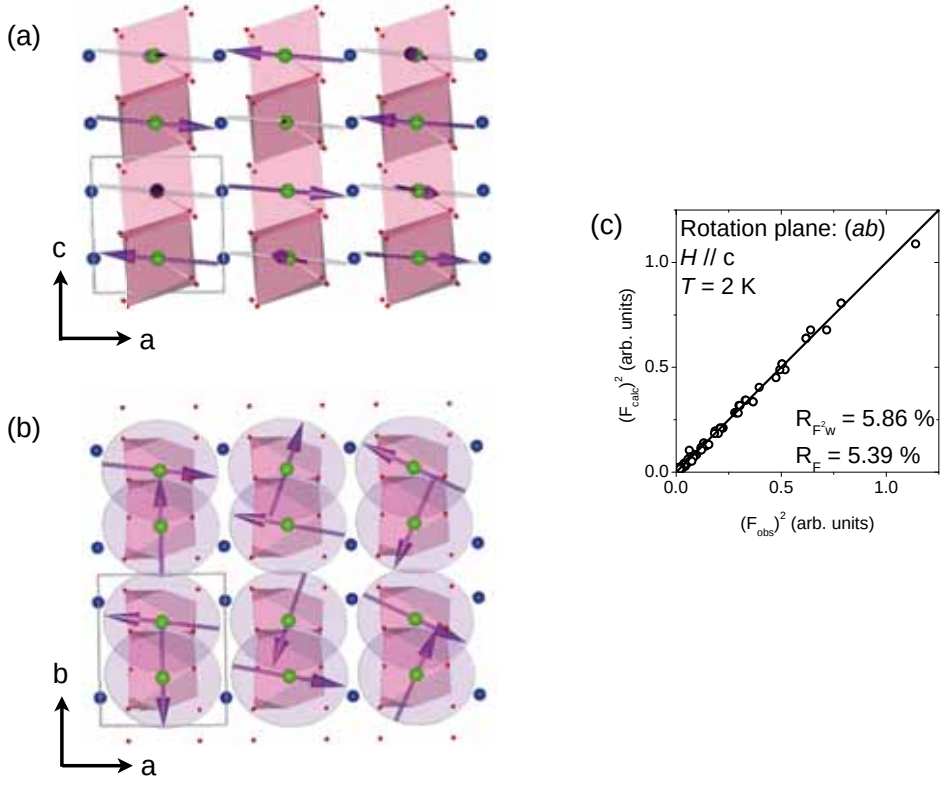

FIGURE 12.4: Magnetic structure of $Mn_{0.90}Co_{0.10}WO_4$ determined at 2 K and 5 T with the magnetic field applied parallel to the *c* axis ($H\|c$). (a) A projection in the *ac* plane of the spin order. (b) Projection of the magnetic structure in the *ab* plane. The spin rotation plane is shown in light purple. (c) Agreement plot of the magnetic refinement.

The influence of the magnetic field on the AF3 phase was also explored. Neutron diffraction data were collected at 12 K and 5 T. Under these conditions the magnetic structure remains collinear and sinusoidally modulated with the same propagation vector. Only a deviation of the moment direction with respect to the c^* axis was observed. The moments remain in the ac plane, but the angle θ formed with the c^* axis decreases: 112(1)$^\circ$ instead of the 124.8(5)$^\circ$ at zero field. Hence, the effect of the field along the c axis on AF3 is to rotate the spins towards the ab plane, in order to diminish their projection onto the direction of the external magnetic field. Thus the field moves the spins away from the equatorial plane of the MO_6 octahedra. This is in good agreement with the ac-susceptibility, from which one should not expect big changes of the AF3 magnetic structure.

Regarding the nuclear structure, the external field does not alter the crystal structure within experimental resolution, and no ferromagnetic component was observed either.

12.2.2 Field along the a axis

As shown in Figs. 12.1 and 12.2, a magnetic field applied along the a axis also induces a magnetic transition in the AF2' structure. In this case, higher field is needed to achieve the spin reorientation and, in addition, the transition is much wider than the one along the c axis. The field dependence of the magnetic satellite $(0\ 1\ 0)^{+\mathbf{k}}$, depicted in Fig. 12.3(b), shows that at 2 K the transition takes place between 5.5 T and 9.5 T. Above 9.5 T the magnetic transition is completed. With decreasing field the integrated intensity exhibits hysteresis. Analyzing the data, a complex behavior of the reflection was observed. Scans along ω angle of the diffractometer were done at increasing and decreasing field, see Figs. 12.5(a) and 12.5(b). With increasing field, the magnetic reflection splits in two at about 7.3 T to finally collapse in a unique peak at about 9.3 T. The resulting reflection is displaced with respect to the initial one which suggests a modification of the propagation vector $\mathbf{k}$. With decreasing field, the splitting of the peak occurs at little lower fields, at about 9 T, at they join back at about 6 T. After undergoing the field ramp, the high field propagation vector becomes stable at zero applied field.

We have studied this new spin order by collecting neutron data at 11 T and 2 K on the D23 diffractometer. Centering of several magnetic reflections concluded that the propagation vector slightly changes compared to the one at zero field becoming $\mathbf{k}$ = [-0.206(3), $\frac{1}{2}$, 0.465(1)]. The spins arrangement was determined based

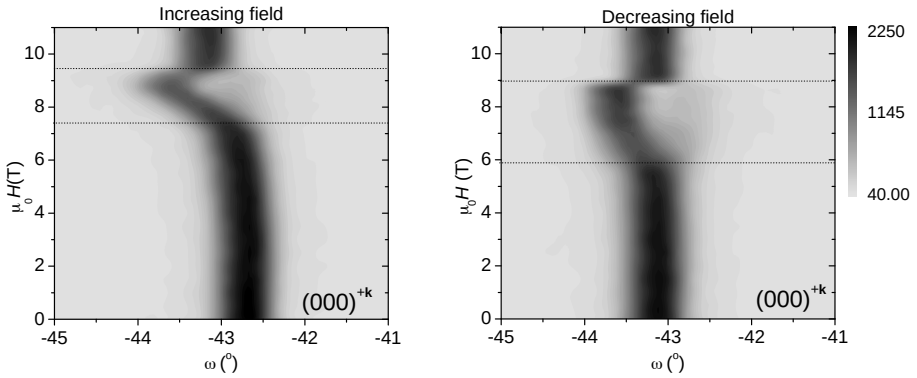

FIGURE 12.5: ω scan of $(010)^{+\mathbf{k}}$ reflection followed at 2 K as (a) the applied field increased and (b) decreased.

on the collected 125 independent reflections. The magnetic structure at 2 K and 11 T is shown in Fig. 12.6 and is described in Table 12.1. The main effect of the field along a is to flip the plane of the spin cycloid from the ac plane ($H = 0$) towards the bc plane ($H \| a = 11$ T). Moreover, as seen in Table 12.1, we observe a significant decrease in the amplitude of the ordered moments. In the $H \| a$ configuration, the eccentricity ($\epsilon = 0.48$) is slightly larger compared to the ground state.

The evolution of the AF3 phase with the magnetic field was not studied since from the macroscopic measurements we did not expect any difference but tilting of the moments towards the bc plane, in analogy with field along the c axis. Neither crystal-structure changes nor ferromagnetic component were detected at 11 K, within the experimental resolution.

12.3 Polarization

Figure 12.7(a) shows the dependence of the a, b and c components of the polarization as a function of the magnetic field applied along the c axis at $T = 2$ K. A sharp decrease of both P_c and P_a components is observed beginning at a threshold field $H_c \sim 2$ T. With increasing the temperature up to $T_{N2} \sim 11$ K, the evolution of the P_c (H_c) and $P_a(H_c)$ remains the same with only the initial polarization decreasing and the threshold field increasing. The temperature dependence of the threshold field for field-induced transition (see the insert in Fig. 12.7) coincides with the one found from the magnetization and ac susceptibility curves along c axis (Figs. 12.1 and 12.2). The inverse Dzyaloshiskii-Moriya interaction in the chains

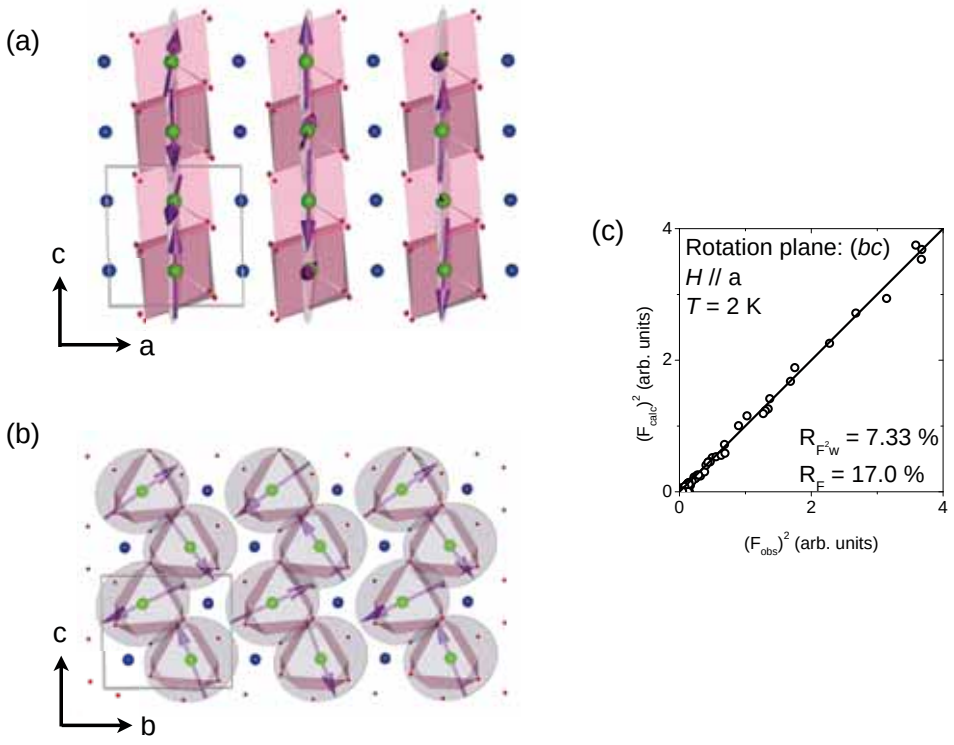

FIGURE 12.6: Magnetic structure of $Mn_{0.90}Co_{0.10}WO_4$ determined at 2K and 11 T with the magnetic field applied along a ($H \| a$). Projection of the magnetic structure in the ac plane (a) and in the bc plane (b). (c) Calculated structure factors are plotted against the experimental ones.

along a axis could contribute to the P_b component of the electric polarization in this field-induced phase. However, only a small variation of P_b component was observed at the threshold field which became more noticeable with increasing T (Fig. 12.7). Whether the small P_b polarization is related to the weaker magnetoelectric parameter along b axis or to a formation of the ferroelectric domains in the field-induced phase (containing of both right- and left-handed spin-cycloids) remains unclear and requires further study.

When the magnetic field is applied parallel to the a axis, similar suppression of the P_a polarization was observed at pulsed field $\sim$ 8.5 T [Fig. 12.7(b)]. This is in agreement with the non-linear increase of magnetization (Fig. 12.1) and the maximum in the field dependence of the ac susceptibility [Fig. 12.2(a)]. It indicates a field-induced spin-flop transition of the cycloid to the bc plane perpendicular to the field.

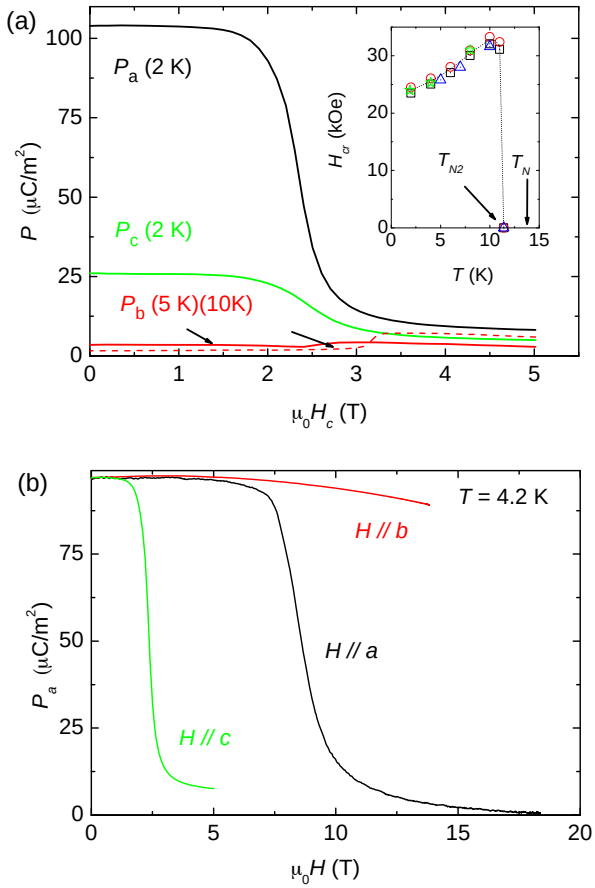

FIGURE 12.7: (a) Dependence of electric polarization along *a*, *b* and *c* axes under magnetic field along the *c*-axis. Insert shows the evolution of the critical field as a function of the temperature, H_{cr}-T diagram, obtained from electric polarization and magnetization data. (b) P_a component of the electric polarization in pulsed magnetic field along *a*-, *b*- and *c*-axes, exhibiting a suppression of P_a for $H \| a$ and $H \| c$ due to the flop of the plane of the cycloidal structure perpendicular to the field. Almost nothing changes for $H \| b$, since *b* is already orthogonal to the rotational plane.

No substantial effects for the electric polarization was found in pulsed magnetic field up to 15 T applied along the *b* axis confirming the absence of field-induced transitions in this direction, in agreement with the magnetic data in Fig. 12.1 and with Ref. [125].

12.4 Summary and conclusions

To summarize, magnetic-field-induced phase-transitions in $Mn_{0.90}Co_{0.10}WO_4$ multiferroic were explored using magnetic and magnetoelectric measurements, and neutron diffraction. Our data consistently reveal that, the multiferroic AF2' phase remains stable in magnetic field as high as 15 T applied along the b axis, while in field along c and a axes the spin cycloid structure flops from the ac plane to directions almost perpendicular to the magnetic field at $\sim$ 3 T and $\sim$ 8.5 T, respectively. Those spin reorientations are accompanied by a dramatic suppression of both P_a and P_c components of the polarization. The refinement of the neutron diffraction data has allowed us to extract the characteristic parameters including wave vectors, orientations of the main elliptical axes of the magnetic structures in the different spontaneous and field-induced phases.

Chapter 13

Magnetic-field-induced transitions in $Mn_{0.80}Co_{0.20}WO_4$

The evolution under applied magnetic field of the magnetic structures of the $x = 0.20$ composition of the $Mn_{1-x}Co_xWO_4$ family has been investigated in this chapter.

13.1 Magnetic and ferroelectric properties under fields perpendicular to α

13.1.1 Re-orientation of the conical antiferromagnetic structure with $H \parallel b$

Figure 13.1(a) shows the temperature dependence of the magnetic ac-susceptibility at fixed dc-fields. One can see that the Néel temperature does not vary up to 9 T. Down to the second transition ($\sim$ 9 K) all the curves collapse in the same line, but below this temperature, the evolution of the susceptibility depends on the intensity of the external field. As the field increases, the susceptibility increases until it reaches a maximum. The maximum has a higher value at higher fields, and that maximum is reached at lower temperatures. After the transition, all the curves decrease in a similar manner.

The behavior of the electric polarization along b in the ferroelectric phase of

$Mn_{0.80}Co_{0.20}WO_4$ with an external field applied along b is depicted in Fig. 13.1(b). With increasing field, P_b decreases and disappears rather abruptly at about 11 T. This transition shows a large hysteresis when ramping down the field.

According to bulk magnetic and polarization measurements, the conical structure is not stable under field aligned parallel to b and tends to disappear at high fields. On the contrary the AF4 phase remains stable, and seems to extend its stabilization range to low temperature at the expenses of the conical structure. However, the latter point has to be taken with some precaution, since we are dealing with partial information, χ_b and P_b.

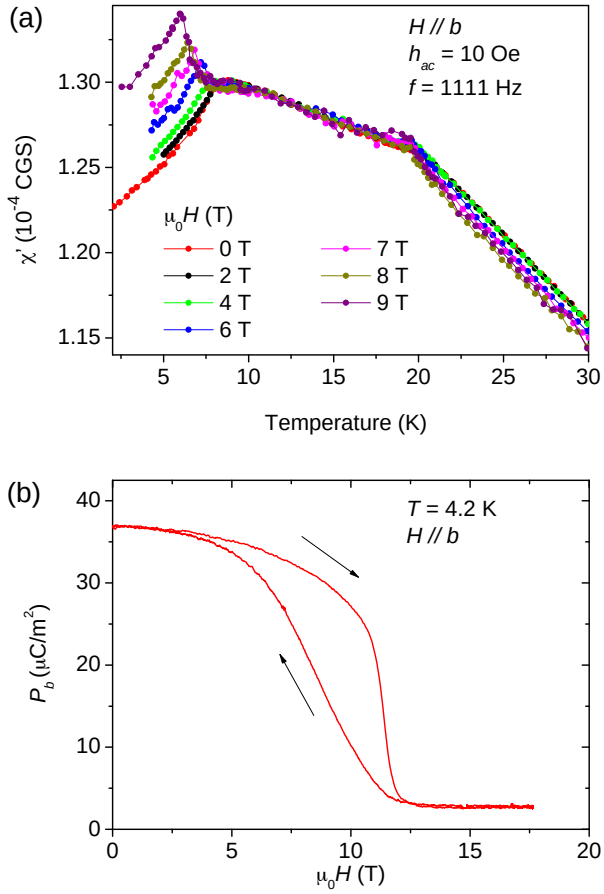

FIGURE 13.1: (a) Temperature dependence of the real ac-susceptibility at fixed superimposed dc fields along b. (b) Field dependence of the component along b of the electric polarization at 4.2 K.

With the aim of establishing the magnetic structures within the $(H \parallel b) - T$

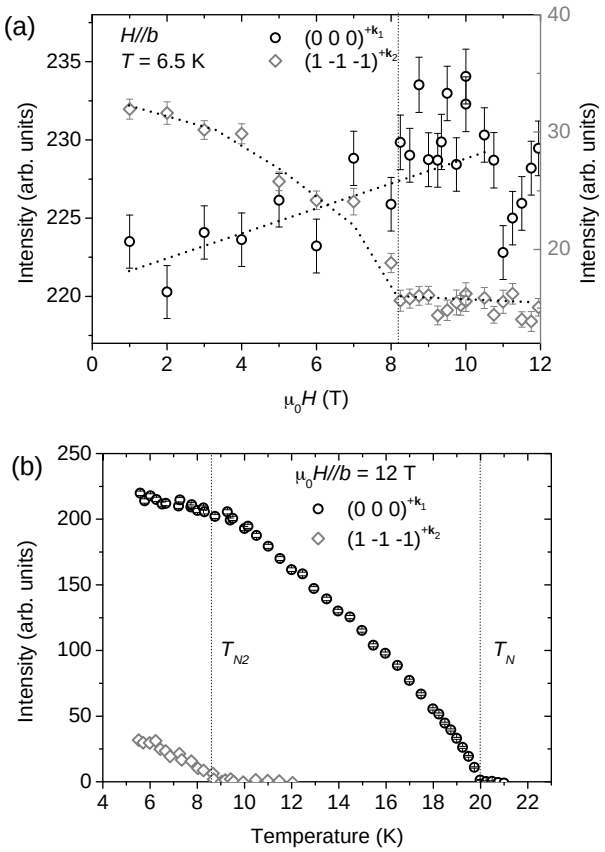

FIGURE 13.2: (a) Field dependence of the $(0\ 0\ 0)^{+\mathbf{k}_1}$ and $(1\ -1\ -1)^{+\mathbf{k}_2}$ magnetic reflections at 6.5 K with magnetic field along b. (b) Temperature dependence of the $(0\ 0\ 0)^{+\mathbf{k}_1}$ and $(1\ -1\ -1)^{+\mathbf{k}_2}$ reflections with 12 T field applied along b.

phase diagram, a neutron diffraction experiment was performed on D23. Figure 13.2(a) illustrates the field dependence of the $(0\ 0\ 0)^{+\mathbf{k}_1}$ and $(1\ -1\ -1)^{+\mathbf{k}_2}$ magnetic reflections at 6.5 K with magnetic field along b, $\mathbf{k}_1 = (\frac{1}{2}, 0, 0)$ being the propagation vector that corresponds to the collinear AF4 phase and $\mathbf{k}_2 \approx$ (-0.211, $\frac{1}{2}$, 0.452) the one associated to the incommensurate part of the conical structure. The evolution of the commensurate reflection does not show any evident indication of any transition, in contrast to the behavior of the incommensurate reflections. The intensity of this latter reflection has a downward tendency up to 8 T: above this field, the intensity becomes constant. It is worth noting that the intensity of the incommensurate peak, even weak, is non-zero above the transition, and consequently, the hypothesis that the AF4 phase alone was extended to lower temperatures is ruled out immediately. The existence of the incommensurate

wave vector was double-checked by monitoring commensurate and incommensurate reflections, as the temperature increases under high field [Fig. 13.2(b)]. The figure shows that the incommensurate reflection exists up to around 8.7 K, coinciding with the T_{N2} transition temperature attributed to the AF4-to-conical transition at zero field, see Chapter 8.

According to these observations, the new high-field state must correspond to a double-**k** structure. The integrated intensity of the magnetic satellites of (h k l)$^{+\mathbf{k}_1}$ and (h k l)$^{+\mathbf{k}_2}$ were collected at 6.5 K at zero field, 7 T and 12 T (about 45 reflections of each kind). The results of the refinements are gathered in Table 13.1 and confirm that a conical spin-arrangement can explain the high field data. The collinear part of the conical structure remains unchanged whereas the incommensurate component, i. e. the cycloidal part, is modified. The plane where the magnetic moments are located turns 90° and becomes perpendicular to the external field. The refinement of the data at 7 T suggest that the transition occurs as it does in the pure $MnWO_4$ when the external field aligned parallel to b, that is, the m_b-spin component decreases with increasing field until it flops perpendicular to the it.

Temperature		T = 6.5 K	T = 6.5 K	T = 6.5 K	T = 6.5 K	T = 6.5 K	T = 6.5 K
Magnetic field ($H \parallel b$)		0 T	0 T	7 T	7 T	12 T	12 T
k		$\mathbf{k}_1^0$	$\mathbf{k}_2^0$	$\mathbf{k}_1$	$\mathbf{k}_2$	$\mathbf{k}_1$	$\mathbf{k}_2$
Mn_1	$\Re(m)(\mu_B)$	2.47(2)	1.71(7)	2.49(2)	1.74(6)	2.47(2)	1.69(9)
	ϕ_u	0°	0°	0°	0°	0°	0°
	θ_u	141(1)°	40(5)°	140(1)°	44(3)°	141(1)°	42(4)°
	$\Im(m)(\mu_B)$		-1.70(2)		-1.18(8)		-0.6(1)
	ϕ_v		90°		90°		0°
	θ_v		90°		90°		-48(4)°
Mn_2		$\mathbf{u}_2 = \mathbf{u}_1$	$\mathbf{u}_2 = -\mathbf{u}_1$	$\mathbf{u}_2 = \mathbf{u}_1$	$\mathbf{u}_2 = -\mathbf{u}_1$	$\mathbf{u}_2 = \mathbf{u}_1$	$\mathbf{u}_2 = -\mathbf{u}_1$
		$\mathbf{v}_2 = \mathbf{v}_1 = 0$	$\mathbf{v}_2 = -\mathbf{v}_1$	$\mathbf{v}_2 = \mathbf{v}_1 = 0$	$\mathbf{v}_2 = -\mathbf{v}_1$	$\mathbf{v}_2 = \mathbf{v}_1 = 0$	$\mathbf{v}_2 = -\mathbf{v}_1$
$\Delta\varphi$		0	$\frac{k_z}{2}$	0	$\frac{k_z}{2}$	0	$\frac{k_z}{2}$
R_{F^2}/%		10.3	14.0	9.25	12.5	8.99	12.6
R_{F^2w}/%		5.40	10.6	5.12	8.11	4.79	6.85
R_F/%		15.3	20.1	13.5	16.6	13.1	26.8
χ^2		4.70	1.43	4.24	0.54	3.59	0.16

TABLE 13.1: Parameters that describe the magnetic structures of the $Mn_{0.80}Co_{0.20}WO_4$ at 6.5 K under 0 T, 7 T and 12 T field along the b axis. For simplicity the following notation has been used: $\mathbf{k}_1 = (\frac{1}{2}, 0, 0)$ and $\mathbf{k}_2$ = [-0.215(1), $\frac{1}{2}$, 0.452(2)].

This new scenario with a high-field-conical structure explains the absence of electric polarization along b. However, this structure could give rise to some polarization within the *ac* plane, and therefore, this should be further studied.

Summarizing, applying an external magnetic field along the b axis of the $Mn_{0.80}Co_{0.20}WO_4$ compound only modifies the conical-antiferromagnetic struc-

ture by re-orienting the semi-axes of the cycloidal part of it. Concomitant to the re-orientation of the rotation plane of the spins, the electric polarization along b disappears, and probably flops onto the ac plane. As a result, we propose the phase diagram of Fig. 13.3 that takes into account all this information.

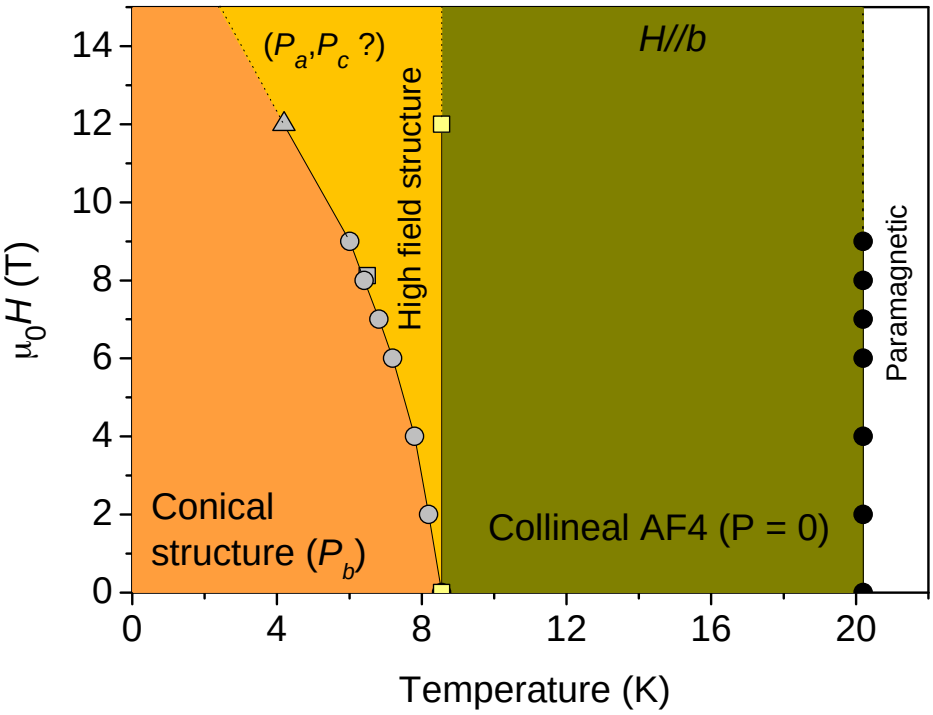

FIGURE 13.3: Phase diagram for $Mn_{0.80}Co_{0.20}WO_4$ compound with $H \parallel b$. Circles come from bulk magnetic measurements, triangles from polarization measurements and squares from neutron diffraction.

13.1.2 Similar behavior for $H \parallel a + 90^\circ$

Bulk magnetic measurements and polarization measurements performed on the same crystal with the field applied along the so-called hard-magnetic axis ($a + 90^\circ$), revealed a behavior similar to the one observed with $H \parallel b$. The real component of the ac-susceptibility along $a + 90^\circ$ mimics the χ'_b as a function of the temperature at different external fields. As observed in Fig. 13.4(a), the Néel temperature is the same for fields up to 9 T, while the second transition (AF4-to-conical) is shifted to lower temperatures as the field increases. The transitions were observed only in the conical phase and require more than 9 T below 5 K [see Fig. 13.4(b)].

The response of the b component of the electric polarization to the field parallel to the hard magnetic axis also mimics the response of $P_b(H \parallel b)$ to field. It disappears at about 12.5 T and exhibits a wide hysteresis (at 4.2 K), illustrated in Fig. 13.4(c).

Therefore, based on these experimental evidences we propose a preliminary phase diagram for this orientation, depicted in 13.4(d). The $H \parallel \alpha + 90^\circ$ phase diagram is very much the same as the one for $H \parallel b$. Of course, further polarization measurements a neutron diffraction experiments are necessary to confirm this hypothesis.

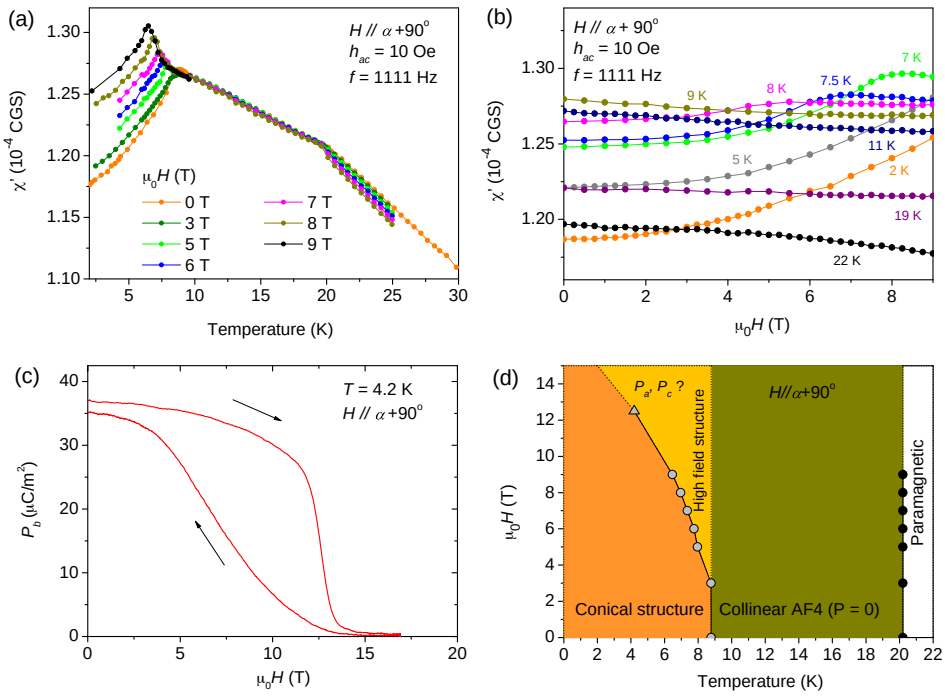

FIGURE 13.4: (a) Temperature dependence of the real ac-susceptibility at fixed superimposed dc fields along $\alpha + 90^\circ$. (b) Field dependence of the real ac-susceptibility at fixed temperatures with the field along $\alpha + 90^\circ$. (c) Field dependence of P_b at 4.2 K. (d) $H - T$ phase diagram proposed for $Mn_{0.80}Co_{0.20}WO_4$ compound with $H \parallel \alpha + 90^\circ$ based on bulk magnetic measurements, polarization measurements and the results obtained with $H \parallel b$. Circles result from bulk magnetic measurements and triangles from polarization measurements.

13.2 Stabilization of the cycloidal AF2 phase in $H \parallel a$ configuration

Applying a magnetic field along the easy-magnetic axis modifies completely the scenario. The stability of the magnetic structures is reversed compared to the previous cases, i. e. the collinear structure is destabilized and disappears, and the incommensurate component of the cone replaces of the collinear part. Bulk magnetic measurements [see Fig. 13.5(a)] show that the maximum in the susceptibility, attributed to the Néel temperature, moves to lower temperatures as the field is increased. Moreover, the AF4-to-conical transition, which is not visible in $\chi_a(H = 0)$ within the experimental resolution, is evidenced as the external field increases, and suggests a reorientation of the moments in the low temperature phase. As observed in Fig. 13.5(b) the behavior of isothermal χ in the conical structure suggests a magnetic transition at field higher than 9 T. For the detection of those transitions, pulsed high fields were used and this technique demonstrates that the conical structure transforms into some other spin configuration at about 12.7 T field, see Fig. 13.5(c). The isothermal dM/dH curves reveal that the transition from the AF4 phase to presumably the paramagnetic state is broader than the transition from the conical structure to the high field phase. Note that the curve labeled as 9.3 K, has actually been measured at somewhat lower temperature which falls in the region where the conical phase exists (below T_{N2} = 8.5 K). This discrepancy has been attributed to the magnetocaloric effect (the change in the spin entropy as a function of magnetic fields) and the lack of time needed to reach thermal equilibrium during the short pulse duration (of the order of few msec). Though the influence of this effect on the temperature in our measurements has been firmly established, it is not easy to say how much the real sample temperature differs from the reading of the thermometer (at least because the magnetocaloric effect at different temperatures is different).

The response of the electric polarization along b, P_b, is completely different to the previous cases. The P_b component of the electric polarization first increases linearly up to 12.5 T and then increases more rapidly, see Fig. 13.6. This behavior agrees with the previously proposed hypothesis: the field along a induces some modification of the incommensurate part of the conical structure, such as a small re-orientation of the semi axes or an increase of the m_b component, and then at about 12.5 T the collinear component of the structure disappears and contributes to the incommensurate one, increasing rapidly the P_b component.

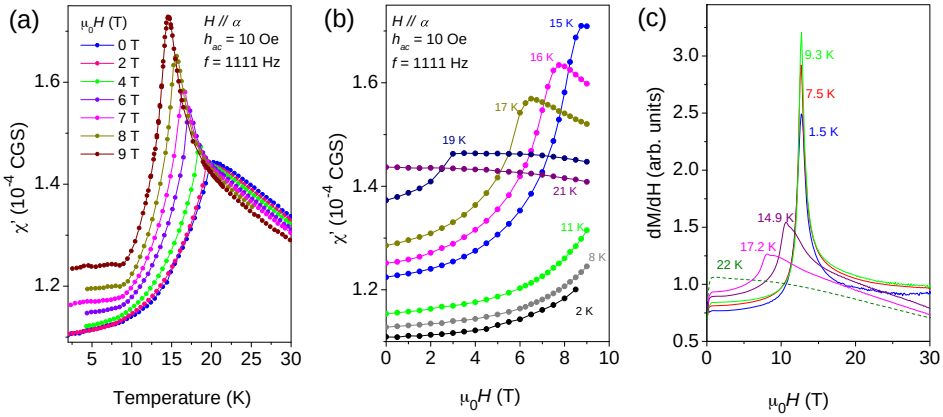

FIGURE 13.5: (a) Temperature dependence of the real ac-susceptibility at fixed superimposed dc fields along a. (b) Field dependence of the real ac-susceptibility at fixed temperatures with the field along a. (c) dM/dH isothermal curves obtained by pulsed magnetic fields.

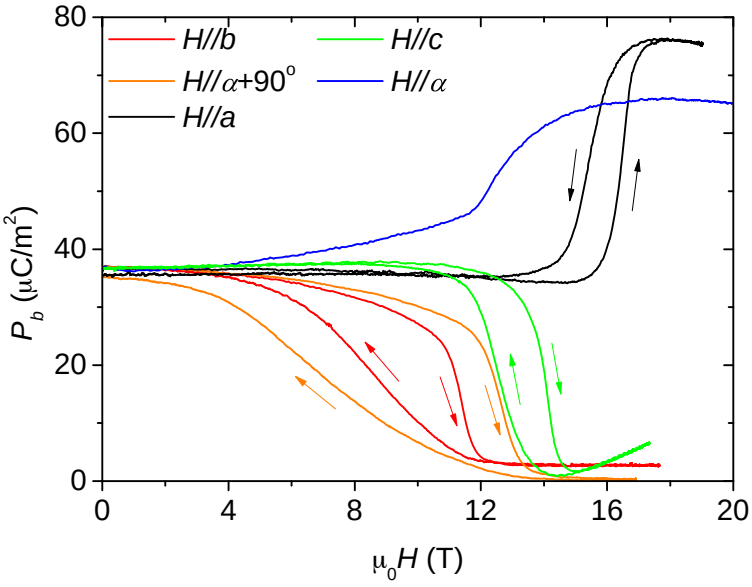

FIGURE 13.6: Field dependence of P_b at 4.2 K with H parallel to b, a, $a + 90°$, a and c.

With all this information we have built phase diagram from the susceptibility in $H \parallel a$ (Fig. 13.7). The black rhombs represent the transition fields obtained by pulsed magnetic fields and because of the magnetocaloric effect they have moved to lower temperatures to match the ac-susceptibility data. The proposed AF2 structure for the high field phase must be checked by neutron diffraction.

The effect of the field on the electric polarization was not only studied along the b axis and the main magnetic axes but also along the crystallographic ones. Figure 13.6 shows that P_b has a similar behavior when the field is along b, c or $\alpha + 90^\circ$, and that this behavior is different when the field is along a or α. Therefore, it is reasonable to study by means of neutrons the effect of the field applied along a to try to elucidate which could be the high field phase in such case. For that experiment on D23, 6 T was the highest field available. However it was enough to see that the amplitude of the commensurate part at 2 K slightly decreases compared to the zero-field AF4 structure (Table 8.4), whereas in the incommensurate part there is a re-orientation of one semi axis towards the c axis (perpendicular to the field) and an augmentation of the m_b spin component. The refined parameters are summarized in Table 13.2.

Temperature		T = 2 K	T = 2 K
Magnetic field ($H \parallel a$)		6 T	6 T
k		$\mathbf{k}_1$	$\mathbf{k}_2$
Mn_1	$\Re(m)(\mu_B)$	3.04(5)	2.80(2)
	ϕ_u	0°	0°
	θ_u	142(2)°	40(7)°
	$\Im(m)(\mu_B)$		-3.0(1)
	ϕ_v		90°
	θ_v		90°
Mn_2		$\mathbf{u}_2 = \mathbf{u}_1$	$\mathbf{u}_2 = -\mathbf{u}_1$
		$\mathbf{u}_2 = \mathbf{u}_1$	$\mathbf{v}_2 = -\mathbf{v}_1$
$\Delta\varphi$		0	$\frac{k_z}{2}$
R_{F^2}/%		5.67	6.41
R_{F^2w}/%		6.16	6.30
R_F/%		6.65	5.58
χ^2		7.14	7.37

TABLE 13.2: Parameters that describe the magnetic structures of the $Mn_{0.80}Co_{0.20}WO_4$ at 2 K under 6 T field along the a axis. For simplicity the following notation has been used: $\mathbf{k}_1 = (\frac{1}{2}, 0, 0)$ and $\mathbf{k}_2$ = [-0.215(1), $\frac{1}{2}$, 0.452(2)].

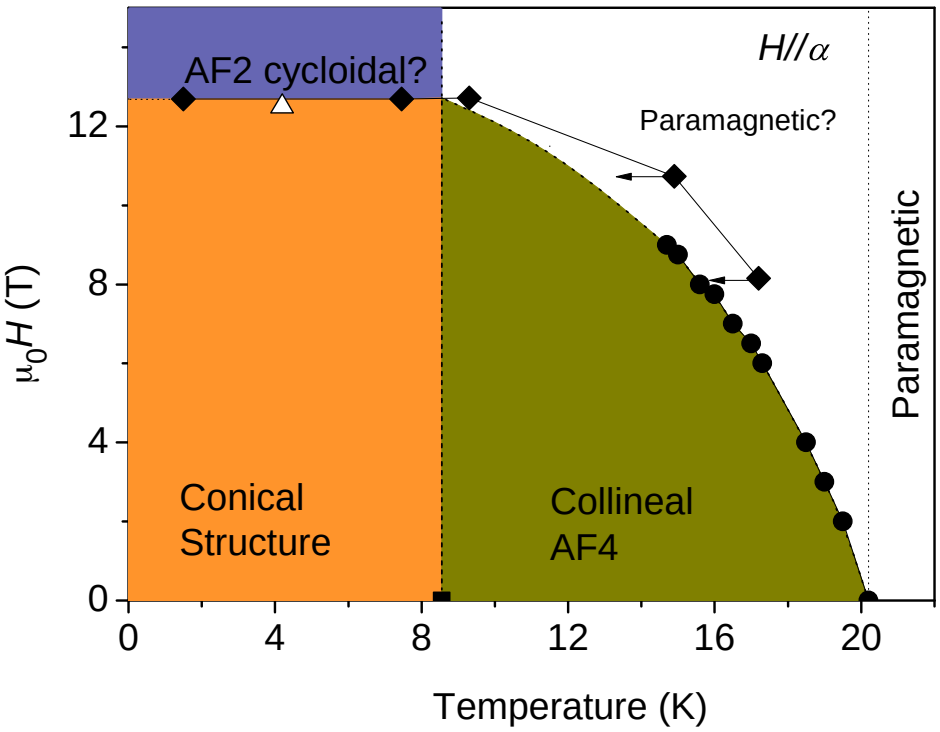

FIGURE 13.7: $H - T$ phase diagram proposed for $Mn_{0.80}Co_{0.20}WO_4$ compound with $H \parallel a$ based on bulk magnetic measurements and polarization measurements with $H \parallel a$. Circles are obtained from magnetic measurements, rhombs from pulsed high field measurements (which has to be moved to lower temperature, as indicated by the arrows to correct for the magnetocaloric effect) and triangles from polarization measurements.

13.3 Summary and conclusions

Along this chapter the influence of an external field in the $Mn_{0.80}Co_{0.20}WO_4$ composition has been investigated and the results demonstrate that the stability of the different phases that appear at zero field strongly depends on the direction along which the field is applied.

When $H \parallel b$ and $H \parallel a + 90^\circ$, the collinear AF4 phase does not undergo any significant change in fields at least up to 12 T, but on the contrary, in the conical structure the rotation plane of the moments flops perpendicular to the field at a critical fields that decrease with increasing temperature (from about 15 T at 2 K towards zero at T_{N2}). This transition is accompanied by the disappearance of P_b. The high field magnetic structure allows electric polarization within the ac plane.

The parameters of this high field structure and how it evolves from the one at zero field have been determined by neutron diffraction.

If the external field is applied along the a axis, the situation is reversed: AF4 becomes unstable and disappears with increasing the field and the incommensurate part of the cone undergoes small variations. At high fields, it is likely that the conical structure becomes a pure cycloidal structure with the electric polarization along b.

Part IV

Summary and Conclusions

Summary and Conclusions

To summarize, throughout the thesis several aspects of the $Mn_{1-x}Cox WO_4$ family (x =0, 0.05, 0.10, 0.15 and 0.20) have been investigated:

(i) Crystalline structure: both the effect of the doping and the influence of the magnetic ordering on the crystal structure has been explored. A very weak spin-lattice coupling detectible only by Larmor diffraction and high resolution X-ray powder diffraction, was documented for three representative $Mn_{1-x}Cox WO_4$ compositions, $x = 0$, $x = 0.05$ and $x = 0.20$. The evolution of the cell parameters across the magnetic transitions of the latter two compounds is different, as their magnetic structures are. The monoclinic angle β decreases monotonously in the $x = 0.05$ composition that does not undergo any change in the orientation plane where spins are confined. On the contrary, in $x = 0.20$, the monoclinic angle has a minimum close to the multiferroic transition, below the transition β starts increasing. This coincides with the appearance of the conical spin arrangement. On the other hand, the unit-cell volume decreases with increasing the Co concentration, with no change in the orientation of the octahedra.

(ii) The zero field magnetic structures of all the compositions have been determined, and therefore a complete description of the structures has been given. Their corresponding electric ordering has being provided as well.

(iii) The detailed study of the magnetic structures allowed us to observe big

temperature-induced-variations in the characteristics of an ellipse (ϵ and amplitudes of the semi-axes) within temperature ranges of about 10 K.

(iv) Co^{2+} (strongly anisotropic ion) substitution for Mn^{2+} (an isotropic ion) above 10% results in anisotropic paramagnetic susceptibility, reflecting in different paramagnetic temperatures along different directions and also suggests an orbital contribution to the effective magnetic moments.

(v) 15 % of cobalt is enough to orient the easy-magnetic axis close to the pure $CoWO_4$'s one. At this doping the AF4 phase (proper of $CoWO_4$) is already very stable, however at low temperatures competing phases emerge and coexist due to high degree of magnetic frustration. This shows that at $x = 0.15$ concentration the effect of the single ion anisotropy of the cobalt is slightly stronger than the rest of the interactions. It could be considered as the boundary concentration that separates two regions: $x < 0.15$, where the Co^{2+} single ion anisotropy competes with the Mn^{2+} one; $x > 0.15$ where the effect of the cobalt is dominant in the system.

(vi) Superspacial formalism[1] has been applied to re-examine the incommensurate magnetic structures of the pure $MnWO_4$. The study let us conclude that the manganese atoms within the crystallographic unit cell are related in the AF3 phase, whereas in the AF2 phase they become independent. Consequently the polarization arises along b. In the case of $x = 0.10$, in the multiferroic phase, both manganese atoms are still related by a mirror plane, and this yields to electric polarization in the ac plane.

This formalism allowed us to propose a new magnetic model for describing the AF3 phase: as an alternative to the widely accepted collinear and sinusoidally modulated structure, a cycloidal magnetic structure is put forward. Though, both manganese atoms have different chirality, which results in opposite electric polarization. This model corresponds to an antiferroelectic one.

(vii) Evidence for coexistence of the nonpolar-collinear commensurate magnetic phase, AF1, and the polar cycloidal structure, AF2, during the field-induced AF2-to-AF1 transition in $MnWO_4$ is provided based on incremental magnetic susceptibility results. These data also suggest that a trace of AF2 domains exist at temperature lower than the AF2-AF1 boundary of the zero

[1]The application of superspace formalism to the analysis of incommensurate magnetic phases is a promising development with yet few examples in the literature.

magnetic field phase diagram (this observation could be regarded as a support for existence of AF2 *embryos* being responsible for the recently published polarization memory effect).

(viii) We have determined the high field X-phase of the pure $MnWO_4$: a cycloidal structure within the *ac* plane that gives rise to electric polarization within the *ac* plane. In analogy to the $Mn_{0.90}Co_{0.10}WO_4$, the X phase has been named as AF2′. An abrupt transition has been proposed to describe the AF2-to-AF2′ transition: a increase of the eccentricity upon increasing field until the rotation plane of the spins flops perpendicular to the field.

(ix) The effect of a magnetic field along the *b* axis on $Mn_{0.95}Co_{0.05}WO_4$ has been investigated: The multiferroic AF2 phase with spin-cycloid structure in the αb plane and with polarization along *b* undergoes a continuos transition from the αb plane to the $w\alpha$ plane, being $w = \alpha + 90^\circ$ the hard direction[2]. A complete phase diagram is proposed based on the results from magnetic, polarization and neutron diffraction studies. Bulk magnetic measurements and the evolution of certain magnetic reflections clearly demonstrate a field-induced transition with $H \parallel \alpha$, though neutron-diffraction experiments were not conclusive about the spin arrangement.

(x) The multiferroic AF2′ of $Mn_{0.90}Co_{0.10}WO_4$ remains stable in magnetic field as high as 15 T applied along the *b* axis, while in field along *c* and *a* axes the spin-cycloid structure flops from the *ac* plane to directions almost perpendicular to the magnetic field at $\sim$ 3 T and $\sim$ 8.5 T, respectively. Those spin reorientations are accompanied by a dramatic suppression of both P_a and P_c components of the polarization.

(xi) The stability of the distinct phases that appear in $Mn_{0.80}Co_{0.20}WO_4$ at zero field strongly depends on the direction along which the field is applied.

When $H \parallel b$ and $H \parallel \alpha + 90^\circ$, the collinear AF4 phase does not undergo any significant change in fields at least up to 12 T. On the contrary, in the conical structure the rotation plane of the moments flops perpendicular to the field at a critical fields. The critical field decreases with increasing temperature (from about 15 T at 2 K towards zero at T_{N2}). This transition is accompanied by the disappearance of P_b. The high field magnetic structure allows electric polarization within the *ac* plane.

[2]This evolution of the plane was suggested by Liang *et. al.* [129] but our neutron diffraction study unambiguously confirmed it.

If the external field is applied along the a axis, the situation is reversed: AF4 becomes unstable and disappears with increasing the field and the incommensurate part of the cone undergoes small variations. At high fields, it is likely that the conical structure becomes a pure cycloidal structure with the electric polarization along b.

(xii) Magnetic phase diagrams for fields along different directions are proposed based on the results from magnetic, polarization and neutron-diffraction studies.

When writing the thesis, several studies on the topic has been advanced or completed, but those results are not included in the thesis. I would like to mention the magnetic studies up to very high fields of up to 60 T, which have allowed us to track all the field-induced transitions that take place before the field finally forces the moments to align parallel to it, and thus to construct the complete magnetic phase diagrams for two of the compositions.

During the thesis we have fulfilled most of our purposes, however new questions have emerged that should be addressed by further investigations:

(i) What is the AF5 magnetic structure? Is it equal to AF2'?

(ii) Is the AF3 phase really an antiferroelectric one?

(iii) What underlying in the $Mn_{0.90}Co_{0.10}WO_4$ to have a completely different symmetry and consequently different properties?

(iv) What is the origin of the magnetic-history effect on zero-field propagation-vector the observed in $Mn_{0.90}Co_{0.10}WO_4$?

(v) What magnetic structures are induced in $Mn_{0.95}Co_{0.05}WO_4$ when the magnetic field is applied along a?

(vi) What are the magnetic structures at high field and low temperature in $Mn_{0.80}Co_{0.20}WO_4$ either with field along a or b axis?

So, finding the answer to those questions could be the continuation of the work in a near future.

Bibliography

[1] W. C. Rôntgen, Ann. Phys. **35**, 264 (1888).

[2] P. Curie, J. Physique **3**, 393 (1894).

[3] D. N. Astrov, Zh. Exp. Teor. Fiz. 38, 984 (1960).

[4] I. Dzyaloshinskii, Zh. Exp. Teor. Fiz., 37, 881 (1959).

[5] G.A. Smolenskii, A.I. Agranovskaya, S.N. Popov, and V.A. Isupov, Zh. Tekh. Fiz. **28**, 2152 (1958) [Sov. Phys. Tech. Phys. **3**, 1981 (1958)].

[6] E. Ascher, H. Rieder, H. Schmid and H. Stössel, J. Appl. Phys. **37**, 1404-1405 (1966).

[7] H. Schmid, Ferroelectrics, **162**, 317 (1994).

[8] W. Eerenstein, N. D. Mathur and J. F. Scott. Nature **442**, 759 (2006).

[9] Nicola A. Hill, J. Phys. Chem. B **104**, 6694-6709 (2000).

[10] W. Kleemann, Physics **2**, 105 (2009).

[11] D. Khomskii, Physics **2**, 20 (2009).

[12] J. Wang, Science **299**, 1719 (2003).

[13] G. A. Smolenskii, I. E. Chupis, Sov. Phys. Usp. **25** 475 (1982)

[14] T. Kimura, et. al. Phys. Rev. B **68** 180401, (2003).

[15] J. van den Brink and D. I. Khomskii, J. Phys.: Condens. Matter **20**, (2008) 434217.

[16] C. Jardon, F. Rivadulla, L. E. Hueso, A Fondado, M. A. Lopez-Quintela, J. Rivas, R. Zysler, M. T. Causa and R. D. Sanchez, J. Magn. Mater. **196** 475, (1999).

[17] S. Mercone, A. Wahl, A. Pautrat, M. Pollet and C. Simon, Jhys. Rev. B **69** 174433, (2004).

[18] G. T. Rado and J. M. Ferrari, Phys. Rev. B **12** 5166 (1975).

[19] Y. Miyamoto and S. Chikazumi J. Phys. Soc. Japan **57** 2040, (1988).

[20] Y. Miyamoto and S. Ishihara, T. Hirano, M. Takada and N. Suzuki, Solid State Sommun. **89** 51, (1994).

[21] N. Ikeda, K. Kohn, N. Myouga, E. Takahashi, H. Kitoh and S. Takekawa, J. Phys. Soc. Japan **69**, 1526 (2000).

[22] B. B. van Aken, T. T. M. Palstra, A. Filippetti and N. A. Spaldin, Nature Mater. **3**, 164 (2004).

[23] T. Kimura, T. Goto, H. Shintani, K. Ishizaka, T. Arima and Y. Tokura, Nature 426, 55-58 (2003).

[24] I. Dzyaloshinskii, J. Phys. Chem. Solids Pergamon Press 1958. Vol. 4. pp. 241-255.

[25] T. Moriya, Phys. Rev. Vol. 120, 1 (1960).

[26] I. A. Sergienko and E. Dagotto, Phys. Rev. B **73**, 094434 (2006).

[27] H. Katsura, N. Nagaosa and A. Balatsky, Phys. Rev. Lett. **95**, 057205 (2005).

[28] N. Nagaosa, J. Phys.: Condens. Matter 20 (2008) 434207.

[29] N. Hur, Nature **429**, 392 (2004).

[30] O. Heyer, H. Hollmann, I. Klassen, S. Jodlauk, L. Bohatỳ, P. Becker, J. A. Mydosh, T. Lorenz and D. Khomskii, J. Phys.: Condens. Matter 18 (2006) L417-L475.

[31] A. H. Arkenbout, T. T. M. Palstra, T. Siegrist, and T. Kimura, Phys. Rev. B 74, 184431 (2006).

[32] T. H. Arima, Jounal of the Physical Society of Japan **76**, 073702 (2007).

[33] Y. J. Choi, H. T. Yi, S. Lee, Q. Huang, V. Kiryukhin, S. -W. Cheong, Phys. Rev. Lett. **100**, 047601 (2008).

[34] J. A. Alonso, J. L. García Muñoz, M. T. Fernandez-Diaz, M. A. G. Aranda, M. J. Martinez-Lope and M. T. Casais, Phys. Rev. Lett. **82** 3871 (1999).

[35] J. L. García Muñoz, J. Rodriguez Carvajal, P. Lacorre, Phys. Rev. B **50** 978 (1994).

[36] S. Picozzi, K. Yamauchi, B. Sanyal, I. A. Sergienko and E. Dagotto, Phys. Rev. Lett. **99** 227201, (2007).

[37] I. A. Sergienko, C. Sen and E. Dagotto, Phys. Rev. Lett. **97**, 227204 (2006).

[38] L. N. Bulaevskii, C. D. Batista, M. V. and D. I. Khomskii, Phys. Rev. B **78**, 024402 (2008).

[39] J. Valasek Phys. Rev. 17, 475 (1921).

[40] http://en.wikipedia.org/wiki/Antiferroelectricity

[41] C. Kittel, Phys. Rev. 82, 729 - 732 (1951).

[42] C. Pulvari, Phys. Rev. 120, 1670-1673 (1960).

[43] K. Lonsdale, Rep. Prog. Phys. 4 368, (1937).

[44] P. Boutron, Phys. Rev. B 9, 7 (1974).

[45] V. Skumryev, M. D. Kuz'min, M. Gospodinov and J. Fontcuberta, Phys. Rev. B 79, 212414 (2009).

[46] L. Néel, Comptes Rendus Hebbdomadaires des Seances de l'Academie des Sciences, 202, 304-306 (1936).

[47] C. G. Shull, W. A. Strauser and E. O. Wollan, Phys. Rev., 83, 333 (1951).

[48] A. Yoshimori, J. Phys. Soc, Jpn, 14 (1959) 807-821.

[49] T. Nagamiya, J. Appl. Phys. 33, 1029 (1962).

[50] Y. Kitano and T. Nagamiya, Progress of Theor. Physics 31, 1-43 (1964).

[51] T. Goto, T. Kimura, G. Lawes, A. P. Ramirez and Y. Tokura, Phys. Rev. Lett. 92, 257201 (2004).

[52] I. Tsukada, X. F. Sun, Seiki Komiya, A. N. Lavrov, and Yoichi Ando, Phys. Rev. B 67, 224401 (2003).

[53] J.T. Chalker, "Introduction to Frustrated Magnetism, Materials, Experiments, Theory" Springer Series in Solid-State Sciences ISSN 0171-1873.

[54] H. T. Diep and H. Giacomini, "Frustrated Spin Systems",

[55] A. P. Ramirez, in Handbook of Magnetic Materials, edited by K. H. J. Buschow, North-Holland, Amsterdam, 2001, Vol. 13

[56] A. A. Tsirlin, A. Möller, B. Lorenz,3 Y. Skourski, and H. Rosner, Phys. Rev. B 85, 014401 (2012).

[57] E. F. Bertaut, 1968 Acta Crystallogr. A 24 217.

[58] E. F. Bertaut, 1971 J. Physique 32 C1-462.

[59] L. D. Landau and E. M. Lifshitz, "Statistical Physics" Pergamon, Oxford, 1958.

[60] A. Janner and T. Janssen 1980 Acta Crystallogr. A 36 399 (1980).

[61] V. Petricek, M. Dusek and L. Palatinus 2006 Jana2006. The crystallographic computing system. Institute of Physics, Praha, Czech Republic.

[62] A. Schonleber, J. Angelkort, S. van Smaalen, L. Palatinus, A. Senyshyn and W. Morgenroth, Phys. Rev. B 80 064426 (2009).

[63] A. M. Abakumov, A. A. Tsirlin, J. M. Perez-Mato, V. Petricek, H. Rosner, T. Yang and M. Greenblatt, Phys. Rev. B 83 214402 (2011).

[64] J. L. Ribeiro, 2010 J. Phys.: Conf. Ser. 226 012013.

[65] J. L. Ribeiro and J. M. Perez-Mato, J. Phys: Condens. Matter 23 (2011) 446003.

[66] J. M. Perez-Mato, J. L. Ribeiro, V. Petricek, M. I. Aroyo, J. Phys.: Condens. Matter 24, (2012) 163201.

[67] M. Janoschek, P. Fischer, J. Schefer, B. Roessli, V. Pomjakushin, M. Meven, V. Petricek, G. Petrakovskii and L. Bezmaternikh, Phys. Rev. B 81 094429 (2010).

[68] V. Petricek, J. Fuksa and M. Dusek, Acta Cryst. A66, 649-655 (2010).

[69] http://en.wikipedia.org/wiki/Hübnerite

[70] R. Bharrati, R. A. Singh and B. M. Wnaklyn, J. Phys. Chem. Solids Vol. 43, No. 7, 641-644 (1982).

[71] M. A. K. L. Dissanayake, O.A. Ileperuma, P.A.G.D Dharmasena, J. Phys. Chem. Solids Vol. 50, No. 4, 359-361 (1989).

[72] M. A. P. Almeida, L. S. Cavalcante, M. Siu Li, J. A. Varela and E. Longo, J Inorg Organomet Polym (2012) 22:264-271.

[73] H. Y. He, Res. Chem. Intermed. (2011) 37:1057-1067.

[74] W. M. Qu, WM, J.U. Meyer, A. Haeusler, Technisches Messen 63, 63-71 (1996).

[75] W. Qu and J. U. Meyer, Sensors and Actuators B: Chemical, Volume 7, Issues 1-3, March 1992, Pages 439-442.

[76] U. Dellwo, P. Keller, J.-U. Meyer Sensors and Actuators A 61 (1997) 298-302.

[77] Y. P. Simanov and R. D. Kurshakova, Zhurnal Fizicheskoi Khimii, 31, 820-824 (1957).

[78] St. Krustev, K. Ivanov and D. Klissurski, Journal of Alloys and Compounds, 182 (1992) 189-193.

[79] Shu-Jian Chen, Xue-Tai Chen, Ziling Xue, Jian-Hao Zhou, Jing Li, Jian-Ming Hong and Xiao-Zeng You, J. Mater. Chem., 2003, 13, 1132-1135.

[80] Shuijin Lei, Kaibin Tang, Zhen Fang, Yuhong Huang and Huagui Zheng, Nanotechnology 16 (2005) 2407-2411.

[81] Lei Zhang, Canzhong Lu, Yuansheng Wang and Yao Cheng, Materials Chemistry and Physics 103 (2007) 433-436

[82] H. Weitzel, Z. Kristallogr. 144, 238 (1976).

[83] L. G. Van Uitert, R. C. Sherwood, H. J. Williams, J. J. Rubin and W. A. Bonner, J. Phys. Chem. Solids 25, 1447-1451 (1964).

[84] H. Dachs, H. Weitzel and E. Stoll, Solid State Communications Vol. 4, 473-474 (1966).

[85] H. Dachs, Solid State Communications, Vol. 7, 1015-1017 (1969).

[86] C. P. Landee and E. F. Westrum, in Magnetism and Magnetic Materials, 1975 Proceedings of the 21^{st} Annual Conference on Magnetism and Magnetic Materials, edited by D. C. Graham and J. J. Thyne, AIP Conf. Proc. No. 29 (AIP, New York, 1976), pp. 445-446; J. Chem. Thermodyn. 8, 663 (1976).

[87] G. Lautenschläger, H. Wietzel, T. Vogt, R. Hock, A. Böhm and H. Fuess, Phys. Rev. B **48**, 6087 (1993).

[88] N. Hollmann, Z. Hu, T. Willers, L. Bohatỳ., P. Becher, A. Tanaka, H. H. Hsieh, H.-J. Lin, C. T. Chen and L. H. Tjeng, Phys. Rev. B 82, 184429 (2010).

[89] F. Ye, R. S. Fishman, J. A. Fernandez-Baca, A. A. Podlesnyak, G. Ehlers, H. A. Mook, Y. Wang, B. Lorenz and C. W. Chu, Phys. Rev. B 83, 140401 (2011).

[90] C. dela Cruz, F. Yen, B. Lorenz, Y. Q. Wang, Y. Y. Sun, M. M. Gospodinov and C. W. Chu, Phys. Rev. B 71, 060407(R) (2005).

[91] C. dela Cruz, B. Lorenz, Y. Y. Sun, C. W. Chu, S. Park and S.-W. Cheong, Phys. Rev. B 74, 180402(R) (2005).

[92] A. K. Zvezdin, G. P. VorobÕev, A. M. Kadomtseva, Yu. F. Popov, A. P. Pyatakov, L. N. Bezmaternykh, A. V. Kuvardin and E. A. Popova, JETP Letters 83, 509-514 (2006).

[93] L. I. Vergara, J. Cao, N. Rogado, Y. Q. Wang, R. P. Chaudhury, R. H. Cava, B. Lorenz and J. L. Musfeldt, Phys. Rev. B 80, 052303 (2009).

[94] H. C.Walker, F. Fabrizi, L. Paolasini, F. de Bergevin, J. Herrero-Martin, A. T. Boothroyd, D. Prabhakaran, D. F. McMorrow, Science 333, 1273 (2011).

[95] R. P. Chaudhury, F. Yen, C. R. dela Cruz, B. Lorenz, Y. Q. Wang, Y. Y. Sun, C. W. Chu, Physica B 403 1428-1430 (2008).

[96] H. Sagayama, K. Taniguchi, Nobuki Abe, Taka-hisa Arima, Minoru Soda, Masato Matsuura and Kazuma Hirota, Phys. Rev. B 77, 220407(R) (2008).

[97] A. Poole, P. J. Brown, A. S. Wills, J. Phys.: Conf. Ser. 145 (2009) 012074.

[98] H. Ehrenberg, H. Weitzel, R. Theissmann, H. Fuess, L. M. Rodriguez-Martinez and S. Welzel, Physica B 276-278 (2000) 644-645.

[99] K. Taniguchi, N. Abe, T. Takenobu, Y. Iwasa and T. Arima, Phys. Rev. Lett. 97, 097203 (2006).

[100] K. Taniguchi, N. Abe, H. Sagayama, S. Ohtani, T. Takenobu, Y. Iwasa, T. Arima, Phys. Rev. B 77, 064408 (2008).

[101] K. Taniguchi, N. Abe, H. Umetsu, H. Aruga Katori, and T. Arima, Phys. Rev. Lett. 101, 207205 (2008).

[102] K. Taniguchi, N. Abe, S. Ohtani, and T. Arima, Phys. Rev. Lett. 102, 147201 (2009).

[103] H. Nojiri, S. Yoshii, M. Yasui, K. Okada, M. Matsuda, J. -S. Jung, T. Kimura, L. Santodonato, G. E. Granroth, K. A. Ross, J. P. Carlo and B. D. Gaulin, Phys. Rev. Lett. 106, 237202 (2011).

[104] S. López-Moreno, A.H. Romero, P. Rodríguez-Hernández and A. Muñoz, High Pressure Research Vol. 29, No. 4, December 2009, 578-581.

[105] P. Becker, L. Bohatỳ, H.J. Eichler, H. Rhee, and A.A. Kaminskii, Laser Phys. Lett. 4, No. 12, 884-889 (2007).

[106] M. N. Iliev, M. M. Gospodinov, and A. P. Litvinchuk, Phys. Rev. B 80, 212302 (2009).

[107] A. B. Harris, Phys. Rev. B 76, 054447 (2007).

[108] P. Toledano, B. Mettout, W. Schranz, G. Krexner, J. Phys.: Condens. Matter 22 (2010) 065901.

[109] H. Ehrenberg, H. Weitzel, C. Heid, G. Wltschek, T. Kroener, J. van Tol and M. Bonnet, J. Phys.: Condens Matter 9 3189-3203 (1997).

[110] H. Ehrenberg, H. Weitzel and H. Fuess, Physica B 234-236 (1997) 560-563.

[111] R. D. Shapovalova, N. P. Mikhailova, and Ya. J. Gerasimov, Russ. J. Phys. Chem. 34, 978 (1960).

[112] J. Ferguson, D. L. Wood and K. Knox, J. Chem. Phys. 39, 881 (1963).

[113] H. Weitzel, Solid State Commun. 8, 2071-2072 (1970).

[114] H. Weitzel and H. Langhof, J. Magn. Magn. Mater. 4, 265-274 (1977).

[115] C. Wilkinson, M. J. Sprague, Z. Kristallogr. 145, 96 (1977).

[116] J. B. Forsyth and C. Wilkinson, K. Phys.: Condens. Matter 6 (1994) 3073-3080.

[117] H. Weitzel, Solid State Commun., Vol.7, pp. 1249-1252, (1969).

[118] E. Garcia-Matres, N. Stüßer, M. Hofmann and M. Reehuis, Eur. Phys. J. B 32, 35-42 (2003).

[119] R.C. Pullar, S. Farrah and N. McN. Alford, Journal of the European Ceramic Society 27 (2007) 1059-1063.

[120] R. P. Chaudhury, B. Lorenz, Y. Q. Wang, Y. Y. Sun and C. W. Chu, Phys. Rev. B 77, 104406 (2008).

[121] F. Ye, Y. Ren, J. A. Fernandez-Baca, H. A. Mook, J. W. Lynn, R. P. Chaudhury, Y.-Q. Wang, B. Lorenz and C. W. Chu, Phys. Rev. B 78, 193101 (2008).

[122] R. P. Chaudhury, B. Lorenz, Y. Q. Wang, Y. Y. Sun and C. W. Chu, New Journal of Physics 11, 033036 (2009).

[123] L. Meddar, M. Josse, P. Deniard, C. La, G. André, F. Damay, V. Petricek, S. Jobic, M.-H. Whangbo, M. Maglione, C. Payen, Chem. Mater., 21, 5203-5214 (2009).

[124] R. P. Chaudhury, F. Ye, J. A. Fernandez-Baca, B. Lorenz, Y. Q. Wang, Y. Y. Sun, H. A. Mook, and C. W. Chu, Phys. Rev. B 83, 014401 (2011).

[125] Y.-S. Song, J.-H. Chung, J. M. S. Park and Y.-N. Choi, Phys. Rev. B 79, 224415 (2009).

[126] Y.-S. Song, Li Qin Yan, Bumsung Lee, Sae Hwan Chun, Kee Hoon Kim, Sung Baek Kim, A. Nogami, T. Katsufuji, J. Schefer, J.-H. Chung, Phys. Rev. B 82, 214418 (2010).

[127] R. P. Chaudhury, F. Ye, J. A. Fernandez-Baca, Y.-Q. Wang, Y. Y. Sun, B. Lorenz, H. A. Mook, and C. W. Chu, Phys. Rev. B 82, 184422 (2010).

[128] M. Maczka, M. Ptak, K. Hermanowicz, A. Majchrowski, A. Pikul, and J. Hanuza, Phys. Rev. B 83, 174439 (2011).

[129] K.-C. Liang, R. P. Chaudhury, Y. Q. Wang, Y. Y. Sun, B. Lorenz, and C. W. Chu , J. Appl. Phys., 111, 07D903 (2012).

[130] Feng Ye, Songxue Chi, Jaime A. Fernandez-Baca, Huibo Cao, K.-C. Liang, Yaqi Wang, Bernd Lorenz, and C. W. Chu, Phys. Rev. B 86, 094429 (2012).

[131] K.-C. Liang, Y.-Q. Wang, Y. Y. Sun, B. Lorenz, F. Ye, J. A. Fernandez-Baca, H. A. Mook and C. W. Chu, New Journal of Physics 14 (2012) 073028.

[132] Francesco Maria Grimaldi, Physico mathesis de lumine, coloribus, et iride, aliisque annexis libri duo (Bologna ("Bonomia"), Italy: Vittorio Bonati, 1665), pages 1-11.

[133] http://en.wikipedia.org/wiki/Diffraction

[134] V. Scagnoli, M. Allieta, H. Walker, M. Scavini, T. Katsufuji, L. Sagarna, O. Zaharko, and C. Mazzoli, Phys. Rev. B 86, 094432 (2012).

[135] M. Garganourakis, Y. Bodenthin, R. A. de Souza, V. Scagnoli1, A. Dönni, M. Tachibana, H. Kitazawa, E. Takayama-Muromachi, and U. Staub, Phys. Rev. B 86, 054425 (2012).

[136] G. E. Johnstone, R. A. Ewings, R. D. Johnson, C. Mazzoli, H. C. Walker, A. T. Boothroyd, Phys. Rev. B, 85, 224403 (2012).

[137] A.-J. Dianoux and G. Lander, "Neutron Data Booklet", 2^{nd} edition (2003).

[138] M.T. Rekveldt, T. Keller, W.H.Kraan, Ellrophys. Lett, 54 (2001), 342-346.

[139] M.T. Rekveldt Maler. Sci. Forulll, 321-324 (2000), 258-263.

[140] M. T. Rekveldt, W. Kraan and T. Keller, Journal of Applied Crystallography ISSN 0021-8898

[141] J. Rodriguez-Carvajal, Physica B 192, 55 (1993).

[142] V. Esteve, *El método de Rietveld*, Publicacions de la Universitat Jaume I, (2006), ISBN 84-8021-575-5.

[143] H. B. Toby, Powder Diffraction, 21, 67-70 (2006).

[144] http://www.ill.eu/instruments-support/instruments-groups/instruments/d23/

[145] http://www.ill.eu/instruments-support/instruments-groups/instruments/in22/

[146] http://www-llb.cea.fr/fr-en/spectros_p.php

[147] http://www.esrf.eu/UsersAndScience/Experiments/Beamlines/beamline-snapshot?BeamlineID=ID31

[148] J. Brown and J. Matthewman, *Cambridge Crystallography Subroutine Library*, Report No. **RAL93-009** (1993).

[149] K. Momma and F. Izumi, J. Appl. Cryst. 44, 1272-1276 (2011).

[150] A. M. Balbashov, S. G. Egorov, J. Crys. Growth, 51, 498 (1981).

[151] L. Vegard. Die Konstitution der Mischkristalle und die Raumfüllung der Atome. Zeitschrift für Physik, 5-17 (1921).

[152] R. D. Shannon, Acta Crystallogr., Sect. A: Crst. Phys., Diffr., Theor. Gen. Crystallogr. A32, 751 (1976).

[153] P. G. Radaelli, and L. C. Chapon, Phys. Rev. B 76, 054428 (2007).

[154] M. I. Aroyo, A. Kirov, C. Capillas, J. M. Perez-Mato and H. Wondratschek, Acta Cryst. A 62 115 (2006).

[155] B. J. Campbell, H. T. Stokes, D. E. Tanner and D. M. Hatch, J. Appl. Cryst. 39607 (2006) and stokes.byu.edu/isodistort.html.

[156] W. C. Hamilton, Acta Cryst. 18, 502 (1965).

[157] Y. Noda, H. Kimura, Y. Kamada, Y. Ishikawa, S. Kobayashi, Y. Wakabayashi, H. Sawa, N. Ikeda and K. Kohn, J. Korean Physical Society 51, 828 (2007).

[158] Y Noda, H. Kimura, M. Fukunaga, S. Kobayashi, I. Kagomiya and K. Kohn, J. Phys.: Condens. Matter 20 (2008) 434206.

[159] H. Schmid, J. Phys.: Condens. Matter **20**, 434201 (2008).

[160] P. Stamenov and J.M.D. Coey, Rev. Sc. Instr. 77, 015106 (2006)

[161] H. Mitamura, T. Sakakibara, H. Nakamura, T. Kimura, and K. Kindo, J. Phys. Soc. Japan 81, 054705 (2012).

[162] H. Mitamura, H. Nakamura, T. Kimura, T. Sakakibara1 and K. Kindo, J. Phys.: Conf. Ser. 150, 0421126 (2009).

[163] V. Felea, P. Lemmens1, S. Yasin, S. Zherlitsyn, K. Y. Choi, C. T. Lin, and Ch. Payen, J. Phys.: Condens. Matter 23, 216001 (2011).

[164] K. Taniguchi, M. Saito, and T. Arima, Phys. Rev. B 81, 064406 (2010).

[165] T. Finger, D. Senff, K. Schmalzl, W. Schmidt, L. P. Regnault, P. Becker, L. Bohatỳ, and M. Braden, Phys. Rev. B 74, 054430 (2010)

Part V

Appendices

Appendix A

Appendix A: How to perform an experiment on D23

The steps to follow to perform an experiment on the sigle-crystal neutron diffractometer D23 with unpolarized neutrons are explained in this appendix.

Actually, the main task is to orient the sample on the instrument. Once this is done, the experiment can run and luckily, there is no need to touch the sample again until the end of it. Nevertheless, orientating a crystal on D23 can be a difficult task, due to the fact that it has to be done manually and that the reflections are collected individually.

The D23 control program is called MAD, like on many other diffractommeters at the ILL.

(i) Cell parameters of the crystal must be known. This information is given to MAD. That way, and knowing the wavelength of the neutron beam, the 2θ of each *hkl* reflection is known.

(ii) If the orientation of the main axes relative to the faces of the crystal are roughly known, work becomes easier, or at least one. For that, usually a Laue diffractogram is done before. Let us assume that we know one face of the crystal, the [010] face, the crystal will be located on the sample table with this face parallel to the neutron beam this way the *b* axis is perpendicular to the beam. If this information is lacking, the procedure becomes more compli-

cated: one has to make some hypothesis about the orientation of the crystal and go on with the orienting process.

(iii) Glue the crystal with plasticine on a goniometric head.

(iv) Once the crystal is mounted in the instrument with the b axis vertical, we know that all $(h0l)$ reflections are located in the $\nu = 0$ plane, i.e. in the equatorial plane. Therefore, we search for those reflections. For making this task easier, and if the crystal structure is known, one can calculate the structure factors for all the reflections and look for the most intense ones.

(v) Look for a $h0l$ reflection (for instance (002)): first, tell MAD to put the detector at the 2θ position that corresponds to the $(h_1 0 l_1) = (002)$ reflection, we make sure that $\nu = 0$ and we scan ω until we observe a peak on the rate meter. When it is found it must be centered (done automatically). If there is not intensity found, one should move ν and repeat the procedure (this means that the b axis is not completely vertical). Command list:

- ◇ `hkl1 0 0 2` Detector positioned at the corresponding 2θ.
- ◇ `pnu 0` $\nu = 0^\circ$.
- ◇ `pom 180` $\omega = 180^\circ$.
- ◇ `pom -180` $\omega = -180^\circ$.

When the peak is detected, stop scan and center the reflection from current position.

- ◇ `cen4 0 0 2` Reflection centered from current position and it is given the (002) name.

The latter command produces a new file called `centra.dat` with optimized values for the angles. If the former procedure is not successful, move ν and repeat the process. Remember that γ is still well positioned.

- ◇ `pnu 2` $\nu = 2^\circ$.
- ◇ `pom 180` $\omega = 180^\circ$.
- ◇ `pom -180` $\omega = -180^\circ$.

(vi) Then, center the Friedel reflection (00-2). Since the angular position of the (002) reflection is already known and the Friedel pair must be at the same 2θ, $\gamma_{(002)} = \gamma_{(00-2)}$, $\omega_{(002)} \pm 180 = \omega_{(00-2)}$ and $-\nu_{(002)} = \nu_{(00-2)}$. Hence,

- ◇ `mom 180`

◇ `pnu -x` x is the value of ν for (002).

◇ `cen4 0 0 -2`

This step is not mandatory. In fact, it is helpful to correct both the height and the precession of the sample.

(vii) Once a Friedel-pair is found, another reflection is needed. It is recommended to find an orthogonal reflection. Let us choose (200) reflection. After centering (200) and (-200) reflections, one will finish with a `centra.dat` file that looks like the following:

```
 0.0   0.0   2.0    0.0   29.673 -171.428    1.165    ...
 2.0   0.0   0.0    0.0   30.864  -81.817   -0.414    ...
 0.0   0.0  -2.0    0.0   29.754    8.611   -1.219    ...
-2.0   0.0   0.0    0.0   30.764   98.134    0.417    ...
```

where the information corresponds to h, k, l, χ, γ, ω and ν.

(viii) Thus, we end up with four reflections with their corresponding angles. Up to now, the names of the reflections were given without paying to much attention to that task. To make sure they are well indexed, one can verify it using the subroutine `indexd23`. With the cell parameters, wavelength and the motor positions of each reflection, it can index the reflections and propose which couple of indexes satisfy the observed angles. It is important to do so, even more in our situation where the structure is monoclinic, $\beta > 90^\circ$ and $\beta^* < 90^\circ$, because the indexation may be wrong, see Fig. A.1.

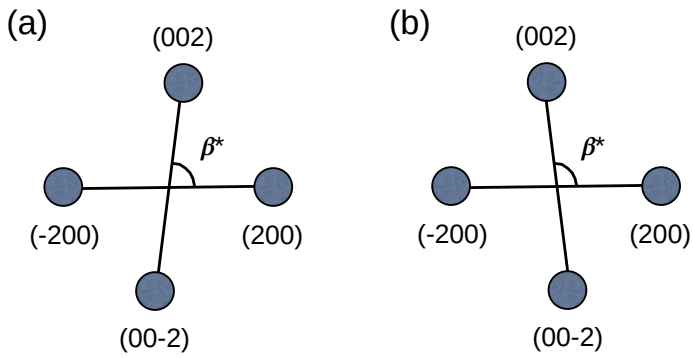

FIGURE A.1: Two possible indexations: (a) the correct one and (b) the wrong one.

(ix) Then, one should run the program `rafin` to produce a UB matrix that relates the laboratory framework (XYZ) and the crystallographic axes of the crystal. The very first time that we run this subroutine none of the parameters should be refined. We are just interested in a raw UB matrix, since there are not enough reflections collected to refine anything. Commands:

- ◇ `rafin 0 0 0 0 0 0 0 0 0 0 0 0` It runs the subroutine and does not make any refinement.
- ◇ `getub`
- ◇ `y` Confirms that you want to download the produced UB matrix.

	X	Y	Z
a^*	-0.20599	-0.02624	-0.00246
b^*	0.00293	-0.00672	-0.17372
c^*	0.02171	-0.19877	0.00805

(x) According to the previous UB matrix, b axis is almost parallel to Z (3^{rd} column) and the sample could be glued in a proper sample holder using an appropriate glue (depending on the characteristics of the material and experimental conditions). It is very unlikely that the manual alignment is so good from the beginning. Usually there is some misalignment between the b axis and Z, which are reflected in the optimized angles of the Friedel pairs in the `centra.dat` file:

(a) $\bar{\nu} = \frac{\nu_1+\nu_2}{2}$: $\bar{\nu} < 0$ or $\bar{\nu} > 0$ when the crystal is then too low or too high, respectively.

(b) $\gamma_{(hkl)} \neq \gamma_{(-h-k-l)}$ the sample is off centered. To fix this, one has to readjust the translations of the goniometer in the plane.

(c)

when all the necessary corrections are done, the centering is performed again and a new and better UB matrix is obtained. Finally the sample is glued on an aluminum pin which will be fixed in the required sample environment.

(xi) Since the sample has been taken out from the instrument, it has to be re-oriented, but this time we have a UB matrix to start with. Hence, the procedure is re-started from the beginning. Command list:

- ◇ `hkl0 0 0 2` Detector positioned at the corresponding 2θ according to the UB matrix.
- ◇ `pnu 0` $\nu = 0^\circ$.

- ◇ `pom 180` $\omega = 180^\circ$.
- ◇ `mom -180` Move omega from current position to $\omega = -180^\circ$.

Again, when the intensity peak is detected, stop scan and center the reflection from current position.

- ◇ `initialize` Re-write `centra.dat` file.
- ◇ `cen4 0 0 2` Reflection centered from current position and it is given (002) name.

(xii) Find other reflections and obtain the preliminary UB matrix. Note that if the sample is mounted in a cryostat of a magnet, and if it is off-centered with respect to the beam, the complete sample-table has to be moved and the program `XYZ` calculates how much.

(xiii) To find a good and definitive UB matrix one should center about 20 or 30 reflections and refine the UB (cell parameters or wavelength). First prepare a file of nuclear reflections and name it, `nucl.hkl` for example. Try to include all type of reflections that can be reached and do not restrict to $(h0l)$, if possible. Command list:

- ◇ `cen5 nucl.hkl` Reflections in the file `nucl.hkl` will be centred.
- ◇ `rafin 0 0 0 0 0 0 1 1 1 0 1 0` a, b, c and β will be refined (if all centered reflections are of the type $(h0l)$, b can not be refined).
- ◇ `getub`
- ◇ `y`

The experiment is ready to be started. Now the experimental conditions need to be fixed (temperature, field...). To collect data to determine a magnetic structure there are certain steps that can be followed.

(i) As for the nuclear structure where one needs to know the cell parameters to start the experiment, to study a magnetic structure one must know roughly the propagation vector $\mathbf{k}$ of the magnetic structure. To increase the accuracy in the value of the propagation vector, it is required to have a good UB matrix with cell parameters refined at the temperature at which the magnetic structure will be measured[1]. Then, $(hkl) \pm \mathbf{k}$ magnetic reflections can be centered and from the obtained angles for each reflection the propagation vector can be refined, which results in $\mathbf{k} = (k_x \pm \delta k_x, k_y \pm \delta k_y, k_z \pm \delta k_z)$.

[1]It is not mandatory to refine the parameters if we know that the do not vary.

(ii) Create a file with all reachable magnetic reflections (`magn.hkl`) and collect them. Do the same for nuclear reflections, `nucl.hkl`. The latter will provide the scale factor that, in turn will give the absolute value of the ordered magnetic moment in the magnetic refinement.

- ◇ `par sps 30000` — Monitor counts.
- ◇ `mes magn.hkl` — Measure reflections in file `magn.hkl`
- ◇ `mes nucl.hkl` — Measure reflections in file `nucl.hkl`

(iii) It might be interesting to collect nuclear data also in the paramagnetic region to see if there is any magneoelastic coupling (a change in the nuclear structure in the magnetically ordered state).

Appendix B

Representation analysis

Representation Analysis can restrict the number of possible magnetic structures of the material. Once the modulation wave vector is known, **k**, the relation between atoms in different unit cells is known, and the number of possible magnetic structures reduced. In the following lines we will show how to obtain the possible magnetic models that are compatible with the crystal structure symmetry. These are the steps to be followed:

(i) Find the little co-group $\overline{G}^k$.

$\overline{G}^k$ is formed by the rotational part of the symmetry operations of the nuclear space group that leave invariant **k**.

$$R\mathbf{k} + \mathbf{K} = \mathbf{k} \tag{B.1}$$

where **K** is a reciprocal lattice vector and $\{R|\mathbf{t}\} = g \in G$.[1]

Being $G = P2/c = \{E, 2_y, I, c\}$ the nuclear space group and the propagation vectors $\mathbf{k}_1 = (\pm\frac{1}{4}, \frac{1}{2}, \frac{1}{2})$ and $\mathbf{k}_2 = (-0.214, \frac{1}{2}, 0.457)$, depending on the magnetic phase, in both cases $\overline{G}^k = m$ (mirror plane).

(ii) Find the little group: G^k.

The little group is a space group formed by the symmetry operations of $\overline{G}^k$ including the translations. So, if we add the translations to $\overline{G}^k = m = \{E, m\}$ we end up with

$$G^k = Pc = \{E, c\} \tag{B.2}$$

[1] Symmetry operations, g, are represented as $\{R|\mathbf{t}\}$ where R is the rotational part and **t** the translational part.

(iii) Find the character table of the little co-group.

Then, the character table of the little group can be obtained using the following equation. (From now on the procedure will be detailed for $\mathbf{k} = \mathbf{k_1}$).

$$\Gamma_{k\nu}(\{R_i|\mathbf{t}_i\}) = e^{-2i\pi\mathbf{k}\cdot\mathbf{t}}\gamma_\nu(\{R_i\}) \tag{B.3}$$

where Γ are the representations.

m	#	1	m
A′	Γ_1	1	1
A″	Γ_2	1	-1

Pc	#	1	c
A′	Γ_1	1	-i
A″	Γ_2	1	i

TABLE B.1: Upper table: character table of the point group m. Lower table: character table of the space group Pc.

(iv) Apply the symmetry operations on the position of the magnetic atoms and on the magnetic moments.

The magnetic atoms Mn_1 and Mn_2 sit on $(\frac{1}{2}, y, \frac{1}{4})$ and $(\frac{1}{2}, -y, \frac{3}{2})$. The effect of the symmetry operations of the little group on the position of the magnetic atoms are the ones shown in Table B.2.

	E	c
1	1	2
2	2	1
χ_{perm}	2	0

TABLE B.2: The effect of the symmetry operations of the space group Pc on the positions of the magnetic atoms. χ_{perm} is the character corresponding to the interchange of the sites of the atoms, the trace of the matrix that represents the effect of the symmetry operation.

In order to see the effect of the symmetry operations on the magnetic moment of each atom, $\mathbf{m}$, one can use the next equation, where m_x, m_y and m_z are the

x, y and z components of the magnetic moment.

$$R\mathbf{M} = Det(R)\Gamma(R) \begin{pmatrix} m_x \\ m_y \\ m_z \end{pmatrix} \tag{B.4}$$

So,

$$E\mathbf{M} = 1 \begin{pmatrix} 1 & 0 & 0 \\ 0 & 1 & 0 \\ 0 & 0 & 1 \end{pmatrix} \begin{pmatrix} m_x \\ m_y \\ m_z \end{pmatrix} = \begin{pmatrix} m_x \\ m_y \\ m_z \end{pmatrix} \qquad \chi_{axial}(E) = 3$$

$$m_y\mathbf{M} = -1 \begin{pmatrix} 1 & 0 & 0 \\ 0 & -1 & 0 \\ 0 & 0 & 1 \end{pmatrix} \begin{pmatrix} m_x \\ m_y \\ m_z \end{pmatrix} = \begin{pmatrix} -m_x \\ m_y \\ -m_z \end{pmatrix} \qquad \chi_{axial}(m_y) = -1$$

χ_{axial} are the characters of the symmetry elements acting on the axial vectors (magnetic moments).

So, combining the effect of the symmetry operations on the sites and on the moments the total effect is shown on Table B.3.

	E	m_y
m_x^1:	m_x^1	$-m_x^2$
m_y^1:	m_y^1	m_y^2
m_z^1:	m_z^1	$-m_z^2$
m_x^2:	m_x^2	$-m_x^1$
m_y^2:	m_y^2	m_y^1
m_z^2:	m_z^2	$-m_z^1$

TABLE B.3: The total effect of the symmetry operations on the positions and magnetic moments of the magnetic atoms. The notation: $m_{component}^{atom}$.

(v) Fill the character table and decompose Γ into irreducible representations.

$$\Gamma = \Gamma_{perm} \otimes \Gamma_{axial} \tag{B.5}$$

Using the following equations the decomposition can be done.

$$\Gamma = \sum n_\nu \Gamma_\nu \tag{B.6}$$

$$n_\nu = \frac{1}{n(G^k)} \sum_g \chi_\Gamma(g) \chi^*_{\Gamma_\nu}(g) \tag{B.7}$$

Pc	1	c
Γ_1	1	-i
Γ_2	1	i
χ_{perm}	2	0
χ_{axial}	3	i
χ	6	0

TABLE B.4: The complete character table of the space group Pc and the permutational and axial part of the reducible representations. $\chi = \chi_{perm} \times \chi_{axial}$.

where $n(G_k)$ is the order of the space group, that is the number of elements in that group.

$$\Gamma = (\Gamma_1 \oplus \Gamma_2) \otimes (\Gamma_1 \oplus 2\Gamma_2) = 3(\Gamma_1 \oplus \Gamma_2) \tag{B.8}$$

There are three different basis vector for each irreducible representation that have to be found. The linear combinations of them describe a possible magnetic structure.

(vi) Find the basis vectors. The basis vectors are

$$V^{\alpha}_{k,\nu} = \sum_g \Gamma^*_{k,\nu}(g) g \cdot m^1_{k,\alpha} \tag{B.9}$$

where g are the elements of Pc in this case, ν corresponds to each representation and, $\alpha = x, y, z$.

Γ_1:	Γ_2:
$V_1^x = m_x^1 + im_x^2 = A_x$	$V_2^x = m_x^1 - im_x^2 = B_x$
$V_1^y = m_y^1 - im_y^2 = B_y$	$V_2^y = m_y^1 + im_y^2 = A_y$
$V_1^z = m_z^1 + im_z^2 = A_z$	$V_2^z = m_z^1 - im_z^2 = B_z$

A general magnetic structure associated with Γ_1 (Γ_2) can be $c_1A_x + c_2B_y + c_3A_z$ ($c_1'B_x + c_2'A_y + c_3'B_z$). We can conclude that in our crystal the relation between the moments of the atoms Mn_1 and Mn_2 is (the result is the same for $\mathbf{k_2}$ but in this case the phase instead of being $e^{-\frac{\pi i}{2}}$ is $e^{-\pi i k_z}$):

$$m_x^1 = \mp e^{-\pi i k_z} m_x^2 \qquad m_y^1 = \pm e^{-\pi i k_z} m_y^2 \qquad m_z^1 = \mp e^{-\pi i k_z} m_z^2$$

Appendix C

Constrains of the magnetic modulation due to magnetic superspace symmetry

In what follows there is a summary of the steps necessary to deduce the constraints in the magnetic modulations introduced by the symmetry elements within the superspace formalism.

The information needed to start the analysis:

(i) Paramagnetic space-group: $P2/c1'$ where $1'$ refers to the time inversion. This space group consists of all the symmetry operations of the ordinary $P2/c$ space group, plus an equal number of operations obtained by multiplying all of them by time reversal $\{1' \mid 0\ 0\ 0\ 0\}$

(ii) Magnetic atom: Mn_1 located in the $2f$ Wyckoff.

- Mn_1: $(\frac{1}{2}\ y\ \frac{1}{4})$
- Mn_2: $(\frac{1}{2}$ -y+1 $\frac{3}{4})$

(iii) Propagation vector: The incommensurate propagation vector, $\mathbf{k} = (-0.214, \frac{1}{2}, 0.457)$, lies on the symmetry line G $(\alpha\ \frac{1}{2}\ \gamma)$ of the Brillouin Zone.

From these information one can deduce the compatible superspace groups: $P2/c1'(\alpha\frac{1}{2}\gamma)00s$ and $P2/c1'(\alpha\frac{1}{2}\gamma)0ss$, as explained in Chapter 7.

The set of generators for each magnetic superspace group can be written as follows:

(i) $mG_1 : P2/c1'(\alpha\frac{1}{2}\gamma)00s$

- $\diamond$ $\{m_y \mid 0\ 0\ \frac{1}{2}\ 0\}$ The glide plane does not invert the magnetic moment and hence, the character for this operator is 1. Within this *irrep*, there is no need to make a phase shift to recover the initial configuration ($t_4 = 0$).
- $\diamond$ $\{\bar{1} \mid 0\ 0\ 0\ 0\}$
- $\diamond$ $\{1' \mid 0\ 0\ 0\ \frac{1}{2}\}$

(ii) $mG_2 : P2/c1'(\alpha\frac{1}{2}\gamma)0ss$. In this case the plane inverts the moment, the character for this operator is -1. Within this *irrep*, a phase shift has to be added to the plane operation.

- $\diamond$ $\{m_y \mid 0\ 0\ \frac{1}{2}\ \frac{1}{2}\}$ In this case the glide plane does invert the magnetic moment, that is why a phase shift must be applied to recover the initial spin configuration, i. e. to obtain an undistinguishable state.
- $\diamond$ $\{\bar{1} \mid 0\ 0\ 0\ 0\}$
- $\diamond$ $\{1' \mid 0\ 0\ 0\ \frac{1}{2}\}$

C.1 $P2/c1'(\alpha\frac{1}{2}\gamma)0ss$

In this sections all the constraints imposed by the symmetry of this superspace group will be deduced step by step.

The symmetry cards of the symmetry operators of this superspace group (obtained from equation (2.31)) are the following:

(i) $\{2_y \mid 0\ 0\ \frac{1}{2}\ \frac{1}{2}\}$: -$x_1$ x_2 -x_3+$\frac{1}{2}$ x_2-x_4+$\frac{1}{2}$ m [H_R = (0 1 0)].

Remember the effect of the two fold axis on $\mathbf{k}$:

$$\begin{aligned} 2_y \cdot \mathbf{k} &= 2_y \cdot (\alpha\frac{1}{2}\gamma) \\ &= (-\alpha\frac{1}{2} - \gamma) \\ &= -(\alpha\frac{1}{2}\gamma) + (010) \end{aligned} \tag{C.1}$$

The R_s matrix can be constructed by comparing equations (2.28) and(C.1).

$$\mathbf{R}_s = \begin{pmatrix} -1 & 0 & 0 & 0 \\ 0 & 1 & 0 & 0 \\ 0 & 0 & -1 & 0 \\ 0 & 1 & 0 & -1 \end{pmatrix} \tag{C.2}$$

and the general translation vector for the two fold axis is $t_s = (00\frac{1}{2}\frac{1}{2})$ in this case.

The same procedure should be followed to obtain the symmetry cards of the rest of operators.

(ii) $\{\bar{1}\,|\,0\,0\,0\,0\}$: -$x_1$ -x_2 -x_3 -x_4 m $\quad$ [H_R = (0 0 0)]

(iii) $\{m_y\,|\,0\,0\,\frac{1}{2}\,\frac{1}{2}\}$: x_1 -x_2 x_3+$\frac{1}{2}$ -x_2+x_4+$\frac{1}{2}$ m $\quad$ [H_R = (0 -1 0)]

(iv) $\{1'\,|\,0\,0\,0\,\frac{1}{2}\}$: x_1 x_2 x_3 x_4+$\frac{1}{2}$ -m $\quad$ [H_R = (0 0 0)]

Once we know the symmetry cards of the superspace group, we should see what are the relationships between the modulation functions of the magnetic moments. Lets start with the restrains on the spin modulations of Mn_1 because of 2_y site symmetry (which keeps the atomic position of Mn_1 invariant):

$$\begin{aligned} \mathbf{M}_1(-x_4+\frac{1}{2}+y_1) &= 2_y \cdot \mathbf{M}_1(x_4) \\ M_{1\alpha}(-x_4+\frac{1}{2}+y_1) &= M_{1\alpha}(x_4) \qquad (\alpha = y) \qquad \text{(C.3)} \\ M_{1\alpha}(-x_4+\frac{1}{2}+y_1) &= -M_{1\alpha}(x_4) \qquad (\alpha = x,z) \qquad \text{(C.4)} \end{aligned}$$

If we write the later explicitly:

$$\begin{aligned} & & \alpha = y & \\ C^s_{1y}\cos(2\pi[-x_4+\frac{1}{2}+y_1]+2\pi\phi^{x_4}_{1y}) &=& C^s_{1y}\cos(2\pi x_4+2\pi\phi^{x_4}_{1y}) & \\ C^s_{1y}\cos(2\pi[x_4-\frac{1}{2}-y_1]-2\pi\phi^{x_4}_{1y}) &=& C^s_{1y}\cos(2\pi x_4+2\pi\phi^{x_4}_{1y}) & \\ \phi^{x_4}_{1y} &=& -\phi^{x_4}_{1y}-y_1-\frac{1}{2} & \\ \phi^{x_4}_{1y} &=& -\frac{y_1}{2}-\frac{1}{4} & \text{(C.5)} \end{aligned}$$

$$\begin{aligned} & & \alpha = x,z & \\ C^s_{1\alpha}\cos(2\pi[-x_4+\frac{1}{2}+y_1]+2\pi\phi^{x_4}_{1\alpha}) &=& -C^s_{1\alpha}\cos(2\pi x_4+2\pi\phi^{x_4}_{1\alpha}) & \\ C^s_{1\alpha}\cos(2\pi[x_4-\frac{1}{2}-y_1]-2\pi\phi^{x_4}_{1\alpha}) &=& C^s_{1\alpha}\cos(2\pi[x_4-\frac{1}{2}]+2\pi\phi^{x_4}_{1\alpha}) & \\ \phi^{x_4}_{1\alpha}- &=& -\phi^{x_4}_{1\alpha}-y_1 & \\ \phi^{x_4}_{1\alpha} &=& -\frac{y_1}{2} & \text{(C.6)} \end{aligned}$$

Mn_1 and Mn_2 are related by the inversion center, so lets see what are the restrictions forced by this relation. $\{\mathrm{I}|0\,0\,0\,0\}\mathrm{Mn}_1 \rightarrow \mathrm{Mn}_2$:

$$\begin{aligned} \mathbf{M}_2(-x_4) &=& \mathbf{M}_1(x_4) \Rightarrow \text{equal amplitude and} & \text{(C.7)} \\ \cos(2\pi[-x_4+\phi^{x_4}_{2\alpha}]) &=& \cos(2\pi[x_4+\phi^{x_4}_{1\alpha}]) & \\ \phi^{x_4}_{2\alpha} &=& -\phi^{x_4}_{1\alpha} \qquad (\alpha = x,y,z). & \text{(C.8)} \end{aligned}$$

To summarize, the $P2/c1'(\alpha\frac{1}{2}\gamma)0ss$ superspace group restrains the magnetic modulations in the following way:

$$M_{1x}(x_4) = M^0_{1x}\cos[2\pi(x_4-\frac{y_1}{2})] \quad \text{(C.9)}$$

$$M_{1z}(x_4) = M^0_{1z}\cos[2\pi(x_4-\frac{y_1}{2})] \quad \text{(C.10)}$$

$$M_{1y}(x_4) = M^0_{1y}\cos[2\pi(x_4-\frac{y_1}{2}-\frac{1}{2})] = M^0_{1y}\sin[2\pi(x_4-\frac{y_1}{2})] \quad \text{(C.11)}$$

$$M_{2x}(x_4) = M^0_{1x}\cos[2\pi(x_4+\frac{y_1}{2})] \quad \text{(C.12)}$$

$$M_{2z}(x_4) = M^0_{1z}\cos[2\pi(x_4+\frac{y_1}{2})] \quad \text{(C.13)}$$

$$M_{2y}(x_4) = -M^0_{1y}\sin[2\pi(x_4+\frac{y_1}{2})] \quad \text{(C.14)}$$

There are 3 independent parameters to refine: M^0_{1x}, M^0_{1y} and M^0_{1z}. The refinement has been done using JANA2006 [61] program. The program does not use the restrictions as in equations (C.9)-(C.14) directly, but it develops those cosines and sines in cosines and sines that are just functions of x_4. So the relation between the equations (C.9)-(C.14) and the parameters that JANA2006 refines is:

$$\begin{aligned} & M^0_{1x}\cos[2\pi(x_4-\frac{y_1}{2})] \\ & = M^0_{1x}[\cos(2\pi x_4)\cos(2\pi\frac{y_1}{2})-\sin(2\pi x_4)\sin(2\pi\frac{y_1}{2})] \end{aligned} \tag{C.15}$$

$$M^0_{1x}\cos(2\pi\frac{y_1}{2}) = M^c_{1x} \tag{C.16}$$

$$M^0_{1x}\sin(2\pi\frac{y_1}{2}) = M^s_{1x} \tag{C.17}$$

C.2 $P2/c1'(\alpha\frac{1}{2}\gamma)00s$

We will see now what are the constraints imposed by the $P2/c1'(\alpha\frac{1}{2}\gamma)00s$ superspace group. The symmetry cards of the operators in this superspace group are listed below:

(i) $\{2_y \mid 0\ 0\ \frac{1}{2}\ 0\}$: -x$_1$ x$_2$ -x$_3$+$\frac{1}{2}$ x$_2$-x$_4$ m [H$_R$ = (0 1 0)].

The R_s matrix is equal to the one of the two fold axis in the previous space group, but the translational part, t_s differs.

$$\mathbf{R}_s = \left(\begin{array}{cccc|c} -1 & 0 & 0 & 0 & 0 \\ 0 & 1 & 0 & 0 & 0 \\ 0 & 0 & -1 & 0 & \frac{1}{2} \\ 0 & 1 & 0 & -1 & 0 \end{array}\right) \tag{C.18}$$

The rest of the operations are:

(ii) $\{\bar{1} \mid 0\ 0\ 0\ 0\}$: -x$_1$ -x$_2$ -x$_3$ -x$_4$ m [H$_R$ = (0 0 0)]

(iii) $\{m_y \mid 0\ 0\ \frac{1}{2}\ \frac{1}{2}\}$: x$_1$ -x$_2$ x$_3$+$\frac{1}{2}$ -x$_2$+x$_4$ m [H$_R$ = (0 -1 0)]

The constraint in the modulations due to the two fold axis are:

$$\begin{aligned}
\mathbf{M}_1(-x_4+y_1) &= 2_y\cdot\mathbf{M}_1(x_4) \\
M_{1\alpha}(-x_4+y_1) &= M_{1\alpha}(x_4) \qquad (\alpha=y) \qquad \text{(C.19)}\\
M_{1\alpha}(-x_4+y_1) &= -M_{1\alpha}(x_4) \qquad (\alpha=x,z) \qquad \text{(C.20)}
\end{aligned}$$

If we write the later explicitly:

$$\begin{aligned}
&\alpha=y \\
C^s_{1y}\cos(2\pi[-x_4+y_1]+2\pi\phi^{x_4}_{1y}) &= C^s_{1y}\cos(2\pi x_4+2\pi\phi^{x_4}_{1y}) \\
\cos(2\pi[x_4-y_1]-2\pi\phi^{x_4}_{1y}) &= \cos(2\pi x_4+2\pi\phi^{x_4}_{1y}) \\
\phi^{x_4}_{1y} &= -\phi^{x_4}_{1y}-y_1 \\
\phi^{x_4}_{1y} &= -\frac{y_1}{2} \qquad \text{(C.21)}
\end{aligned}$$

$$\begin{aligned}
&\alpha=x,z \\
C^s_{1\alpha}\cos(2\pi[-x_4+y_1]+2\pi\phi^{x_4}_{1\alpha}) &= -C^s_{1\alpha}\cos(2\pi x_4+2\pi\phi^{x_4}_{1\alpha}) \\
C^s_{1\alpha}\cos(2\pi[x_4-y_1]-2\pi\phi^{x_4}_{1\alpha}) &= C^s_{1\alpha}\cos(2\pi[x_4+\frac{1}{2}]+2\pi\phi^{x_4}_{1\alpha}) \\
\phi^{x_4}_{1\alpha} &= -\phi^{x_4}_{1\alpha}-y_1-\frac{1}{2} \\
\phi^{x_4}_{1\alpha} &= -\frac{y_1}{2}-\frac{1}{4} \qquad \text{(C.22)}
\end{aligned}$$

In this also case the inversion center relates the Mn_1 and Mn_2 as it did in the previous case, see (C.7) and (C.8). So, the modulation functions can be expressed as follows:

$$M_{1x}(x_4)=M^0_{1x}\cos[2\pi(x_4-\frac{y_1}{2}-\frac{1}{4})]=M^0_{1x}\sin[2\pi(x_4-\frac{y_1}{2})] \qquad \text{(C.23)}$$

$$M_{1z}(x_4)=M^0_{1z}\sin[2\pi(x_4-\frac{y_1}{2})] \qquad \text{(C.24)}$$

$$M_{1y}(x_4)=M^0_{1y}\cos[2\pi(x_4-\frac{y_1}{2})] \qquad \text{(C.25)}$$

$$M_{2x}(x_4)=M^0_{1x}\cos[2\pi(x_4+\frac{y_1}{2}+\frac{1}{4})]=-M^0_{1x}\sin[2\pi(x_4+\frac{y_1}{2})] \qquad \text{(C.26)}$$

$$M_{2z}(x_4)=-M^0_{1z}\sin[2\pi(x_4+\frac{y_1}{2})] \qquad \text{(C.27)}$$

$$M_{2y}(x_4)=M^0_{1y}\cos[2\pi(x_4+\frac{y_1}{2})]. \qquad \text{(C.28)}$$

The number of independent parameters in this case is the same, 3.

C.3 $P21'(\alpha\frac{1}{2}\gamma)0s$

In Chapter 7 we have seen that the superspace group $P21'(\alpha\frac{1}{2}\gamma)0s$ in the primitive lattice describes properly the magnetic structure of the multiferroic AF2 phase. Now we will derive the constraints forced by this symmetry.

The symmetry operators that are contained in this group and their symmetry cards are listed below:

(i) $P21'(\alpha\frac{1}{2}\gamma)0s$:

- $\diamond$ $\{2_y \mid 0\ 0\ \frac{1}{2}\ \frac{1}{2}\}$: -x_1 x_2 -x_3+$\frac{1}{2}$ x_2-x_4+$\frac{1}{2}$ m
- $\diamond$ $\{1' \mid 0\ 0\ 0\ \frac{1}{2}\}$: x_1 x_2 x_3 x_4+$\frac{1}{2}$ -m

Since Mn_1 and Mn_2 are related by the glide plane and this element is lost, the two Mn atoms in the crystallographic unit cell become independent. So, a priori there will be six parameters to refine (three per atom). However the magnetic modulation functions for each atom are constrained by the 2_y symmetry operation in the same way that they were in $P2/c1'(\alpha\frac{1}{2}\gamma)0ss$.

$$\begin{aligned}
\mathbf{M}_i(-x_4+\frac{1}{2}+y_i) &= 2_y\cdot\mathbf{M}_i(x_4) \\
M_{i\alpha}(-x_4+\frac{1}{2}+y_i) &= M_{i\alpha}(x_4) \qquad (\alpha=y) \qquad \text{(C.29)}\\
M_{i\alpha}(-x_4+\frac{1}{2}+y_i) &= -M_{i\alpha}(x_4) \qquad (\alpha=x,z) \qquad \text{(C.30)}
\end{aligned}$$

where the index i refers to Mn_1 and Mn_2. So, from this we can conclude that

$$\begin{aligned}
\phi_{iy}^{x_4} &= -\frac{y_i}{2}-\frac{1}{4} \qquad \text{(C.31)}\\
\phi_{i\alpha}^{x_4} &= -\frac{y_i}{2} \qquad (\alpha=x,z) \qquad \text{(C.32)}
\end{aligned}$$

and the modulation functions can be described as

$$M_{1x}(x_4) = M_{1x}^0\cos[2\pi(x_4-\frac{y_1}{2})] \qquad \text{(C.33)}$$

$$M_{1z}(x_4) = M_{1z}^0\cos[2\pi(x_4-\frac{y_1}{2})] \qquad \text{(C.34)}$$

$$M_{1y}(x_4) = M_{1y}^0\sin[2\pi(x_4-\frac{y_1}{2})] \qquad \text{(C.35)}$$

$$M_{2x}(x_4) = M_{2x}^0\cos[2\pi(x_4-\frac{y_2}{2})] \qquad \text{(C.36)}$$

$$M_{2z}(x_4) = M^0_{2z}\cos[2\pi(x_4 - \frac{y_2}{2})] \tag{C.37}$$

$$M_{2y}(x_4) = -M^0_{2y}\sin[2\pi(x_4 - \frac{y_2}{2})]. \tag{C.38}$$

C.4 Non-conventional centering X

The conditions of the modulations can be simplified if the propagation vector (α $\frac{1}{2}$ β) is changed to (α 0 β) by using a double unit cell along b. The component $\frac{1}{2}$ of the propagation vector only means that the magnetic moment, **M**, of atoms related by lattice translations (0 1 0) are in anti phase:

$$\mathbf{M} \text{ at cell } (0\,0\,0) = -\mathbf{M} \text{ at cell } (0\,1\,0)). \tag{C.39}$$

This can be described more simply by using a cell: a, $2b$, c such that now we have four Mn atoms per unit cell; but we include in the symmetry a centering (0 $\frac{1}{2}$ 0 $\frac{1}{2}$). If

$$Mn_1 : (\frac{1}{2}\,\frac{y_1}{2}\,\frac{1}{4}) \qquad Mn_2 : (\frac{1}{2} - \frac{y_1}{2}\,\frac{3}{4}) \tag{C.40}$$

$$Mn_{11} : (\frac{1}{2}\,\frac{y_1+1}{2}\,\frac{1}{4}) \qquad Mn_{22} : (\frac{1}{2} - \frac{y_1+1}{2}\,\frac{3}{4}) \tag{C.41}$$

the modulations of the atoms Mn_{11} and Mn_{22} are determined by those of Mn_1 and Mn_2:

$$\mathbf{M}_{Mn_{11}}(x_4) = \mathbf{M}_{Mn_1}(x_4 + \frac{1}{2}) \tag{C.42}$$

$$\mathbf{M}_{Mn_{22}}(x_4) = \mathbf{M}_{Mn_2}(x_4 + \frac{1}{2}) \tag{C.43}$$

The symmetry group of AF3 can then be described as $X2/c1'(\alpha 0\gamma)0ss$ with symmetry operators:

(i) $\{2_y \,|\, 0\,0\,\frac{1}{2}\,\frac{1}{2}\}$

(ii) $\{\bar{1} \,|\, 0\,0\,0\,0\}$

(iii) $\{\mathrm{m}_y \,|\, 0\,0\,\frac{1}{2}\,\frac{1}{2}\}$

(iv) $\{1' \,|\, 0\,0\,0\,\frac{1}{2}\}$

and the X meaning the centering (0 $\frac{1}{2}$ 0 $\frac{1}{2}$). The modulation function are now reduced to either cosine or sine functions:

(i) $\{2_y \mid 0\ 0\ \frac{1}{2}\ \frac{1}{2}\}$:

$$\begin{aligned}
\mathbf{M}_1(-x_4+\frac{1}{2}) &= 2_y \cdot \mathbf{M}_1(x_4) && \text{(C.44)}\\
M_{1x}(x_4) &= M^c_{1x}\cos(2\pi x_4) && \text{(C.45)}\\
M_{1z}(x_4) &= M^c_{1z}\cos(2\pi x_4) && \text{(C.46)}\\
M_{1y}(x_4) &= M^s_{1y}\sin(2\pi x_4) && \text{(C.47)}\\
& && \text{(C.48)}
\end{aligned}$$

The change of origin along x_4 can make $\{2_y \mid 0\ 0\ \frac{1}{2}\ 0\}$, and sine and cosine are interchanged.

(ii) $\{\bar{1} \mid 0\ 0\ 0\ 0\}$:

$$\begin{aligned}
\mathbf{M}_2(-x_4) &= -\mathbf{M}_1(x_4) && \text{(C.49)}\\
M_{2x}(x_4) &= -M_{1x}(x_4) = M^c_{1x}\cos(2\pi x_4) && \text{(C.50)}\\
M_{2z}(x_4) &= -M_{1y}(x_4) = M^c_{1z}\cos(2\pi x_4) && \text{(C.51)}\\
M_{2y}(x_4) &= -M_{1z}(x_4) = M^s_{1y}\sin(2\pi x_4) && \text{(C.52)}
\end{aligned}$$

Check: For the previous description, the x_4 of an atom Mn_1 was: $x_4 = \mathbf{q}\cdot(\mathbf{R} - \mathbf{r}_\nu) = \frac{k_x}{2} + \frac{k_z}{4} + \frac{y_1}{2} + \mathbf{k}\cdot\mathbf{R}$, in the new description, $x'_4 = \frac{k_x}{2} + \frac{q_z}{4} + \mathbf{k}\cdot\mathbf{R}$, hence, $\cos(2\pi x_4 - \frac{y_1}{2}) = \cos(2\pi x'_4)$.

$P21'(\alpha\frac{1}{2}\gamma)0s$ becomes $X21'(\alpha 0\gamma)0s$ and the conditions restricting $Mn_1(x_4)$ and $Mn_2(x_4)$ are maintained but their interrelations disappear.

Appendix D

How to intersect the space groups associated to mG_1 and mG_2

In the case of the symmetry operations transforming $\mathbf{k}$ into $-\mathbf{k}$, the translational part along the coordinate x_4 depends on the choice of the origin in the internal space, i. e. it depends on the global phase associated with the modulation. In order to derive the symmetry of the superposition of two active *irreps*, one must then explicitly consider this dependence. When there is a single *irrep* incommensurate modulation, one is always allowed to choose this phase as zero. However, if two primary *irrep* modulations are superposed, only one of the modulation phases can be arbitrarily chosen by fixing an origin, and the relative phase difference between the two modulations becomes physically relevant. Consequently, the global superspace symmetry depends in general on the relative phase shift of the two *irrep* magnetic modulations.

If an incommensurate system has a generic symmetry operation $\{\mathbf{R}, \theta|\mathbf{t}, \tau_0\}$, a shift of the global phase of the modulation by a quantity ϕ (in 2π units), is equivalent to a translation of the origin of the internal coordinate x_4 by $-\phi$. Under this origin shift, the above symmetry operation becomes $\{\mathbf{R}, \theta|\mathbf{t}, \tau_0 - R_I\phi + \phi\}$, where R_I is defined in equation (2.28). This means that the operations that keep $\mathbf{k}$ invariant do not change, while those transforming $\mathbf{k}$ into $-\mathbf{k}$ transform into $\{\mathbf{R}, \theta|\mathbf{t}, \tau_0 + 2\phi\}$. In our case, the inversion center and the two fold axis transform $\mathbf{k}$ into $-\mathbf{k}$, but the plane does not. Hence, the glide plane must be unchanged, whereas the inversion center and the two fold axis should be transformed.

- mG_1: $X2/c1'(\alpha\frac{1}{2}\gamma)00s$:
  - $\{\mathrm{m}_y \,|\, 0\ 0\ \frac{1}{2}\ 0\}$
  - $\{\bar{1} \,|\, 0\ 0\ 0\ 2\phi\}$
  - $\{2_y \,|\, 0\ 0\ \frac{1}{2}\ 2\phi\}$
  - $\{1|0\frac{1}{2}0\frac{1}{2}\}$
- mG_2: $X2/c1'(\alpha\frac{1}{2}\gamma)0ss$.
  - $\{\mathrm{m}_y \,|\, 0\ 0\ \frac{1}{2}\ \frac{1}{2}\}$
  - $\{\bar{1} \,|\, 0\ 0\ 0\ 2\phi'\}$
  - $\{2_y \,|\, 0\ 0\ \frac{1}{2}\ \frac{1}{2}{+}2\phi'\}$
  - $\{1|0\frac{1}{2}0\frac{1}{2}\}$

The intersection of the symmetry groups for the different primary *irrep* modes depends on their global phases. Let us start by calculating the operations derive from different ϕ values.

(i) mG_1: $\phi = 0, \frac{1}{2}$

- $\{\mathrm{m}_y \,|\, 0\ 0\ \frac{1}{2}\ 0\}$
- $\{\bar{1} \,|\, 0\ 0\ 0\ 0\}$
- $\{2_y \,|\, 0\ 0\ \frac{1}{2}\ 0\}$
- $\{1|0\frac{1}{2}0\frac{1}{2}\}$

(ii) mG_1: $\phi = \frac{1}{4}, \frac{3}{4}$

- $\{\mathrm{m}_y \,|\, 0\ 0\ \frac{1}{2}\ 0\}$
- $\{\bar{1} \,|\, 0\ 0\ 0\ \frac{1}{2}\}$
- $\{2_y \,|\, 0\ 0\ \frac{1}{2}\ \frac{1}{2}\}$
- $\{1|0\frac{1}{2}0\frac{1}{2}\}$

(iii) mG_1: ϕ = arbitrary

- $\{\mathrm{m}_y \,|\, 0\ 0\ \frac{1}{2}\ 0\}$
- $\{\bar{1} \,|\, 0\ 0\ 0\ 2\phi\}$
- $\{2_y \,|\, 0\ 0\ \frac{1}{2}\ 2\phi\}$

- $\diamond$ $\{1|0\frac{1}{2}0\frac{1}{2}\}$

(iv) mG_2: $\phi' = 0, \frac{1}{2}$

- $\diamond$ $\{\mathrm{m}_y \,|\, 0\; 0\; \frac{1}{2}\; \frac{1}{2}\}$
- $\diamond$ $\{\bar{1} \,|\, 0\; 0\; 0\; 0\}$
- $\diamond$ $\{2_y \,|\, 0\; 0\; \frac{1}{2}\; \frac{1}{2}\}$
- $\diamond$ $\{1|0\frac{1}{2}0\frac{1}{2}\}$

(v) mG_2: $\phi' = \frac{1}{4}, \frac{3}{4}$

- $\diamond$ $\{\mathrm{m}_y \,|\, 0\; 0\; \frac{1}{2}\; \frac{1}{2}\}$
- $\diamond$ $\{\bar{1} \,|\, 0\; 0\; 0\; \frac{1}{2}\}$
- $\diamond$ $\{2_y \,|\, 0\; 0\; \frac{1}{2}\; \frac{3}{2}\}$
- $\diamond$ $\{1|0\frac{1}{2}0\frac{1}{2}\}$

(vi) mG_2: ϕ' = arbitrary

- $\diamond$ $\{\mathrm{m}_y \,|\, 0\; 0\; \frac{1}{2}\; \frac{1}{2}\}$
- $\diamond$ $\{\bar{1} \,|\, 0\; 0\; 0\; 2\phi'\}$
- $\diamond$ $\{2_y \,|\, 0\; 0\; \frac{1}{2}\; \frac{1}{2}{+}2\phi'\}$
- $\diamond$ $\{1|0\frac{1}{2}0\frac{1}{2}\}$

So, now two *irrep* modes have to be intersected. Remember that both magnetic modes may have the same symmetry and therefore, one has to intersect a mG_i mode with another mG_i mode or a mG_j mode. The phase of the former will be fixed to zero.

Appendix E

Symmetry of the AF2' multiferroic phase of $Mn_{0.90}Co_{0.10}WO_4$

In the case of the 10% doped compound the polarization arises in the *ac* plane. Therefore, we should first try the $Xc1'(\alpha 0\gamma)ss$ group, which emerges from the intersection of the mG_2 mode that describes AF3 phase with another mode of the same symmetry but phase shifted, with $\Delta\phi$ arbitrary. In order to know the restrictions imposed on the magnetic modulations by this superspace group, we will repeat the procedure as for the pure compound. The symmetry operations of this group can be expressed as:

(i) $\{m_y \,|\, 0\ 0\ \frac{1}{2}\ \frac{1}{2}\}$: x_1 -x_2 x_3+$\frac{1}{2}$ x_4+$\frac{1}{2}$ m

(ii) $\{1' \,|\, 0\ 0\ 0\ \frac{1}{2}\}$: x_1 x_2 x_3 x_4+$\frac{1}{2}$ -m

In this case, Mn_1 and Mn_2 are related by glide plane. So, both atoms are not independent.

$$\begin{aligned} \mathbf{M}_2(-x_4+\frac{1}{2}) &= -m_y\mathbf{M}_1(x_4) \\ \alpha = y & \\ \phi_{1y}^{x_4}+\phi_{2y}^{x_4} &= -\frac{1}{2} \end{aligned} \tag{E.1}$$

$$\begin{aligned} \alpha = x,z & \\ \phi_{1\alpha}^{x_4}+\phi_{2\alpha}^{x_4} &= 0 \end{aligned} \tag{E.2}$$

and the modulation functions can be described as

$$M_{1x}(x_4) = M^0_{1x}\cos[2\pi(x_4+\phi_{1x})] \quad \text{(E.3)}$$
$$M_{1z}(x_4) = M^0_{1z}\cos[2\pi(x_4+\phi_{1z})] \quad \text{(E.4)}$$
$$M_{1y}(x_4) = M^0_{1y}\cos[2\pi(x_4+\phi_{1y})] \quad \text{(E.5)}$$
$$M_{2x}(x_4) = M^0_{1x}\cos[2\pi(x_4+-\phi_{1x})] \quad \text{(E.6)}$$
$$M_{2z}(x_4) = M^0_{1z}\cos[2\pi(x_4-\phi_{1z})] \quad \text{(E.7)}$$

$$M_{2y}(x_4) = M^0_{1y}\cos[2\pi(x_4-\phi_{1y}-\frac{1}{2})] = M^0_{1y}\sin[2\pi(x_4-\phi_{1y})]. \quad \text{(E.8)}$$

As there are no operations in the superspace group with $R_I = -1$ (change x_4 to $-x_4$), one of the phases can be chosen arbitrarily. The parameters that describe the magnetic structure at 2 K have been obtained from the refinement of 273 independent reflections averaged from 482 reflections with $R_{int} = 2.24$. The agreement factors and the parameters are summarized in Table E.1.

Temperature	M^s_{1x}	M^s_{1y}	M^s_{1z}	M^c_{1x}	M^c_{1y}	M^c_{z1}
2 K	-2.33(9)	-0.08(7)	-3.28(8)	0.00**	0.00(6)	-2.33(8)
	R_F = 5.17%, R_{wF} = 5.99% and R_{wF^2} = 9.95%					
** Fixed manually.						

TABLE E.1: Refined parameters of the multiferroic phase of the pure $Mn_{0.90}Co_{0.10}WO_4$ 2 K in the superspace group $Xc1'(\alpha 0\gamma)ss$.

Publications

Directly related to the thesis

(i) **I. Urcelay-Olabarria**, E. Ressouche, A. A. Mukhin, V. Yu. Ivanov, A. M. Balbashov, G. P. Vorob'ev, Yu. F. Popov, A. M. Kadomtseva, J. L. García-Muñoz, and V. Skumryev.
"*Neutron diffraction, magnetic and magnetoelectric studies of phase transitions in* $Mn_{0.90}Co_{0.10}WO_4$ *multiferroic.*"
Phys. Rev. B 85, 094436 (2012).

(ii) **I. Urcelay-Olabarria**, E. Ressouche, A. A. Mukhin, V. Yu. Ivanov, A. M. Balbashov, J. L. García-Muñoz, and V. Skumryev.
"*Conical antiferromagnetic order in the ferroelectric phase of* $Mn_{0.80}Co_{0.20}WO_4$ *resulting from the competition between collinear and cycloidal structures.*"
Phys. Rev. B 85, 224419 (2012).

(iii) **I. Urcelay-Olabarria**, J. L. García-Muñoz, E. Ressouche, V. Skumryev, V. Yu. Ivanov, A. A. Mukhin and A. M. Balbashov.
"*Lattice anomalies at the ferroelectric and magnetic transitions in cycloidal* $Mn_{0.95}Co_{0.05}WO_4$ *and* $Mn_{0.80}Co_{0.20}WO_4$ *multiferroics.*"
Phys. Rev. B 86, 184412 (2012).

(iv) **I. Urcelay-Olabarria**, J. M. Perez-Mato, J. L. Ribeiro, J. L. García-Muñoz, E. Ressouche, V. Skumryev and A. A. Mukhin.
"*Incommensurate magnetic structures of multiferroic* $MnWO_4$ *studied within the superspace formalism.*"
accepted in Phys. Rev. B.

(v) **I. Urcelay-Olabarria**, E. Ressouche, A. A. Mukhin, V. Yu. Ivanov, A. M. Kadomtseva, Yu. F. Popov, and G. P. Vorob'ev, A. M. Balbashov, J. L. García-Muñoz and V. Skumryev.
"*Evolution of $MnWO_4$ magnetic structure and electric polarization across phase transition induced by magnetic field along b axis.*"
to be submitted to Phys. Rev. B.

Other publications during the PhD period

(i) A. Faik, E. Iturbe-Zabalo, **I. Urcelay** and J. M. Igartua.
"*Crystal structures and high-temperature phase transitions of the new ordered double perovskites Sr_2SmSbO_6 and Sr_2LaSbO_6.*"
Solid State Chemistry 182 (2009) 2656-2663.

(ii) A. Faik, **I. Urcelay**, E. Iturbe-Zabalo and J. M. Igartua.
"*Cationic ordering and role of the A-site cation on the structure of the new double perovskites $Ca_{2-x}Sr_xRSbO_6$ (R = La, Sm) $(x = 0, 0.5, 1)$.*"
J. of Molecular Structure 963 (2010) 145-152.

(iii) T.I. Milenov, P.M. Rafailov, **I. Urcelay-Olabarria**, E. Ressouche, J. L. García-Muñoz, V. Skumryev, M. M. Gospodinov.
"*Magnetic behavior of $La_2CoMnO_{6-\delta}$ crystal doped with Pb and Pt.*"
Materials Research Bulletin 47 (2012) 4001Ð4005.